Approche expérimentale et numérique en morphodynamique des cours d'eau : application à la gestion de la mobilité latérale de la Moselle sauvage

Guillaume Piasny

To cite this version:

Guillaume Piasny. Approche expérimentale et numérique en morphodynamique des cours d'eau : application à la gestion de la mobilité latérale de la Moselle sauvage. Géographie. Université de Strasbourg, 2023. Français. NNT : 2023STRAH010 . tel-04633276

HAL Id: tel-04633276
https://theses.hal.science/tel-04633276
Submitted on 3 Jul 2024

UNIVERSITÉ DE STRASBOURG

ÉCOLE DOCTORALE N°413 : SCIENCES DE LA TERRE ET DE L'ENVIRONNEMENT

CNRS UMR 7362

THÈSE

présentée par :

Guillaume PIASNY

décembre 2023

pour obtenir le grade de : **Docteur de l'université de Strasbourg**

Discipline/ Spécialité : Géomorphologie, hydraulique fluviale & modélisation numérique

Approche expérimentale et numérique en morphodynamique des cours d'eau : application à la gestion de la mobilité latérale de la Moselle sauvage

THÈSE dirigée par :	
M. SCHMITT Laurent	Professeur des universités, Université de Strasbourg
THÈSE encadrée par :	
M. GARAMBOIS Pierre-André	Chargé de recherches, Aix Marseille Université – INRAE
M. FINAUD-GUYOT Pascal	Maitre de conférences, Université de Montpellier – Polytech
RAPPORTEURS :	
M. RECKING Alain	Chercheur HDR, INRAE Grenoble
M. FRANCA Mario	Professeur des universités, Karlsruhe Institut für Technology
AUTRES MEMBRES DU JURY :	
Mme ROUX Hélène	Professeur des universités, Université de Toulouse
M. HOUBRECHTS Geoffrey	Professeur des universités, Université de Liège

---

INVITÉ : M. GOETGHEBEUR Philippe Agence de l'eau Rhin-Meuse

Résumé

Cette thèse porte sur le suivi et la modélisation de la dynamique morphologique du dernier tronçon de grand cours d'eau à lit mobile du nord-est de la France, situé au sein de la réserve naturelle régionale de la "Moselle Sauvage". Ce tronçon à fort enjeux présente d'importantes évolutions latérales et verticales résultant d'activités humaines passées, notamment à la suite d'extractions de granulat et de stabilisations de berges en amont et en aval. L'évolution récente conduit à un risque de défluviation pouvant déstabiliser des ouvrages tels que le pont de Bainville-aux-miroirs.

Afin d'évaluer et d'anticiper ces évolutions, un diagnostic morphodynamique détaillé et des modélisations numériques fines ont été réalisés. Les dimensions latérales, longitudinales et temporelles des processus physiques sont abordés à des échelles spatio-temporelles emboitées sur la base (i) d'une analyse historique, (ii) d'une importante instrumentation pour le suivi de la dynamique morpho-sédimentaire et (iii) de modélisations de complexité adaptée aux données. Le suivi de terrain (4 ans) a consisté en (i) des acquisitions topo-bathymétriques (LIDAR), (ii) des mesures de niveau d'eau, de vitesse et de débit (12 limnimètres, nombreux profils ADCP) et (iii) un suivi de la charge de fond (mesures granulométriques, placettes peintes, chaînes d'érosion, 2500 traceurs RFID, mesures acoustiques, campagnes Helley-Smith).

Les modélisations hydro-sédimentaires 2D (Telemac 2D-Sisyphe) ont été mises en place pour reproduire les évolutions passées, comprendre les dynamiques actuelles et anticiper les évolutions futures du site. Les paramètres-clés de la dynamique du transport sédimentaire ont été déterminés au travers d'une méthodologie menée à des échelles spatio-temporelles croissantes, de la mise en mouvement du sédiment jusqu'à l'effet des processus couplés sur la morphologie du tronçon. On s'intéresse ainsi successivement aux contraintes critiques de mise en mouvement, au débit solide ponctuel et à l'échelle d'une crue et au transport sédimentaire multi-classes granulométriques.

L'estimation du seuil critique de mise en mouvement a été réalisé à partir de l'évaluation de la compétence de l'écoulement basée sur des placettes peintes et des traceurs RFID. La mise en évidence d'effets de masquage et de surexposition des particules sur les conditions de leur mise en mouvement a conduit à une amélioration de l'estimation de la contrainte critique.

Les mesures in situ de la charge de fond en crue ont permis de choisir et de caler une formule de transport solide adaptée au site d'étude. Des mesures indirectes de transport sédimentaire à l'aide d'un hydrophone ont permis d'estimer la dynamique du débit solide à l'échelle d'une crue. La confrontation des flux sédimentaires modélisés et obtenus par mesure acoustique révèle la richesse informative de cette dernière, en particulier une hystérésis entre flux liquide et flux solide sur l'ensemble de l'évènement, ainsi que la robustesse de l'estimation des volumes charriés.

La vitesse virtuelle de déplacement des traceurs RFID, dont nous montrons qu'elle augmente avec la taille des particules, a été utilisée pour déterminer un facteur de correction "trapping factor" du taux de transport sédimentaire en fonction de la taille des particules. Ce facteur permet d'améliorer la prise en compte de composition granulométrique de la rivière pour la modélisation de la charge de fond.

A partir de la détermination des principaux paramètres hydrodynamiques et de transport sédimentaire sur des tronçons relativement rectilignes, il a également été possible d'investiguer la dynamique latérale. La modélisation morphodynamique d'un méandre a été initiée sur la base d'un suivi fin réalisé au cours de la thèse (suivi photogrammétrique, profils de vitesses d'écoulement en crue, traçage de la charge de fond provenant du sapement de berge).

Cette recherche doctorale a permis de produire un jeu de données particulièrement varié et abondant, sans précédent pour ce type d'étude, d'améliorer la connaissance des processus physiques morpho-sédimentaires et de mettre au point des modélisations pertinentes, ces deux derniers volets étant combinés de façon inédite. Cette base doit permettre de proposer des scénarios d'évolution morpho-sédimentaire, pour différents forçages hydrologiques et choix opérationnels, et ainsi d'éclairer la prise de décision en terme de gestion durable de la Moselle Sauvage.

L'ensemble de cette recherche interdisciplinaire est transposable à toute rivière alluviale présentant d'importants enjeux de gestion.

Abstract

This thesis deals with the monitoring and modelling of the morphological dynamics of the last reach of large mobile gravel-bed river in north-eastern France, located within the "Wild Moselle" regional nature reserve. This reach of interest has experienced significant lateral and vertical adjustments as a result of past human activities, notably sediment extraction and bank stabilization upstream and downstream. Recent evolutions have led to a risk of avulsion, which could destabilize structures such as the Bainville-aux-miroirs bridge.

In order to assess and anticipate these changes, a detailed morphodynamic diagnosis and detailed numerical modelling were carried out. The lateral, longitudinal and temporal dimensions of the physical processes are addressed at embedded spatio-temporal scales based on (i) a historical analysis, (ii) extensive instrumentation for monitoring morpho-sedimentary dynamics and (iii) modelling of a complexity adapted to the data. Field monitoring (4 years) consisted of (i) topo-bathymetric acquisitions (LIDAR), (ii) water level, velocity and flow measurements (12 limnimeters, numerous ADCP profiles) and (iii) bedload monitoring (grain size measurements, painted patches, erosion chains, 2.500 RFID tracers, acoustic measurements, Helley-Smith campaigns).

2D hydro-sediment modelling (Telemac 2D-Sisyphe) was used to reproduce past developments, understand current dynamics and anticipate future developments at the site. The key parameters of sediment transport dynamics were determined using a methodology based on increasing spatiotemporal scales, from the beginning of the sediment motion to the effect of coupled processes on the morphology of the section. We focus successively on the critical bed shear stress for sediment transport, on bedload transport punctual and at a flood scale, and on multi-grain class sediment transport.

The critical threshold for movement was estimated by evaluating flow competence using painted bed patches and RFID tracers. The identification of hiding and exposure effects on the conditions under which particles are set in motion led to an improved estimate of the critical shear stress.

In situ measurements of the bedload were used to select and calibrate a solid transport formula adapted to the study site. Indirect measurements of sediment transport using an hydrophone enabled us to estimate the dynamics of solid discharge on a flood scale. Comparison of the sediment discharge modelled and those obtained by acoustic measurement revealed the richness of the latter, in particular the hysteresis between liquid and solid discharge over the entire event, as well as the robustness of the carried estimated volumes.

The virtual velocity of RFID tracers, which we show increases with particle size, was used to determine a trapping factor for the sediment transport rate as a function of particle size. This factor allows us to take better account of the granulometric composition of the river when modeling the bedload.

By determining the main hydrodynamic and sediment transport parameters on a relatively straight reach, it was also possible to investigate lateral dynamics. Morphodynamic modelling of a meander was initiated on the basis of detailed monitoring carried out during the thesis (photogrammetric monitoring, velocity profiles, eroded bank material tracking).

This doctoral research has produced a particularly varied and abundant dataset, unprecedented for this type of study, improved our knowledge of physical morpho-sedimentary processes and enabled us to develop relevant modelling, the last two aspects being combined in an unprecedented way. This basis makes it possible to propose morpho-sedimentary evolution scenarios, for different hydrological forcings and operational choices, and thus to inform decision-making in terms of sustainable management of the Moselle river.

All of this interdisciplinary research can be transposed to any alluvial river presenting major management challenges.

Remerciements

Je tiens à exprimer ma profonde gratitude envers mes co-directeurs de thèse, **Laurent Schmitt**, **Pierre-André Garambois** et **Pascal Finaud-Guyot**, pour leur dévouement et leur bienveillance tout au long de cette aventure. Travailler à vos côtés à été un privilège et une expérience inestimable tant du point de vue professionnel que personnel. Laurent, merci d'avoir cru en moi et de m'avoir permis de réaliser cette thèse dans les meilleurs conditions possibles, Pierre, merci de m'avoir permis de m'épanouir et de progresser scientifiquement, et Pascal, merci pour ta pédagogie et ton aide dans l'encadrement des étudiants.

J'aimerais remercier l'**Agence de l'eau Rhin-Meuse** et à la région **Grand Est** pour leur soutien financier sans lequel cette thèse n'aurait pas été possible. De plus, je tiens à remercier l'INSA de Strasbourg pour sa participation à l'achat d'un ADCP, un instrument qui a grandement contribué à la réussite de ce travail de recherche.

Je souhaite remercier les rapporteurs **Alain Recking** et **Mario Franca**, ainsi que les examinateurs **Goeffrey Houbrechts** et **Hélène Roux** pour m'avoir fait l'honneur d'accepter d'évaluer cette thèse. Un grand merci pour vos expertises, relectures et analyses attentives, ainsi que pour vos remarques détaillées, qui m'ont permis, je l'espère, de prendre davantage de recul et d'améliorer mon manuscrit.

Je voudrais exprimer ma sincère reconnaissance envers les membres de mon comité de suivi de thèse, **Kamal El Kadi Abderrezzak** et **Stéphane Rodrigues**, pour leur disponibilité et leurs conseils avisés qui ont grandement contribué à l'avancement de mes travaux de recherche.

Je désire remercier chaleureusement toutes les personnes avec qui j'ai eu la chance de collaborer et qui m'ont permis d'acquérir de la donnée ou de développer de nouvelles compétences dans le suivi des évolutions morphologiques (**Mathieu Koehl** et **Samuel Guillemin**), l'estimation du transport de la charge de fond (**Thomas Geay** et **Sébastien Zanker**) et la modélisation hydro-sédimentaire 2D (**Kamal El Kadi Abderrezzak**, **Riadh Ata** et **Eddy Langendoen**).

Un grand merci à tous mes collègues du Laboratoire Image Ville et Environnement pour leur accueil et leur soutien tout au long de ma thèse. Je tiens plus particulièrement à remercier **Estelle Baehrel** pour sa très grande disponibilité, **Grzegorz Skupinski** pour sa polyvalence, « grand frère » **David Eschbach** pour son soutien indéfectible, **Valentin Chardon** pour son aide précieuse et **Gilles Rixhon** pour sa bienveillance, sans oublier toutes celles et ceux qui m'ont accompagné au quotidien ou sur le terrain : Jordane, Etienne, Agnès, Cassandra, Caline, Quentin, Aurélia, Benoît Valentin et Romain.

Merci aux collègues de la plateforme hydraulique de l'INSA de m'avoir accueilli et intégré au sein de l'équipe MécaFlu. Cette opportunité a été très enrichissante et m'a permis d'élargir mes connaissances en modélisation physique et numérique des écoulements. Je tiens particulièreme à remercier **Léandro Duarte**, qui a toujours été présent pour répondre à mes questions, ainsi que **Guilhem** et **Nicolas Dellinger** avec qui j'ai passé de bons moments, que ce soit autour d'un café ou d'un verre.

Tous mes remerciements aux membres du Conservatoire des Espaces Naturels de Lorraine de Bainville-aux-miroirs, pour m'avoir ouvert leurs portes lors de mes missions de terrain. Je tiens tout spécifiquement à remercier **Cathy Gruber**, avec qui j'ai eu un réel plaisir à travailler tout au long de cette étude. J'en profite également pour remercier Monique, dit « Moon », qui m'a accueillie dans son établissement et qui a toujours été aux petits soins pour moi, de même que les différents agriculteurs qui ont dépanné mon véhicule.

Mille mercis aux stagiaires, étudiants ou connaissances m'ayant aidé à collecter et/ou traiter de la donnée : Michel, Valentin, Hugo, Guillaume, Thomas, Lara, Laure, Doriane et Juliette.

Je remercie chaleureusement mes différents colocataires, Dudu, Antoine, Salomé, Baptiste et Florian pour leur soutien et leur bienveillance durant ces années de thèse. Je tiens également à remercier du fond du cœur mes amis, Marc, Lola, Philippe, Franck et leurs moitiés, pour m'avoir épaulé au cours de cette aventure. Je souhaite enfin dire un très grand merci aux GE pour leur soutien inestimable et plus particulièrement à Colin, Dada, Dudu, Hélène, Julie et Madou pour leur aide sur le terrain.

Merci infiniment à tous les membres de ma famille, ma mère qui a bravé sa peur de l'eau pour m'accompagner en bateau (troué !) sur le terrain, mon grand-père qui a toujours été là pour moi et sans qui je ne serais pas qui je suis, ma marraine qui est venue me récupérer en rade à la gare, mon cousin qui est venu m'aider à la dernière minute pour faire des mesures de charriage depuis le pont et Jeanmi et kitou pour m'avoir accueilli pendant la COVID.

Enfin, du plus profond de mon cœur, un immense merci à ma copine Juliette qui s'est engagée corps et âme à mes côtés. Tu as toujours été là pour discuter de mes galets et de mes galères, et a su trouver les mots justes pour m'aider à avancer. Merci pour tout, de la mesure acoustique au petit matin du 25 décembre à la relecture de ce manuscrit jusqu'au bout de la nuit; sans toi je n'aurais jamais pu y arriver ! <3

Un dernier mot pour Aro, alias Bibu, mon fidèle compagnon lagomorphe. Merci de m'avoir accompagné durant toutes ces années. Sache que ta présence a été d'un très grand soutien.

Contents

1 Introduction **9**
1.1 Dynamique morphologique des cours d'eau 9
1.1.1 Le système fluvial 9
1.1.2 Fonctionnement du système fluvial 10
1.1.3 Ajustements spatio-temporels des cours d'eau 12
1.1.4 Anthropisation des cours d'eau 14
1.2 Processus physiques du transport sédimentaire 15
1.2.1 Contrainte de cisaillement 15
1.2.2 Mise en mouvement des sédiments 17
1.2.3 Taux de transport sédimentaire 20
1.3 Modélisation morpho-dynamique 23
1.3.1 Modélisation hydraulique 23
1.3.2 Modélisation morpho-sédimentaire 26
1.4 Objectifs et démarche scientifique 28

2 Présentation et évolutions morphologiques de la Moselle **31**
2.1 Caractéristiques topographiques et géologiques du bassin versant 31
2.1.1 Dans le massif des Vosges 31
2.1.2 Le plateau lorrain 32
2.1.3 Le tronçon d'étude 34
2.2 Caractéristiques hydrologiques de la Moselle 35
2.2.1 Régime hydrologique de la Moselle 35
2.2.2 Hydrologie de la Moselle dans les Vosges 37
2.2.3 Hydrologie de la Moselle dans le plateau lorrain 38
2.2.4 Hydrologie des affluents de la Moselle 40
2.3 Anthropisation de la vallée de la Moselle 42
2.3.1 Aménagements antérieurs au XIXème siècle 42
2.3.2 Aménagements du XIXème siècle 44
2.3.3 Extraction de granulats en lit mineur 46
2.3.4 Extractions de granulats en lit majeur 48
2.3.5 Capture de la Moselle par une gravière 50
2.3.6 Prélèvements en eau potable 52
2.4 Conséquences sur le fonctionnement morpho-sédimentaire de la "Moselle Sauvage" 53
2.4.1 Grands traits des évolutions géomorphologiques entre 1950 et 1980 53
2.4.2 Déstabilisation de l'équilibre morphodynamique entre 1980 et 1990 54
2.4.3 Réajustement morphologique de la Moselle entre 1990 et 2000 57

3 Effective determination of critical bed shear stress from multi-source measurement of flow competence for 2D hydro-sedimentary modelling 63
3.1 Introduction 63
3.2 Study site 66
3.3 Methods 68
    3.3.1 Flow competence estimation 69
    3.3.2 Bed shear stress estimation 72
    3.3.3 Assessment of the critical shear stress estimation 75
3.4 Results and discussion 76
    3.4.1 Flow competence estimation 76
    3.4.2 Critical bed shear stress estimation 80
    3.4.3 Assessment of the critical shear stress estimation 85
3.5 Conclusion 87

4 Flood scale dynamic bedload transport estimation through acoustic measurements compared to 2D hydro-sedimentary modeling 89
4.1 Introduction 89
4.2 Study site 91
4.3 Methods 92
    4.3.1 Acoustic-based estimation of the bedload transport 93
    4.3.2 Hydraulic model-based estimation of the bedload transport 98
4.4 Results and discussion 104
    4.4.1 Acoustic model calibration 104
    4.4.2 Numerical model calibration 110
    4.4.3 Comparison of bedload fluxes estimated using acoustic and numerical models 114
4.5 Conclusion 118

5 Calibration of non-uniform bedload transport 2D model using particle tracing 121
5.1 Introduction 121
5.2 Study site 125
5.3 Methods 126
    5.3.1 Tracer travel distance estimation 128
    5.3.2 Duration of competent flow 131
    5.3.3 Calibration of the non-uniform sediment transport 136
5.4 Results and discussion 140
    5.4.1 Tracer travel distance estimation 140
    5.4.2 Duration of competent flow 143
    5.4.3 Calibration of non-uniform sediment transport 147
5.5 Conclusions 152

6 General conclusions and perspectives 155
6.1 Conclusion Générale 155
6.2 Perspectives de travail 157
    6.2.1 Modélisation de la mobilité latérale 158
    6.2.2 Modélisation d'un recoupement de méandre 160
    6.2.3 Approfondissement des résultats des suivis morpho-sédimentaires 160
    6.2.4 Co-construction de scénarios de gestion durable de la mobilité latérale de la Moselle sauvage 161

Bibliography 169

Chapitre 1

Introduction

1.1 Dynamique morphologique des cours d'eau

1.1.1 Le système fluvial

En géomorphologie fluviale, l'approche systémique appliquée au cours d'eau repose sur deux concepts fondamentaux : le système fluvial et l'hydrosystème fluvial. Le concept de système fluvial défini par Schumm (1977) s'intéresse à l'organisation spatiale du transfert des sédiments dans la dimension longitudinale d'un bassin versant selon trois grands secteurs : (i) une zone de production située en tête de bassin versant où l'érosion des versants domine, qui permet d'alimenter le système fluvial en sédiments, (ii) une zone de transfert où le budget érosion/dépôt est globalement nul, qui asssure le transit des sédiments au sein du système et (iii) une zone de stockage où le processus de dépôt est dominant, qui permet le développement progressif de formes d'accumulations sédimentaires (Figure 1.1).

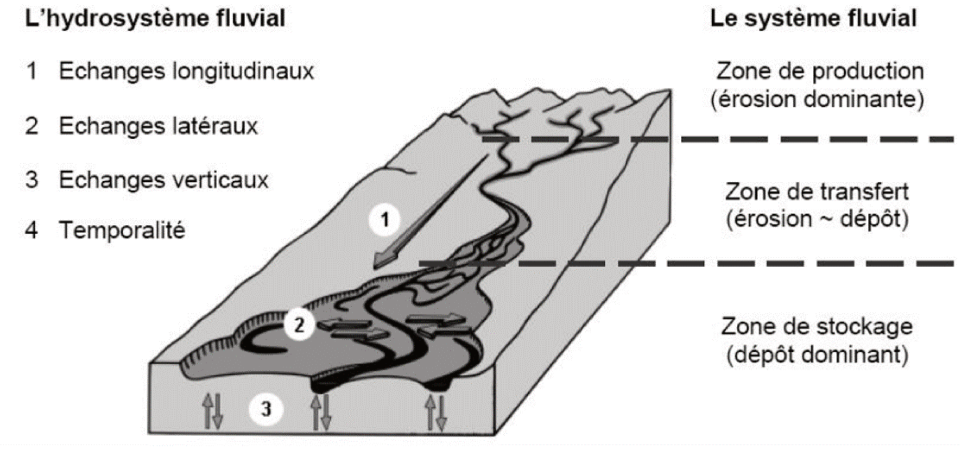

FIGURE 1.1 : Les quatre dimensions de l'hydrosystème fluvial d'après Amoros and Petts (1993).

Le concept d'hydrosystème fluvial défini par Amoros and Petts (1993) est un sous-ensemble du système fluvial et se rapporte à un tronçon de cours d'eau incluant son lit mineur, son lit majeur, sa nappe d'accompagnement et les milieux aquatiques et riverains qu'ils contiennent au sein du bassin versant. L'hydrosystème fluvial se focalise sur les flux de matière (eau, sédiments, nutriments, matière organique), d'énergie et d'organismes vivants dans quatre dimensions : (i) longitudinale entre les zones de production et de stockage (ii) latérale entre la rivière et la plaine alluviale ou entre le chenal principal et les chenaux latéraux, (iii) verticale entre la rivière et la nappe d'accompagnement et (iv) temporelle d'un évènement hydrologique à des évolutions pluri-séculaires voire pluri-millénaires, incluant les impacts anthropiques (Arnaud and Schmitt). Ces échanges sont multi-directionnels et peuvent être analysés à des échelles spatiales emboitées, du bassin versant aux microhabitats. On s'intéressera dans ce travail à des échelles allant de la section en travers de cours d'eau à des biefs de plusieurs kilomètres.

1.1.2 Fonctionnement du système fluvial

Le transfert des sédiments au sein d'un système fluvial résulte de processus d'érosion, de transport et de dépôt, contrôlés par la capacité de transport de l'écoulement et la disponibilité des matériaux. Cette capacité de transport, i.e. la capacité de travail que peut effectuer une rivière, est définie en fonction de la puissance de l'écoulement Ω $[W/m]$, qui correspond au produit de la pente de la ligne d'énergie J $[m/m]$, du débit liquide Q $\left[m^3/s\right]$ et le poids spécifique de l'eau $\gamma = \rho g$ $\left[N/m^3\right]$, avec ρ $\left[kg/m^3\right]$ la masse volumique de l'eau et g $\left[m/s^2\right]$ l'accélération de la gravité) (Bagnold, 1966). La puissance spécifique ω permettant de comparer des systèmes de tailles et de caractéristiques sédimentologiques différentes est alors définie comme étant le rapport entre la puissance brute Ω et la largur du lit w :

$$\omega = \frac{\Omega}{w} = \frac{\gamma J Q}{w} \tag{1.1}$$

La pente de la ligne d'énergie dépend de la topographie locale, tandis que le débit liquide varie en fonction du type de climat et des variabilités météo-hydrologiques induites, des propriétés physiques du bassin versant (nature des roches, du sol, du couvert végétal et de l'occupation des sols du bassin versant). Cette puissance quantifie l'énergie mécanique de l'écoulement transitant dans le système, dont une partie est dissipée via le transport des sédiments, que ce soit par charriage ou dans une moindre mesure par suspension. Le charriage correspond au transport sur le fond, de particules grossières de diamètre $D > 0.5mm$, se déplaçant par glissement, roulement ou saltation (Bravard and Petit, 1997; Knighton, 1998).

La suspension correspond au transport de particules fines, se déplaçant dans la colonne d'eau, sous l'effet des fluctuations verticales de la vitesse de l'écoulement. Le transport de la charge de fond induit la majorité des évolutions morphologiques du cours d'eau, tandis que le dépôt de la charge en suspension dans le lit majeur favorise la stabilité des berges et la végétalisation du lit. Les matériaux transportés par le cours d'eau peuvent provenir du lit mineur, par incision du « matelas » alluvial, ou du lit majeur par érosion des berges. Leur disponibilité dépend (i) de la morphologie et du remplissage du fond de vallée, dont la largeur et l'épaisseur influence respectivement les dynamiques latérales et verticales du cours d'eau, (ii) de la nature des alluvions du fond de vallée, dont la granulométrie et le degré de cohésion déterminent leur érodabilité et (iii) de la présence de végétation rivulaire, dont la nature et la densité tend à limiter l'érosion des berges (Beeson and Doyle, 1995). Ces paramètres varient en fonction de la lithologie du bassin versant, qui dépend de l'histoire géologique ancienne ou récente de la région, et de son occupation du sol, qui évolue en fonction du climat et des actions anthropiques.

Les liens fonctionnels entre les principales composantes du système fluvial et les variables de contrôle, établis à partir d'une approche typologique par Schmitt (2010) sont présentés dans la Figure 1.2.

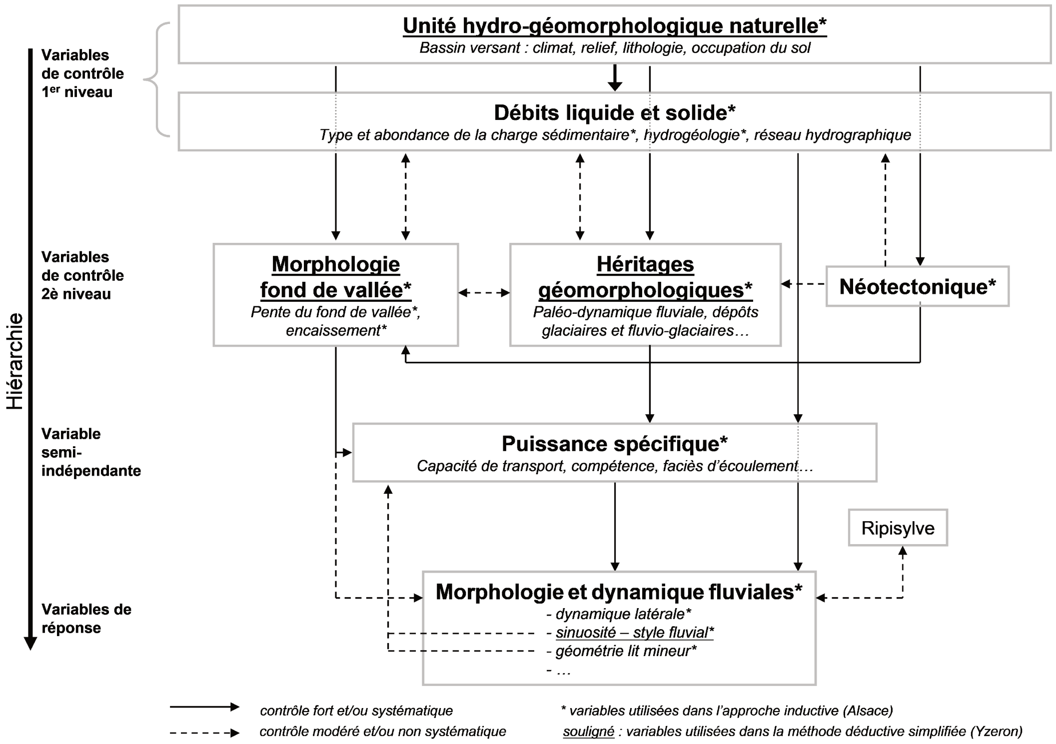

FIGURE 1.2 : Modèle conceptuel hiérarchique des liens fonctionnels entre les principales composantes du système fluviale, d'après Schmitt (2010).

Localement, en fonction de sa capacité de transport et des apports sédimentaires (volume et granulométrie), le cours d'eau adapte sa morphologie et la rugosité de son lit, pour permettre le transit des débits liquides et solides tout en minimisant les pertes d'énergie (Yang et al., 1981; White et al., 1982; Davies and Sutherland, 1983). Cette adaptation de la morphologie du cours d'eau s'opère principalement via l'ajustement de trois grandeurs : la pente du fond I, la largeur au miroir W et la hauteur d'eau h (Richards, 1982), qui représentent les degrés de liberté du système (Hey, 1988). Le système fluvial est donc un système ouvert à processus-réponse (Schumm, 1977; Knighton, 1998) dont les formes ou les différents paramètres géométriques (variables internes ou variables de réponse), résultant de l'interaction des écoulements liquides et solides (variables externes ou variable de contrôle ; semi-dépendantes), fluctuent autour de conditions moyennes. Ces états moyens résultent d'un équilibre dynamique du système fluvial, défini par (Lane, 1955) comme un équilibre entre flux liquides et solides : le flux liquide, qui s'écoule sur une pente donnée, possède une énergie mécanique qui lui permet de transporter, sous réserve de disponibilité des matériaux, une quantité déterminée de sédiments d'une taille donnée.

La variabilité naturelle des variables de contrôle de la morphologie et de la dynamique fluviale, hiérarchisées dans la figure 1.2, se traduit par une diversité de morphologies et dynamiques fluviales.

1.1.3 Ajustements spatio-temporels des cours d'eau

À l'échelle d'un réseau hydrographique, les caractéristiques physiques du système fluvial évoluent de manière longitudinale (Montgomery and Buffington, 1997). D'amont en aval, la pente et la taille des sédiments diminue, tandis que le débit et la disponibilié en sédiment augmente (Church, 2002; Peiry, 1989). Cette évolution des caractéristiques physiques entraine une structuration longitudinale de la morphologie des cours d'eau et de leur morphodynamique (Rosgen, 1994; Peiry, 1989). Cette structuration n'est cependant pas continue du fait des variations locales de la capacité de transport ou de la fourniture sédimentaire, par exemple au droit des confluences (Rice et al., 2008), ainsi que de contrôles physiques locaux (affleurement rocheux, rétrécissement de la vallée, etc.). Le système fluvial se caractérise ainsi par une succession de tronçons "homogènes", séparés par des discontinuités en termes de transport sédimentaire et d'ajustements morphodynamiques. Dans un tronçon homogène, pour une capacité de transport donnée (i) un excédent de charge de fond provenant de l'amont entraîne une multiplication des chenaux, pouvant aboutir à la formation d'un lit en tresses, alors (ii) qu'un déficit de charge de fond induit une concentration des écoulements dans un chenal unique, éventuellement en contraction, plus ou moins sinueux voire méandriforme. Un style intermédiaire existe, les chenaux divagants, caractérisés par une dynamique active dans un lit moyen large, alternant des portions sinueuses à chenal unique et des portions en tresses (Church, 1983; Ferguson and Werritty, 1983; Rice et al., 2009; Malavoi and Bravard, 2010). Une schématisation des principaux styles et formes fluviales, dans leur dimension longitudinale et latérale en lien avec les facteurs de contrôle, est présentée Figure 1.3.

Les lits en tresses se retrouvent principalement en piémont où la rivière a un espace de liberté suffisant et une faible pente (ex. Brahmapoutre, Pô, Durance). Ils se caractérisent par des chenaux multiples divergeants et convergeants, très mobiles dans l'espace et dans le temps. Ces chenaux instables sont séparés par des bancs pas ou peu végétalisés du fait de l'arrachement de la végétation qui s'y développe lors de crues annuelles ou biennales, conduisant à un rajeunissement fréquent de la végétation alluviale (Tal and Paola, 2010). Pour caractériser les différents motifs de tressage, plusieurs indices ont été proposés, en se basant notamment sur la mesure du nombre de chenaux actifs le long de transects perpendiculaires à l'axe de l'écoulement (Ashmore, 1991; Bridge, 2005), ou sur le rapport de la longueur totale des chenaux à la longueur principale du chenal (Mosley, 1981; Richards, 1982; Peiry, 1989).

Les rivières à méandres sont généralement des cours d'eau de plaine aux pentes moyennes ou faibles présentant un rapport d'aspect (ratio de la longueur du cours d'eau sur sa profondeur moyenne) moyen ou faible (Knighton, 1998). Les rivières méandriformes se caractérisent par un chenal unique sinueux dont l'indice de sinuosité du tracé en plan est supérieur à 1,3 (Brice, 1975; Schumm, 1977) ou 1,5 (Leopold and Wolman, 1957; Leopold et al., 1964). Cet indice de sinuosité correspond au rapport entre la longueur curviligne du lit et la longueur de l'axe central de l'enveloppe de méandrage (Malavoi and Bravard, 2010) ou de l'axe passant par tous les points d'inflexion de la rivière (Allen, 1984). Les méandres se distinguent selon deux grands types : (i) les méandres encaissés, qui se développent en incisant le substratum pour former une vallée encaissée ou un canyon, caractérisés par une dynamique très lente (ex. Colorado ou la basse vallée de la Seine) et (ii) les méandres libres, qui se forment à la surface de la plaine alluviale, sont caractérisés par une grande mobilité latérale (ex. Yukon). La sinuosité des méandres libres, inversement proportionnelle au débit solide amont, a tendance à augmenter en fonction de l'érodabilité des berges (Schumm, 1963), qui est liée à la présence de sédiments fins (limons, argiles) et de la végétation de berge. Le développement de ces méandres peut être limité latéralement par la vallée encaissante, pouvant conduire à une dissymétrie du tracé en plan.

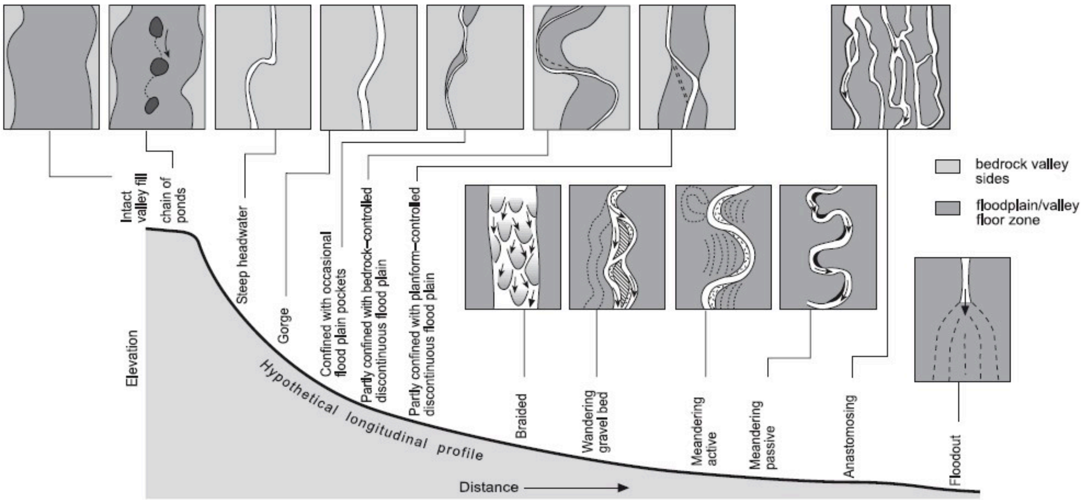

Valley setting	Laterally un–confined	Confined	Partly – confined	Laterally unconfined					
Dominant instream geomorphic units		Sculptured erosional bedrock	Sculptured or erosional and some depositional	Depositional mid–channel		Depositional bank–attached		Sculptured, erosional fine–grained	
Flood plain type	Low energy, fine–grained	n/a	High energy, non–cohesive or cohesive	Medium energy, non–cohesive			Low energy, fine–grained		
Dominant flood plain formation process	Vertical accretion	n/a	Vertical accretion	Lateral accretion and braid channel accretion			Vertical accretion		
Dominant forms of lateral instability	n/a		Channel expansion and contraction	Thalweg shift	Avulsion	Meander growth and shift		Avulsion	n/a
Number of channels	None	One		> 3	< 3	One			None
Sinuosity	n/a	1 – 1.05			Variable	> 1.3			n/a
Channel geometry	n/a	irregular	asymmetrical moderate $w:d$	irregular high $w:d$		asymmetrical moderate $w:d$		symmetrical or compound moderate $w:d$	n/a
Slope	Low	→ Decreasing channel gradient from very steep to low →							
Stream power	Low	→ Decreasing stream power from very high to low →							
Bed material texture	Fine-grained	→ Decreasing sediment calibre from boulders to fine-grained →							
Primary controls on river morphology	low slope fine-grained no channel	high slope confined valley imposed morphology	high slope & energy partly-confined valley sediment stores reworked	high energy non-cohesive banks bedload dominated		moderate energy freely-adjusting mixed load dominated	low energy cohesive banks suspended load dominated		

FIGURE 1.3 : Vue longitudinale et en plan des formes et processus fluviaux et des facteurs de contrôle associés, d'après Brierley and Fryirs (2013).

Si les formes fluviales se répartissent dans l'espace en fonction de leur position au sein du système fluvial, elles évoluent également dans le temps (Figure 1.4). Les variations temporelles des facteurs de contrôle (débits liquides et solides) entrainent des ajustements morphologiques sur différentes échelles temporelles. La variation du débit liquide lors d'une crue conduit à un ajustement des mésoformes du lit (dunes, bancs alluviaux, etc.) (Jackson, 1976), la variation interannuelle du régime hydrologique induit une évolution de la section en travers et du tracé en plan du cours d'eau (Doering et al., 2007), tandis que la variation des apports liquides et/ou solides, liée à des modifications climatiques ou anthropiques sur une échelle temporelle pluri-décennale à pluri-séculaire, entraîne un ajustement du profil en long du cours d'eau (Bravard and Peiry, 1993). Ces ajustements fluviaux, sur différentes temporalités, peuvent évidemment se combiner, conduisant à des réponses fluviales complexes (Schumm, 1973).

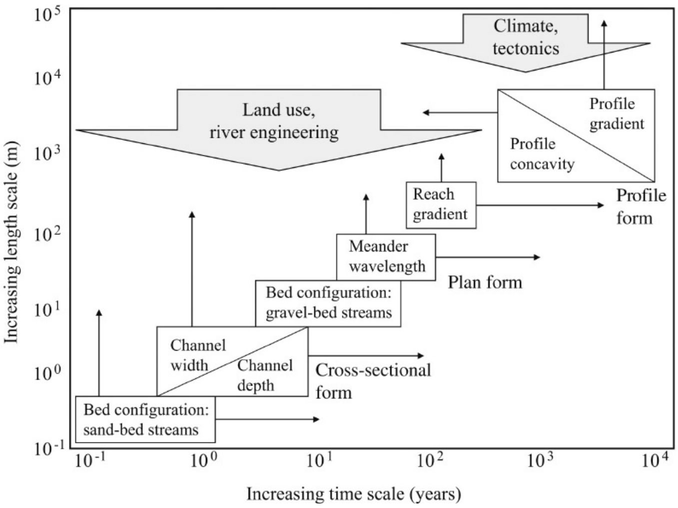

FIGURE 1.4 : Echelles temporelles et spatiales de l'ajustement des différentes composantes morphologiques du chenal. Les longueurs, indicatives, sont appliquées à un cours d'eau tempérés, d'après Knighton (1998).

1.1.4 Anthropisation des cours d'eau

De nombreux cours d'eau ont été aménagés par l'Homme afin de réduire les risques d'inondation, de développer la production d'électricité, d'améliorer la navigation fluviale ou encore d'augmenter les surfaces cultivables (Bravard, 1994). De plus, les cours d'eau ont été exploités comme sources de matériaux de construction, et de grandes quantités d'alluvions ont été prélevées des lits mineurs et majeurs pour répondre aux besoins croissants en granulats pour la construction d'infrastructures routières ou de logements (Edelblutte, 2000). La modification des variables de contrôle de l'hydrosystème (régime hydrologique et transit sédimentaire) résultant de ses activités anthropiques a conduit à une altération de la dynamique hydromorphologique et des fonctionnalités écologiques des cours d'eau (Grospretre, 2011). Parmis ces pressions anthropiques, on distingue des actions (i) directes sur la morphologie du lit et des berges (chenalisation, recoupement de méandres, construction d'ouvrages latéraux et transversaux, suppression de la végétation rivulaire, prélèvements d'eau et de matériaux, etc.) et (ii) indirectes (modification de l'occupation du sol et du réseau de drainage à l'échelle du bassin versant, transferts hydriques inter-bassins, etc.) (Dinger et al., 1982; Landon, 2007).

- La chenalisation consiste à modifier le tracé en plan et/ou la géométrie du lit à travers différents types d'interventions (recalibrage, rectification, endiguement en berge, reprofilage, stabilisation de berge, entretien et curage), afin d'augmenter la capacité hydraulique ou le tirant d'eau pour réduire les risques d'inondation ou faciliter la navigation (Brookes, 1988). La modification du tracé en plan et de la géométrie du cours d'eau engendre une augmentation de la pente et du débit à pleins bords, ce qui tend à entrainer une incision du chenal. La stabilisation des berges interrompt la fourniture latérale en sédiments et contribue à amplifier cette incision du lit (Wasson et al., 1995).

- Le creusement d'une fosse d'extraction sédimentaire dans le lit mineur d'un cours d'eau conduit à interrompre localement le transit sédimentaire aval par piégage des sédiments. En amont, l'augmentation locale de la pente de la ligne d'eau accroit la capacité de transport du cours d'eau, ce qui engendre une érosion régressive. En aval, le débit liquide n'étant plus saturé en débit solide (Degoutte, 2006), le cours d'eau creuse son lit pour compenser ce déficit, engendrant une érosion progressive. La propagation opposée de ces ajustements morphologiques peut induire une incision générale du lit avec un abaissement du toit de la nappe alluviale et/ou à une destabilisation d'ouvrages, comme les piles de ponts (Bravard, 1994).

- Les barrages permettent de stocker de l'eau pour produire de l'énergie, écrêter les crues et/ou soutenir les étiages, favoriser l'irrigation, etc. Il existe deux types d'ouvrages : les barrages mobiles et fixes (Petts, 1984). Les barrages mobiles peuvent s'effacer pour permettre le transit des sédiments en crue, alors que les barrages fixes piègent les sédiments dans la retenue (Vericat et al., 2006). Ce déficit sédimentaire engendre une incision du lit en aval de l'ouvrage, qui peut être limitée par la formation d'une couche d'armurage et/ou l'apparition d'affleurements rocheux, ce qui a des conséquences écologiques négatives (Wasson et al., 1995; Bravard et al., 1997). La présence de ces ouvrages modifie également la durée, l'intensité et la fréquence des crues (Brandt, 2000), ainsi que le régime thermique (Casado, 2013).

1.2 Processus physiques du transport sédimentaire

Précédemment abordé à l'échelle de l'hydrosystème, dans sa dimension longitudinale, le transport de sédiments en rivière met en jeu des processus complexes à plusieurs échelles qui présentent de fortes variabilités spatio-temporelles. En effet, il s'agit d'interactions entre un écoulement, souvent turbulent, et des sédiments plus ou moins homogènes voire cohésifs. On s'intéresse ici à une description mécaniste de la contrainte de cisaillement au fond exercée par l'écoulement, au bilan des forces à l'échelle du grain, aux conditions de mise en mouvement, et enfin à la capacité de transport d'un écoulement. Cette description s'appuie sur les cours de Dufresne and Isenmann (2020), Recking (2012a) et Camenen and Melun (2021).

1.2.1 Contrainte de cisaillement

La contrainte de cisaillement au fond τ_b $\left[N/m^2\right]$ correspond à la force de l'écoulement exercée sur le lit de la rivière. Dans un cours d'eau, en écoulement uniforme, toutes les forces qui s'exercent sur un volume d'eau sont en équilibres, les forces de frottement sur le fond compensent l'accélération de la gravité (Ancey, 2016), ce qui permet d'écrire la relation suivante :

$$\rho g A d_x sin\alpha = \tau_b P d_x \tag{1.2}$$

où ρ correspond à la masse volumique de l'eau $\left[kg/m^3\right]$, g l'accélération de la gravité $\left[m/s^2\right]$, A l'aire mouillée $\left[m^2\right]$, d_x la longueur selon l'écoulement du volume d'eau $[m]$, α l'angle de la pente de la ligne d'eau, P le périmètre mouillé $[m]$ et τ_b $\left[N/m^2\right]$ la contrainte de cisaillement au fond, qui correspond à la force de l'écoulement excercée sur le fond et les berges. Dans le cas de rivières à faible pente, on peut approximer la pente de ligne d'eau par $S \approx sin\alpha$. Dans le cas d'un rapport largeur/profondeur faible et en supposant la section en travers rectangulaire, on peut supposer que le rayon hydraulique $R_h = A/P = Wh/\left(W + 2h\right) \approx h$ avec h la hauteur d'eau $[m]$ et W la largeur du cours d'eau $[m]$. Sous ces hypothèses, τ_b la contrainte de cisaillement sur le fond peut être approximée par :

$$\tau_b = \rho g h S \tag{1.3}$$

La contrainte de cisaillement totale au fond inclut en réalité les frottements liés à la résistance des grains, mais également les frottements liés à la résistance des formes de fond (rides, dunes, antinudes) et des macroformes (seuil-mouilles, bancs alternés, sinosité, ...). Cependant, seule la contrainte de cisaillement liée à la résistance des grains est responsable du transport de sédiments par charriage. Afin de distinguer la résistance exercée par les grains de la résistance totale que le lit exerce sur l'écoulement, la contrainte de cisaillement au fond τ_b est généralement décomposée selon trois composantes (Einstein, 1950) :

$$\tau_b = \tau' + \tau'' + \tau''' \tag{1.4}$$

où τ' est la contrainte de cisaillement de peau (ou de grain) qui est responsable du transport sédimentaire, τ'' est la contrainte de cisaillement de formes et τ''' est la contrainte de cisaillement liée à la géométrie de la rivière. τ'' peut être estimée en fonction de la géométrie des formes de fond, tandis que τ' peut être estimée en fonction de la granulométrie du lit.

Localement la contrainte de cisaillement au fond τ peut être estimée à partir de la vitesse de frottement u_* où $\tau = \rho u_*^2$. Cette vitesse de frottement u_* $[m/s]$ peut être déterminée à partir du profil vertical théorique de répartition des vitesses (cf. Figure 1.5). En particulier au sein d'une petite épaisseur, la couche limite, proche de la paroi où la vitesse varie de zéro à la paroi à la vitesse de l'écoulement (cf. Chassaing (1997)). Pour un écoulement turbulent rugueux (cf. section 1.2.2), le profil vertical de vitesse longitudinale u est généralement considéré comme étant logarithmique et définit selon le concept de la longueur de mélange (Yalin, 1992), comme suit :

$$\frac{u(z)}{u_*} = \frac{1}{\kappa} \ln\left(\frac{z}{z_0}\right) \tag{1.5}$$

où $u(z)$ est la vitesse longitudinale $[m/s]$ à la côte z au-dessus du fond où la vitesse est nulle, κ est la constante de von Kármán égale à 0.41 et z_0 est un coefficient appelé longueur de rugosité. Cette longueur peut être associée à la rugosité hydraulique h'_s, où $z_0 = h'_s/30$, qui est généralement liée à la taille des particules au fond, telle que $h'_s = \alpha D_{90}$ avec α une constante ($\alpha = 2$ selon Yalin (1992)) et D_{90} le diamètre représentatif des particules de surface les plus grossières.

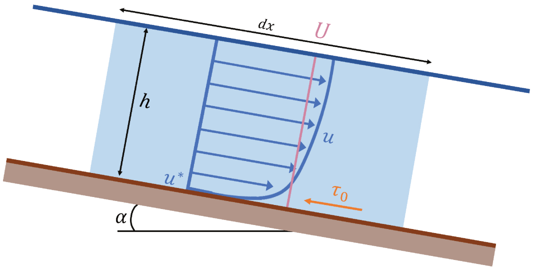

FIGURE 1.5 : Bilan des forces s'exerçant sur un volume d'eau en écoulement uniforme et répartition verticale des vitesses d'écoulement sur la colonne d'eau.

En considérant un profil logarithmique de répartition des vitesse sur la colonne d'eau, la vitesse de frottement u_* peut être définie en fonction de la vitesse moyennée sur la verticale U, estimée à partir de mesures *in situ* ou par modélisation hydraulique.

$$\frac{u_*}{U} = \frac{\kappa}{1 + ln(z_0/h)} \tag{1.6}$$

1.2.2 Mise en mouvement des sédiments

Une particule immergée au fond d'un cours d'eau est soumise à différentes forces $[N]$: la gravité F_G (liée à la masse de la particule), la poussée d'Archimède F_B (liée à la masse du fluide déplacée par la particule), la force de traînée F_D (liée à la vitesse de l'écoulement) et la force de portance F_L (liée à la variation de la vitesse de l'écoulement entre le bas et le haut de la particule). Le bilan des forces appliquées à une particule immergée est schématisé sur la Figure 1.6.

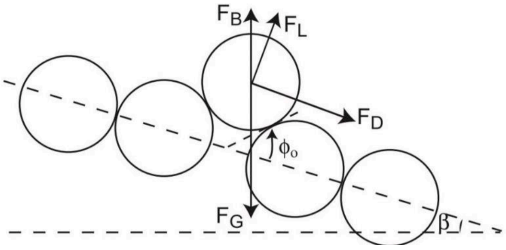

FIGURE 1.6 : Bilan des forces s'exerçant sur une particule au sein d'un écoulement, d'après Lamb et al. (2008).

Cette particule est mise en mouvement lorsque les forces hydrodynamiques (la traînée et la portance) sont supérieures aux forces stabilisatrices (le poids moins la poussée d'Archimède appelé le poids déjaugé). La mobilité d'une particule dépend ainsi de plusieurs paramètres $(D, \rho_s, u_*, \rho, \mu, g)$, et on peut décrire le problème à l'aide de trois variables adimentionnelles :

$$\theta = \frac{\rho u_*^2}{(\rho_s - \rho)\, gD} = \frac{\tau}{(\rho_s - \rho)\, gD} \tag{1.7}$$

$$Re_* = \frac{\rho u_* D}{\mu} = \frac{\rho^{1/2}\tau^{1/2}D}{\mu} \tag{1.8}$$

$$\rho_* = \frac{\rho_s - \rho}{\rho} \tag{1.9}$$

où θ est le paramètre de Shields qui correspond à la contrainte de cisaillement moyenne τ adimentionnalisée par les caractéristiques des particules, i.e. la différence de masse volumique de la particule ρ_s et de l'eau ρ et le diamètre D de la particule. Re_* est le nombre de Reynolds particulaire permettant de caractériser la turbulence au niveau de la particule en faisant intervenir la vitesse de frottement u_* comme vitesse caractéristique, le diamètre d de la particule comme longueur caractéristique et la viscuosité dynamique μ. ρ_* est le rapport des masses volumiques permettant de caractériser la masse volumique du matériaux ρ_s par rapport à la masse volumique du fluide ρ.

A partir d'expériences en laboratoire, Shields (1936) a estimé un paramètre critique de Shields θ_{cr} de mise en mouvement des sédiments en fonction du nombre de Reynold particulaire Re_* de l'écoulement. Ces expériences ont été réalisées à partir de matériaux de différents rapports de masse volumique ρ_*, variant entre 0.06 et 3.3, présentant une granulométrie relativement uniforme caractérisée par un diamètre médian D_{50}. Le diagramme de Shields (Figure 1.7) montre que la mise en mouvement des sédiments est indépendante du type de matériaux utilisés, et par conséquent aux rapports des masses volumiques ρ_*. Seul le nombre de Reynolds particulaire et le paramètre de Shields sont donc des variables d'influence de la mise en mouvement des sédiments.

Pour un nombre de Reynolds particulaire supérieur à 1000 (écoulements rugueux), le paramètre critique de Shields tend vers une valeur de 0.06, ce qui suggère qu'en rivière naturelle ($Re^* > 500$; Dingman, 1984) le seuil critique de mise en mouvement des sédiments est constant.

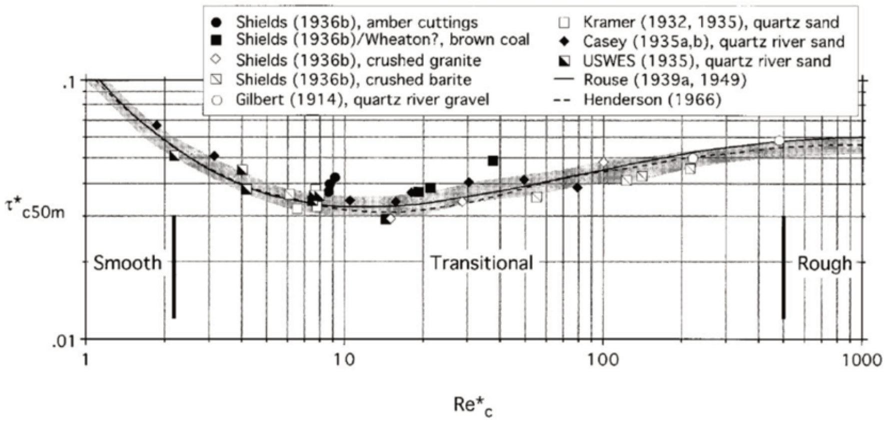

FIGURE 1.7 : Diagramme de Shields dans Garcia et al. (2000).

En ajoutant à la courbe de Shields des valeurs de contrainte critique de mise en mouvement déterminées par différents auteurs, pour une gamme de Reynolds particulaire plus élevée, (Miller et al., 1977) obtient une valeur asymptotique de 0.045 pour les plus grands Re^*. Buffington and Montgomery (1997) ont compilé l'ensemble des valeurs de θ_{cr} disponibles dans la littérature et ont montré que cette valeur pouvait varier de 0.03 à 0.07. Cette dispersion peut s'expliquer par les différentes méthodes utilisées selon les auteurs pour définir la mise en mouvement des sédiments : l'extrapolation à zéro ou à une valeur finie des mesures de débit solide, l'étude de la compétence du cours d'eau à transporter un diamètre maximum donné ou la mesure visuelle du déplacement des grains (Wilcock, 1988). En compilant l'ensemble des données disponibles dans la littérature, Lamb et al. (2008) ont également montré que θ_{cr} variait en fonction de la pente du chenal (Figure 1.8).

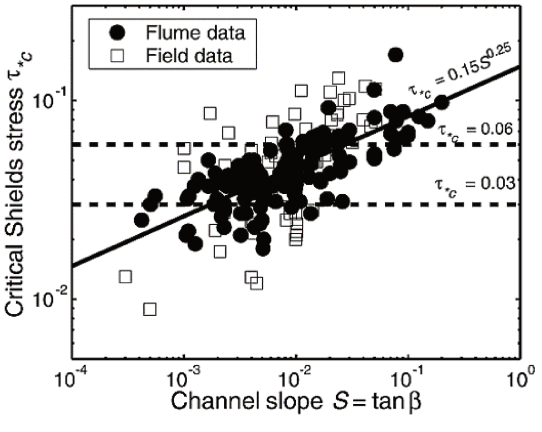

FIGURE 1.8 : Compilation de données montrant la variation du paramètre critique de Shields en fonction de la pente moyenne du fond, d'après Lamb et al. (2008).

Ce résultat indique que θ_{cr} augmente en fonction de la pente, alors que l'on pourrait s'attendre au résultat inverse du fait de l'augmentation des effets de gravité avec la pente (Chiew and Parker, 1994). A partir d'un bilan des forces, Lamb et al. (2008) et Recking (2009) ont montré que cette propriété s'explique en tenant compte des changements affectant la turbulence et le profil de vitesses, pour de fortes pentes de cours d'eau. Recking (2009) a proposé une formule permettant d'estimer θ_{cr} en fonction de la pente du fond du lit S valide pour des matériaux uniformes :

$$\theta_{cr} = 0.15S^{0.275} \tag{1.10}$$

Lorsque la granulométrie est étendue, les particules peuvent interagir entre-elles modifiant localement la mobilité des sédiments selon leur taille. Les particules les plus fines sont protégées de l'écoulement et bloquées (ou piégées) par les particules plus grossières, ce qui tend à augmenter θ_{cr} par rapport à la valeur définie pour une granulométrie uniforme. A l'inverse, les particules les plus grossières peuvent être plus exposées à l'écoulement, ce qui tend à diminuer θ_{cr} par rapport à la valeur définie pour une granulométrie uniforme. Pour tenir compte de ces effets de masquage et de surexposition, Parker and Klingeman (1982) ont proposé d'exprimer le paramètre de Shields critique θ_{cr,D_k} d'une particule de diamètre D_k, à partir de sa valeur $\theta_{cr,D_{50}}$ pour un diamètre moyen D_{50} du mélange sédimentaire, de la manière suivante :

$$\theta_{cr,D_k} = \theta_{cr,D50} \left(\frac{D_k}{D_{50}}\right)^{-b} \tag{1.11}$$

avec b un coefficient de masquage/surexposition pouvant varier entre 0 (les particules n'ont aucune influence entre elles ; la contrainte de cisaillement critique est presque proportionnelle au poids) et 1 (les différences d'exposition des particules et d'angles de frottement compensent complètement les différences de poids des particules ; la valeur de la contrainte de cisaillement critique est la même pour toutes les tailles de particules). Recking (2009) a adapté cette formulation aux variations de pentes, afin de proposer la relation suivante :

$$\theta_{cr,D_k} = (1.32S + 0.037) \left(\frac{D_k}{D_{50}}\right)^{-0.93} \tag{1.12}$$

où S correspond à la pente du chenal. Cette équation donne des résultats similaires à l'équation 1.10 établie pour des sédiments uniformes pour $D_k/D_{50} \approx 1.4$, ce qui correspond approximativement au diamètre médian des granulométries étendues en rivières à gravier, où on retrouve généralement $D_{84}/D_{50} \approx 2.2$ (Rickenmann and Recking, 2011).

Pour une granulométrie étendue, θ_{cr} peut également varier dans le temps, en fonction de l'historique des écoulements (Paphitis and Collins, 2005; Masteller et al., 2019). A l'échelle d'un évènement hydrologique, θ_{cr} peut augmenter entre la montée et la descente de crue (Mao, 2012). Cette augmentation est attribuée à des changements temporels dans le degré d'organisation et de complexité de la surface du lit. Pretzlav et al. (2020) a montré que θ_{cr} augmente progressivement avec la contrainte de cisaillement cumulative τ jusqu'à ce qu'une crue suffisamment importante se produise pour perturber la surface du lit et "réinitialiser" l'historique de l'écoulement. La contrainte de cisaillement cumulative tend à accroître la stabilité du lit à travers divers mécanismes tels que l'armurage de surface (Pfeiffer et al., 2017), la compaction du lit (Marquis and Roy, 2012), le changements de la distribution granulométrique (Humphries et al., 2012), l'approvisionnement en sédiments (Recking, 2012b), le regroupement (Strom et al., 2004) et l'imbrication des grains (Yager et al., 2018).

1.2.3 Taux de transport sédimentaire

Une fois la contrainte adimensionnelle seuil θ_{cr} dépassée, le mouvement de certaines particules est initié et un débit solide est transporté par l'écoulement. Ce transport solide s'effectue sous forme de charriage (roulement, glissement ou saltation au fond) ou de suspension (porté par l'écoulement dans la colonne d'eau), en fonction des caractéristiques hydrodynamiques de l'écoulement et des caractéristiques des particules. De nombreuses formules permettant d'estimer le transport solide, que ce soit par charriage (ex. Meyer-Peter and Müller (1948)), suspension (ex. Engelund and Hansen (1967)) ou par charriage et suspension (ex. Van Rijn (1989)) ont été proposées dans la littérature.

Dans le cadre de cette thèse, seules les formules permettant d'estimer le transport de la charge de fond sont abordées, étant donné que le charriage est le mode de transport qui induit la majorité des évolutions morphologiques du cours d'eau. La plupart de ces formules sont semi-empiriques, reposant sur une base théorique plus ou moins élaborée, avec des paramètres ajustés sur un jeu de données expérimentales. Ces données proviennent principalement de mesures de transport solide effectuées en canal de laboratoire, avec des écoulements satisfaisant la condition d'équilibre (pente stabilisée pour des débits solide et liquide constants en entrée). Ces formules semi-empiriques établissent généralement une relation entre un paramètre caractérisant l'hydraulique et un paramètre caractérisant le transport de sédiments, permettant d'estimer la capacité de transport d'un écoulement. Selon les auteurs, l'hydraulique peut être caractérisée par la puissance de l'écoulement w (Bagnold, 1980), le débit spécifique q (Schoklitsch, 1962; Rickenmann, 1990), le débit total Q (Couvert et al., 1991; Lefort, 2007) ou, le plus souvent, par le paramètre de Shields θ (Brown, 1950; Einstein, 1950; Engelund and Hansen, 1967). Le transport sédimentaire est généralement caractérisé par le débit solide adimentionnel appelé paramètre d'Einstein Φ_b qui s'écrit :

$$\Phi_b = \frac{q_{sb}}{\sqrt{\left(\frac{\rho_s}{\rho}-1\right) g D_{50}^3}} = \alpha\left(\theta-\theta_{cr}\right)^{\beta} \tag{1.13}$$

avec Φ_b le flux sédimentaire par charriage $[-]$,q_{sb} la valeur dimensionnelle du flux de transport $[m^3/s/m]$.

Les grandeurs permettant de caractériser l'hydraulique et le transport sédimentaire sont habituellement adimensionnalisées, afin de réduire la dispersion des résultats due aux conditions expérimentales et d'ajuster les points sur une relation supposée unique.

Il existe deux grandes familles d'équations (Figure 1.10) : les formules à seuils de la forme $\Phi = f\left(\theta-\theta_{cr}\right)$ et les formules sans seuil de la forme $\Phi = f\left(\theta/\theta_{cr}\right)$.

Les formules à seuil considèrent un transport nul lorsque $\theta < \theta_{cr}$, ce qui les rend très dépendantes de l'estimation de θ_{cr}. Etant donnée la grande difficulté à mesurer, voire même à définir un seuil (cf. 1.2.2) des formules sans seuil, moins restrictive, ont été proposées (Parker and Klingeman, 1982; Parker et al., 1982; Wilcock, 2001; Wilcock and Crowe, 2003). Ces formules sans seuil font intervenir le taux de transport θ/θ_{cr}, permettant de prédire un transport, même très faible, lorsque θ tend vers 0, comme le suggèrent des observations de laboratoire pour des granulométries étendues (Paintal, 1971).

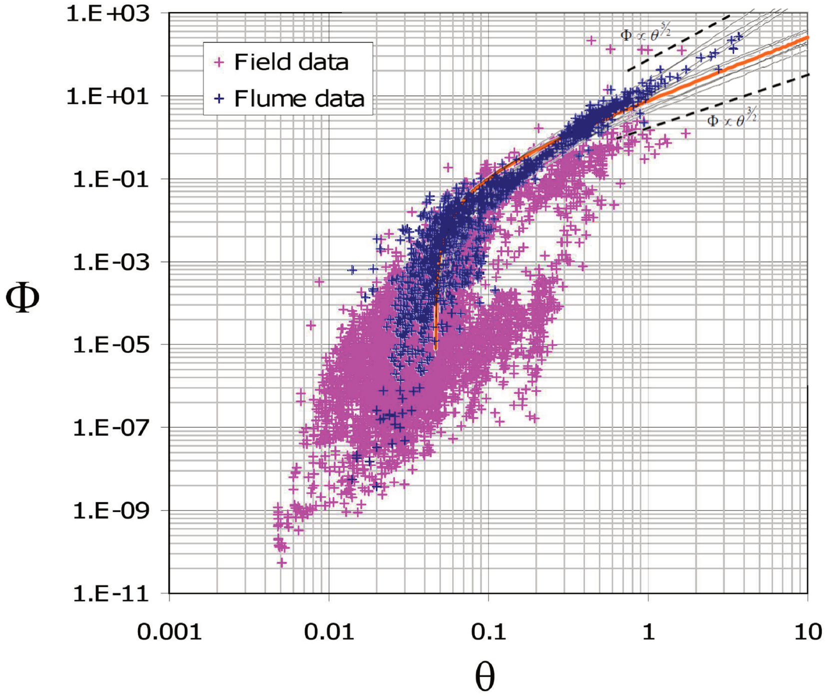

FIGURE 1.9 : Compilation de 8700 mesures collectées sur plus de 100 cours d'eau (pente $0.0001 < S < 0.1$) et de 1317 mesures issues du laboratoire (matériaux quasi-uniformes) avec la courbe rouge représentant la relation de Meyer-Peter and Müller (1948), modifié d'après Recking (2012a) et Recking (2006).

La plupart de ces formules de transport ont été établies en laboratoire pour un diamètre unique D et sont utilisées sur le terrain avec un diamètre médian D_{50} supposé représentatif de la distribution granulométrique des sédiments. Pour représenter l'étendue granulométrique et l'existence d'un transport partiel des sédiments, Parker and Klingeman (1982) ont proposé de calculer le débit solide non pas pour un diamètre unique représentatif, mais pour l'ensemble des classes granulométriques. Ce calcul fractionné fait l'hypothèse qu'une formule de transport sédimentaire f établie pour un diamètre D, en fonction de la contrainte θ et d'un contrainte critique θ_{cr}, reste valide pour chaque classe granulométrique D_k d'un mélange sédimentaire, ce qui permet d'écrire :

$$q_{s,k} = p_k f(D_k, \theta_k, \theta_{cr,k}) \tag{1.14}$$

où p_k représente la proportion de matériau de la classe k dans le mélange sédimentaire, $\theta_{cr,k}$ correspond au paramètre de Shields critique pour la taille D_k représentative de la classe k et $q_{s,k}$ est le débit solide associé à ce diamètre. $\theta_{cr,k}$ est généralement exprimée en fonction de $\theta_{cr,D_{50}}$ (paramètre de Shields critique estimé pour le diamètre médian D_{50}) à partir d'une fonction de masquage/surexposition (équation 1.11 ou 1.12). Le débit solide total $q_{s,t}$ est calculé en additionnant les débits solides $q_{s,k}$ estimé pour chaque classe k :

$$q_{s,t} = \sum q_{s,k} \tag{1.15}$$

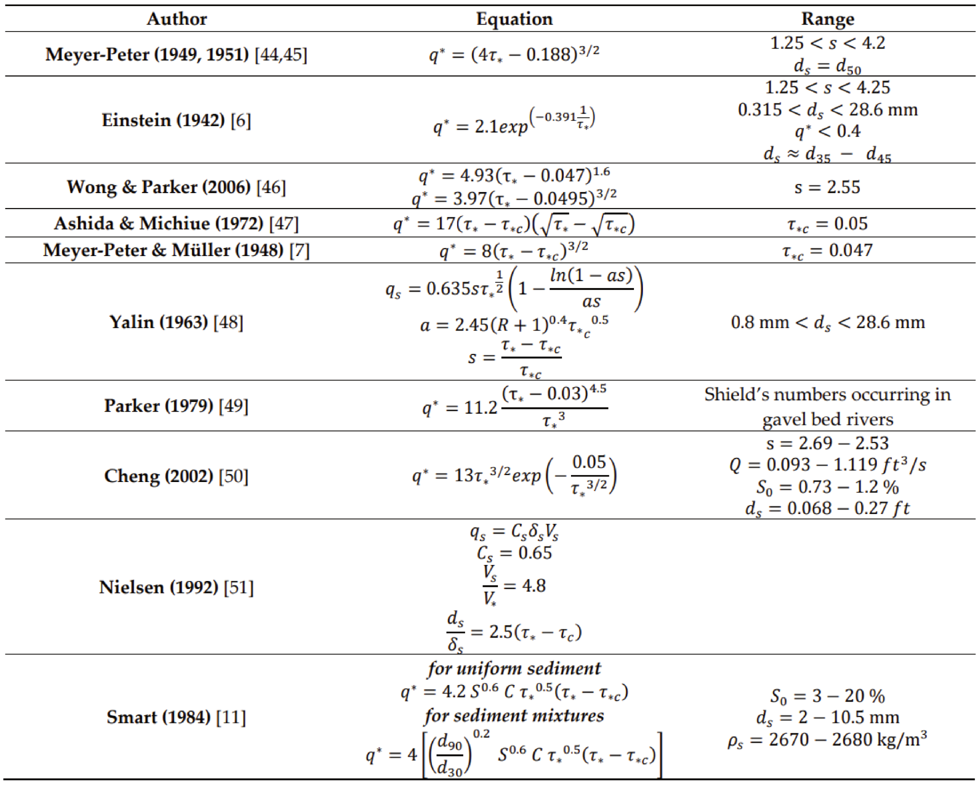

Author	Equation	Range
Meyer-Peter (1949, 1951) [44,45]	$q^* = (4\tau_* - 0.188)^{3/2}$	$1.25 < s < 4.2$ $d_s = d_{50}$
Einstein (1942) [6]	$q^* = 2.1exp^{\left(-0.391\frac{1}{\tau_*}\right)}$	$1.25 < s < 4.25$ $0.315 < d_s < 28.6$ mm $q^* < 0.4$ $d_s \approx d_{35} - d_{45}$
Wong & Parker (2006) [46]	$q^* = 4.93(\tau_* - 0.047)^{1.6}$ $q^* = 3.97(\tau_* - 0.0495)^{3/2}$	$s = 2.55$
Ashida & Michiue (1972) [47]	$q^* = 17(\tau_* - \tau_{*c})\left(\sqrt{\tau_*} - \sqrt{\tau_{*c}}\right)$	$\tau_{*c} = 0.05$
Meyer-Peter & Müller (1948) [7]	$q^* = 8(\tau_* - \tau_{*c})^{3/2}$	$\tau_{*c} = 0.047$
Yalin (1963) [48]	$q_s = 0.635 s \tau_*^{\frac{1}{2}}\left(1 - \frac{ln(1 - as)}{as}\right)$ $a = 2.45(R + 1)^{0.4}{\tau_*}_c^{\;0.5}$ $s = \frac{\tau_* - \tau_{*c}}{\tau_{*c}}$	0.8 mm $< d_s <$ 28.6 mm
Parker (1979) [49]	$q^* = 11.2\frac{(\tau_* - 0.03)^{4.5}}{\tau_*^{\;3}}$	Shield's numbers occurring in gavel bed rivers
Cheng (2002) [50]	$q^* = 13\tau_*^{\;3/2} exp\left(-\frac{0.05}{\tau_*^{\;3/2}}\right)$	$s = 2.69 - 2.53$ $Q = 0.093 - 1.119\, ft^3/s$ $S_0 = 0.73 - 1.2$ % $d_s = 0.068 - 0.27\, ft$
Nielsen (1992) [51]	$q_s = C_s \delta_s V_s$ $C_s = 0.65$ $\frac{V_s}{V_*} = 4.8$ $\frac{d_s}{\delta_s} = 2.5(\tau_* - \tau_c)$	
Smart (1984) [11]	*for uniform sediment* $q^* = 4.2\, S^{0.6}\, C\, \tau_*^{\;0.5}(\tau_* - \tau_{*c})$ *for sediment mixtures* $q^* = 4\left[\left(\frac{d_{90}}{d_{30}}\right)^{0.2} S^{0.6}\, C\, \tau_*^{\;0.5}(\tau_* - \tau_{*c})\right]$	$S_0 = 3 - 20$ % $d_s = 2 - 10.5$ mm $\rho_s = 2670 - 2680$ kg/m^3

FIGURE 1.10 : Exemples de formules de transport de la charge de fond applicables aux cours d'eau graveleux, avec leur plage de validité, d'après Carrillo et al. (2021).

Ce calcul fractionné est bien adapté aux formules à seuils, mais donne des incohérences pour les formules sans seuil (Recking, 2012a). De grosses incertitudes existent cependant sur la fonction de masquage/surexposition et le paramètre de Shields critique de référence à employer (Barry et al., 2004). Wilcock (2001) suggère de réaliser un calage de ces différents paramètres à partir de mesures de terrain. Ce calcul par classe granulométrique nécessite également une bonne connaissance de la granulométrie de surface ou de subsurface, selon la formule utilisée.

Par ailleurs, toutes ces formules de transport solide doivent être utilisées avec précaution, car elles ont été établies à partir de mesures en laboratoire ou sur le terrain, dans des conditions particulières de pente, de granulométrie et de vitesse d'écoulement. Les conditions d'établissement de ces formules ne permettent cependant pas de définir leur domaine de validité (Recking, 2012a). Indépendamment de la qualité d'une formule, la performance de sa prédiction demeurera toujours étroitement dépendante de la qualité des données, en particulier des valeurs décrivant l'hydraulique, la pente et la granulométrie du lit. Il vaudra toujours mieux utiliser ces formules en tentant de les recaler (Degoutte, 2006), à partir de mesures directes (ex. prélèvement) ou indirectes (ex. mesure acoustique) du transport solide. Quelle que soit la méthode de mesure employée , les résultats de ces mesures seront influencés par les fluctuations inhérentes au phénomène de charriage, liées à la turbulence de l'écoulement, aux formes de fond, au tri granulométrique et à la saisonnalité (Ancey, 2020).

1.3 Modélisation morpho-dynamique

La démarche de modélisation consiste généralement en l'établissement d'un modèle mathématique reflétant la perception de la physique, puis de sa résolution analytique ou numérique. Une modélisation (mathématique ou numérique) d'un système physique est nécessairement une simplification de la complexité du réel. La démarche de modélisation est généralement un compromis entre (1) les objectifs de modélisation, (2) les données disponibles et (3) la complexité du modèle. Ces travaux de thèse s'inscrivent dans une volonté de mise en cohérence d'un modèle hydro-sédimentaire avec des données multi-sources de terrain.

Les modèles numériques hydro-sédimentaires sont largement utilisés pour des applications d'ingénierie hydraulique. Parmi les outils existants on peut citer le modèle 1D HEC-RAS (Brunner, 2010), Mike-21 (Warren and Bach, 1992), Delft3D (Lesser et al., 2004), le modèle 2D ou 3D Telemac-Sisyphe (Villaret et al., 2013).

L'objectif de ces travaux nécessite de représenter la variabilité longitudinale, latérale et temporelle des écoulements fluides et des évolutions morphologiques associées. Ainsi, un modèle hydro-sédimentaire 2D est l'outil approprié qui sera utilisé dans ces travaux. Le modèle mathématique présenté dans ce qui suit, est celui résolu dans Telemac2D-Sisyphe. Ce modèle numérique a été choisi pour ces travaux car il est très utilisé, performant et robuste, open source et modifiable (Hervouet, 2007). De plus il permet des calculs parallèles efficaces sur des maillages conséquents ce qui permet d'étudier des zooms très détaillés ou encore des domaines spatio-temporels relativement importants. Un modèle hydraulique 1D avec les ouvrages a été réalisé avec HEC-RAS sur une zone englobant la zone d'étude hydro-sédimentaire, afin d'estimer les conditions aux limites du modèle 2D.

1.3.1 Modélisation hydraulique

L'hydraulique fluviale est une discipline appliquée de la mécanique des fluides, qui étudie le mouvement des liquides. Les lois de conservation de la masse et du moment sont mises en œuvre sur un volume de liquide (hypothèses de milieu continu, voir Chassaing (1997)). Dans les écoulements en rivière, divers processus physiques ont lieu à de multiples échelles, de celle de structures turbulentes très localisées dans les couches limites (e.g. Nikora et al. (2004)) à des propagations d'ondes à plus grande échelle (e.g. Dingman (2009); Thual (2010)). Les deux principales forces à l'œuvre dans les écoulements à surface libre sont les forces de gravité et de cisaillement qui proviennent de la résistance par friction basale avec les effets visqueux et turbulents ; une autre force de surface en jeu est la force de pression. La variabilité des écoulements à surface libre résulte de l'équilibre des forces et des masses qui se reflète dans les variabilités des champs de vitesse et dans les déformations de la surface libre et peut être prédite par la théorie hydraulique (cf. Dingman (2009); Thual (2010); Ancey (2016)). La complexité des écoulements dans un tronçon de rivière peut varier en fonction des échanges latéraux, de la forme et de la sinuosité du chenal, des pentes, des berges et de la rugosité du fond, de la présence de végétation, de confluences ou de diffluences, ou de structures artificielles en ligne (ponts, déversoirs, barrages) ou latérales (déversoirs latéraux, digues) (cf. Graf and Altinakar (2000)).

Les modèles hydrauliques sont à base physique et dénomment ici des équations différentielles de bilans permettant de décrire le mouvement de l'eau dans un écoulement à surface libre. Il est question des équations de Navier Stokes incompressibles (cf. Chassaing (1997)) intégrées sur la verticale et simplifiées dans différentes versions des équations de Barré de Saint-Venant.

La viscosité de l'eau et les effets de cisaillement sont classiquement pris en compte dans les modèles hydrauliques au travers d'un terme de friction pariétale, exprimé à l'aide d'une loi empirique établie à partir de mesure d'écoulements (cf. Chow (1959); Ancey (2016)). Les modèles hydrauliques sont mécanistes, déterministes, et spatialement distribués (Roux (2004)). Selon la complexité des écoulement étudiés et les données disponibles, des modèles 1D ou 2D sont couramment utilisés.

En effet, la résolution d'un modèle hydraulique nécessite des données pour décrire a minima les paramètres de bathymétrie et de friction sur le domaine et les conditions aux bords du domaine. Les modèles mathématiques et numériques 1D et 2D utilisés dans ces travaux sont présentés ci-après avec les principales hypothèses sur lesquelles ils reposent.

1.3.1.1 Modèle Saint-Venant 1D

L'obtention des équations de Saint-Venant à partir des équations de Navier-Stokes est par exemple présentée dans Thual (2010) pour un canal de section rectangulaire et pour une section quelconque dans Malou (2022); Pujol (2022). Les principales hypothèses simplificatrices permettant d'obtenir les équations de Saint-Venant sont (cf. Chow (1959); Ancey (2016)) :

1. L'axe d'écoulement est quasi rectiligne - profil bidimensionnel curviligne dont les variations sont faibles (rayon de courbure local grand).

2. L'écoulement d'eau est quasi monodimensionnel - la côte et la vitesse sont constants dans toute section perpendiculaire à l'écoulement.

3. La section d'écoulement et les hauteurs d'eau varient doucement et progressivement sur de courtes distances. On parle de régime graduellement varié aussi appelé approximation des grandes longueurs d'onde. Dans ce cas, en introduisant des échelles caractéristiques de hauteur H_0 et de longueur L_0 de la surface libre, le rapport d'aspect $\epsilon = H_0/L_0$ est supposé petit devant 1 ($\epsilon \ll 1$).

4. Les lignes de courant au sein de l'écoulement ne subissent pas de bifurcation brutale.

5. En cas d'apport (resp. perte) à la partie dynamique, la vitesse d'injection (resp. fuite) est égale à la vitesse de l'écoulement (resp. nulle).

6. La surface d'écoulement exerce une contrainte de frottement τ_p sur le lit de la rivière considéré comme fixe (pas d'érosion ni de dépôt) et dont la rugosité est supposée uniforme le long d'un bief.

On considère une portion de réseau hydrographique décrite par des segments connectés, et on note $t \in]0, T]$ le temps physique et x l'abscisse curviligne. Soit $A\left(x,t\right)$ $\left[\mathrm{m}^2\right]$ la section en travers d'écoulement et $Q\left(x,t\right)$ $\left[\mathrm{m}^3/\mathrm{s}\right]$ le débit tel que $Q = UA$ avec $U\left(x,t\right)$ la vitesse moyenne [m/s] sur une section en travers d'écoulement. On définit le nombre de Froude en section quelconque $\mathrm{Fr} = {}^{U}\!/_{c} = \sqrt{{}^{Q^2W}\!/_{gA^3}}$, où W est la largeur au miroir, et qui compare la vitesse d'écoulement U à la célérité c des ondes ; Fr^2 compare l'énergie cinétique du fluide en mouvement à l'énergie potentielle de la pesanteur.

Les équations de Saint-Venant 1D sous forme conservative avec prise en compte d'une section variable A avec apports latéraux s'écrivent

$$\mathcal{M}_{SW1D}:\begin{cases}\dfrac{\partial A}{\partial t}+\dfrac{\partial Q}{\partial x} & =q_l\\ \frac{\partial Q}{\partial t}+\frac{\partial}{\partial x}\left(\frac{Q^2}{A}\right) & =-gA\left(\frac{\partial Z}{\partial x}-S_f\right)+U\delta_l q_l\\ (1)\qquad (2) & \qquad\quad (3)\qquad (4)\qquad\quad (5)\end{cases}\tag{1.16}$$

où $Z\left(x,t\right)$ est l'altitude de la surface libre en [m] et $Z=\left(b+h\right)$ avec $b\left(x\right)$ l'altitude du point le plus profond d'une section en travers et $h\left(x,t\right)$ la hauteur d'eau en[m], g l'accélération de la pesanteur en $\left[\mathrm{m/s^2}\right]$ et $q_l\left(x,t\right)$ le débit linéique latéral d'apport/perte en $\left[\mathrm{m^2/s}\right]$ et $\delta_l=1$ si $q_l>0$ sinon $\delta_l=0$. Le terme de friction est classiquement exprimé avec la loi de Manning-Strickler établie empiriquement pour des écoulements uniformes et qui s'écrit :

$$S_f=\frac{\left|Q\right|Q}{K^2A^2R_h^{4/3}}\tag{1.17}$$

avec K le coefficient de Strickler en $\left[\mathrm{m^{1/3}/s}\right]$, $R_h\left(x,t\right)={}^{A}/_{P_h}$ le rayon hydraulique et $P_h\left(x,t\right)$ le périmètre mouillé en[m].

Les cinq termes de l'équation de quantité de mouvement sont les termes inertiels, i.e.(1) l'accélération locale et (2) l'accélération convective, puis (3) le gradient de pression, (4) le terme source de friction et (5) le terme source d'échange de moment dû aux échanges latéraux ; leur importance relative varie notamment selon les régimes d'écoulement et peuvent être étudiés via une adimensionnalisation des équations (cf. Dingman (2009); Thual (2010); Malou (2022)).

Afin d'obtenir un problème bien posé, il est nécessaire d'ajouter des conditions initiales et aux limites pour les variables d'écoulement. En général il est nécessaire d'imposer une ou des séries temporelles de débit au points d'injection amont(s) et éventuellement latéraux, $Q_{in}\left(t\right)$ et $q_{l,d}\left(t\right)$, $d\in\left[1..N_d\right]$ respectivement aux points d'injection à amont(s) et latéraux. On définit le nombre de Froude en section quelconque $\mathrm{F}={}^{U}/_{c}=\sqrt{{}^{Q^2W}/_{gA^3}}$, où W est la largeur au miroir, et qui compare la vitesse d'écoulement U à la célérité c des ondes ; F^2 compare l'énergie cinétique du fluide en mouvement à l'énergie potentielle de la pesanteur. Une condition limite aval sur la hauteur d'eau notée $h_{av}(t)$ suffit pour les écoulements en régime fluvial ($\mathrm{F}<1$), est nécessaire à l'amont pour les écoulements torrentiels. Les conditions initiales sont classiquement définies à partir de la solution du modèle en régime stationnaire appelée courbe de remous ou $Z_0\left(x\right)=Z\left(Q_{in}\left(t_0\right),q_{l,1..N_d}\left(t_0\right),h_{av}\left(t_0\right)\right)$.

Dans ce travail le modèle numérique HEC-RAS a été utilisé, en particulier son solveur permanent qui résout une équation de charge par veine d'écoulement, lit mineur et lits majeurs par exemple (Brunner, 2010).

1.3.1.2 Modèle shallow water 2D

Le modèle hydraulique 2D présenté ici est celui résolu dans Telemac2D-Sisyphe (Hervouet, 2007; Villaret et al., 2013) qui est utilisé dans ces travaux.

On considère un domaine de rivière 2D, $t \in]0, T]$ le temps physique, et un repère cartésien 2D où les coordonnées sont notées x et y. Les équations 2D shallow water (SW) avec prise en compte de la turbulence s'écrivent dans leur forme conservative :

$$\frac{\partial h}{\partial t} + \frac{\partial (hu)}{\partial x} + \frac{\partial (hv)}{\partial y} = 0 \tag{1.18}$$

$$\frac{\partial u}{\partial t} + u\frac{\partial u}{\partial x} + v\frac{\partial u}{\partial y} = -g\frac{\partial Z_s}{\partial x} + \frac{\tau_x}{h} + \frac{1}{h}div(h\nu.grad(u)) \tag{1.19}$$

$$\frac{\partial v}{\partial t} + u\frac{\partial v}{\partial x} + v\frac{\partial v}{\partial y} = -g\frac{\partial Z_s}{\partial y} + \frac{\tau_y}{h} + \frac{1}{h}div(h\nu.grad(v)) \tag{1.20}$$

où h est la hauteur d'eau $[m]$, $\boldsymbol{u} = (u, v)^T$ est le vecteur vitesse 2D moyenné sur la verticale $[m/s]$ avec u la composante selon x et v la composante selon y , g est l'accélération de la gravité $\left[m/s^2\right]$, Z_s est l'altitude de la surface libre $[m]$, t est le temps $[s]$, x et y sont les coordonnées spatiales horizontales $[m]$, ν est la viscosité turbulente moyennée sur la verticale $\left[m^2/s\right]$ et τ_x (resp. τ_y) est la contrainte de cisaillement basal $\left[N/m^2\right]$ selon x (resp. y).

La contrainte de cisaillement basale totale s'écrit alors

$$\tau_b = \sqrt{\tau_x^2 + \tau_y^2} = \sqrt{\left(\frac{1}{2}\rho C_f u^2\right) + \left(\frac{1}{2}\rho C_f v^2\right)} \tag{1.21}$$

avec ρ la masse volumique de l'eau $\left[kg/m^3\right]$ et C_f un coefficient de friction adimensionnel tel que :

$$C_f = \frac{2g}{K_s^2 h^{1/3}} \tag{1.22}$$

avec $K_s\,(x, y)$ le coefficient de Strickler $\left[m^{1/3}/s\right]$ qui requiert généralement un calage à partir d'observations de l'écoulement. Ce coefficient de frottement hydraulique est considéré comme spatialisé, ce qui est abordable avec notre jeu de données dense, afin de compenser finement les erreurs entre les données et le modèle.

1.3.2 Modélisation morpho-sédimentaire

Le modèle morpho-sédimentaire présenté ici est celui résolu dans Telemac2D-Sisyphe (Hervouet, 2007; Villaret et al., 2013) qui est utilisé dans ces travaux.

La contrainte de cisaillement totale τ_b calculée à partir de la modélisation hydrodynamique 2D est corrigée, à l'aide d'un facteur μ, pour obtenir la contrainte de cisaillement de peau (ou de grain, cf. section 1.2.1, Equation 1.4), qui est la seule composante agissant sur le transport de sédiments.

$$\tau' = \mu \tau_b \tag{1.23}$$

où le facteur de correction $\mu = C'_f/C_f$ correspond au rapport entre le coefficient de friction C_f issu de la modélisation hydrodynamique (Equation 1.22) et le coefficient de friction C'_f dû à la friction de peau qui s'écrit :

$$C_f' = 2\left(\frac{\kappa}{log(12h/h_s')}\right)^2 \tag{1.24}$$

où κ est la constante de von Kármán, h la hauteur d'eau et $h_s^{'}$ la longueur de rugosité (m) définie par :

$$h_s^{'} = \alpha_{h_s'} D_{50} \tag{1.25}$$

avec $\alpha_{h_s'}$ un paramètre à caler (3 par défaut ; Tassi and Villaret (2014)) et D_{50}le diamètre médian des sédiments.

Supposons une discrétisation en K classes de la courbe granulométrique tel que $D_k \in [D_k', D_{k+1}']$ est la moyenne logarithmique des diamètres compris entre les bornes D_k' et D_{k+1}' de la classe $k \in 1..K$; on note p_k la proportion volumique de chaque classe dans la couche active.

Le transport de la charge de fond est calculé en fonction du paramètre de Shields θ_k estimé pour la classe k qui s'écrit :

$$\theta_k = \frac{\tau'}{(\rho_s - \rho) g D_k} \tag{1.26}$$

avec τ' de cisaillement de peau (ou de grain) donnée par l'équation 1.23, ρ et ρ_s sont respectivement la masse volumique du fluide et des sédiments, g est l'accélération de la gravité, D est le diamètre représentatif de la classe k.

Le taux de transport adimensionnel induit par l'écoulement, noté $\Phi_{b,k}$ est calculé pour chaque classe de taille k à l'aide d'une formule de transport sédimentaire, dont l'une des plus couramment utilisées est celle proposée par Meyer-Peter and Müller (1948) :

$$\Phi_{b,k} = \alpha_{MPM} p_k (\theta_k - \theta_{cr,k})^{\beta_{MPM}} \tag{1.27}$$

où $\Phi_{b,k}$ est le taux de transport adimensionnel, de la classe de taille k, α_{MPM} et β_{MPM} sont les coefficients empiriques de MPM, p_k est la fraction de la classe k disponible dans la couche active, θ_k est le paramètre de Shields pour la classe k et $\theta_{cr,k}$ est le paramètre de Shields critique pour la class k.

Le taux de transport adimensionnel q_b $\left[m^2/s\right]$ par unité de largeur sans pores, est calculé comme :

$$q_{b,k} = \Phi_{b,k}\sqrt{\left(\frac{\rho_s}{\rho} - 1\right) g D_k^3} \tag{1.28}$$

où Φ_b est le taux de transport adimensionnel de la charge de fond.

Le taux de transport total q_t de la charge de fond par unité de largeur est calculé en sommant les $q_{b,k}$ pondérés par les p_k

$$q_t = \sum p_k q_{b,k} \tag{1.29}$$

L'évolution de l'élévation du lit Z_b est finalement calculée en utilisant l'équation d'Exner pour la continuité sédimentaire qui décrit la conservation de la masse entre les sédiments dans le lit et les sédiments transportés :

$$(1 - \lambda)\frac{\partial Z_b}{\partial t} + \nabla . q_t = 0$$

où λ est la porosité du lit, t est le temps.

1.4 Objectifs et démarche scientifique

L'objectif général de cette thèse est d'améliorer la compréhension du transport de la charge de fond et des évolutions morphodynamiques d'une portion d'une grande rivière à méandres divagants, des processus physiques associés, ainsi qu'à améliorer leur représentation numérique, dans l'optique d'un appui à la gestion de la mobilité latérale des cours d'eau en général, et de la Moselle sauvage en particulier, une rivière à forts enjeux.

Le site de la "Moselle sauvage", dernier tronçon à forte mobilité latérale de grande rivière du nord-est de la France, offre une large gamme d'évolutions morpho-sédimentaires et de processus physiques associés. Bien que cette portion de la Moselle n'ait pas connu d'actions anthropiques directes lourdes, ses évolutions morphologiques sont influencées par des actions menées en amont et en aval du secteur étudié, mais aussi par des fluctuations climatiques sur les temps plus longs (plusieurs décennies à siècles). Afin de pouvoir estimer la trajectoire temporelle des réajustements morphologiques de cette portion de cours d'eau, il est nécessaire (1) d'appréhender finement la compréhension physique des processus et (2) de suivre leur évolution dans le temps et l'espace.

Les processus en jeu sont complexes, couplés, avec une forte variabilité spatio-temporelle. A une échelle locale (section en travers), cette complexité est fortement liée aux interactions fluide-grain dans des écoulements à surface libre turbulents, ce qui reste difficile à mesurer et représenter. Cette complexité est accentuée à l'échelle du tronçon de rivière, avec une granulométrie et des faciès morphodynamiques hétérogènes, soumis aux variations météo-hydrologiques et de fourniture sédimentaire. Une approche par échelles spatio-temporelles emboîtées s'avère donc indispensable.

De plus, l'observabilité sur le terrain étant limitée, et dépendante des échelles spatiales et temporelles, le recours à des modélisations de complexité adaptée à la physique et aux objectifs, ainsi qu'au contenu informatif des données, est indispensable. Nous avons ainsi développé une approche innovante combinant des mesures *in situ* variées, denses et complémentaires (basée sur des mesures ponctuelles distribuées dans le temps et l'espace d'ordre hydrauliques, morphologiques et sédimentaires), avec des modélisations 2D hydrauliques et morpho-sédimentaires.

Les **objectifs spécifiques** de la thèse concernent la détermination des paramètres cruciaux pour la modélisation du transport solide et de la dynamique des formes fluviales, depuis la mise en mouvement du sédiment jusqu'à l'effet des processus couplés sur la morphologie du lit fluvial. Plus précisément, cela nous a conduit à procéder par étapes en cherchant à estimer :

1. **les contraintes critiques de mise en mouvement de la charge de fond ;**

2. **les flux solides ponctuels (section en travers) et à l'échelle d'une crue ;**

3. **le transport sédimentaire multi-classes à l'échelle du tronçon ;**

4. **les évolutions morphodynamiques dans une perspective d'aide à la gestion.**

Les processus en jeu et les évolutions morphologiques résultantes ont pu être observés sur une large gamme d'évènements hydrologiques le long d'un linéaire de 13km. Pour ce faire, un important protocole de mesures combinant diverses techniques a été mis en œuvre. Le suivi de terrain (4 ans) a consisté en (i) des acquisitions topo-bathymétriques (LIDAR), (ii) des mesures de niveau d'eau, de vitesse et de débit (12 limnimètres, nombreux profils ADCP) et (iii) un suivi de la charge de fond (mesures granulométriques, placettes peintes, chaînes d'érosion, 2500 traceurs RFID, mesures acoustiques, campagnes Helley-Smith). Les protocoles d'acquisition ainsi que les traitements mis en œuvre sont détaillés précisément dans les chapitres suivants.

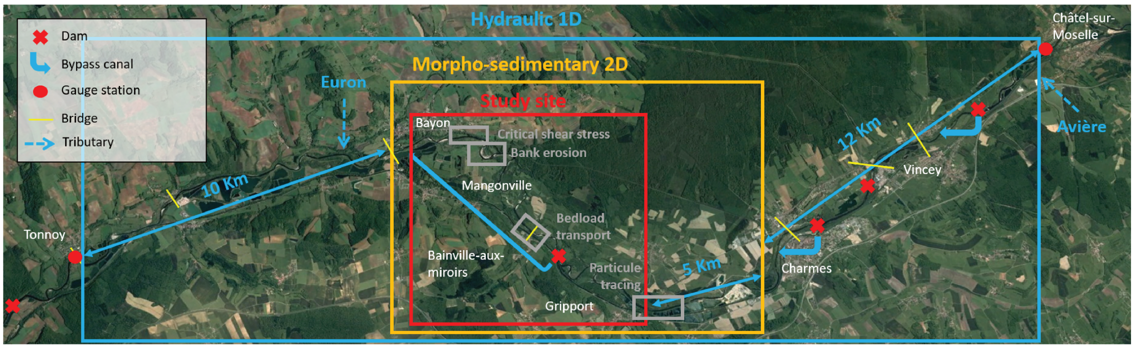

FIGURE 1.11 : Zone d'étude et emprises des différents modèles hydrauliques emboités, modèles de zooms en gris.

Sur la base des données topographiques et hydrologiques, une stratégie de modélisation hydraulique emboîtée a été construite (cf. Figure 1.11). Des modélisations hydrauliques fines ont pu être mises au point, notamment avec le calage spatialisé de modèles 2D haute résolution de plusieurs zones d'intérêt, rendu possible par la densité et le contenu informatif du jeu de données multi-sources.

Les chapitres suivants présentent successivement ces aspects, sous la forme de trois articles (non soumis à ce stade), puis d'une conclusion générale et de travaux en cours sur la modélisation hydro-morphologique d'un méandre densément instrumenté et suivi (qui est un jalon important pour l'aide à la gestion). Préalablement, ce chapitre a dressé un état de l'art large en géomorphologie fluviale, transport solide et modélisation. Le chapitre suivant présente la zone d'étude et les différents travaux qui s'y sont intéressés.

Sont présentés en annexe, des travaux en collaboration réalisés dans le cadre de cette thèse : un article de conférence sur le suivi diachronique de l'érosion de la berge concave d'un méandre de la Moselle par mesures photogrammétriques réalisées à l'aide d'un drone (Koehl et al., 2020) et un article méthodologique sur la comparaison d'outils de traitement d'images pour l'estimation de la granulométrie de surface (Chardon et al., 2021a).

Chapitre 2

Présentation et évolutions morphologiques de la Moselle

Une présentation de la zone d'étude dans son bassin versant est effectuée dans ce chapitre. Il s'intéresse aux caractéristiques physiques et à la caractérisation hydrologique du bassin, puis à une analyse historique des actions anthropiques entreprisent dans la vallée de la Moselle, et enfin aux conséquences sur le fonctionnement morpho-sédimentaire du cours d'eau en particulier sur la zone d'étude de la Moselle Sauvage.

2.1 Caractéristiques topographiques et géologiques du bassin versant

2.1.1 Dans le massif des Vosges

Le bassin versant de la Moselle (Figure 2.1) se partage entre le massif montagneux des Vosges et le plateau lorrain, dont la limite se matérialise par le horst d'Epinal. Le bassin versant de la Moselle supérieure ($1215km^2$) est très ramassé et se subdivise en plusieurs sous-bassins Vosgiens très compacts : la Moselotte ($352km^2$) et la Vologne ($369km^2$) (Maire and Lasserre, 1991). La Moselle prend sa source au Col de Bussang à $1226m$ d'altitude et draine l'ensemble du versant occidental des Vosges du Sud entre le Hohneck ($1362m$) et le ballon d'Alsace ($1247m$) (Maire and Corbonnois, 2000).

Le Massif des Vosges (Figure 2.2) se compose essentiellement de roches dures, cristallines (granites) ou métamorphiques (gneiss) provenant du socle hercynien. Ces roches imperméables affleurent principalement aux altitudes les plus élevées et constituent les trois-quart de la surface du bassin versant amont (Maire and Corbonnois, 2000). A plus basses altitudes, on retrouve des affleurements de formations gréseuses issues de l'érosion du socle (Trias) et des formations glaciaires (Quaternaire) qui occupent les flancs et les fonds de vallées (Remy, 2009). Le profil en long de la Moselle (Figure 2.3) se caractérise par une pente d'environ 10% à l'extrémité amont, qui diminue rapidement à 2% à proximité de Thillot, pour atteindre une valeur de $0,4\%$ au niveau de Remiremont (AERM, 1992). La prédominance des roches imperméables dans les secteurs à forte pente contribue ainsi à la génération d'écoulements abondants et à leur propagation rapide jusqu'à Epinal (Maire and Corbonnois, 2000). La physiographie du bassin versant tend à amplifier ce phénomène, en favorisant la concomitance des pics de crues ce qui peut conduire à la formation d'ondes de crues très puissantes (Maire and Lasserre, 1991).

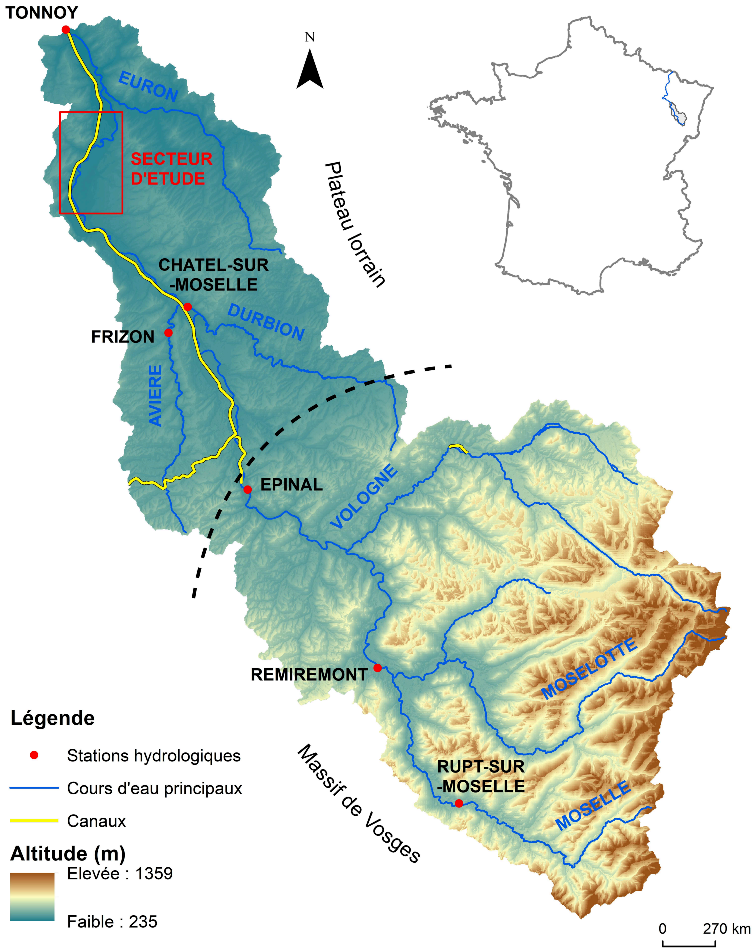

FIGURE 2.1 : Topographie du bassin versant de la Moselle en amont de Tonnoy

2.1.2 Le plateau lorrain

A l'aval d'Epinal, la Moselle s'encaisse dans le plateau lorrain qui se situe en périphérie de l'Est du Bassin parisien entre $300m$ et $400m$ d'altitude (Figure 2.1). Le cours d'eau draine une vallée dont les versants ont une centaine de mètres de hauteur. La pente longitudinale moyenne est de $1,7$‰ et est alimentée par plusieurs affluents : l'Euron ($147km^2$), le Durbion ($145km^2$) et l'Avière ($116km^2$) (Maire and Corbonnois, 2000). Le substratum, du Secondaire, se compose d'une superposition de couches sédimentaires, à faible pendage vers le Nord-Ouest, dont la lithologie est essentiellement calcaire et marneuse (Figure 2.2). La largeur de la vallée varie selon la nature du substratum encaissant, de $400m$ dans la traversée des roches calcaires à $2500m$ au niveau des versants marneux ou argileux (Beck and Corbonnois, 2003).

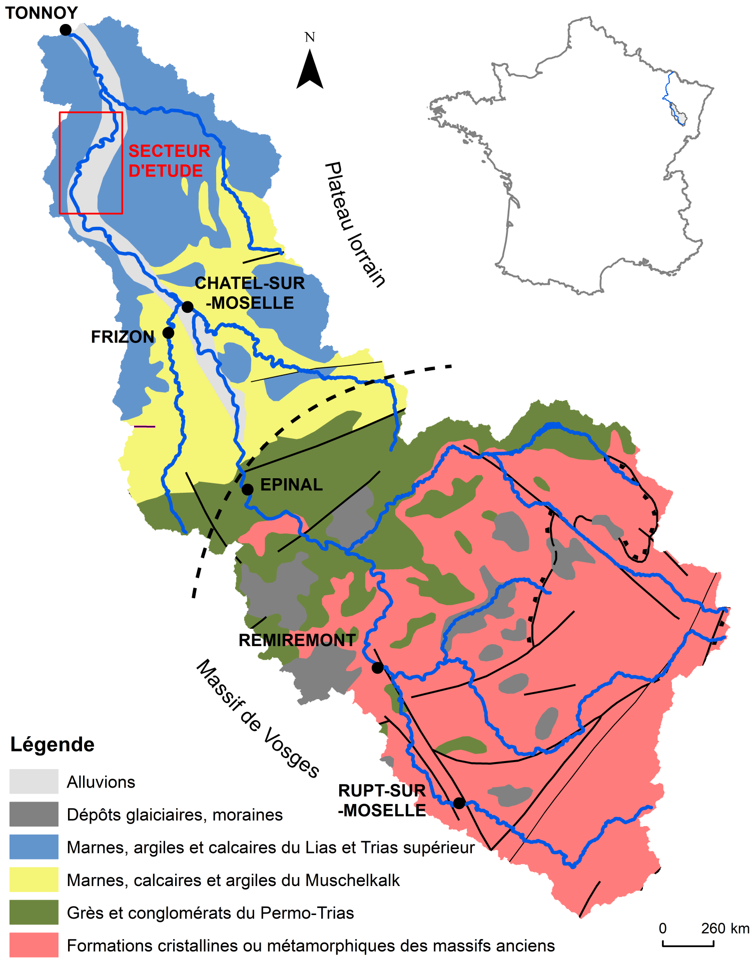

FIGURE 2.2 : Carte géologique simplifiée du bassin versant de la Moselle en amont de Tonnoy

Plusieurs niveaux de terrasses s'inscrivent dans la vallée, les terrasses les plus élevées sont attribuées au Mindel (50 à 100m) et les plus basses au Würm (5 et 20m) (Maire and Lasserre, 1991). Le rebord de ces terrains fluviatiles ou fluvioglaciaires datés du Quaternaire est cependant rarement en contact avec le lit majeur et procure donc très peu de matériaux à la rivière. La fourniture sédimentaire du cours d'eau se fait principalement par remaniement des sédiments du fond alluvial holocène (Maire and Lasserre, 1991). Cet héritage fluvial constitue un ruban continu d'alluvions, d'une épaisseur de 3 à 5m, principalement composé de sables et de galets, ayant été charriés par la Moselle depuis les Vosges. En fonction des secteurs, les matériaux redistribués proviennent soit de l'incision du cours d'eau, de la reprise de bancs alluviaux ou du recul de berge (Beck and Corbonnois, 2003). La Moselle possède une dynamique de lit à fond mobile assez active, l'amplitude des oscillations du tracé du lit mineur est identique à la largeur du cours d'eau (coefficient de sinuosité de $1,16$). Cette dynamique naturelle peut cependant être localement influencée par l'ossature rocheuse de la vallée (affleurements ou butée), ainsi d'après Maire and Lasserre (1991) 90% du linéaire entre Epinal et Méréville est liée à cette structuration.

2.1.3 Le tronçon d'étude

Dans notre secteur d'étude (Figure 2.2), la configuration de la vallée de la Moselle se singularise par l'élargissement du fond alluviale ($2000 - 2200m$ entre Socourt et Virecourt) et l'augmentation de l'épaisseur d'alluvions (8 à $10m$ de dépôts sablo-graveleux) (Maire and Lasserre, 1991; Carcaud, 1992). Sur la partie amont du linéaire (Figure 2.4), le lit mineur de la Moselle se localise essentiellement du côté gauche de la plaine d'inondation (Charmes à Bainville-aux-miroirs), tandis que sur la partie aval de la zone d'étude, la rivière vient au contact du talus rocheux situé à droite du lit majeur (Virecourt à Bayon). Cette disposition a pour conséquence d'accompagner et d'amplifier le balancement général du tracé en “S“ de la vallée qui est probablement lié à des causes tectoniques (Maire and Corbonnois, 2000).

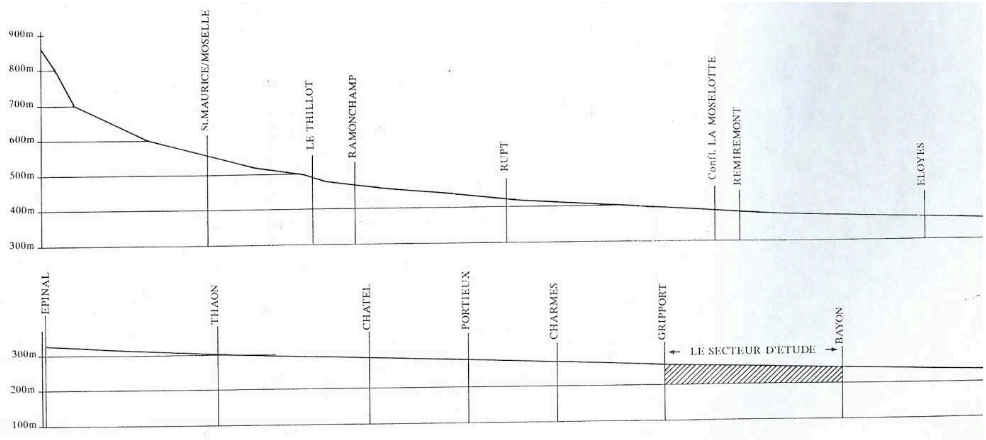

FIGURE 2.3 : Profil en long de la Moselle, d'après AERM (1992)

Sur ce tronçon de $12km$ de long (Figure 2.4), la Moselle possède une pente d'environ $1,2$‰, une largeur moyenne de $60m$ et une puissance spécifique de l'ordre de $45W/m^2$ avec des variations locales plus ou moins importantes (Beck and Corbonnois, 2016). Le tracé de ce cours d'eau cours de moyenne énergie est globalement très sinueux (indice de sinuosité moyen de $1,37$), mais comporte localement des tronçons pouvant être rectilignes (Virecourt ; $1,01$), sinueux (Bainville-aux-miroirs ; $1,11$) ou méandriformes (Mangonville ; $1,72$). Cette disparité spatiale s'explique en partie par la présence de facteurs structuraux. En effet, d'après Chardon (2014), 20% de la sinuosité du lit mineur est indépendante des seules conditions actuelles de l'écoulement. Le passage d'un versant à l'autre se fait entre Bainville-aux-miroirs et Virecourt au niveau d'un unique grand “travers”, dont le tracé général du lit s'oriente obliquement dans la vallée (Maire and Lasserre, 1991). Sur ce tronçon affranchi d'incidences structurales, le tracé de la Moselle s'ordonne en train de méandres (longueur d'onde $900 - 1000m$, amplitude $400 - 700m$, indice de sinuosité $1,72$) évoluant par migration progressive vers l'aval et recoupement naturel par débordement. Cette dynamique latérale active est amplifiée par une faible cohésion des alluvions des berges, dont la granulométrie décroît d'amont en aval, passant d'un D_{50} de 20 à $15mm$ et d'un D_{90} de 60 à $50mm$ entre Charmes et Bayon (Maire and Lasserre, 1991). Ces matériaux constituent l'essentiel des sédiments grossiers des bancs et des radiers. La présence de bancs vifs indique par ailleurs que ces dépôts peuvent facilement être mis en mouvement lors de crues. Une pente relativement marquée et une dynamique de lit à fond mobile sont autant de caractéristiques d'un cours d'eau de piémont (AERM, 1998).

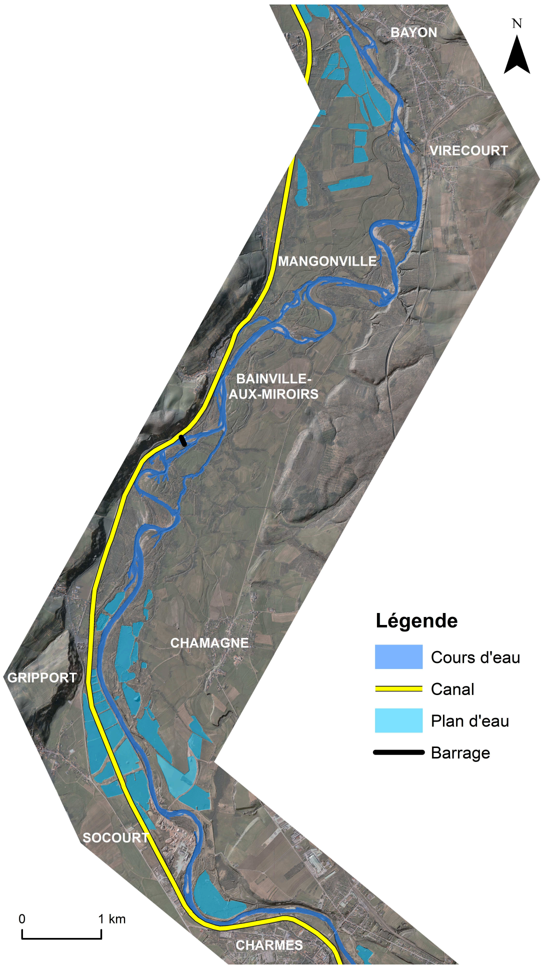

FIGURE 2.4 : Linéaire d'étude de la Moselle entre Charmes et Bayon

2.2 Caractéristiques hydrologiques de la Moselle

2.2.1 Régime hydrologique de la Moselle

Le réseau d'isohyètes moyennes (Figure 2.5) réalisé à partir de séries pluviométriques d'une période de 19 ans (1971-1990) montre une forte distorsion spatiale des apports en eau à l'échelle du bassin versant. Les précipitations moyennes annuelles sur le plateau lorrain sont d'environ $800mm$ contre 1000 à $2100mm$ sur le massif des Vosges avec d'importantes variations locales (Beck and Corbonnois, 2016). Les cumuls pluviométriques les plus importants se trouvent sur la partie supérieure du bassin, entre le môle topographique de Gérardmer ($1600mm$) et la ligne des crêtes ($> 2000mm$) (Maire and Lasserre, 1991). Les apports mensuels sont de 50 à $80mm$ en plaine et supérieurs à $100mm$ en montagne avec un contraste saisonnier marqué de plus de $200mm$ pendant les mois d'automne-hiver. Ces précipitations abondantes et régulières, constituent une large proportion des écoulements de la Moselle, qui bénéficie ainsi d'un débit soutenu tout au long de l'année. L'étendue de son réseau hydrographique sur le versant ouest du massif Vosgien, en fait le cours d'eau le mieux alimenté du Nord-Est de la France (Beck and Corbonnois, 2003).

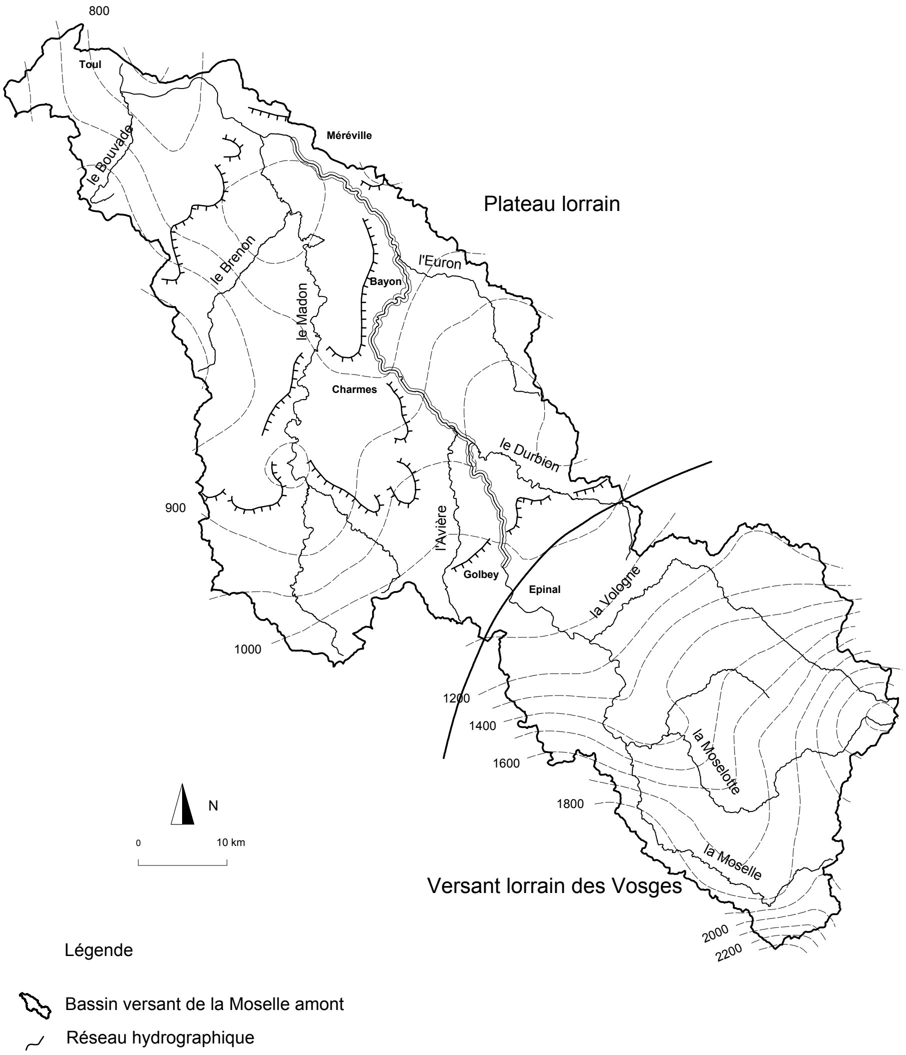

FIGURE 2.5 : Précipitations moyennes annuelles (en mm) dans le bassin versant de la Moselle (période de référence 1971 – 1990), d'après Beck and Corbonnois (2003)

Le régime hydrologique de la Moselle est de type pluvio-évaporal (ou pluvio-océanique) se caractérisant par de hautes eaux en hiver et au début du printemps (novembre-avril) et de basses eaux en été (mai-octobre). Ce régime simple fonctionne selon un rythme annuel de remplissages et de vidanges, comportant 6 mois excédentaires et 6 mois déficitaires, dont le rapport est de 3 pour 1 (Maire and Corbonnois, 2000). Les extrêmes hydrologiques comprennent des crues plus fortes et plus fréquentes en période hivernale et des étiages plus ou moins marqués en période estivale. La saisonnalité et l'amplitude de ces évènements dépend principalement de l'historique des précipitations et de l'état de développement de la végétation. Les crues surviennent majoritairement pendant les saisons froides, lorsque l'évapotranspiration est la plus faible et que d'abondantes précipitations s'abattent sur des sols déjà saturés. Au contraire, les étiages sont liés aux faibles précipitations des saisons chaudes et à une forte évapotranspiration.

Dans un contexte de changement climatique, à l'échelle du bassin versant, une augmentation moyenne de la température de $+1,4°c$ enregistrée en un siècle s'est traduit par une augmentation de $+50mm$ de l'évapotranspiration potentielle, ce qui à conduit a des étiages plus importants.

2.2.2 Hydrologie de la Moselle dans les Vosges

La plus ancienne station hydrométrique installée sur le linéaire français de la Moselle se situe au niveau d'Epinal à $324m$ d'altitude (Figure 2.1) et draine un bassin versant de $1217km^2$. Cette station a été mise en service en 1951 et dispose de données valides de hauteurs d'eau et de débits sur une série de plus de 60 ans, pour la période 1960-2022 (source Banque hydro - eau France). La distribution des débits moyens mensuels (Figure 2.6) se caractérise par un unique maximum l'hiver (décembre-janvier) de l'ordre de $60m^3/s$ et un unique minimum l'été (août) inférieur à $20m^3/s$.

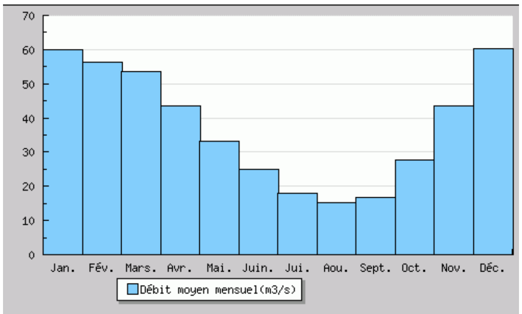

FIGURE 2.6 : Ecoulements mensuels à Epinal calculés sur 60 ans (Banque hydro)

Ce régime pondéré masque des écarts interannuels pouvant être prononcés comportant des débits mensuels extrêmes allant de $3,16m^3/s$ (août 1983) à $152,5m^3/s$ (janvier 2017), soit un rapport de 1 à 48. A l'échelle d'une année hydrologique, la répartition des écoulements peut également fortement varier, en 1983 plus de 50% du volume annuel moyen (786 millions de m^3) s'est écoulé en 60 jours et 10% (154 millions de m^3) en 4 jours (Maire and Lasserre, 1991). A la sortie du massif des Vosges, à Epinal, le module interannuel de la Moselle est de $37,7m^3/s$, ce qui correspond à un débit spécifique de $31l/s/km^2$ et une lame d'eau écoulée de $980mm$. En se basant sur le rapport pluie-débit (période de référence 1952-1968) R. Frecaut (1972) calcule un coefficient d'écoulement de l'ordre de 0,6, le déficit d'écoulement étant principalement imputable à l'évapotranspiration. Les débits instantanés de pointes enregistrés sur ces 60 dernières années (1969-2019) sont survenus le 19 novembre 1972 ($642m^3/s$), 9 avril 1983 ($717m^3/s$), 15 février 1990 ($805m^3/s$), 26 janvier 1995 ($700m^3/s$) et le 5 janvier 2018 ($619m^3/s$). Sur cette période de référence, un ajustement des débits maximums instantanés à une loi de Gumbel (Tableau 2.1) donne, pour ces différentes crues, des périodes de retours comprises entre 10 et 50 ans.

La plus forte crue connue a eu lieu le 29 décembre 1947 ($> 300mm$ de pluie en 5 jours sur les Vosges) avec un débit de pointe estimé à $901m^3/s$ pour une période de retour assimilée à un évènement centennal (Maire and Lasserre, 1991). D'autres crues de bien moindre importance, de périodes de retour de 2 à 5 ans, ont eu lieu en hiver 1998-1999 (notamment le 29 octobre 1998, 21 février et le 10 mars 1999) avec un niveau d'eau élevé, proche du niveau à pleins bords pendant de longues durées (Maire and Corbonnois, 2000).

Fréquence	QJX (m^3/s)	QIX (m^3/s)
Xo	250.0	326.0
Gradex	88.6	122.0
Biennale	280.0 [270.0 ;300.0]	370 [350.0 ;400.0]
Quinquennale	380.0 [360.0 ;420.0]	510.0 [470.0 ;560.0]
Décennale	450.0 [420.0 ;500.0]	600.0 [560.0 ;670.0]
Vicennale	510.0 [470.0 ;580.0]	690.0 [630.0 ;780.0]
Cinquantennale	600.0 [540.0 ;680.0]	800.0 [730.0 ;920.0]
Centennale	Non calculée	Non calculée

TABLE 2.1 : Plus fort débit journalier (QJX) et plus fort débit instantané (QIX) avec les périodes de retour associées pour la Moselle à Epinal, calculés sur 58 ans (Banque hydro).

2.2.3 Hydrologie de la Moselle dans le plateau lorrain

La station hydrométrique de Tonnoy, située $60km$ en aval d'Epinal (Figure 2.1), permet d'estimer la contribution hydrologique du piémont montagneux du bassin versant de la Moselle. L'installation se trouve à $231m$ d'altitude, à l'exutoire d'un versant topographique d'une surface de $1976km^2$ et fournit des données limnimétriques et débitmétriques depuis sa mise en service en 1980 (série de 40 ans).

La distribution saisonnière des écoulements est comparable à celle de la station d'Epinal (Figure 2.6 et 2.7), à l'exception d'un léger creux observé en février à la station de Tonnoy (Remy, 2009). Cette variation mensuelle est liée au stockage temporaire des précipitations sous forme de neige en altitude (Maire and Corbonnois, 2000) et tend à disparaître en raison des changements climatiques.

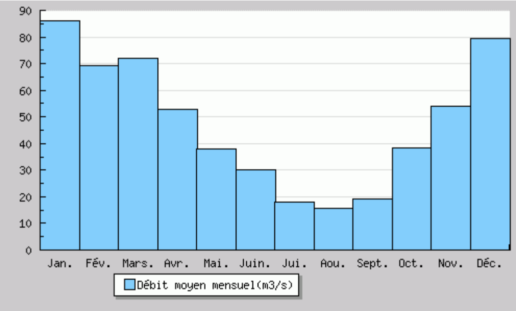

FIGURE 2.7 : Ecoulements mensuels à Tonnoy calculés sur 40 ans (Banque hydro)

Les étiages sont également plus creusés en août à Tonnoy qu'à Epinal, avec des coefficients d'écoulements respectifs de 0,29 et 0,4 (Banque hydro-CRUCAL). Cette différence s'explique de part la morphologie de la rivière, en effet l'élargissement du chenal au piémont est d'avantage favorable aux échanges nappe-rivière et à l'implantation d'espèces pionnières consommatrices en eau (Maire and Corbonnois, 2000). La comparaison des débits caractéristiques calculés pour chaque station montre une augmentation des débits instantanés maximaux de l'ordre de 18% pour les différentes périodes de retour (Tableau 2.1 et 2.2). On estime que le débit de la crue historique de 1947 est de l'ordre de $1000m^3/s$ avec une période de retour de 100 ans.

Fréquence	QJX (m^3/s)	QIX (m^3/s)
Xo	348.0	406.0
Gradex	124.0	144.0
Biennale	390.0 [360.0 ;430.0]	460 [420.0 ;510.0]
Quinquennale	530.0 [490.0 ;610.0]	620.0 [570.0 ;710.0]
Décennale	630.0 [570.0 ;730.0]	730.0 [660.0 ;850.0]
Vicennale	720.0 [640.0 ;850.0]	830.0 [750.0 ;990.0]
Cinquantennale	830.0 [740.0 ;1000.0]	970.0 [860.0 ;1200.0]
Centennale	Non calculée	Non calculée

TABLE 2.2 : Plus fort débit journalier (QJX) et plus fort débit instantané (QIX) avec les périodes de retour associées pour la Moselle à Tonnoy calculées sur 39 ans (Banque hydro)

Le profil hydrologique de la Moselle (Figure 2.8) montre une augmentation lente et régulière des volumes écoulés entre la sortie des Vosges (Epinal point kilométrique (PK) 540) et l'aval du plateau lorrain (Tonnoy PK 600). Sur ce tronçon, près de la moitié des apports proviennent de 4 affluents principaux : Saint-Oger $0,8m^3/s$, Durbion $1,2m^3/s$, l'Avière $1,25m^3/s$ et l'Euron $1,1m^3/s$ (Maire and Lasserre, 1991). Ces affluents étant majoritairement localisés à l'amont de Bayon (Figure 2.1), on considère que les données enregistrées à Tonnoy sont davantage représentatives des volumes écoulés au niveau du site d'étude que celles enregistrées à Epinal. Le module interannuel passe de $37,7m^3/s$ à $47,60m^3/s$ d'amont en aval, soit une hausse de 26% pour une augmentation de la surface drainée de 62%. Cette distorsion spatiale met en évidence la part prédominante de la zone montagneuse dans la constitution des écoulements de la Moselle et la modestie des apports latéraux plus en aval.

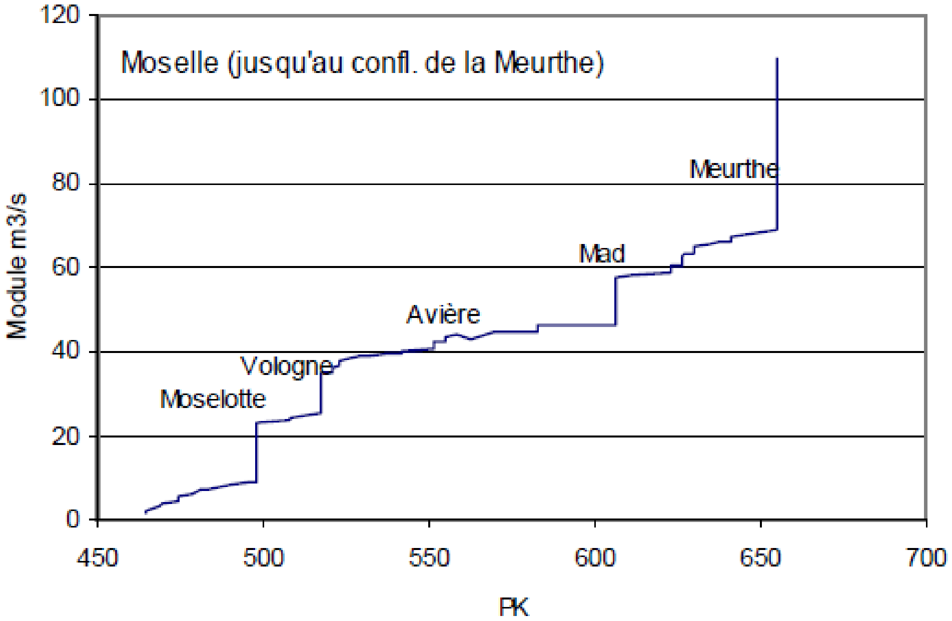

FIGURE 2.8 : Apports des affluents, d'après CEGUM (2006)

2.2.4 Hydrologie des affluents de la Moselle

Une station de mesure complémentaire a été installée à Châtel-sur-Moselle (Figure 2.1) en 2014, entre la confluence avec le Durbion et l'Avière, à l'exutoire d'un bassin versant de $1491km^2$. Cette station étant relativement récente, la chronique disponible (2014-2019) est trop réduite pour permettre une estimation statistique sur les débits de crue et périodes de retour associées. Une méthode d'interpolation par transfert (Piton, 2014) basée sur le rapport d'aires drainées est alors employée (algorithme 2.1) afin d'estimer ces débits à la station de Châtel-sur-Moselle en se basant sur les données issues des stations situées à l'amont (Epinal) et à l'aval (Tonny).

Algorithme 2.1 Méthode d'estimation du débit par rapport d'aires drainées

On considère que le débit Q varie en loi puissance avec l'aire drainée $\mathcal{A}$ amont :

$$Q = a \times \mathcal{A}^b$$

avec a et b des constantes. Cela repose sur une hypothèse forte d'homogénéité des facteurs physiographiques.

On peut alors pour deux points du réseau hydrographique écrire $Q_{amont}/Q_{aval} = (a \times \mathcal{A}^b_{amont})/(a \times \mathcal{A}^b_{aval})$, avec Q_{amont} xxx et Q_{aval} xxx.

$$b = ln(Q_{amont}/Q_{aval})/ln(\mathcal{A}_{amont}/\mathcal{A}_{aval})$$

$$a = Q_{amont}/\mathcal{A}^b_{amont} = Q_{aval}/\mathcal{A}^b_{aval}$$

On obtient un coefficient b de $0,41 \pm 0,04$, cette valeur est relativement constante pour chacun des débits caractéristiques interpolés, mais inférieure à la valeur moyenne de 0.83 déterminée à l'échelle de la France métropolitaine (Cipriani et al., 2012). Le module interannuel interpolé à la station de Châtel-sur-Moselle est de $41,57m^3/s$, contre $37,7m^3/s$ à Epinal ($20km$ en amont) et $47,6m^3/s$ à Tonnoy ($38km$ en aval) (Figure 2.1). Ce résultat indique une augmentation quasi-linéaire du module sur ce secteur, avec un apport moyen de $0,17m^3/s/km$, une tendance que l'on observe également à l'échelle du profil hydrologique de la Moselle (Figure 2.8). Le débit instantané maximal enregistré par la station de Châtel-sur-Moselle est de $675m^3/s$ (Figure 2.9), d'après les valeurs du tableau 2.3 cette crue a une période de retour de 10 ans.

Fréquence	QIX (m^3/s)
Xo	357.0
Gradex	131.0
Biennale	405.0
Quinquennale	553.0
Décennale	651.0
Vicennale	746.0
Cinquantennale	867
Centennale	Non calculée

TABLE 2.3 : Débits caractéristiques interpolés pour la station de Châtel-sur-Moselle

La station de Frizon permet de jauger l'Avière, le seul affluent notable de la Moselle sur le tronçon Châtel-Bayon, avec un module interannuel de $1,25m^3/s$ (Figure 2.1). Cette station située, à $3km$ en amont de la confluence avec la Moselle, dispose de chroniques de débits sur une période de 48 ans (1970-2019) pour un sous-bassin versant de $105km^2$(Figure 2.8). En additionnant les débits mesurés aux stations de Frizon et Châtel-sur-Moselle, on obtient une valeur relativement précise du débit de la Moselle à Nomexy (commune située $2km$ en aval de Châtel-sur-Moselle) au droit de la confluence avec l'Avière.

A l'aval, de petits ruisseaux de quelques kilomètres de long, majoritairement localisés en rive gauche, collectent les précipitations sur une surface d'environ $180km^2$ entre Nomexy et Bayon. Sur ce tronçon, les apports latéraux en crue doivent être comparables aux valeurs enregistrées à la station de Frizon, dont la surface drainée est relativement proche pour une physiographie identique. Sur le secteur Bayon-Tonnoy, l'Euron ($147km^2$) collecte une grande partie des écoulements et vient gonfler le débit de la Moselle d'environ $1,1m^3/s$ (Maire and Lasserre, 1991) à $2km$ en aval du site d'étude. Ce cours d'eau n'est pas instrumenté mais, d'après Maire and Lasserre (1991), la contribution des affluents aux pics de crues de la Moselle est proportionnellement moindre, ou du même ordre de grandeur, que pour le module (Figure 2.8). Maire and Lasserre (1991) affirme ainsi que les apports latéraux entre Epinal et Tonnoy sont insuffisants pour créer une véritable distorsion dans l'évolution longitudinale des débits sur ce secteur.

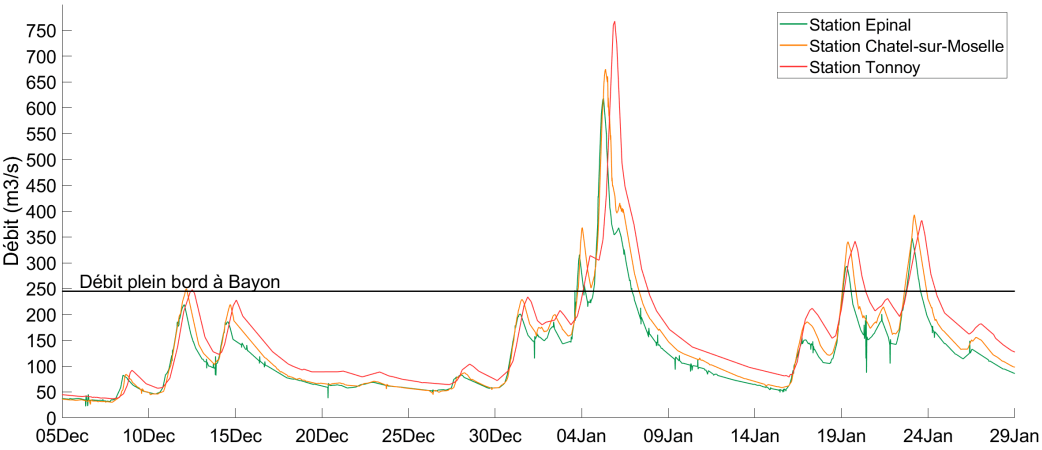

FIGURE 2.9 : Hydrogramme de la Moselle au cours de l'hiver 2017-2018 (Banque hydro)

On observe au contraire une stagnation voire une diminution des débits maximaux instantanés enregistrés entre les stations de Châtel-sur-Moselle et de Tonnoy, pour des écoulements supérieurs à $230m^3/s$, à l'exception de la crue décennale de janvier 2018 (Figure 2.9). Cette valeur est proche du débit à pleins bords de la Moselle estimé par Corbonnois et al. (2006) à Bayon, à l'aval de notre secteur d'étude, de $245m^3/s$. L'écrêtement des pics de crues s'explique par l'élargissement du lit majeur dans le secteur Charmes-Bayon et la présence de nombreux chenaux latéraux favorisant l'expansion rapide du champs d'inondation (Figure 2.4). Lors de la crue la plus importante (15 février 1990), le débit maximum instantané mesuré à Epinal était de $805m^3/s$, pour un débit journalier de $600m^3/s$, puis avec un jour de retard les valeurs étaient respectivement de 789 et $621m^3/s$ à Tonnoy. Globalement, on estime que la vitesse de propagation d'une onde de crue sur la Moselle est de l'ordre de $10km/h$.

2.3 Anthropisation de la vallée de la Moselle

2.3.1 Aménagements antérieurs au XIXème siècle

L'influence notable des actions anthropiques sur le cours de la Moselle remonte au Moyen-Age suite à l'installation de l'Homme dans le fond de vallée (château de Charmes) et à l'établissement de ports fluviaux (Gripport) (Bonnefont and Carcaud, 1997). En effet, à l'époque médiévale un épais couvert forestier limite l'érosion du massif des Vosges et un climat très tempéré (optimum climatique médiéval) permet un régime fluviale pondéré favorable à la navigation. Entre le XIIIe et le XVIe siècle, une augmentation de la pression agricole et le déboisement consécutif des versants entraînent l'érosion torrentielle dans le massif des Vosges et un alluvionnement dans les fonds de vallées. A compter de la fin du XVe siècle, le refroidissement climatique du Petit Age Glaciaire, s'ajoute aux effets du retrait forestier, ce qui conduit à une augmentation de la fréquence et de l'intensité des crues hivernales, pouvant encore être aggravées par des débâcles de glace. La conjugaison de ces facteurs intensifie l'activité morphologique du XVe au XVIIIe siècles, par ailleurs renforcée par l'abondante fourniture sédimentaire issue de l'érosion des versants.

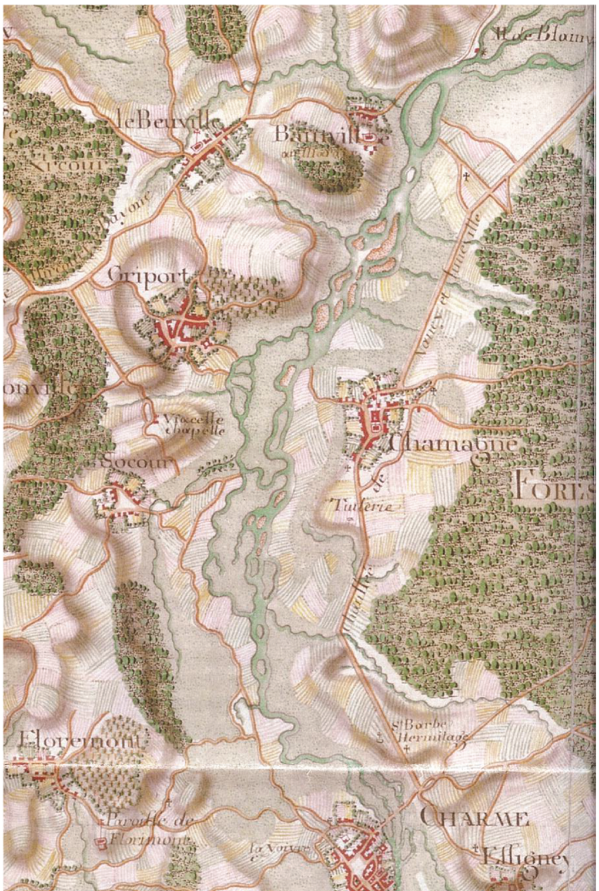

FIGURE 2.10 : Alternance de tronçons à méandrage et à tressage dans le secteur Charmes-Bainville aux XVIIIe siècle (extrait de la carte Naudins env. 1730)

L'intensification de la dynamique fluviale du Moyen-Âge à l'époque moderne, se traduit par une mobilité latérale accrue du lit fluvial avec des changements de lit (destruction du moulin de Mangonville), favorisés par le défrichement du fond de vallée (Remy, 2009). Les dommages des crues sont accentués par la multiplication de petits aménagements hydrauliques locaux (moulins, canaux de dérivation, endiguements, etc.) qui freinent les écoulements et augmentent l'épaisseur de la lame d'eau. Dès la fin du XVIe siècle, en réponse aux variations hydroclimatiques et de l'occupation du sol du bassin versant, la Moselle développe un style fluvial à méandres très mobiles puis, au début du XVIIIe siècle, des secteurs en tresses apparaissent ponctuellement (Figure 2.10). Cette métamorphose partielle du style fluvial met en évidence que la Moselle n'a localement plus la capacité d'évacuer la charge sédimentaire fournie par le bassin versant (Remy, 2009). Malgré une occupation humaine relativement diffuse dans le fond de vallée, les tronçons en tresses se situent principalement à proximité de constructions humaines (moulin, château). L'impact de ces aménagements sur les écoulements (ralentissement) et le transport sédimentaire (piégeage) peut donc être à l'origine de la distribution longitudinale des différents types de styles fluviaux (Bonnefont and Carcaud, 1997). Les aménagements (digues, barrages, canal de dérivation) réalisés entre le XVIe et le XVIIIe siècle pour lutter contre les crues ou gagner des surfaces de prairies manquent cependant de solidité et de coordination. A cette époque, le fond de vallée est donc voué principalement au pâturage car la forte mobilité des bras de la Moselle entraîne la disparition des terres arables en les inondant très fréquemment et intensément. De ce fait, il n'existe aucun pont sur ce secteur, seul un bac permettant la traversée de la Moselle au droit de Bayon.

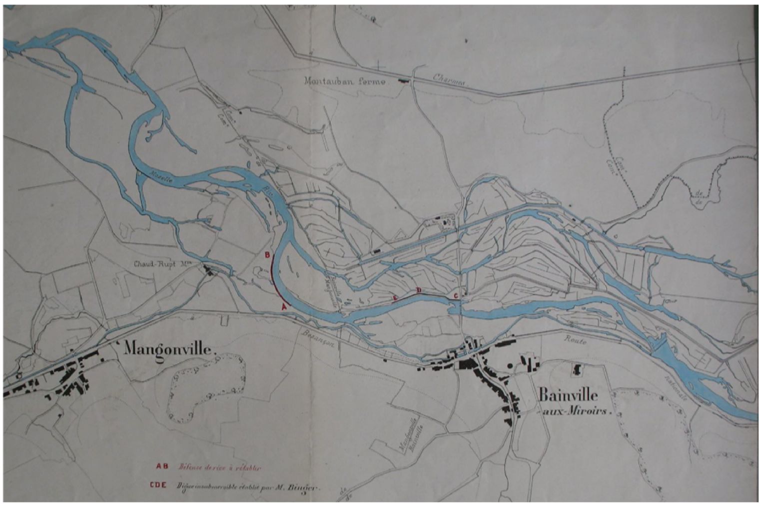

Figure 2.11 : Réseau d'irrigation des prairies aux environs de Bainville en 1878 (Archives 54)

Au début du XIXe siècle, les frères Dutac et leurs successeurs ont entrepris d'aménager la haute Moselle et de conquérir de nouveaux espaces grâce à la construction de digues et de barrages permettant d'alimenter un réseau d'irrigation (Figure 2.11). Dans le secteur de Charmes-Gripport, ces travaux ont permis de limiter la divagation latérale du cours d'eau et d'assurer une irrigation et une fertilisation des terrains graveleux via l'apport et le dépôt de matières en suspension sur des surfaces graveleuses (Remy, 2009).

2.3.2 Aménagements du XIXème siècle

Les grands aménagements du XIXe siècle débutent en 1860 par la canalisation partielle de la Moselle en aval de Neuves-Maisons (Bonnefont and Carcaud, 1997). Cette voie de navigation est constituée d'une alternance de biefs régulés par des barrages et de secteurs en dérivation. A l'amont, plutôt que d'aménager le cours d'eau pour le rendre navigable, un canal latéral à la Moselle est construit entre Neuves-Maisons et Epinal. La construction du canal de l'Est (branche sud) dans les années 1870-1890, entraîne la déconnexion de certains bras de la Moselle (canal d'amené au moulin de Gripport) et la déviation de certains tronçons du cours d'eau (barrage de Bainville). Ces différents aménagements conduisent à une multiplication des points de buté latéraux du lit mineur, qui viennent s'additionner aux éléments géologiques structurant de la vallée. Bien que localement la construction de ce canal préserve en grande partie le tracé naturel du cours d'eau, à l'échelle régionale, la pression anthropique s'intensifie en raison de l'impact de ces aménagements sur les écoulements (Figure 2.12).

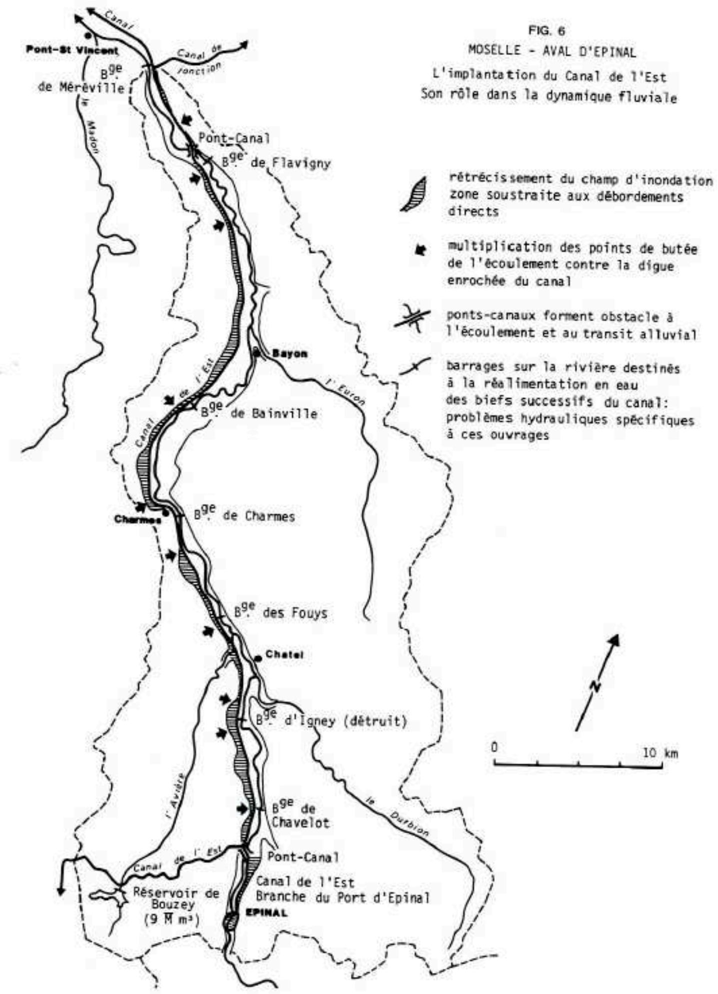

FIGURE 2.12 : Implantation du Canal de l'Est et son rôle dans la dynamique latérale de la Moselle, d'après Maire and Lasserre (1991)

En effet, les digues de protection du canal limitent l'étalement des crues en lit majeur ce qui provoque un rehaussement du niveau d'eau et accroit localement la capacité de transport du cours d'eau. Ainsi, le rétrécissement du champs d'inondation a entrainé un surcreusement et un encaissement du lit principal de la Moselle, conduisant à un abandon ou à un comblement rapide des chenaux secondaires (Maire and Lasserre, 1991). Cette simplification du tracé du cours d'eau est le principal facteur du retour au méandrage de la Moselle, mais la subsistance de chenaux secondaires souligne une mutation encore incomplète du style fluvial (Bonnefont and Carcaud, 1997). La variation spatiale de l'évolution du style fluvial, avec un maintien plus ou moins tardif du tressage entre le XVIIe et le XXe siècle, est cependant liée à la présence de contraintes morpho-sédimentaires locales. Maire and Corbonnois (2000) cartographie de petits secteurs en tresses sur la Moselle jusque dans les années 1960 (en aval de Gripport), mais considère qu'en dépit de ces épiphénomènes le système est en équilibre au milieu du XIXe siècle.

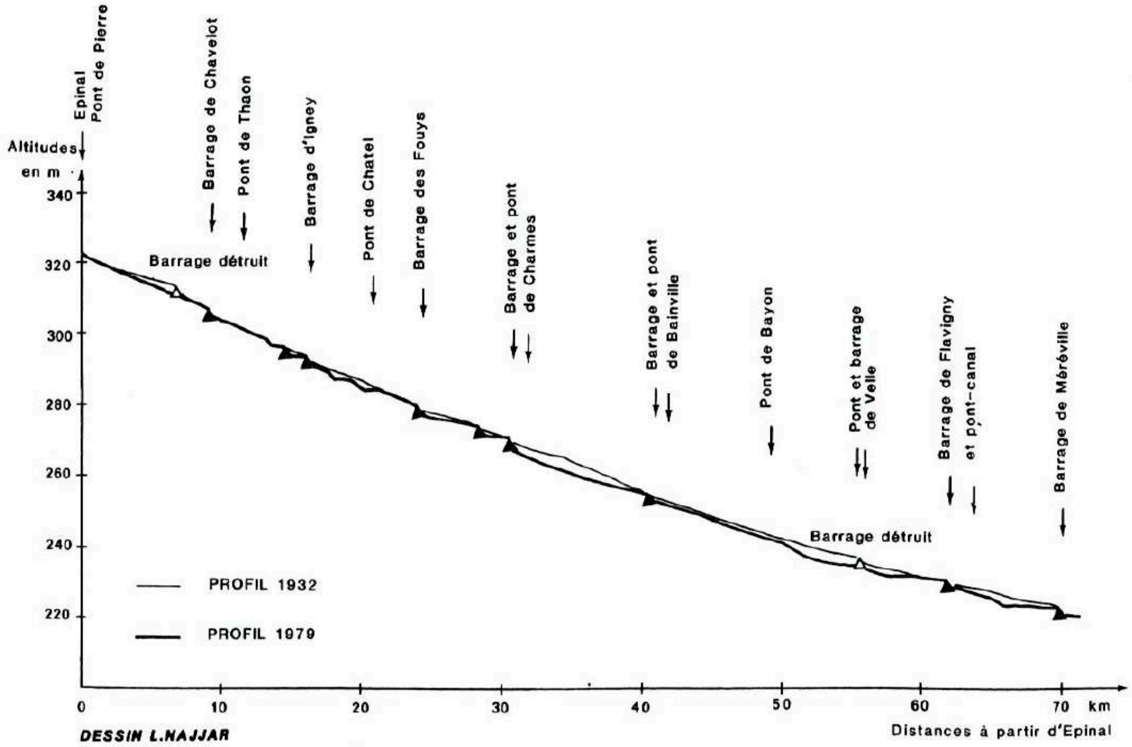

FIGURE 2.13 : Profil en long de la Moselle en 1932 et 1979, d'après Maire and Lasserre (1991)

L'alimentation des biefs du canal de l'Est nécessite également la construction de prises d'eau latérales successives associées à des barrages, réparties sur l'ensemble du linéaire de la Moselle (Figure 2.12). Ces barrages modifient localement la compétence du cours d'eau : à l'amont le remous hydraulique du barrage entraîne un dépôt de sédiments et facilite les débordements, tandis qu'à l'aval les écoulements contribuent à l'affouillement et à l'incision du lit. La multiplication de ces ouvrages impacte le transit sédimentaire à l'échelle du bassin versant ce qui engendre des ajustements morphologiques du lit de la rivière. En 1932, soit un demi-siècle après la construction du canal de l'Est, on constate que la majorité des barrages semblent être comblés. Ils seraient donc relativement transparents du point de vue de la continuité sédimentaire (Figure 2.13).

La construction du barrage de Bainville est antérieure aux aménagements du canal de l'Est et date de 1830. A cette époque, cet ouvrage permet d'alimenter trois moulins situés sur un bras de la Moselle passant par Bainville, Mangonville et Roville (Remy, 2009). Grâce à un droit d'eau datant du XVIIIe siècle, ce barrage a pu être réaménagé à plusieurs reprises, afin d'alimenter deux microcentrales situées à Bainville et Mangonville. Actuellement, la cote de la crête du barrage est de $254,55m$, avec dans les conditions hydrologiques normales un débit turbiné de $4m^3/s$, pour une hauteur de chute de $2m$ (Sinbio, 2010). Voies navigables de France (VNF) prélève également de l'eau au droit du barrage pour alimenter le canal de l'Est .

Au XIXe siècle, d'autres aménagements lourds sont ponctuellement effectués afin de protéger des habitations (par ex. une digue de défense de Mangonville), des voies de communications (par ex. un perré longeant le talus de soubassement du chemin de fer à Virecourt) ou favoriser le franchissement de la rivière (par ex. pont de Bainville) (Remy, 2009). L'implantation du pont s'accompagne cependant d'une contraction latérale du lit mineur et d'un affouillement autour des piles, tandis que les chaussées surhaussées forment des digues transversales aux écoulements qui cloisonnent le lit majeur.

2.3.3 Extraction de granulats en lit mineur

L'extraction industrielle d'alluvions dans le lit mineur de la Moselle démarre après la seconde guerre mondiale, à proximité des villes (Nancy et Epinal) et des principales voies de communication (Edelblutte, 2000). Les prélèvements directs s'intensifient considérablement au cours des années 1960, puis s'étendent inégalement dans le fond de vallée jusqu'aux années 1980, à l'exception du secteur Bainville-Virecourt (Maire and Lasserre, 1991). Ces zones d'extraction en lit mineur forment de vastes fosses (Figure 2.14) qui piègent la totalité de la charge de fond et contribuent à sectoriser le transit sédimentaire (Beck and Corbonnois, 2003).

Le comblement progressif de ces fosses perturbe l'équilibre morphodynamique de la Moselle et engendre la propagation de fronts d'érosion de part et d'autre des zones d'extractions (Maire and Corbonnois, 2000). A l'amont, l'augmentation locale de la pente du fond provoque une vague d'érosion régressive conduisant à un abaissement du plancher alluvial pouvant aboutir à la mise à nu du substratum rocheux (Figure 2.14). A l'aval, le déficit sédimentaire occasionné par le piégeage des matériaux est compensé par une érosion progressive à l'origine d'un creusement vertical du lit (Maire and Lasserre, 1991). La propagation de ces ajustements morphologiques sur le linéaire de la Moselle entraine ainsi l'ablation d'un important volume de sédiment au cours du XXe siècle. Durant cette période, on estime qu'en moyenne $79000 tonnes/an$ de matériaux sont exportés du tronçon situé entre Epinal et Velle-sur-Moselle (Maire and Lasserre, 1981; BCEOM, 1981). Cette vidange du remplissage alluvial provoque une incision quasi-généralisée du lit avec des valeurs pouvant atteindre $-4m$ (Figure 2.13) au droit des sites d'extraction (BCEOM, 1981).

La pérennité de certains ouvrages d'art étant menacée par cette incision (par ex. l'effondrement du pont de Charmes en 1966), la réglementation interdit progressivement les extractions en lit mineur vers la fin des années 1970. Cependant, malgré cette interdiction et le comblement progressif des fosses d'extraction le phénomène se poursuit en raison de la modification locale des forçages hydrodynamiques (Figure 2.14). L'enfoncement du lit a engendré une réduction de la fréquence des débordements en lit majeur, ce qui limite le mécanisme de détente hydrocinétique et accroit la capacité érosive de la Moselle (Maire and Lasserre, 1991). Le réajustement du plancher alluvial à ces nouvelles conditions hydrodynamiques passe par une réduction de la pente du cours d'eau, qui se traduit par une incision du lit à l'amont et un exhaussement à l'aval.

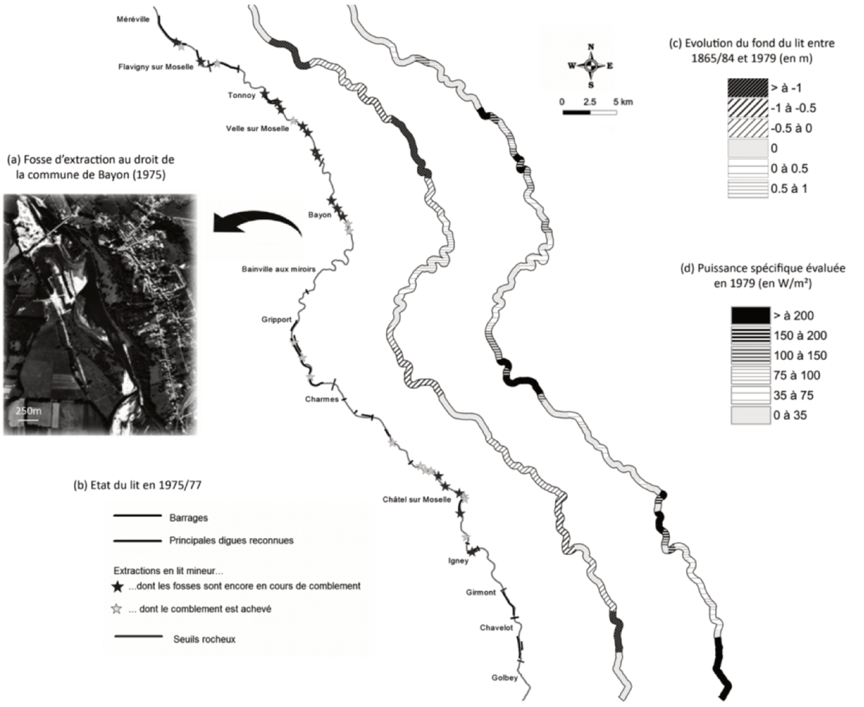

Données sources: Photographies aériennes de 1975/1977, profil en long des Grandes Forces Hydrauliques de 1865/84 et levés topographiques de 1979 (BCEOM, 1981)

FIGURE 2.14 : Extraction de granulats en lit mineur et modification du cours d'eau, d'après Beck and Corbonnois (2016)

Cette reconquête d'un nouvel équilibre dynamique se fait de proche en proche, (Figure 2.14) avec une alternance de secteurs à forte puissance spécifique (incision du chenal) avec des secteurs à faible puissance spécifique (fosse d'extraction en comblement). L'évolution de la surface de la bande active et des zones végétalisées (Figure 2.15), indique toutefois qu'en 1979 l'ampleur de cette nouvelle dynamique fluviale est encore spatialement déséquilibrée (Beck and Corbonnois, 2003). Suite aux fortes incisions du lit et aux apports sédimentaires provenant de l'amont, les fosses d'extraction situées entre Epinal et Châtel-sur-Moselle sont majoritairement comblées. Cette vidange sédimentaire a conduit à la mise à nu du substratum rocheux sur une bonne partie du linéaire et au contournement de certains ouvrages tel que le barrage d'Igney en 1983 (Figure 2.13). Les matériaux emportés tendent à s'accumuler à l'aval de cette zone de fourniture sédimentaire, entre Gripport et Tonnoy, mais le comblement en cours des fosses induit une sectorisation du transit sédimentaire.

Cette évolution complexe est commandée par plusieurs types de dynamiques qui résultent indirectement des extractions passées et freinent le transfert amont-aval de la charge de fond. Le comblement des fosses et leur végétalisation contribuent au rétrécissement de la bande active, ce qui favorise des dépôts régressifs (amont de Bayon) et ralentit, voire bloque, la charge grossière. L'apparition de seuils rocheux, à la suite de l'incision du planché fluvial, ralentit également le transit sédimentaire et immobilise la charge de fond par dépôts progressifs. L'exhaussement du lit engendre une érosion et un recul de berges, ce qui engraisse les bancs et facilite les dépôts progressifs.

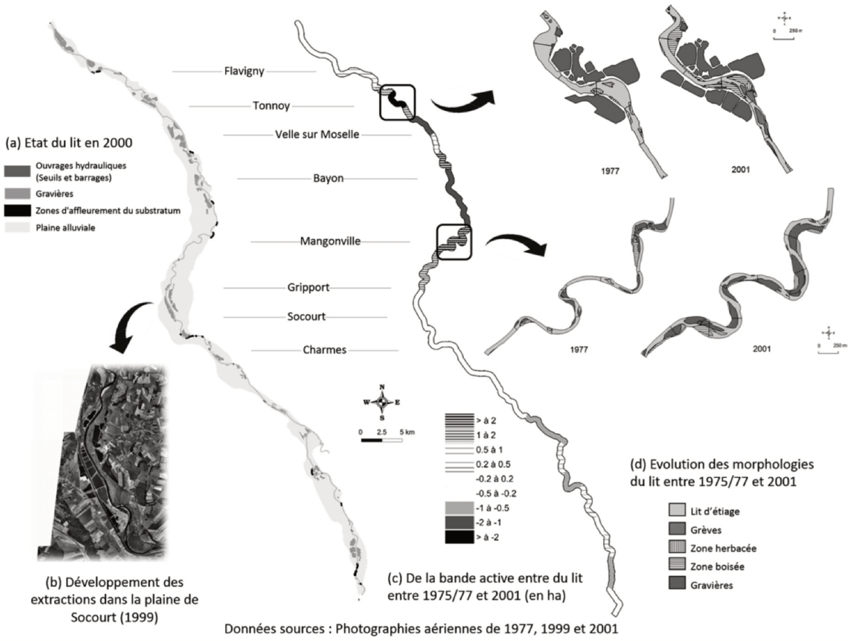

Données sources : Photographies aériennes de 1977, 1999 et 2001

FIGURE 2.15 : Evolution de la dynamique de la Moselle à la suite de l'arrêt des extractions en lit mineur, d'après Beck and Corbonnois (2016)

Les ouvrages impactent à leur tour la dynamique de la Moselle. Sur le secteur Châtel-Gripport, une succession de barrages permet de stabiliser le lit de la rivière sur ce tronçon. La reconstitution d'un nouvel équilibre dynamique est longue et passe par plusieurs stades intermédiaires étalés sur des décennies, mais cette évolution peut être accélérée ou freinée par des évènements hydrologiques (fortes crues), géomorphologiques (défluviation) ou anthropiques (endiguement) (Remy, 2009). Ainsi, d'après Maire and Lasserre (1991), les crues morphogènes de 1982-1983 ont permis le comblement des anciennes fosses d'extraction et d'initier un processus d'auto-restauration du cours d'eau en vue de rétablir la continuité fonctionnelle du lit.

2.3.4 Extractions de granulats en lit majeur

L'abandon progressif des prélèvements en lit mineur s'amorce peu avant 1980 en raison du non renouvellement des autorisations préfectorales d'extraction venues à échéances (Maire and Corbonnois, 2000). Ces contraintes réglementaires entraînent un report massif des extractions en lit majeur et l'ouverture, de 1980 à 1990, de nombreuses gravières dans le fond de vallées (Figure 2.16). L'exploitation de granulats dans la plaine alluviale s'accompagne de la construction de digues en bordure du lit mineur permettant de protéger les gravières des divagations latérales de la Moselle. Ces aménagements sont mis en place hâtivement, à partir de matériaux de type "tout venant", puis sont progressivement consolidés par des enrochements ou des blocs de béton afin de former une barrière quasi-imperméable (Maire and Lasserre, 1991). L'endiguement du cours d'eau est souvent assorti d'une rectification du chenal, qui accélère les vitesses d'écoulement, et d'un surhaussement des berges, qui augmente le rayon hydraulique de la section. Cette canalisation restreint latéralement le champ d'inondation et concentre les débits dans la rivière, ce qui rehausse le tirant d'eau et accroît la capacité de transport.

Ces contraintes hydrauliques se superposent localement aux perturbations de la dynamique fluviale, liées aux prélèvements en lit mineur, ce qui peut exacerber l'incision du lit. L'enfoncement du chenal est d'autant plus marqué lorsque des enrochements protègent les berges et empêchent l'érosion latérale susceptible de compenser le déficit sédimentaire (Chardon, 2014). Le matériel repris du fond tend à s'accumuler en aval du secteur endigué car la rivière n'a localement plus la capacité de transporter le surplus sédimentaire. Des dépôts conduisent à l'exhaussement du plancher alluvial ce qui favorise les débordements. Ce phénomène d'ablation/accumulation se transfère en s'amortissant, tant vers l'amont que vers l'aval, et conduit à la mise en place d'un profil longitudinal basculé (Maire and Lasserre, 1991). Les travaux d'endiguements et d'enrochements impactent donc les processus d'ajustement du cours d'eau et peuvent aggraver les risques d'inondation.

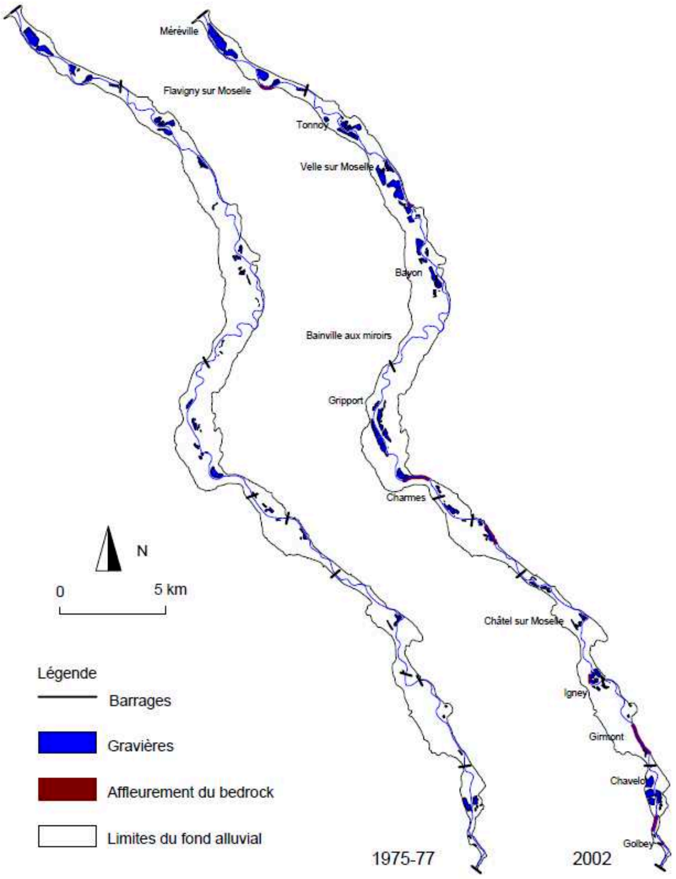

FIGURE 2.16 : Evolution des aires d'extraction de granulats en lit majeur entre 1975 et 2002, d'après Beck and Corbonnois (2003)

A partir de 1990-2000, les extractions en lit mineur sont totalement interdites (arrêté du 22 septembre 1994 relatif aux carrières) et il n'y a plus d'ouverture de gravières dans la bande active de la Moselle. L'occupation du sol de la vallée est plus ou moins figée (Figure 2.16) et l'obligation de "remise en état du site" datant de 1971, contraint les carriers à renforcer les berges des gravières désaffectées avec des enrochements.

La gestion et l'entretien de ces zones "évidées" d'alluvions (220ha du lit majeur entre Charmes et Bayon) incombe ensuite aux communes, qui louent ces étangs et plans d'eau aux associations de pêche afin de bénéficier d'un revenu régulier. L'endiguement du lit mineur et la multiplication des extractions à proximité directe de la Moselle engendre cependant un risque de rupture de digue pouvant conduire à la capture de la Moselle par des gravières. En effet, ces aménagements peuvent être déstabilisés en crue par l'affouillement du pied de berge, aggravé par l'incision du lit, la surverse des écoulements débordants (rehausse du tirant d'eau en crue) et/ou sous l'effet de la pression hydrostatique (renard hydraulique).

2.3.5 Capture de la Moselle par une gravière

L'impact d'une capture sur le transit alluvial est comparable au comblement des anciennes fosses d'extractions en lit mineur, avec le piégeage de la totalité de la charge de fond et le développement de fronts d'érosions progressive et régressive. Au point de rupture, la chute de la capacité de transport du lit court-circuité favorise l'engravement en lit mineur, tandis qu'au point de restitution, le "vidage" de la gravière dans le lit peut entrainer une surcharge alluviale locale (Maire and Corbonnois, 2000). L'interruption du transport solide causée par le déversement de la rivière dans la gravière peut durer sur plusieurs décennies, selon le volume à combler, le transport solide amont et les aléas hydrologiques. Afin d'atténuer le risque de capture de la Moselle, le principe de cloisonnement transversal des anciennes gravières est mise œuvre peu avant 1990, au niveau des plans d'eau de Bayon et de Socourt. Les digues séparatives du lit mineur sont également renforcées à la suite de la capture partielle de la Moselle par un étang à Bayon, lors des crues de 1982 et 1983. Des déversoirs enrochés sont mis en place dans le corps des digues pour favoriser les connexions hydrauliques entre les étangs et la rivière en crue (Figure 2.17). Ces aménagements doivent permettre aux plans d'eau de jouer un rôle d'écrêtement des crues, par le remplissage différé des gravières. Le volume disponible est cependant souvent trop faible pour réduire les inondations. De même, le faible coefficient de rugosité de ces surfaces en eau, par rapport à la surface du sol peut accélérer le cheminement d'une onde de crue en direction de l'aval.

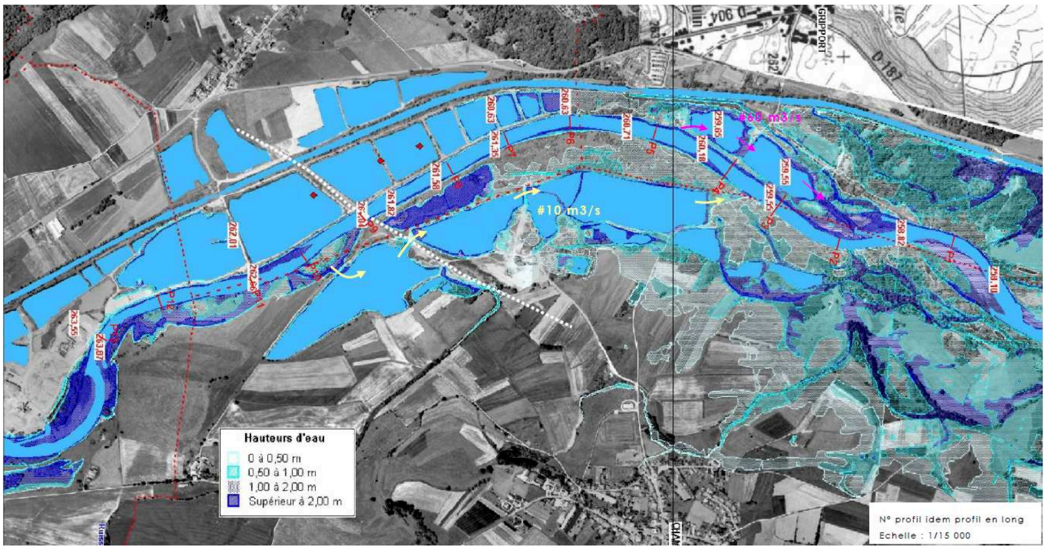

FIGURE 2.17 : Modélisation des surfaces inondées pour une crue décennale dans le secteur de Gripport (Atlas Sogreah)

Lors de la crue de 1990 (période de retour 20 ans), aucun seuil de connexion n'est aménagé au niveau des gravières de Socourt et de Chamagne (Figure 2.17). Cet évènement a engendré 3 brèches entre les plans d'eau de la rive droite, ce qui a conduit à la mise à nu du pipeline Marseille-Strasbourg. A la suite de cette crue, la commune de Socourt a dû abaisser la digue enrochée et créer des déversoirs pour faciliter les écoulements entre la Moselle et les étangs dans le but d'éviter un phénomène de capture en chaine (Edelblutte, 2000). L'enchainement des évènements hydrologiques de période de retour 20 ans, en 1983 et 1990, initie par ailleurs l'érosion de la berge amont et du cordon inter-plan des anciennes gravières de Gripport. La submersion répétée sous environ $1,5m$ d'eau de la berge séparative de la gravière amont conduit à une réduction de la couverture végétale arborescente de la ripisylve à la veille de la crue de janvier 1995. Les deux étangs de $2ha$ et $3ha$ sont capturés par la Moselle lors de cet épisode de crue décennale, suite à une déstabilisation de la partie amont du cordon de séparation avec le cours d'eau et à une brèche centrale entre les étangs (Figure 2.18).

FIGURE 2.18 : Photographie aérienne de la capture de la Moselle par les gravières de Gripport en 1995 (Source IGN)

Des travaux d'urgence sont effectués afin de rétablir l'écoulement dans le lit du cours d'eau (creusement d'un chenal préférentiel dans la Moselle et deux épis de fond en enrochement en rive gauche) et de reconstruire la digue de séparation entre la Moselle et les étangs (double cordon de gabions enserre un remblai en partie végétalisé). Dans le but d'améliorer la connexion hydraulique avec les plans d'eau, un déversoir amont est installé au niveau du premier étang et deux collecteurs avals sont mis en place au niveau du second étang. La Moselle est à nouveau capturée au cours de la crue de décembre 2001 (période de retour 10 ans), les écoulements ont arraché les aménagements en génie végétal et engendré une importante érosion du remblai entre les deux rangées de gabions. Depuis cette date, l'érosion du remblai se poursuit, la rangée de gabions se trouvant à coté de la Moselle est pratiquement détruite et des griffes d'érosion continuent de se propager entre les deux plans d'eau et au niveau de la connexion aval.

Actuellement, le plan d'eau amont est connecté avec le cours d'eau pour un débit proche du module ($42m^3/s$), mais à court ou à moyen terme la déstabilisation totale des protections engendrera une capture de la Moselle (Champalbert Expertises and hydro expertise, 2008). La gestion de ces deux gravières abandonnées depuis les années 80 revient à la commune de Gripport, plusieurs scénarii extrêmes d'aménagement sont à l'étude, dont la capture du cours d'eau ou le remblai total ou partiel des étangs. La capture du cours d'eau se traduit par un abaissement rapide des fonds (0,6 à 1m) en direction de l'amont, jusqu'au prochain point dur et une interruption du transport solide à l'aval pendant plusieurs décennies (Champalbert Expertises and hydro expertise, 2008). En 2008, le coût du comblement total des deux gravières ($95000m^3$) s'élevait de 800 000€ à 1 340 000€, ce qui explique le choix des gestionnaires de ne pas intervenir pour le moment.

2.3.6 Prélèvements en eau potable

L'extraction de granulats en lit majeur réduit la capacité de filtration de la plaine alluviale et perturbe les échanges nappe-rivière à proximité des gravières (Edelblutte, 2000). Face aux menaces que font peser les carriers sur l'alimentation et la qualité de l'eau potable, le préfet de Meurthe-et-Moselle a refusé d'attribuer de nombreuses autorisations de carrières dans le secteur d'étude (Bainville, Gripport et Virecourt). En effet, sur le linéaire de la Moselle, seul le secteur de Mangonville serait en mesure de relayer la prise d'eau de Méréville et d'assurer une alimentation en eau potable suffisante au grand Nancy (Edelblutte, 2000). La préservation du secteur de la "Moselle sauvage" dans les année 1990 est donc fortement motivée par la volonté de préserver l'importante réserve en eau potable de la nappe d'accompagnement de la Moselle. Cette opération foncière a été réalisée malgré les avances au droit de fortage, versées par les carriers pendant 10 ans aux communes concernées, ce qui a conduit à d'importants conflits d'usages dans le fond de vallée. En effet, en 1990 la redevance au m^3 extrait du droit de fortage représente un enjeux économique et financier très important pour les communes (75% recettes de Socourt), dont le prix des terrains graviérables est très élevé (Bainville $136964F/ha$). Ainsi, les communes de Gripport et Bainvillle ont très difficilement accepté le prix à l'hectare offert par le Conservatoire des Sites Lorrains (Edelblutte, 2000).

FIGURE 2.19 : Station de pompage de Virecourt (Photographie M. et Mme Tacail)

2.4 Conséquences sur le fonctionnement morpho-sédimentaire de la “Moselle Sauvage”

2.4.1 Grands traits des évolutions géomorphologiques entre 1950 et 1980

Dès 1950, des dragues flottantes prélèvent des alluvions dans le lit mineur du cours d’eau, aux extrémités du secteur de la Moselle sauvage, entre Charmes et Socourt et à l’aval du pont de Bayon (Maire and Corbonnois, 2000). A l’extrémité amont, la propagation de fronts d’érosion progressive engendre une incision du lit entre Charmes et le barrage de Bainville, allant jusqu’à la mise à nu du substratum à l’aval de Charmes (Figure 2.13). L’enfoncement du lit à l’amont de Bainville s’accompagne d’un rétrécissement de la bande active sur la période 1949-1965 et plus particulièrement à proximité de Gripport, à la suite de l’ouverture de la gravière au début des années 1960 (Chardon, 2014). La chenalisation du cours d’eau au droit de la gravière, exacerbe localement l’incision du lit, alimentant un petit secteur en tresses situé à l’aval immédiat, dont la largeur de la bande active s’accroît en 1965 (Figure 2.20). Par la suite, l’incision du lit se poursuit plus en aval, ce qui conduit à la disparition du secteur en tresse dans les années 1970, au profit d’un lit unique modérément sinueux (Maire and Corbonnois, 2000). Dans la partie aval de la Moselle sauvage, une vague d’érosion régressive remonte depuis la fosse d’extraction de Bayon (Figure 2.20) et fait disparaître un second secteur en tresses situé à Virecourt. Cette métamorphose locale du style fluviale s’effectue dès les années 1960, avec la formation de deux méandres en “genoux successifs” et la réduction de la largeur de la bande active sur ce secteur (Chardon, 2014). Sur le tronçon médian de la Moselle sauvage, au niveau du “grand travers”, l’amplitude et la demi-longueur du train de méandres varient peu entre 1950 et 1980.

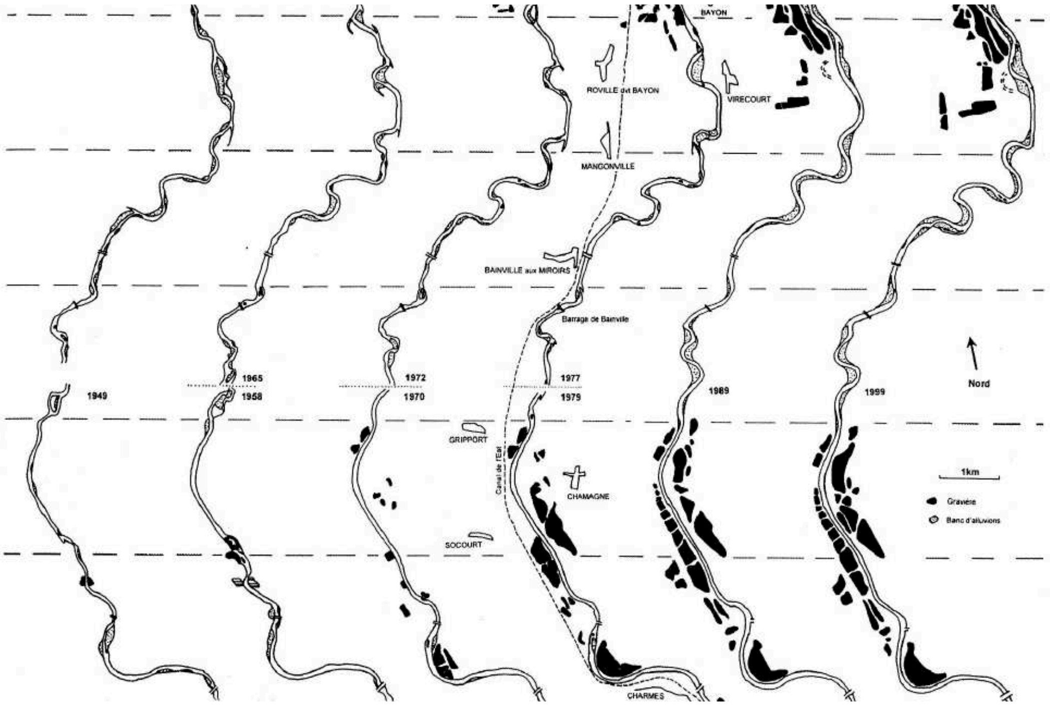

FIGURE 2.20 : Evolution du lit et du milieu riverain de la Moselle entre 1950 et 2000, d’après Maire and Corbonnois (2000)

Contrairement à la dynamique d'incision du linéaire, décrite en amont et en aval de ce secteur, le tronçon Mangonville-Virecourt est en exhaussement entre 1900 et 1979 (Figure 2.14). Cette dynamique peut s'expliquer par une diminution locale de la pente, qui favorise les dépôts à l'aval de Bainville, et par la préservation de ce secteur de tout prélèvement direct en lit mineur (CEGUM, 2006). L'évolution de la largeur de la bande active, au niveau du train de méandres, indique que la dynamique d'exhaussement tend à se décaler vers l'aval et à s'amplifier au cours du temps (Chardon, 2014). En effet, l'élargissement de la bande active, en lien avec l'exhaussement du lit, débute à proximité de Mangonville entre 1949-1961 (maximum de 8m/an), puis s'étend vers Virecourt entre 1961-1981 (maximum >10m/an). Cette migration aval, semble révéler une progression aval de la dynamique d'incision du lit, engendrée par les prélèvements effectués plus en amont (Chardon, 2014). Sur l'ensemble du linéaire de la Moselle sauvage, la surface de la bande active est donc relativement stable entre 1949 et 1980, mais avec de fortes disparités spatiales, liées à l'évolution verticale du lit. A l'échelle du fuseau de mobilité de la rivière, l'évolution de l'occupation du sol est plus marquée, avec une diminution des surfaces ouvertes ($-68ha$) et une augmentation des surfaces boisées ($+37ha$) (Chardon, 2014). Cette évolution est principalement d'origine anthropique, en raison de l'expansion de la superficie des gravières et d'une déprise agricole initiée dans les années 1960. Au début des années 1970, les extractions en lit majeur se localisent d'abord principalement en aval de Charmes, au niveau de la grande convexité de rive droite, où $40ha$ furent totalement vidés. Ces extractions se sont étendues vers l'aval en rive gauche et en rive droite dans la plaine de Socourt, à Chamagne ($50ha$), mais aussi en amont et en aval du pont de Bayon ($40ha$).

2.4.2 Déstabilisation de l'équilibre morphodynamique entre 1980 et 1990

A la fin des années 1970, le report des prélèvements de granulats en lit majeur s'accompagne de la construction de digues au droit des gravières, afin de protéger ces zones d'extraction des crues. Dans le secteur de la "plaine de Socourt" (Figure 2.20), la canalisation du cours d'eau par de hautes berges, accroît localement la capacité de transport de la rivière, ce qui exacerbe l'incision du lit initiée par les prélèvements en lit mineur. A cette vidange partielle des alluvions du lit de la Moselle, s'ajoute une réduction de la charge de fond transitant depuis Charmes, en raison de prélèvements effectués plus en amont. Ces divers facteurs convergent pour engendrer une incision de plus de $2m$ du lit mineur entre les gravières de Socourt et de Chamagne sur la période 1950-1980 (Figure 2.15).

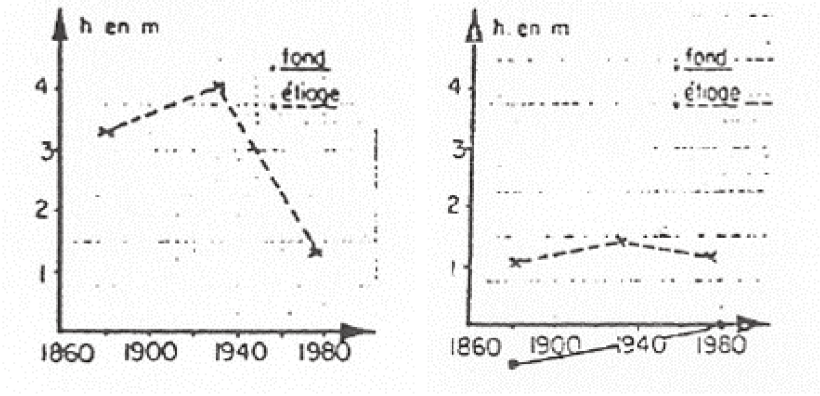

FIGURE 2.21 : Evolution du lit à Charmes (gauche) et Bainville (droite) (BCEOM, 1981)

Les matériaux déstockés se déposent à la sortie du tronçon endigué, où la capacité de transport du cours d'eau est inférieur, et s'accumulent à l'aval de Gripport, ce qui entraîne un exhaussement de $0,6m$ du lit au doit des courbures (Figure 2.22). Le basculement du profil longitudinal de la Moselle se traduit en aval par un engraissement des bancs de convexités des courbures du secteurs de Gripport au cours des années 1980 (Figure 2.20). La modification de la géométrie du cours d'eau favorise localement l'érosion des berges, ce qui accentue la sinuosité des courbures et conduit à la formation d'un véritable train de méandres à l'amont du barrage de Bainville (Maire and Corbonnois, 2000).

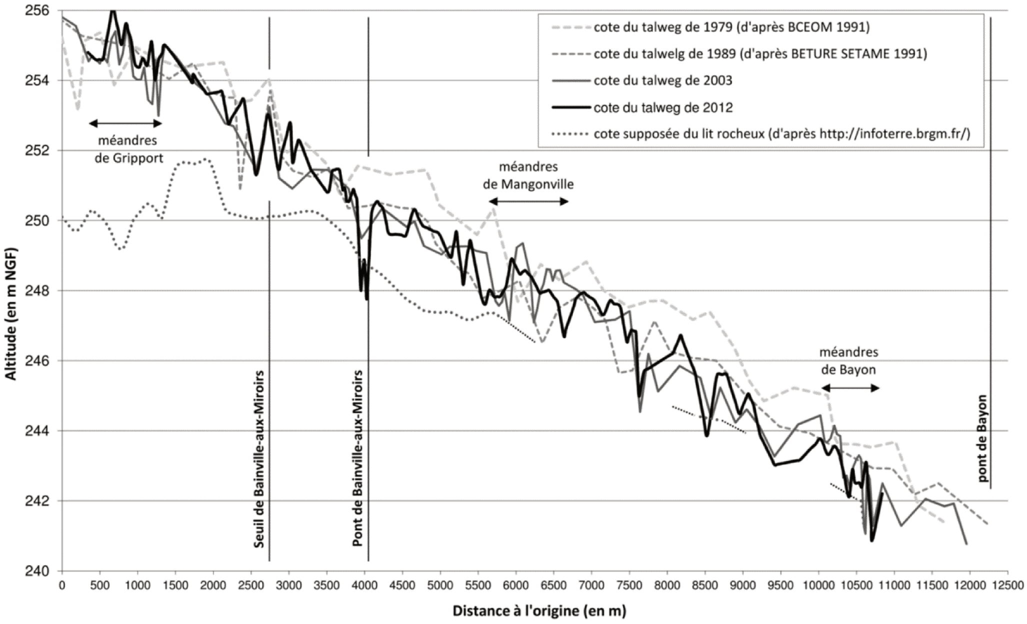

FIGURE 2.22 : Evolution du profil en long de la Moselle sur le secteur Gripport-Bayon, d'après Beck and Corbonnois (2016)

A l'échelle du linéaire de la Moselle sauvage, la sinuosité de la quasi-totalité des méandres s'est accentuée entre 1981 et 1995, du fait de la fréquence et de l'amplitude des crues morphogènes sur cette période (Chardon, 2014). L'occurrence d'évènements hydrologiques importants contribue au recul de berge et au développement des méandres en aval de Gripport et au niveau du "grand travers". L'augmentation de la surface de la bande active est significatif (Chardon, 2014). Son élargissement représente près de la moitié de la surface perdue respectivement par les milieux boisés ($-51ha$) et les milieux ouverts ($-9ha$) au niveau du fuseau de mobilité de la Moselle sauvage. L'intensification des activités agricoles et le déboisement du fond de vallée permet cependant de compenser la perte de surfaces ouvertes et de stabiliser cette valeur au cours de la période 1981-1995. La vague d'érosion régressive issue des fosses d'extractions de Bayon, provoque le recoupement du méandre en genou situé à proximité de Virecourt, au cours de la crue vicennale d'avril 1983. Le chenal de recoupement emprunte les tracés de chenaux préexistants et "file tout droit" (Figure 2.20), puis s'enfonce et s'élargit lors de la crue décennale de mai 1983 (Maire and Corbonnois, 2000). La quantité de matériaux remaniés permet, en aval, de combler totalement la fosse résiduelle de Bayon, tandis que l'abondant définitif de l'ancien méandre, se traduit par un rétrécissement de la bande active (Chardon, 2014).

Le comblement de cette ancienne zone d'extraction entraîne un exhaussement du lit de la Moselle à l'extrémité aval du site d'étude (Figure 2.22) et permet de rétablir la continuité du transit de la charge de fond. La progression de la vague d'érosion est accrue par ce recoupement, l'augmentation locale de la pente du fond accroît la capacité de transport du cours d'eau et l'incision du lit remonte en amont des méandres de Bayon. A l'exception de l'extrémité amont et aval du linéaire de la Moselle sauvage et d'un petit secteur vers Mangonville, le cours d'eau s'est globalement incisé (Figure2.22) de 0,7 m/an entre 1979-1989 (Chardon, 2014). A proximité de Bainville, l'enfoncement du lit peut être lié aux "opérations blanches" effectuées par VNF au cours des années 1980, afin d'alléger la surcharge alluviale du lit engendrée par les crues de 1982-1983 (CEGUM 2006). Des travaux d'excavations sont réalisés à environ 600*m* en amont du barrage en 1984, puis au voisinage de l'ouvrage en 1989-1990, car ce bief rectiligne s'inscrit mal dans la continuité du nouveau tracé de la Moselle (Maire and Corbonnois, 2000). En effet, lors de la migration vers l'aval du train de méandre de Gripport, effecté par sapement des berges concaves (Figure 2.20), le cours d'eau se heurte en rive gauche au pied de la digue du canal de l'Est. La présence de ce point dur entraîne un phénomène de buté, qui exacerbe localement l'affouillement du lit et provoque des dépôts semi-forcés en amont du point de contact. Une vague de dépôts régressifs s'ajoute au remous solides du barrage, dont la progression vers l'amont exhausse le lit du cours d'eau et engraisse les bancs de convexités (Figure 2.23), ce qui accroit l'érosion des berges. Cette dynamique latérale alimente le profil en long de la Moselle, tenu par le barrage, et rehausse la cote de l'eau, facilitant ainsi les débordements et provoquant un risque de contournement du barrage.

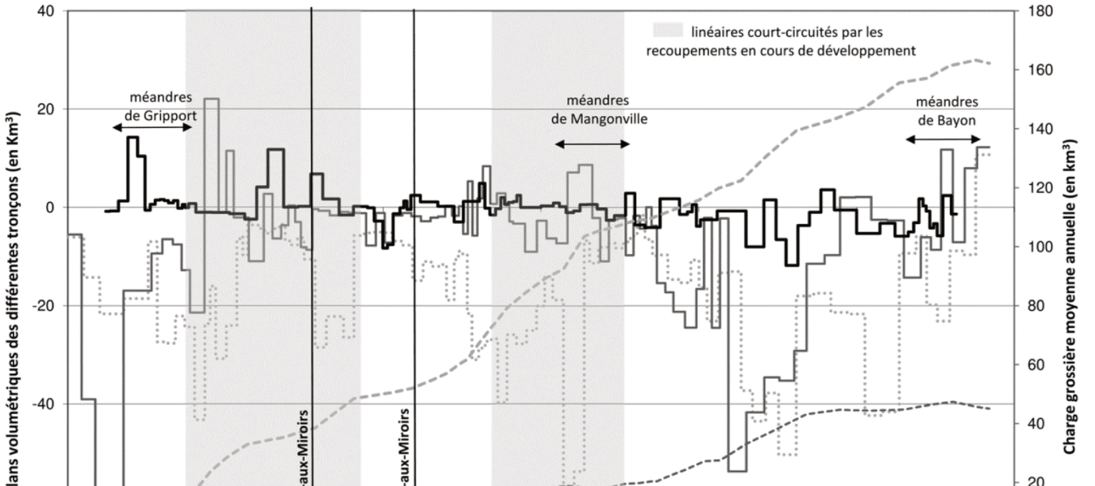

FIGURE 2.23 : Evolution des volumes charriés de 1979 à 2012 d'après, Beck and Corbonnois (2016)

Des alluvions sont également excavées, à environ $1km$ en aval du pont de Bainville, au niveau de la première boucle de méandre du “grand travers”, suite au remblai du tronçon lors des crues de 1982-1983. Cette abondante charge sédimentaire provient de l’affouillement du lit, par des “eaux affamées”, dans la fosse de dissipation d’énergie située au pied du barrage de Bainville (Figure 2.22). Le sapement de la longue berge concave se trouvant en rive droite entre le barrage et le stade de Bainville, d’une hauteur de 2 à $3m$, fournit également une importante quantité de matériaux (Maire and Corbonnois, 2000). Ces sédiments se déposent et s’accumulent en aval, dans le secteur de Mangonville, en raison d’une diminution locale de pente et d’une réduction de la capacité d’écoulement du lit mineur sur ce tronçon (CEGUM 2006). La réduction de la pente et les débordements précoces, restreignent localement la capacité de transport et favorisent l’alluvionnement. Le pivot de ce profil basculé, entre le barrage et le train de méandre de Mangonville, se place aux environs du pont de Bainville et tend à se déplacer vers l’amont à mesure que des dépôts régressifs s’accumulent depuis l’aval (Maire and Corbonnois, 2000). L’opération blanche réalisée à la fin des années 1980, vise ainsi à limiter les débordements de la Moselle aux abords de la ferme de Chaudrupt et à éviter un recoupement du méandre, en enfonçant le lit du cours d’eau (Figure 2.20).

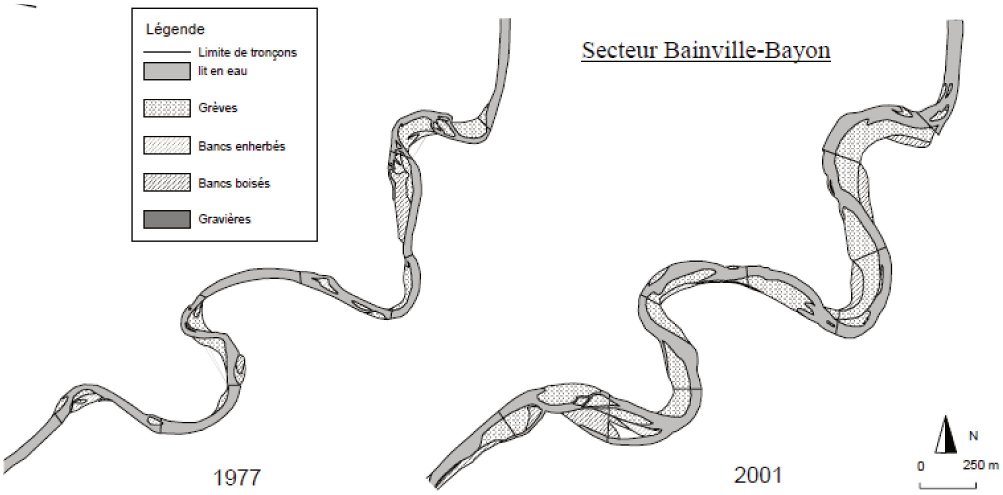

FIGURE 2.24 : Évolution de la bande active des méandres du grand travers, d’après Corbonnois et al. (2006)

2.4.3 Réajustement morphologique de la Moselle entre 1990 et 2000

A partir des années 1990, les extractions d’alluvions cessent dans la bande active de la Moselle entre Charmes et Bayon, que ce soit à travers des prélèvements directs, via l’ouverture de nouvelles gravières ou pour le réaménagement du lit (Maire and Corbonnois, 2000). Suite à une vidange partielle des alluvions et au comblement des anciennes fosses d’extractions lors des crues de 1982-1983, la continuité fonctionnelle du lit est rétablie et une phase d’auto-restauration du milieu fluvial est initiée. Entre 1991 et 2003, l’incision moyenne du chenal est plus faible, de l’ordre de 0,012 m/an (Figure 2.22), mais cette évolution est contrastée par la présence de courts tronçons en approfondissement et d’autres en exhaussement (Chardon, 2014). Dans le secteur de la plaine de Socourt, l’incision du lit se stabilise et le comblement des anciennes fosses permet de lisser progressivement le profil longitudinal (Champalbert Expertises and hydro expertise, 2008).

Les apports sédimentaires provenant de l'amont et transitant par la barre rocheuse de Charmes sont probablement très faibles en raison des nombreuses déstabilisations du lit (empreints passés et barrage à Charmes) ayant contribué à la mise à nu du substratum. Ainsi, la principale source d'approvisionnement sédimentaire du tronçon endigué des étangs de Socourt est la rive concave du méandre situé en face de l'exploitation SRDE (Figure 2.17). Dans ce secteur, le lit de la Moselle s'est fortement incisé à la suite des perturbations anthropiques (fronts d'érosions régressive et progressive), ce qui explique la hauteur actuelle de la berge de 4 à $5m$ et le pavage du fond. Le matériel repris de cette berge transite rapidement sur le tronçon rectiligne Charmes-Gripport car l'endiguement du lit accroît localement la capacité de transport du cours d'eau et atténue les dépôts (Maire and Corbonnois, 2000). Sur la période 1995-2004, l'analyse de la mobilité latérale du cours d'eau permet d'estimer que le volume érodé en rive droite est de 7000 à $9000m^3$ (Sogreah, 2006). Lors de la capture de la rivière par les gravières de Gripport en 1995 (Figure 2.18), l'abondance de la charge de fond de la Moselle engendre un dépôt de près de $10000m^3$ de matériaux dans le chenal court-circuité (Champalbert Expertises and hydro expertise, 2008).

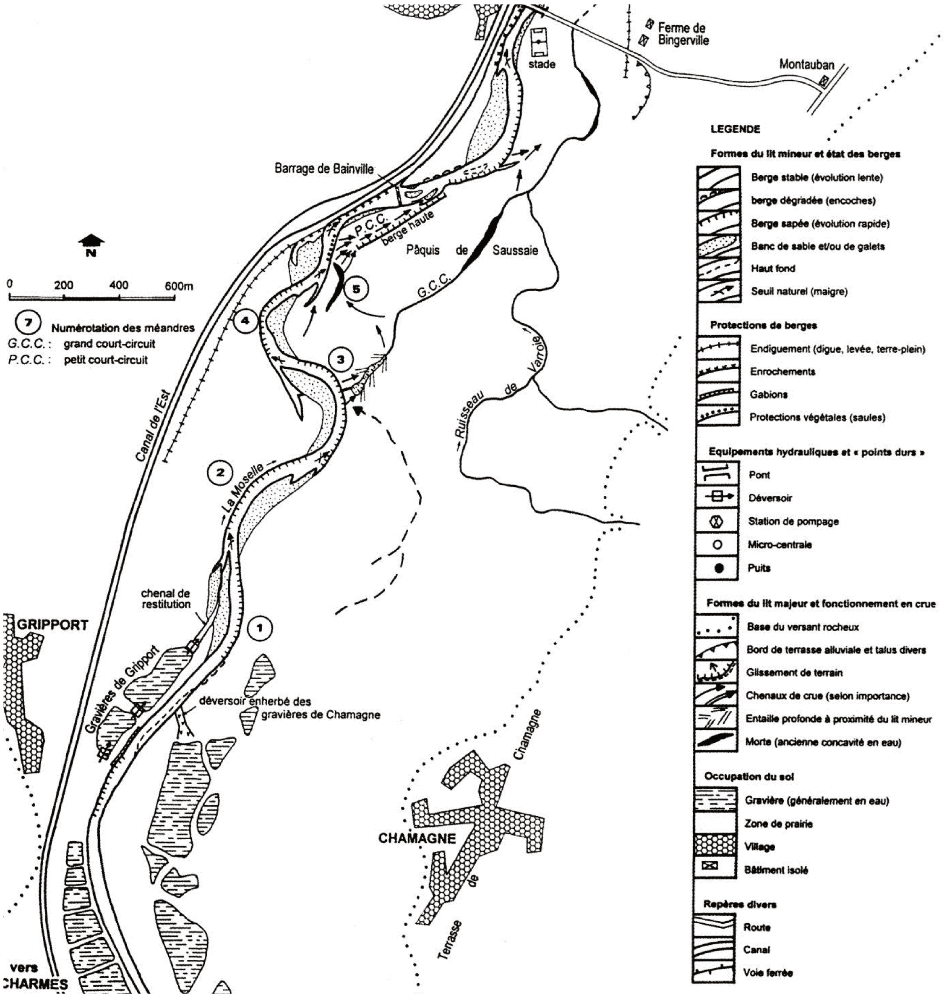

FIGURE 2.25 : Lit de la Moselle avec les principales structures du fond de vallée entre Charmes et Bainville en 2000, d'après Maire and Corbonnois (2000).

L'engravement du lit s'accompagne d'un stockage de la charge de fond dans la gravière, ce qui provoque une interruption du transit sédimentaire pendant la crue de 1995. Les eaux de la Moselle, délestées de leur charge solide, érodent un volume de matériaux plus important sur les tronçons situés entre le point de restitution aval des gravières et l'amont des méandres de Gripport (Figure 2.23). Un basculement consécutif du profil longitudinal entre 1995 et 2003 entraîne une réduction de la surface de la bande active en amont du train de méandres et une augmentation plus en aval (Chardon, 2014). L'engraissement des bancs de convexité exacerbe le processus d'érosion latérale (le sommet du méandre 3 recule de $80m$ en 10 ans ; Figure 2.25) et conduit à l'augmentation de la sinuosité des méandres (Maire and Corbonnois, 2000). L'allongement de la rivière et la migration vers l'aval du train de méandres dans les années 1990 rend cependant délicate l'analyse de l'évolution des points bas et l'ondulation du profil en long durant cette période (Figure 2.22). L'incision du lit enregistrée entre 1989 et 2003 à l'extrémité amont de la Moselle sauvage est probablement liée à l'arrêt temporaire de la fourniture sédimentaire durant la capture par les gravières de Gripport (Chardon, 2014).

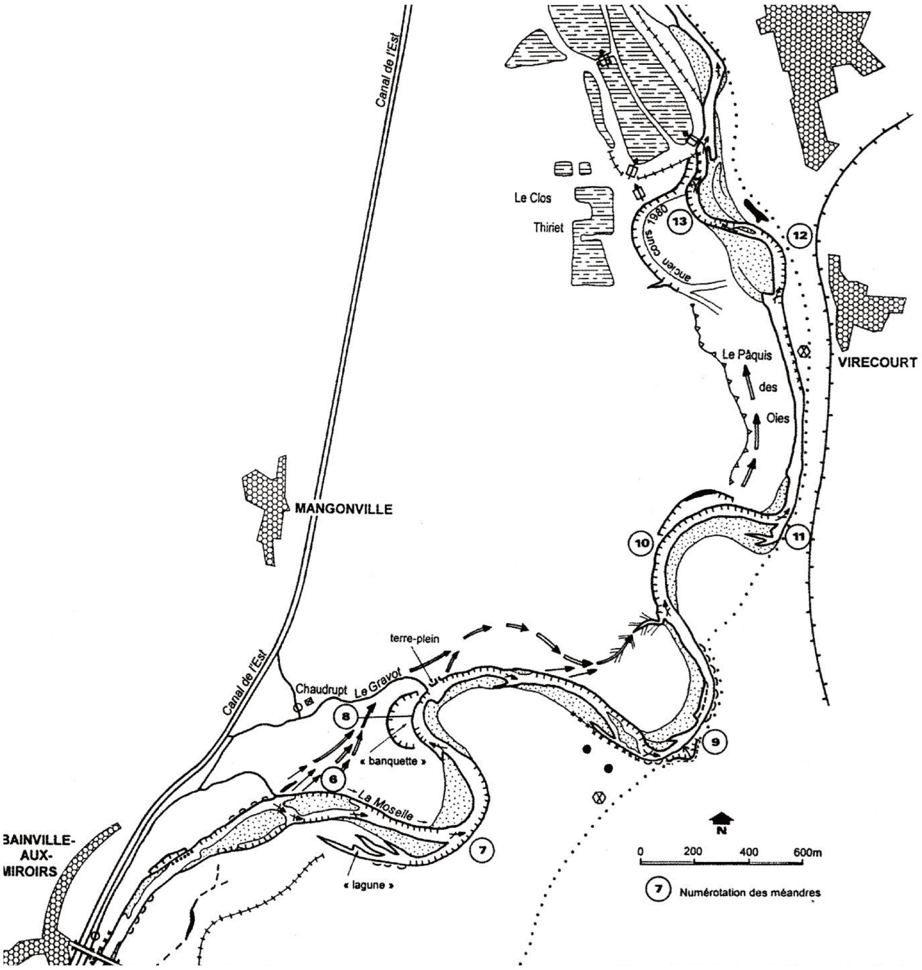

FIGURE 2.26 : Lit de la Moselle avec les principales structures du fond de vallée entre Bainville et Bayon en 2000, d'après Maire and Corbonnois (2000).

La raréfaction et le stockage des sédiments en amont du barrage de Bainville, alimente la dynamique de réajustement morphologique initié dans les années 1980, au niveau du tronçon situé en aval de l'ouvrage. L'enfoncement du lit de la Moselle se poursuit au pied du barrage et le sapement de la rive concave (droite) située en amont du pont de Bainville s'intensifie à la suite du développement d'un banc de galets en rive convexe (Figure 2.25). La migration latérale du cours d'eau accroît la sinuosité du tronçon, qui vient buter en rive gauche contre la digue du canal de l'Est, ce qui augmente localement les vitesses d'écoulements et favorise l'affouillement du lit au droit du pont de Bainville. L'incision du lit progresse en direction de l'aval jusqu'à la première boucle de méandre du grand travers (Figure 2.22).

Les matériaux érodés s'accumulent dans le secteur de Mangonville (Figure 2.24) en raison des conditions hydrodynamiques locales (diminution de la pente et faible débit à pleins bords), qui favorisent l'alluvionnement. Malgré les "opérations blanches" réalisées sur ce tronçon à la suite des crues de 1982-1983, le lit de la Moselle est en exhaussement à proximité de la ferme de Chaudrupt (Figure 2.20). Le basculement du profil en long se traduit par une diminution de la bande active sur la partie amont et un engraissement des bancs sur la partie aval (Chardon, 2014). Le surplus d'alluvions déposé durant les années 1990 en aval du pont de Bainville (Figure 2.24) provoque une réduction de la section d'écoulement dans le méandre de Mangonville. Ceci engendre une accélération des vitesses d'écoulement en crue à l'origine d'une reprise de la dynamique d'érosion latérale dans ce secteur. L'adaptation morphologique du cours d'eau se traduit par un recul de berge, renforcé par la faible cohésion de celle-ci (matériaux gravelo-sableux) et de l'absence d'aménagements anthropiques sur ce tronçon (CEGUM 2006). La position semi-axiale des bancs formés au cours de cette période (Figure 2.24) favorise l'érosion des berges situées en rive gauche et en rive droite du chenal (Maire and Corbonnois, 2000). Cette forte mobilité latérale (taux d'érosion moyen du méandre 6 supérieur à 11m/an) est à mettre en relation avec l'augmentation de la fréquence des évènements morphogènes (Q2 à Q5) entre 1994 et 2001, dont plusieurs crues débordantes (FLUVIAL.IS, 2015). La réduction de la capacité du chenal en lien avec l'exhaussement du lit facilite les débordements par dessus la berge concave très basse du méandre de Mangonville (Figure 2.26). La diminution des forces tractrices au sein du chenal alimente le processus de dépôt dans ce secteur. Les débordements en lit majeur s'organisent sous forme de larges nappes, les écoulements engendrent le creusement de mini-sillons à 50 m en retrait des rives, qui constituent les prémisses d'une défluviation future (Maire and Corbonnois, 2000).

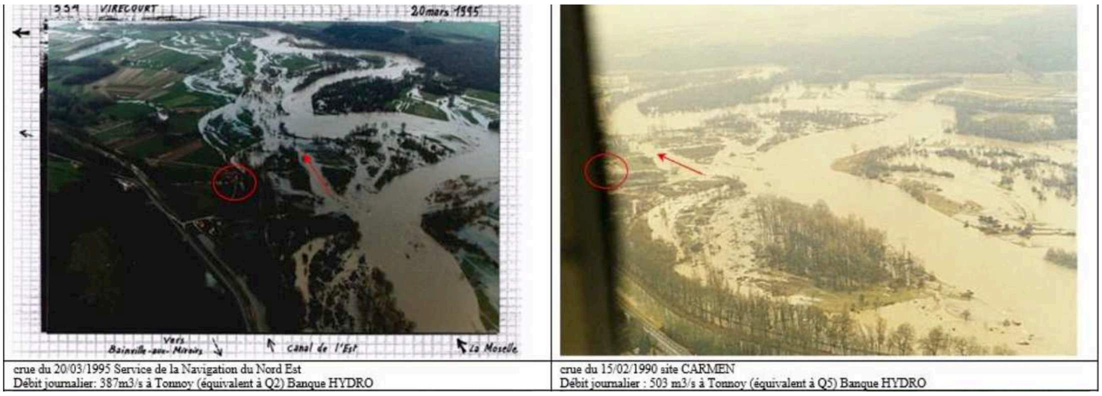

crue du 20/03/1995 Service de la Navigation du Nord Est
Débit journalier: 387m3/s à Tonnoy (équivalent à Q2) Banque HYDRO

crue du 15/02/1990 site CARMEN
Débit journalier : 503 m3/s à Tonnoy (équivalent à Q5) Banque HYDRO

Figure 2.27 : Photographie aérienne de la Moselle en crue dans le secteur de Mangonville

La propagation de ces différents ajustements morphologiques se poursuit encore de nos jours et ont fait l'objet d'un suivi annuel réalisé à l'aide d'un LiDAR topo-bathymétrique. Ces relevés ont permis de décrire la morphodynamique actuelle du cours d'eau et de mettre au point des modélisations hydrauliques et morpho-sédimentaires à des échelles spatiales variables. Les méthodologies et les données employées pour calibrer ces différentes modélisations seront présentées dans les prochains chapitres.

Chapter 3

Effective determination of critical bed shear stress from multi-source measurement of flow competence for 2D hydro-sedimentary modelling

En accord avec les objectifs de la thèse, ce chapitre étudie la détermination d'une première quantité clé : la contrainte critique de mise en mouvement des sédiments. A partir de l'étude diachronique de la morphodynamique du cours d'eau, de son suivi et d'un jeu de données particulièrement varié, une nouvelle méthode est proposée pour la détermination du paramètre de Shields critique. Elle est basée sur l'estimation de la compétence de l'écoulement définie à l'aide de placettes peintes et de traceurs RFID, ainsi que d'un modèle hydraulique 2D. La pertinence de l'estimation du paramètre de Shields critique est évaluée en comparant les zones érodées observées grâce aux relevés LiDAR topo-batymétrique fins réalisés avant et après des crues morphogènes, et la carte de cisaillement au fond simulée par le modèle hydraulique 2D en crue.

3.1 Introduction

Numerical modelling of sediment transport and river morphodynamics have been increasingly used for river management, engineering works, and restoration projects and research purposes (e.g. Brousse et al. (2022); El Kadi Abderrezzak et al. (2016); Yu et al. (2022); Iwasaki et al. (2016); Nelson et al. (2015)). Since sediment movement is induced by flow forces, the bed shear stress τ_b is one of the most used parameter to quantify the bedload sediment transport in river morpho-sedimentary modelling. The sediment transport laws (Meyer-Peter and Müller, 1948; Einstein, 1950; van Rijn, 1984; Wong and Parker, 2006) are generally based on the Shields parameter θ which is the dimensionless shear stress and corresponds to the ratio of the fluid forces, tending to initiate motion of a particle, to the gravity force tending to keep it at rest.

$$\theta = \frac{\tau_b}{(\rho_s - \rho)gd} \tag{3.1}$$

were the bed shear stress $\tau_b = \rho g h S$ (N/m^2), with h is the water depth (m), S is the bed or water-surface slope (m/m), g is the gravitational acceleration (m/s^2), d is the grain size diameter (m) and ρ and ρ_s, which are respectively the fluid and sediment densities (kg/m^3).

Note that τ_b can be estimated from flow velocity, such as done morpho-sedimentary model, given access to sub-reach variabilities. The bedload transport rates q_s are usually computed (Meyer-Peter and Müller, 1948; Wong and Parker, 2006) as a function of the Shields parameter θ relative to the critical Shields parameter θ_{cr} as follows:

$$q_s \propto \alpha(\theta - \theta_{cr})^{\beta} \tag{3.2}$$

were α and β are empirical coefficients and θ_{cr} corresponds to dimensionless critical shear stress for the incipient motion of particles. As the computed sediment transport rates (equation 3.2) is a nonlinear function of the bed shear stress τ_b through the Shields parameter (equation 3.1), uncertainties in the determination of θ_{cr} can lead to large errors in bedload transport estimation. These effects are particularly important in the range of bed shear stress slightly above the threshold for motion τ_{cr}, where transport rates may increase by one order of magnitude for small changes in τ_b. The threshold value for particle entrainment can be determined using the diagram proposed by Shields (1936), which establishes a relation between the dimensionless shear stress at incipient motion and the particle Reynolds number Re^* defined as:

$$Re^* = \frac{uD}{\nu} \tag{3.3}$$

were u is the flow velocity, D is the grain size and ν is the kinematic viscosity of the fluid. The Shields curve was obtained from laboratory-flume experiments using uniform grain size submitted under different flow conditions in order to estimate the shear stress required to move a particle of a given size. Results shows that the dimensionless critical Shields parameter θ_{cr} approaches a constant value of 0.06 for $Re^* > 10^2$, which means that in natural rivers (typically $Re^* > 500$, e.g. Dingman, 1984) θ_{cr} is supposed to be independent of the grain size. Although other authors found the same conclusions, many studies estimating the dimensionless shear stress under turbulent flow conditions found different threshold values significantly lower than 0.06 (Komar and Carling, 1991; Andrews, 1983; Miller et al., 1977). This scatter between results is attributed to the variation in the definition of the initial motion of particle, the methods used to determine the critical condition for sediment entrainment and the estimation of the flow conditions (Buffington and Montgomery, 1997). By reanalyzing the Shield's data, Gessler (1971) found that the value of 0.06 was overestimated because the dimensionless shear stress was computed using the total shear stress τ_b were:

$$\tau_b = \tau' + \tau'' \tag{3.4}$$

which is the sum of a grain shear stress τ' and a bedform shear stress τ''. However, only the grain shear stress component of the total shear stress intervenes in the sediment transport since the bedform shear stress is dissipated in overcoming bedform resistance such as channel walls or bed morphology. Therefore, by applying a correction for side-wall effects and form drag, Gessler (1971) determined a critical Shields parameter close to 0.045, a threshold which was also found by Komar (1987) and Miller et al. (1977). Nevertheless, the partitioning between total and grain shear stress is usually difficult to identify, because of the complexity of estimating the loss of energy caused by bedforms.

The most common method used to estimate the grain shear stress is to compute the ratio between the total friction coefficient n_t and the skin friction coefficient n_0 as follows:

$$\tau' = \left(\frac{n_0}{n_t}\right)^{3/2} \tau \tag{3.5}$$

were n_t is determined from Manning-Strickler equation and n_0 is predicted according to the median particle size D_{50} with $n_0 = 0.048 D_{50}^{1/6}$. Although many of the flume experiments used a sidewall correction to estimate the critical Shields parameter, most of field measurements used the total shear stress, which could lead to a slope-dependency (Lamb et al., 2008). By studying particle entrainment in naturally sorted riverbeds, Andrews (1983) also show that the values discrepancy in the critical Shields parameter estimations for a given grain size is related to the size of the surrounding particles. The results suggest that relatively smaller particles tend to be hidden by their larger neighbors, resulting in higher θ_{ci}, whereas relatively larger particles tend to protrude and exhibit lower θ_{ci}. The initiation of motion of particle i, in poorly sorted gravel beds, should therefore be expressed as a function of the particle relative size (D_i/D_r) where variations in θ_{ci} estimation caused by hiding and protrusion effects (Wilcock, 1988) can be expressed as:

$$\theta_{ci} = \theta_{cr} \left(\frac{D_i}{D_r}\right)^{-b} \tag{3.6}$$

were b is a hiding factor and θ_{ci} and θ_{cr} are respectively the critical Shields parameters determined for a particle size D_i and a reference particle size D_r. This reference particle corresponds to the particle size that is not affected by the hiding/exposure effects and is often assumed to be the median grain size of the bed surface (Komar, 1987). The hiding factor represents the influence of hiding and protrusion effects on particle entrainment and varies from 0 (particles have no influence on each other so the value of the critical shear stress is almost proportional to the particle weight) to 1 (differences in particle exposure and friction angles completely offset differences in particle weight so the value of the critical shear stress is the same for all particle size). The value of b indicates if the entrainment of particles of different sizes occur in a size-selective way ($b < 1$) rather than in equal mobility ($b \approx 1$) (Parker and Klingeman, 1982; Andrews, 1983). Flume and field measurements suggests that the value of b ranges between 0.6 and 1, but it depends on the employed method (reference or competence flow method) and on the flood magnitude (Ashworth and Ferguson, 1989). Other studies also show that the dimensionless critical shear stress for a given bed shear stress and grain size increases with the river slope. By compiling existing data, Lamb et al. (2008) found the following relationship

$$\theta_{cr} = 0.15 S^{0.25} \tag{3.7}$$

where S is the river slope with $S = tan\beta$ and β corresponds to the bed-slope angle from horizontal. Nevertheless, this slope-dependency contradicts the models that predict an increased mobility of sediment with an increasing slope due to the added gravitational force in the downstream direction (Wiberg and Smith, 1987). Shvidchenko et al. (2001) demonstrated that this dependency is associated to the relative depth, since the critical Shields parameter tends to increase as the ratio of flow depth to grain diameter decreases and the flow depth is inversely proportional to the channel slope. Lamb et al. (2008) indicated that the relationship between the channel slope and the relative roughness is a combination of multiple effects, as the particle emergence is reduced upstream and the intensity of the near-bed turbulence is increased downstream. Hence, after comparing eight decades of field and flume data Buffington and Montgomery (1997) concluded that there is no constant value of critical Shields parameter for all natural rivers.

Furthermore, studies of the temporal evolution of the critical Shields parameter also show the influence of the flow history in the sediment mobility (Paphitis and Collins, 2005). In natural gravel-bed rivers, Pretzlav et al. (2020) demonstrated that θ_{cr} progressively increases with cumulative shear stress until a sufficiently large flood event occurred to disrupt the bed surface and "reset" the flow history, as suggested by Masteller et al. (2019).

However, many morpho-sedimentary modelling use a critical Shields parameter determined from flume experiments (Meyer-Peter and Müller, 1948; van Rijn, 1984; Wong and Parker, 2006) without considering the possible influence of local river properties (sediment mixture, hiding/exposure effects, channel slope, relative roughness, etc). Some of them adjust the Shields parameter θ computation (equation 3.1) in order to match observed and modeled bedload (equation 3.2) according to the critical Shields parameter θ_{cr} defined from the literature (Mendoza et al., 2017). This adjustment derives from a modification in the total shear stress partitioning (equation 3.4) though the calibration of the skin friction coefficient which is involved in the skin friction computation (equation 3.5).

Nevertheless, although the skin friction coefficient and the Shields parameter are the most influencing parameters after the sediment diameter, a significant part of their influence is due to the correlation between the variable (Mouradi et al., 2016). Therefore, calibrating the Shields parameter using the skin friction rather than modifying the value of the critical Shields parameter could lead to parameter identifiability issues in the sediment transport modelling. Furthermore, when studying sediment transport in gravel-bed rivers, bedload measurements are rarely available due to the complexity of the sampling methods (cost, equipment, time, flow conditions, etc).

Therefore, the present contribution proposes a new effective method for critical Shields parameter estimation, based on flow competence estimation from (i) accurate local information from painted patches and over a wide grain size range with RFID tracers and (ii) a 2D hydraulic model. Thanks to a detailed field monitoring, which includes LiDAR topo-bathymetric acquisitions, before and after morphogenic floods, the validity of the estimated threshold value is assessed by comparing (i) the maximum Shields parameter modeled over eroded areas to (ii) the critical Shields parameter $\theta_{cr,D50}$ estimated for the bed surface D_{50}.

The remainder of this article is organized as follows: section 2 presents the site and the general context of this study, section 3 details the field measurements performed to estimate the flow competence and calibrate the 2D hydraulic model used to estimate the corresponding grain shear stress, section 4 describes the results and discussed about the capacity of the 2D hydraulic model to predict sediment motion using the critical Shields parameter estimated previously.

3.2 Study site

The Moselle river is $560km$ long from its source at the pass of Bussang in the northeast of France to its confluence with the Rhine river at Koblenz in Germany (Figure 3.1 a). The upper part of the Moselle river drains a catchment area of $1,976\,\mathrm{km}^2$ from the western side of the southern Vosges Mountains to the gauging station of Tonnoy on the Lorraine plateau. The geology of the Vosges Mountains consists mainly in crystalline (granites) and metamorphic (gneiss) rocks originating from the Hercynian basement, while the substratum of the Lorraine plateau is composed by a superposition of limestone and marl sedimentary layers (Maire and Corbonnois, 2000).

The longitudinal profile of the Moselle river is characterized by a slope of 10% at its upstream extremity, rapidly decreasing to 0.4% at Remiremont and reaching an average value of 1.7‰ further downstream. The predominance of impermeable rocks and steep sectors contributes to propagate rapidly the flows to Epinal, while the physiography of the catchment contributes to the flood peaks concomitance, which generates major hydrological events downstream (Maire and Lasserre, 1991).

The precipitation are unevenly distributed with a mean annual value of $800mm$ over the Lorraine plateau versus $1100mm$ over the Vosges mountains, where important variations are observed with locally more than $2000mm$ on the crest (Beck and Corbonnois, 2003). Precipitations occurs mainly during the winter (November-February) with monthly more than $200mm$ over the Vosges Mountains. The river hydrological regime is pluvial with high flows in the winter-spring (2- and 10-year floods are $405m^3/s$ and $651m^3/s$ respectively) and low flow in the summer, while the mean interannual flow is of $42m^3/s$ at the gauging station of Châtel-sur-Moselle.

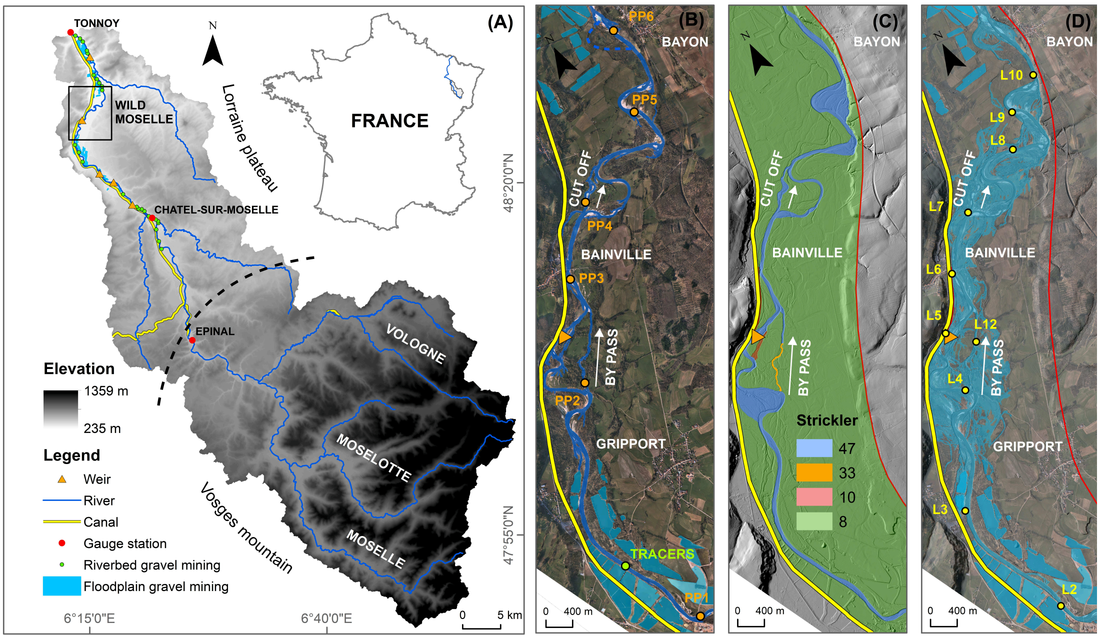

Figure 3.1: Study site (A) location of the "Wild Moselle river" in the Moselle Basin, (B) longitudinal extension of the natural regional reserve with orange points indicating the positions of painted bed patches PP_n and the green points indicating the initial positions of the tracers, (C) longitudinal extension of the 2D hydro-sedimentary model (red solid line), spatial distribution of the Strickler coefficients, with yellow points indicating the positions of the limnimeters L_n, (D) spatial extent of flood areas simulated during the peak of the flood event F_1 ($Q = 300m^3/s$).

The sediment supply of the Moselle river arises mainly from the remobilization of Holocene alluvial deposits composed of gravel and sand carried by the river from the Vosges Mountains (Maire and Lasserre, 1991). This sediment redistribution occurs primarily though bed and/or bank erosion, where the lateral mobility is strongly influenced by the valley width that varies according to the nature of the eroded substratum.

The river morphodynamic was altered by (i) the construction of a canal which reduced laterally the flood expansion area and concentrates the flow into the river bed, (ii) the construction of dams which locally modify the river competence and interrupt the sediment transport and (iii) the massive sediment extraction which occurred in the river bed (1950-1980) and thereafter in the floodplain (Figure 3.1 a). The destabilization of the river morphodynamic equilibrium conducted to morphological adjustments that results into the river bed incision which induced locally an emptying of the river bed sediment stock (Beck and Corbonnois, 2003).

A meandering reach of $12km$ length, located between Gripport and Bayon at the western foothills of the Vosges Mountains, was however relatively less affected by human activities (Figure 3.1 a). This section was classified in 2006 as regional natural reserve (the "Wild Moselle") in order to protect the water resources as well as the biodiversity (Figure 3.1 b). This reach of moderate energy, with an average specific stream power of $50W/m^2$, represents one of the most dynamic section of large rivers in the northeast of France. It is characterized by a catchment area of $1,758\,\mathrm{km}^2$, a sinuosity of 1.4, an average slope of 1.2‰, a bankfull width (resp. discharge) of about $60m$ (resp. $250m^3/s$) and a surface (resp. subsurface) D_{50} of $30mm$ (resp. $13mm$).

Although this sector was protected, the propagation of morphodynamic adjustments (regressive and progressive erosion) initiated by actions carried out at the edge of the natural reserve converge towards the central part of the reach. This trajectory, towards a new dynamic equilibrium, could induce a river avulsion which may destabilize infrastructures. A capture of the river by two floodplain gravel pits is also possible. The present research is part of a project aiming to study different scenarios of management/restoration of the lateral mobility of the "Wild Moselle" river, based on 2D morpho-sedimentary simulations. The calibration of the critical Shields parameter transport presented in this article is therefore crucial, since θ_{cr} strongly influences the prediction of the bedload transport and, thus the modelling of the river morphological evolution.

3.3 Methods

The critical Shields parameter for particle motion can be estimated according to different methods used in the determination of particle initial motion and in the computation of the corresponding bed shear stress. They are two main methods described by Wilcock (1988) to quantify the critical conditions for particles movement:

(i) The reference method, which consists to measure the bedload transport at different flow conditions and extrapolate the sediment transport rating curve to a reference value (Parker et al., 1982) in order to find the corresponding critical shear stress.

(ii) The flow competence method defined above, which consists to measure the maximum size of particles that are mobilized for a given shear stress using bedload sampler, sediment trap or marked particles.

The estimation of the critical Shields parameter varies depending of the method employed, with values obtained using the competence method generally being smaller than those obtained using the reference method (Wilcock, 1988). The bed shear stress τ_b used in both methods can be computed at the cross-section scale, using the depth-slope product, or more locally using flow velocities determined from field measurements or numerical modeling. The critical Shields parameter can be computed with or without shear stress partitioning (equation 3.4), but the values found using total shear stress τ_b are generally higher than those using the grain shear stress τ' (Petit et al., 2005).

As part of this study, the critical Shields parameter of our 2D hydro-sedimentary model is calibrated using the flow competence method where the bed shear stress is locally computed according to the model default shear stress partitioning. Indeed, the bedload measurements required to employ the reference method or calibrate the bed shear stress partitioning are rarely available, and complex to collect, while the flow competence method is much easier to set up and less costly. The flow competence will be estimated using painted bed patches and tracers mobility to determine the largest particle size transported by the river during the largest flood observed between two surveys. A relationship will be established between the size of this particle and the maximal grain shear stress locally computed by the 2D hydraulic model to estimate the critical Shields parameter for each particle size. The ability of this model to predict the sediment motion, using the estimated thresholds value, was assessed by comparing (i) the maximum Shields parameter modeled over eroded areas to (ii) the critical Shields parameter $\theta_{cr,D50}$ estimated for the bed surface D_{50}.

3.3.1 Flow competence estimation

The critical Shields parameter is estimated using the flow competence method which consists in identifying the largest particles transported by the river (Wilcock, 1992; Thompson and Croke, 2008). These sizes of this particle is determined by measuring the diameter of the particles transported out of painted bed patches, whose grain size distribution and grain imbrication are representative of the bed surface. However, this estimation is local and only valid if the size of transported particles is smaller than the size of the coarsest particle available for transport, which corresponds to the maximum particle size of the bed surface. As all particle sizes may move within a narrow range of bed shear stress (Parker et al., 1982; Andrews, 1983), it may reduce the range of flow conditions available to estimate the flow competence. Therefore, we also used sediment tracers whose (i) grain size distribution was coarser than the bed surface and (ii) positions were laterally distributed across the river section, which allows estimating the flow competence over a wider range of flow conditions. Nevertheless, contrarily to the particles of the painted bed patches, the imbrication of the sediment tracers may not be natural, so coarsest particles may protrude and could be entrained more easily. Hence, to avoid underestimating of the threshold for motion, we used immobile tracers to estimate the critical Shields parameter and mobile tracers to validate this estimation.

3.3.1.1 Painted bed patches approach

Painted bed patches were set in March 2018 (PI) at 6 different sites longitudinally distributed along the Moselle studied reach, on easily accessible unvegetated gravel bars (Figure 3.1 b). The patches were painted on various riverbed sediment mixtures (Table 3.1) found on flat bed surfaces emerging at moderate flow and located close to the river mobile-bed. Each patches of $1m^2$ were painted using a $1 \times 1m$ wood frame and a high resistance multi-support universal spray paints of different colors according to the survey (orange and red). The four corners of the patches were leveled using a centimeter-accurate differential GPS (DGPS) to record their position and facilitate their recovery. The patches were photographed using a 12-MP Olympus TG-5 camera with a ground reference, to measure the size of the largest painted particles, without disturbing the sediment imbrication. The size of these particles is compared to the size of the largest transported particle observed in order to verify that all available particle sizes were not transported during the flood. However, to be consistent with most of the flume experiments, the flow competence was only estimated according to the largest particle transported without considering the size of the remaining particles. The mobility of the particles of the painted bed patches was monitored (Figure 3.2) in February 2019 (E_1) and May 2019 (E_2).

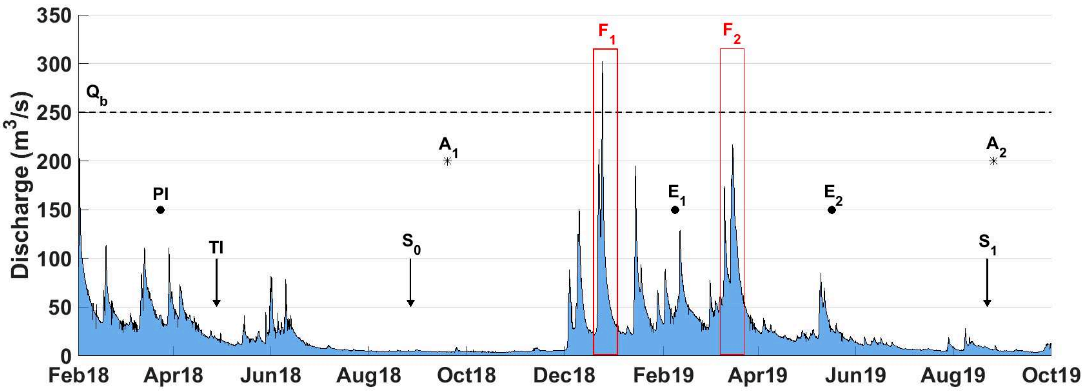

Figure 3.2: Monitoring framework related to the flow hydrograph of the Moselle river at the Châtel-sur-Moselle gauging station. A_n indicates the dates of the aerial topo-bathymetric acquisitions, E_n indicates the dates of the painted bed patches surveys, PI indicates the patches installation and TI the tracers injection, F_n indicates the floods for which the flow competence is estimated and S_n indicates the dates of the tracer surveys.

The definition of transported particles usually varies according to the traveled distances (Mao et al., 2008; Houbrechts et al., 2012; Petit et al., 2015), which involves to know exactly the position of each particle before and after the morphological floods. By superimposing pictures of the painted bed patches taken before and after the flood events it is possible to identify differences in particle positioning, thus concluding that missing particles were transported. However, some particles may simply be turned over or covered by other particles and thus considered as transported. Therefore, to avoid this potential methodological bias, we measured only the size of particles transported out of the painted bed patches of which the minimum mobility is ensured. Of course, this result is highly dependent on the recovering rate of mobile particles which varies according to the distance traveled by a particle and the visible side (colored or not) at which the particle rests. But as we are looking for the largest transported particle, the probability of recovering this specific particles size is higher, because they are transported during a shorter period, thus over a shorter distance and are visually easier to identify.

Measuring the maximum size of particles transported out of the patches is however not always the best size indicator to estimate the flow competence. Indeed, the motion of this particle may by influenced by local flow conditions (disturbance due the presence of vegetation), the interaction with other particles (hiding/protrusion effects) or particle properties (shape). Several studies shows that the D_{95} of the grain size distribution of the transported particles constitutes the best indicator of flow competence (Komar and Carling, 1991; Whitaker and Potts, 2007). Therefore, as proposed by Houbrechts et al. (2011) to approximate the D_{95}, we measured the mean diameter of the ten largest particles transported to estimate the river flow competence. The sizes of these particles were always measured through particle digitalization to ensure method consistency, but using different data according to the painted bed patches evolution:

- For patches with either total sediment transport or without sediment transport, we digitalized the b-axis of the ten largest particles observable on the picture taken before the morphological floods. Hence, we considered that either all or none off them were transported out of the painted bed patches.

- For patches with partial sediment transport, we collected pictures of the dispersed colored particles observed downstream of the patches to built an orthophotographies mosaic using photogrammetry; then we digitalized the b-axis of the ten largest particles transported out of the painted bed patches.

As part of this study, the evolution of patches covered by sediments was not studied because the moment when the deposits occurred during the flood is unknown. Indeed, if painted particles were buried at the maximum shear stress they may be protected from flow therefore the largest particle transported observed may not be representative of the flow competence.

3.3.1.2 Sediment tracers approach

In order to get complementary information on sediment transport processes, 2000 tracers were injected at 5 different sites longitudinally distributed along the Moselle river and the dam bypass channel. However, the use of these tracers to estimate the critical Shields parameter depends on the ability of the 2D hydraulic model to predict the bed shear stress towards these sites of injections (velocity lateral distribution, channel morphological evolution, vegetation, etc). Therefore, we only study the mobility of the 450 tracers injected at the upstream part of the reserve along a large straight reach with high banks, a flat bed, quasi-trapezoidal cross-sections, and where no significant morphological evolution was observed.

These 450 particles taken from the Moselle River were equipped with low-frequency passive integrated transponders (RFID PIT tags) distributed by Texas Instruments. Transponders of 32mm-long were rather used than 23mm-long within the limit of particle size and preferentially inserted in the shortest particles axis to allow a better detection (Arnaud et al., 2015). Tracers representative of the river granulometry ($16-128mm$) were equally distributed into 5 grain size classes in order that particles of each grain sizes class has the same probability to be recovered. Clusters of 25 tracers (5 by class) were seeded around 18 points laterally distributed at $5m$ intervals along 2 transects separated by $10m$ to avoid particles hiding effects. Tracers were injected (PI) in spring 2018 (Figure 3.2) on wadeable areas, expecting that a morphological flood occurred before the initial state survey (S_0), performed the next summer. Their mobility was assessed during the first field survey (S_1) performed when the riverbed was again wadeable in summer 2019.

Tracers were recovered by pedestrian searches using a $1.2m$ long and $0.5m$ wide rectangular antenna connected to a control box which sends tags IDs to a computer recording date and time of their detection. The antenna position was measured every second using a centimeter-accuracy differential GPS (DGPS), which allows to locate the detected pit-tags by synchronizing computer records and GPS tracks. This radio frequency identification (RFID) technology enabled to detect pit-tags located $1.8m$ around the center of the antenna, with a maximum vertical detecting distance of approximately $0.9m$. Thus, the antenna was pulled along successive $50m$ bands, materialized by two strings separated by $1.5m$, to minimize overlap between passes and optimize the field survey. When tracers were detected multiple times, the central position of their different detected locations was computed. Thank to this method the overall positioning accuracy of tracers was estimated at $3m$. The flow competence was estimated using only tracers recovered at S_0 and S_1. Tracers injected at less than $7m$ from the left bank were excluded from the dataset due to the presence of blocks that could locally modify flow conditions and/or trap injected particles. Tracers were considered mobile when the distance between their X,Y positions exceeded $5m$.

3.3.2 Bed shear stress estimation

The bed shear stress is estimated using a 2D hydraulic model Telemac-2D, internally coupled to the sediment transport and bed evolution module Sisyphe of the Telemac-Mascaret modeling system (Hervouet, 2007). This is an open-source well-tested and widely-used software employed in many fields of application, which was developed by the French Electricity Board (EDF). All modules of these suites of solvers consist in finite-element or finite volume algorithms that allows to run parallel computations on unstructured meshes. As part of this study, a 2D hydrodynamic model was constructed along the studied reach, based on an high-resolution digital elevation model and calibrated using a dense dataset of water levels time series. The largest flood event (F_n), which occurred between each painted bed patches (E_n) and tracers (S_n) survey, were modelled though unsteady simulations (Figure 3.2). The maximum bed shear stresses modelled during each of these floods were extracted at the patches and tracers location, from results of the coupled 2D morphodynamic model run without activating bedload transport or morphological evolution since only this hydraulic variable is of interest.

3.3.2.1 Mathematical flow model

Telemac-2D hydraulic model solves the shallow water equations (SWE) in their conservative forms (continuity and momentum along x and y directions) which are derived from the full 3D Navier-Stokes equations (Villaret et al., 2013; Ancey, 2016; Dingman, 1984). These equations were simplified in the vertical direction assuming hydrostatic pressure distribution and negligible vertical acceleration wherein turbulence effects are taken into account using a constant viscosity model. The first term on the right hand side of the momentum equations is the pressure gradient, the second is the bottom friction and the third is the horizontal diffusion:

$$\frac{\partial H}{\partial t} + \frac{\partial (UH)}{\partial x} + \frac{\partial (VH)}{\partial y} = 0 \tag{3.8}$$

$$\frac{\partial U}{\partial t} + U\frac{\partial U}{\partial x} + V\frac{\partial U}{\partial y} = -g\frac{\partial Z_s}{\partial x} + \frac{\tau_x}{h} + \frac{1}{h}div(h\nu.grad(U)) \tag{3.9}$$

$$\frac{\partial V}{\partial t} + U\frac{\partial V}{\partial x} + V\frac{\partial V}{\partial y} = -g\frac{\partial Z_s}{\partial y} + \frac{\tau_y}{h} + \frac{1}{h}div(h\nu.grad(V)) \tag{3.10}$$

where h is the water depth (m), U and V are horizontal mean velocity components (m/s), g is the gravity acceleration (m/s^2), Z_s is the free surface elevation (m), t is the time (s), x and y are horizontal space coordinates (m), ν is the depth-averaged eddy viscosity (m^2/s) and τ_x (resp. τ_y) is the bed shear stress (N/m^2) along the Cartesian x-axis (resp. y-axis) as

$$\tau_b = \sqrt{\tau_x^2 + \tau_y^2} = \sqrt{\left(\frac{1}{2}\rho C_f U^2\right) + \left(\frac{1}{2}\rho C_f V^2\right)} \tag{3.11}$$

were ρ is the water density (kg/m^3) and C_f is a dimensionless quadratic friction coefficient calculated as

$$C_f = \frac{2g}{K_s^2 h^{1/3}} \tag{3.12}$$

were $K_s\,(x, y)$ is the Strickler coefficient ($m^{1/3}/s$) that generally needs to be calibrated to fit flow observations. This hydraulic friction coefficient is considered spatialized which is affordable with our dense dataset, in order to finely compensate data-model errors.

Sisyphe model corrects the total bed shear stress τ_b (N/m^2) issued from the hydrodynamic model (equation 3.11) using a factor μ to express the grain shear stress τ' (N/m^2), which is the only component acting on the bedload transport (Mendoza et al., 2017).

$$\tau' = \mu \tau_b \tag{3.13}$$

were the correction factor $\mu = C'_f / C_f$ corresponds to the ratio between friction coefficient C_f defined in equation 3.12 and the friction coefficient C'_f only due to the skin friction given by:

$$C'_f = 2 \left(\frac{\kappa}{log(12h/h'_s)} \right)^2 \tag{3.14}$$

were κ is the von Karman coefficient, h the water level (m) and $h^{'}_s$ the roughness height (m) defined as

$$h^{'}_s = \alpha_{h'_s} D_{50} \tag{3.15}$$

were $\alpha_{h'_s}$ is a calibration parameter (3 by default; Tassi and Villaret, 2014) and D_{50} (m) is the sediment mean diameter. This parameter of calibration varies according to the presence of bedforms, Mendoza et al. (2017) found $\alpha_{h'_s} = 37$ for dunes and $\alpha_{h'_s} = 3.6$ for bars.

3.3.2.2 Numerical model construction and calibration

Domain meshing and boundary conditions

The computational domain of the 2D numerical model covers a 17 km-long section of the Moselle river located between Charmes and Bayon (Figure 3.1). The domain was longitudinally extended out of the "Wild Moselle" river section in order to reduce the influence of the boundary conditions within the studied area. The upstream and downstream limits of the domain were set on reaches where the cross-section is laterally reduced (valley narrowing and transverse road embankment) and the channel bottom is stable (substratum outcrop and bridge foundations). The domain was laterally extended from hills at the right side to the canal at the left side, since field observations shows that the canal dikes were not submerged for a 10-years flood. This domain was discretized into a computational grid composed of $1,018,976$ triangular elements and 511296 nodes generated using Bluekenue software. This grid is composed of structured submeshes into the riverbed along the main flow direction to the downstream direction and unstructured mesh in the floodplain. The mesh size varies from 3.5 to $10m$ between the main channel and the floodplain with locally refined areas as for the diversion canal of the Bainville dam where the mesh size was set to $2m$. The mesh node elevations were interpolated from an accurate digital elevation model (DEM) generated from a LiDAR topo-bathymetric acquisition of the Moselle river (see sections 3.3.3.1 and 3.3.3.2).

The numerical model has 4 boundary conditions distributed along the Moselle river: one upstream at Charmes, one lateral on the diversion canal of the Bainville dam and two downstream before the bridges of Bayon. At the upstream boundary condition we imposed the discharge recorded at 1 hour interval by the Châtel-sur-Moselle gauging station (Figure 3.1) located $12km$ upstream considering that (i) lateral contributions of tributaries over this short unmodeled upstream reach do not change significantly the flood magnitudes and that (ii) for non-overflowing floods the hydrograph shape is unchanged. At the lateral boundary condition, we imposed a constant output discharge of $3.2m^3/s$ which corresponds to the diversion canal discharge measured using an Acoustic Doppler Current Profiler (ADCP) minus the estimated lateral inflows from the “Wild Moselle” tributaries. At the two downstream boundary conditions, we imposed rating curves derived from the outputs of a 1D hydraulic model constructed between Bayon and Tonnoy, using HEC-RAS software (5.0.7). This 1D model was preferred to a 2D model in this area since it enables to integrate hydraulic structures or other civil engineering works into the model such as the arched bridges of Bayon. The 1D model was calibrated by comparing the simulated WSE to the river free surface elevation measured during the LiDAR acquisition. The influence of this downstream boundary conditions on modelling results within the studied area was determined through a sensitivity analysis carried out by modifying of $\pm 1m$ the depth into the downstream imposed rating curves.

Hydraulic calibration

The hydraulic model was calibrated by adjusting spatially distributed Strickler coefficient patches along the domain in order that simulations results corresponds to observed free surface elevation and flow distribution. The choice is made to use a friction coefficient that is spatially uniform in the main channel, except in the dam bypass channel, and spatially uniform into the floodplains. This revealed to be sufficient to get a fairly good model-data fit as shown bellow. The calibration of the WSE was carried out using 10 limnimeters distributed along the studied reach (Figure 3.1), with a measuring interval of 5 min and an accuracy of $\pm 0.05\%$ FS. These devices (Leveloggers Edge M10) were inserted in strainer tubes sank into the riverbed near the bank and leveled using a centimetric-accuracy Leica Viva GNSS. The limnimeter elevations were readjusted, by comparing the WSE recorded by the devices to the free surface elevation measured by the LiDAR, which enabled a vertical accuracy estimated at $\pm 3cm$. WSE data derived from LiDAR acquisition could however not directly be used to calibrate the model, because during the airborne survey (few hours) discharges varied significantly along the reach due to a dam operation. Therefore, the friction coefficient of the riverbed was calibrated using free surface elevation recorded by each limnimeter successively in time, at a “plateau” value, corresponding to the propagation of a discharge of $40m^3/s$.

Steady state simulations were conducted at this discharge, using different Strickler coefficient and the sum of absolute differences between modelled and observed WSE were calculated, to identify the best-fitting coefficient. The limnimeters L4, L5 and L12 were excluded from this calibration process, considering that the WSE may locally be influenced by the distribution of the flow between the main and dam bypass channel (Figure 3.1). This flow distribution was subsequently calibrated by adjusting the friction coefficient into the dam bypass channel to match modelled and observed discharges measured within this reach during the LiDAR survey using a current meter. Thereafter, the friction coefficient of the Bainville dam downstream face was calibrated, in order to match modelled and observed WSE recorded at the limnimeter L5. Finally, the first studied flood (Figure 3.2) was simulated, during which the floodplain Strickler coefficient was calibrated, to match time-series of modelled and observed WSE recorded at all the limnimeters. The validity of those friction coefficients for the second studied flood (Figure 3.2) was assessed by comparing time-series of modelled and observed WSE recorded at all the limnimeters. This second unsteady simulation was performed using the DEM from 2019 instead of 2018 one in order to take into account of the river morphological evolutions. Furthermore, a mesh sensitivity analysis was also performed to ensure that the calibration of the friction coefficient was independent of the mesh size.

Shear stress computation

The unsteady simulations of the studied flood F_1 and F_2 (Figure 3.2) were performed using the finite-element numerical solver of Telemac-2D (version 8.1) run in parallel on 42 processors, with a constant time-step of 0.5, which enabled to respect a CFL value of 1 on each studied cases. The hydraulic model outputs, corresponding to the maximum flow velocity modeled at each patches and tracers location, served as hot-starts to compute the total bed shear stress τ_b and the correction factor μ in Sisyphe. This correction factor μ was computed based on a roughness height determined (equation 3.15) with a D_{50} of $30mm$ considered representative of the riverbed and a coefficient $\alpha_{h'_s}$ of 3 assuming flat bed conditions during the floods (Villaret et al., 2013). Both τ_b and μ were extracted from numerical results at each patches and tracers initial position, to compute (equation 3.13) the grain shear stress τ' acting on the particles mobility. The Shields parameter θ was computed (equation 3.1) based on the grain shear stress τ' modeled at each studied location, and the size D of each studied particles (tracers diameter or median diameter of the ten largest particles transported out of the patches). Then, θ was plotted as a function of D in order to visually determine the critical Shields parameter according to the mobility or not of each of the studied particles.

3.3.3 Assessment of the critical shear stress estimation

The ability of the 2D hydro-sedimentary model to predict the sediment motion, using the threshold value θ_{cr} estimated in this study, was assessed at the scale of the “Wild Moselle River“, by comparing (i) the maximum Shields parameter modeled over eroded areas to (ii) the critical Shields parameter $\theta_{cr,D50}$ estimated for the bed surface D_{50}. The maximum bed shear stress was estimated during the highest flow event (F_1) observed between two LiDAR surveys, from which eroded areas were identified. The areas of sediment deposits were however not considered since this mechanism depends on local flow velocities as well as on upstream sediment supply.

3.3.3.1 LiDAR acquisitions

The two airborne LiDAR topo-bathymetric acquisitions were performed along the studied reach at low water levels in summer 2018 and 2019 (Figure 3.2). Those aerial acquisitions were carried out with an Optech Titan sensor using both near-infrared and green lasers to measure the topography and the shallow bathymetry, respectively (Lague and Feldmann, 2020). The flights were achieved at an elevation of $450m$, which allowed a ground resolution of $38pts/m^2$and $7pts/m^2$ at emerged and submerged areas, respectively. The relatively low density of underwater measurements is due to a sensor malfunctioning, as all discrete returns were not recorded, which conducted to use full-waveform data whose recording frequency is divided by two. The point cloud density was however sufficient to build digital elevation models (DEM) of $1m$ resolution, were 95% of the river submerged areas (depth $> 2.4m$) were covered.

3.3.3.2 Bathymetric campaign

To complete the DEMs over submerged uncovered areas, bathymetric campaigns were performed following the LiDAR acquisitions. The campaigns were performed from a boat using an Acoustic Doppler Current Profiler (ADCP) coupled with a centimetric-accuracy differential GPS (DGPS). Water depths were recorded every second and associated with DGPS coordinates during post-processing, by synchronizing both devices. The boat trajectory followed a zigzag path from one river side to the other in order to optimize the riverbed mapping and simplifying bathymetric transects interpolation. The ADCP vertical beams were interpolated using the Triangular Irregular Networks tools (TIN) of ArcGIS software and edges were manually adjusted to map the riverbed as observed in the field. The TIN which elevation accuracy was estimated at $\pm 5cm$, were rasterized into $1m$ cells and vertically shifted, in order to overlap with the LiDAR DEMs throughout merging process.

3.3.3.3 Eroded areas

The difference of elevation between DEMs of 2018 and 2019 was computed using ArcGIS software and cells located into the riverbed were extracted from the resulting raster. These cells were converted into points, in order to select areas where observed erosion was higher or equal to $0.1m$, considering that lower values are within uncertainty bounds of LiDAR measurements. The points located on areas completed by bathymetric campaigns were excluded from this dataset, considering that riverbeds mapping was not detailed enough to be compared between surveys. Furthermore, the points located in river sections where bank erosion or sediment deposits occurred were excluded, since these morphological evolutions can locally change the bed shear stress distribution, but are not considered in the numerical model. Other points located close to river singularities (bridge, log-jams, etc.) or isolated were also manually removed.

3.3.3.4 Modelled Shields parameter

The maximum bed shear stress τ_b and the corresponding correction factor μ modelled over each of the selected points, during the highest flood event (F_1) observed between the two LiDAR surveys, was extracted from numerical results. The Shields grain shear stress τ' was computed (equation 3.13) at each point and adimensionalized (equation 3.1) based on a grain size of $30mm$ corresponding to the bed surface D_{50}. The cumulative frequency of θ_{D50} was compared to the critical Shields parameter $\theta_{cr,D50}$ of 0.035 estimated previously to determine the proportion of eroded areas, where the 2D model predicted sediment transport. This comparison was done with both DEMs in order to considered morphological evolutions, which could occur before the studied flood.

3.4 Results and discussion

This section presents the results of the critical Shields parameter estimation determined by comparing the observed river flow competence to the modelled grain shear stress. First, we describe the results of both painted bed patches and tracer surveys, which allowed to estimate the river flow competence. Then, we show the results of the 2D hydraulic model calibration from which grain shear stress is computed and the corresponding Shield parameter is plotted as a function of grain size. Finally, we assess the critical Shields parameter estimated with our proposed approach, by comparing the maximum grain shear stress modeled over observed eroded areas to the critical grain shear stress estimated for different particle sizes.

3.4.1 Flow competence estimation

The first survey of both painted bed patches erosion and tracer displacement took place 4 months after their installation, in August 2018 (Figure 3.2). During this period, only a minor flood occurred in June 2018, with a peak flow estimated at $90m^3/s$, equivalent to approximately 0.36 times the bankfull discharge. Since painted bed patches remained intact, and the first field survey only allowed to identify the initial positions of the RFID tracers, we considered that our monitoring began at September 2018.

3.4.1.1 Painted bed patches

The first survey of the painted patches evolutions (E_1) was performed in February (Figure 3.2), after a flood peak (F_1) estimated at $303m^3/s$, which occurred the 25th December 2018. The results of this survey are presented in table 3.1. Two patches were missing (erosion), two patches were partially eroded (partial) and two patches were covered by sediments (deposits). For missing patches, we consider that the D_{95} of the mobilized particles corresponds to the D_{95} of the patches, which gives maximum sizes of transported particles ranging from 7 to $10cm$. For partially eroded patches, the comparison between the patches D_{95} and the mobile particles D_{95} shows that transported particles (Figure 3.3) were smaller than the bed surface D_{max}. This observation indicates that coarser particles were available for transport on each patches, which valids the use of these results to estimate the flow competence.

First field survey of painted bed patches evolution (E_1)

Name	Evolution	Patch D_{95}	Mobilized D_{95}	Model GSS	Shields parameter
PP1	erosion	$10cm$	$10cm$	$33.5N/m^2$	0.021
PP2	erosion	$7cm$	$7cm$	$32.5N/m^2$	0.029
PP3	deposits	X	X	$18.6N/m^2$	X
PP4	partial	X	$4.9cm$	$19.8N/m^2$	0.025
PP5	deposits	X	X	$54.4N/m^2$	X
PP6	partial	X	$5.5cm$	$22.3N/m^2$	0.025

Second field survey of painted bed patches evolution (E_2)

Name	Evolution	Patch D_{95}	Mobilized D_{95}	Model GSS	Shields parameter
PP1	erosion	$9.8cm$	$9.8cm$	$35.2N/m^2$	0.022
PP2	X	X	X	X N/m^2	X
PP3	deposits	X	X	X N/m^2	X
PP4	none	$7.2cm$	$0cm$	$2.5N/m^2$	0.002
PP5	deposits	X	X	X	X
PP6	none	$7.4cm$	$0cm$	$14.9N/m^2$	0.012

Table 3.1: Evolution of the painted bed patches PP_n at each survey (E_n). Erosion indicates that the patch was totally eroded, Partial indicates that the patch was partially eroded, Deposits indicates that the patch was covered by sediments deposits and none indicate that no evolution was observed. The patch D_{95} corresponds to the averaged diameter of the ten largest particles measured in pictures taken at the installation of the patch. The D_{95} mobilized corresponds to (i) 0 when no evolution was observed, (ii) the patch D_{95} when it was totally eroded or to (iii) the average diameter of the ten largest particles measured out of the patch when it was partially eroded. The Shields parameter is computed (equation 3.1) according to (i) the maximum grain shear stress (GSS) modelled at each patch during F_n and to (ii) either the patch D_{95} when no evolution was observed or to the mobilized D_{95} when the patch was totally or partially eroded.

For the following monitoring, new patches were painted were added next to the existing ones with another color, except patch PP_2, which was located on a gravel bar that was totally eroded during F_1 and is now submerged. The second survey (E_2) was conducted in May 2019, after a flood peak lower than during the first field monitoring (Figure 3.2), which was estimated at $214m^3/s$ and occurred on the 16 March 2019 (F_2). During this second survey (E_2), we observed one missing patch (total), two patches without sediment transport (none) and two patches covered by sediments (deposits).

For a same particle size, the patch PP_1 was totally eroded during both monitored floods F_1 and F_2, even if the second flood peak (F_2) was less important than the first one (F_1). This confirms that the critical discharge for particles motion was largely exceeded during the first flood (F_1). As well, patches PP_4 and PP_6 , where partial transport occurred during the first flood (F_1), remained intact during the second flood (F_2). This gives us confidence in the method and confirms that mobile particles recovered during the first survey (E_1) provide a good estimation of the flow competence. These results also demonstrate that partial sediment transport occurred during both studied floods.

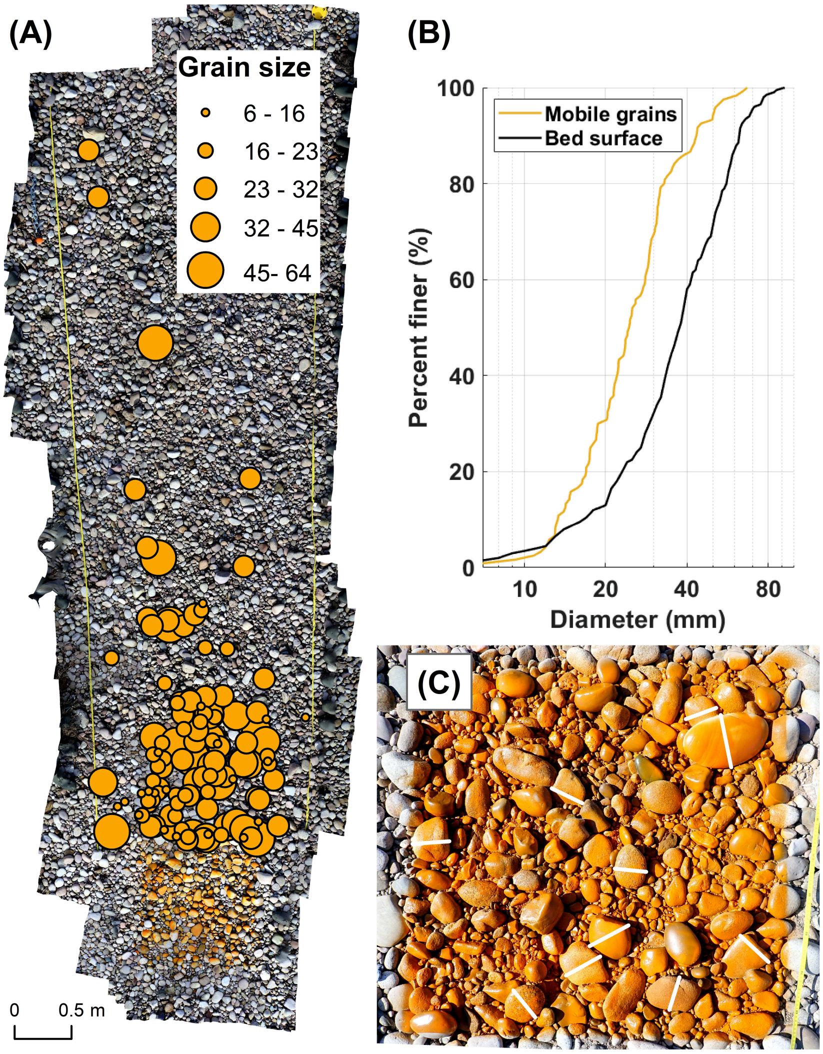

Figure 3.3: Example of (A) an orthophoto mosaic built from pictures taken at PP_6 during survey E_1, when partial transport was observed. Orange circles indicate the diameters, measured on the orthophoto, of particles recovered out of the patch, (B) a cumulative frequency distribution of mobile particles size measured on the orthophoto and of particles measured in the field at riverbed surface, (C) picture showing a digitalization of the ten largest particle observed on the patch PP_1 set at PI.

3.4.1.2 RFID tracers

The initial position (S_0) of tracers was recorded in August 2018, along a 40-m-long reach of $0.2ha$ (Figure 3.2), where 288 of the 450 injected tracers were recovered. Given the relatively low recovery rate of 64% achieved using the 1.2m-long antenna, the survey was completed using a 0.46m-diameter loop antenna, to reduce masking effects during detection, resulting in an improved recovery rate of 83%. The tracers recovered using the loop antenna were, however, excluded from this study due to the lower positioning accuracy compared to the wide antenna, where the GPS antenna could be positioned directly above the detected area. The first survey (S_1) of the tracer locations was achieved in August 2019, along a 750-m-long-reach of $2.5ha$ (Figure 3.2), where 388 tracers were found. The obtained recovery rate of 86% was higher than at S_0, as tracer were more widely distributed in the downstream direction, reducing masking effects during detection. The recovery rate of smaller tracers was relatively lower than for other tracers at S_0 and S_1, probably because they were equipped with 23 mm-long tags, whose distance of detection is shorter.

Size class (mm)	N_S	S_0	S_1	S_0^* and S_1^*	$Mobile^*$	$Immobile^*$
16 – 22.6	87	46	67	37	34	3
22.6 – 32	87	51	72	43	41	2
32 – 45.3	86	54	78	48	43	5
45.3 – 64	86	56	76	48	44	4
64 – 90.5	86	65	79	61	43	18
90.5 – 128	18	15	16	14	6	8
Total number	450	287	388	251	211	40
Recovery rate	100%	64%	86%			

Table 3.2: Statistical parameters for each particle tracking survey, indicating the total number N_s of tracers injected and recovered at survey S_n or S_n and S_{n+1} (*denoting that tracers located at less than 7m from the left bank were excluded from data), with the number of mobile and immobile tracers among recovered ones.

Considering only tracers injected at distance greater than $7m$ from the left bank and recovered at S_0 and S_1, the number of studied tracers is reduced to 251 (Table 3.2). Among these tracers, 211 were mobile (traveled distance $> 5m$) and 40 immobile. Coarser tracers exhibited lower mobility (42%) compared to finer tracers (91%), which is consistent with observations made using painted bed patches, suggesting that the sediment transport was size-selective. This mode of sediment transport was also corroborated by Piasny et al. (2023a), who demonstrated that finer particles traveled further ($350m$) than coarser ($27m$) particles. Coarse immobile tracers were distributed throughout the entire river section, whereas finer immobile tracers were predominantly located near river banks (Figure 3.4). This lateral distribution enabled to estimate flow competence under a wide range of flow conditions.

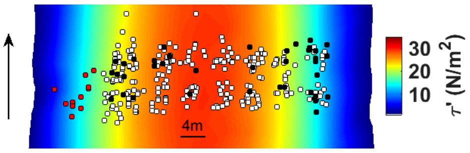

Figure 3.4: Grain shear stress τ' modelled at the peak of the flood F_1 ($Q = 303m^3/s$) over tracers injection site. Points indicate mobile (white), immobile (black), and excluded (red) tracers.

3.4.2 Critical bed shear stress estimation

The spatially distributed friction parameter of the 2D hydraulic model was calibrated for the flood F_1 (Figure 3.2), from which the flow competence was estimated using both painted bed patches and tracers. This flood lasted approximately 170 hours and consisted of two distinct peaks, reaching 211 and $303m^3/s$, respectively, which allowed us to study the dynamics of both filling as well as emptying of the domain. As part of this study, the primary focus was on accurately modeling of flood peaks. However, simulations were extended to cover the entire duration of the event to assess the impact of morphological changes on model calibration. The validity of this calibration for the flood F_2 (Figure 3.2), reaching a maximum discharge of $214m^3/s$, was verified by comparing observed and modelled WSE from simulations based on the DEM of summer 2019. The results of this comparative analysis being as good as results of calibration in terms of WSE reproduction, only the latter will be presented into the next subsection. Thereafter, we will consider that our calibrated hydraulic model is valid for both floods. The maximum bed shear stress was extracted from this model, where the studied particles are located, in order to compare the computed Shields parameters to the observed flow competence and determine the critical values.

3.4.2.1 Hydraulic model calibration

The Strickler coefficient of the main and bypass channel riverbeds was calibrated by comparing observed and modelled hydraulic variables measured during the first LiDAR survey (A_1) carried out at a discharge of $40m^3/s$. Steady state simulations performed at this discharge indicated that the sum of absolute differences between observed and modelled WSE of all limnimeters (except L4, L5 and L12) was the lowest ($4cm$) when using a Strickler coefficient of $47m^{1/3}/s$. Using this coefficient, the discharge modelled within the dam bypass channel ($5.3m^3/s$) was, however, slightly higher than that measured in the field ($5m^3/s$). This difference was reduced to a few liters per second by setting a Strickler coefficient of $33m^{1/3}/s$ in the upstream part of the dam bypass channel to modify the flow distribution with the main channel. This higher coefficient of friction can be explained by log-jams located in this part of the bypass channel, which reduce the cross-section area (L'Hommedieu et al., 2020) and increase the channel roughness (Hygelund and Manga, 2003). After calibrating the flow distribution between the dam bypass channel and the Moselle river, results indicated that the WSE modeled at L5 was $20cm$ lower than observed. This difference was reduced to one centimeter by setting a Strickler coefficient of $8m^{1/3}/s$ over the downstream face of the dam. Furthermore, a sensitivity analysis shows that all calibrated friction values are independent of the mesh size.

The Strickler coefficient of the floodplain was calibrated, by comparing observed and modelled WSE, during the flood F_1. This flood occurred 6 months after the LiDAR survey A_1, during which the Strickler coefficient of the riverbed was calibrated, with an initial discharge close to the value of calibration (Figure 3.2). The simulation results (Figure 3.5), show that the model is still well calibrated at the beginning of this flood for all limnimeters, expect for L10, where the modelled WSE was $10cm$ below the observed value. This difference may arise from an increase of the riverbed elevation ($\sim 50cm$), which was observed along the reach located downstream of the limnimeter, when comparing the 2018 and 2019 DEMs. As tracers injected across this reach remained in place during the studied flood, it tends to indicate that they were likely buried before the event. This field observation therefore confirms our assumption of an increase of the riverbed elevation between the LiDAR survey A_1 and the flood F_1, resulting in an underestimation of the modeled WSE. By modeling the flood using the DEM of 2019, which takes into account these morphological evolutions, the difference of WSE was suppressed at the start of the simulation.

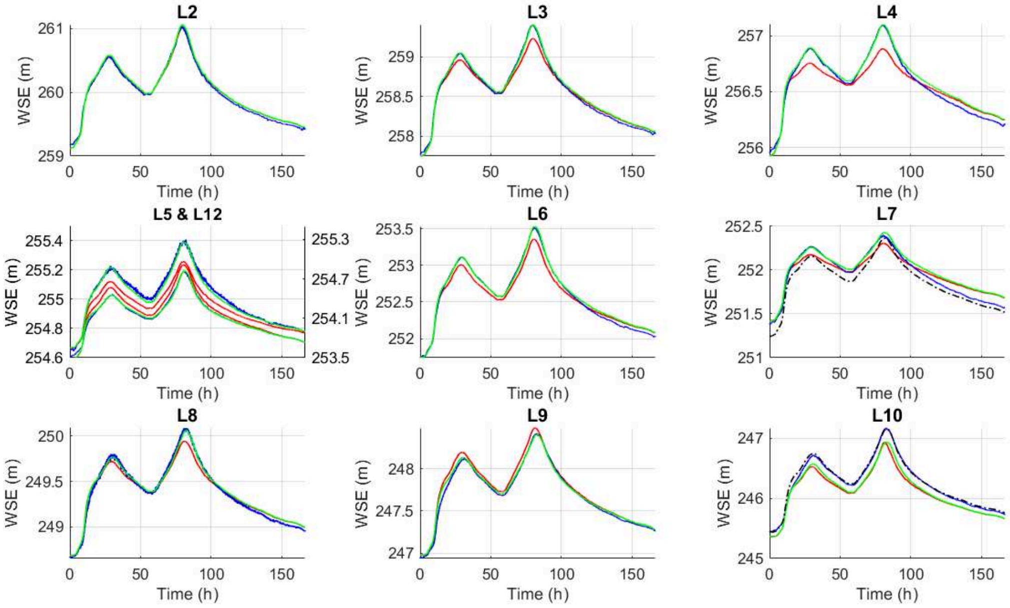

Figure 3.5: Comparison between observed and modelled WSE during the flood event F_1 (discharges ranging from 40 to $303m^3/s$). Blue solid line indicate the WSE recorded by the limnimeter L_n distributed along the Moselle river (Figure 3.1 D). Red and green solid line indicates the WSE modelled using the DEM of 2018, with a Strickler coefficient in the floodplain of $47m^{1/3}/s$ and $8m^{1/3}/s$, respectively. Dashed black line indicates, at L7 and L10, the WSE modelled using the DEM of 2019 with a Strickler coefficient in the floodplain of $8m^{1/3}/s$.

At the flood peaks (Figure 3.5), the model significantly underestimated WSE at all limnimeters, except at L2 and L10, where observed and modelled WSE fit very well. The correspondence of stage graphs recorded at the upstream part of the reach indicates that this underestimation is not related to model inflows, thus confirming the suitability of the upstream gauge station's hydrograph. The fact that these limnimeters are the only two located within non-overflowing reach states that the underestimation of WSE observed at the other limnimeter is associated to the friction coefficient set into the floodplain. Indeed, the stall between curves generally occurs after 14h of simulation, at $142m^3/s$, when water levels exceed the bankfull level at the diffluences with the dam bypass channel and the meander cutoff. Based on this discharge, a steady state simulation was performed to determine the limit between submerged areas, where the friction coefficient is well calibrated and emerged areas, where the friction coefficient needs to be calibrated. The calibration of the Strickler coefficient in these emerged areas, which roughly corresponds to the floodplain, was performed by testing different uniform values, while retaining the previously set coefficients in the emerged areas, in order to find the best-fitting friction coefficient. Results show that best correspondences between observed and modeled WSE were obtained at the flood peak, with a Strickler coefficient in the floodplain of $8m^{1/3}/s$ (Figure 3.5).

By applying this coefficient on a vegetated secondary channel located in the floodplain, between L8 and L9 (Figure 3.1), it significantly reduced flows in this channel during the flood. As flows were concentrated into the main channel, the distance traveled by the water between these two limnimeters was doubled, which shifted in time the peaks of WSE modelled at L9. The magnitude of these peaks of WSE modelled at L9 were, however, higher than observed. This may be caused by a reduction of flows in the secondary channels bypassing the meander along the hillslope, when applying a Strickler coefficient of $8m^{1/3}/s$ into the floodplain. By applying the Strickler coefficient of the riverbed over the floodplain located along the hillslope (Figure 3.1), it facilitates flow in the secondary channels, resulting in a reduction of the WSE modeled at L9. WSE modeled at the flood peak, was also higher than observed at L4, when applying a coefficient of $8m^{1/3}/s$ into the floodplain. By applying the friction coefficient of the riverbed to a portion of the floodplain located between the upstream and downstream meanders of the diffluence (Figure 3.1), it facilitates flow over this area, resulting in a reduction of the WSE modeled at L4. Throughout this calibration process, the position of the boundary between the riverbed and floodplain Strickler coefficients was also laterally adjusted along some sections of the river (vegetated bank, backwater, etc.) to fine-tune the alignment with observed WSE.

Although this calibration of the friction coefficients strongly improved the hydrodynamic modelling of flood peaks, results show that WSE were largely overestimated at L7 after 160 h of simulation. This overestimation is due to an incision and enlargement of the cutoff channel located downstream of the limnimeter, which occurred during the flood, but that was no taken into account in the hydrodynamic model. Therefore, by using the DEM of 2018 without modelling this morphological evolution, the deviation from observed WSE starts following the first peak and progressively increases during the studied flood. By using the DEM of 2019, as expected, modelled WSE were underestimated at the start of the simulation, but also at the end, as floods of March 2019 also contribute to the riverbed morphological evolution. At the flood peak, observed WSE lies between both curves, then as part of this study the maximum bed shear stress was determined at the painted bed patches P4 by computing the mean value.

3.4.2.2 Bed shear stress and flow competence

Expect for P4, the maximum grain shear stress was computed at each painted patch using the DEM of 2018 for the flood of December 2018 and the DEM of 2019 for the flood of February 2019. Table 3.1 shows that the modelled grain shear stress ranges between 2.5 and $33.5N/m^2$, the highest value of $54.4N/m^2$ being modelled at the painted patch P5, located at the convex bank of a meander. The velocities modelled at this convex bank may be overestimated as depth-averaged model are unable to predict the migration of high velocity toward the concave bank of a meander bend, without adding some correction for interaction between lateral curvature and vertical nonuniform velocity (Bernard and Schneider, 1992). The flow competence estimates at the patches P5 was therefore excluded from the dataset. As expected, the grain shear stress modelled at each patch decreased during the second flood F_2 of lower magnitude, apart at patch P1, where modelled grain shear stress was relatively constant. A large amount of sediment deposits ($\sim 30cm$) was observed between DEM of 2018 and 2019, over the gravel bar where the patch P1 was set, locally reducing the river section and thus increasing the flow velocity. This local variation of the river section explains why the grain shear stress modelled at P1 using the DEM of 2019 did not decrease at a lower flood peak. Results shows that particles were not transported for a grain shear stress lower than $15N/m^2$, partial transport occurred between 19.8 and $22.3N/m^2$, while total transport happened above $32.5N/m^2$. These observations being coherent, it gives us confidence in the method used to estimate the flow competence. The grain shear stress τ' modelled at each patch was adimentionalized, to express the Shields parameter θ (equation 3.1), based on the diameter of the ten largest particles ($\sim D_{95}$) measured either within (no erosion and total erosion) or out (partial erosion) of the patches. The estimated Shields parameter values ranged from 0.002 to 0.029.

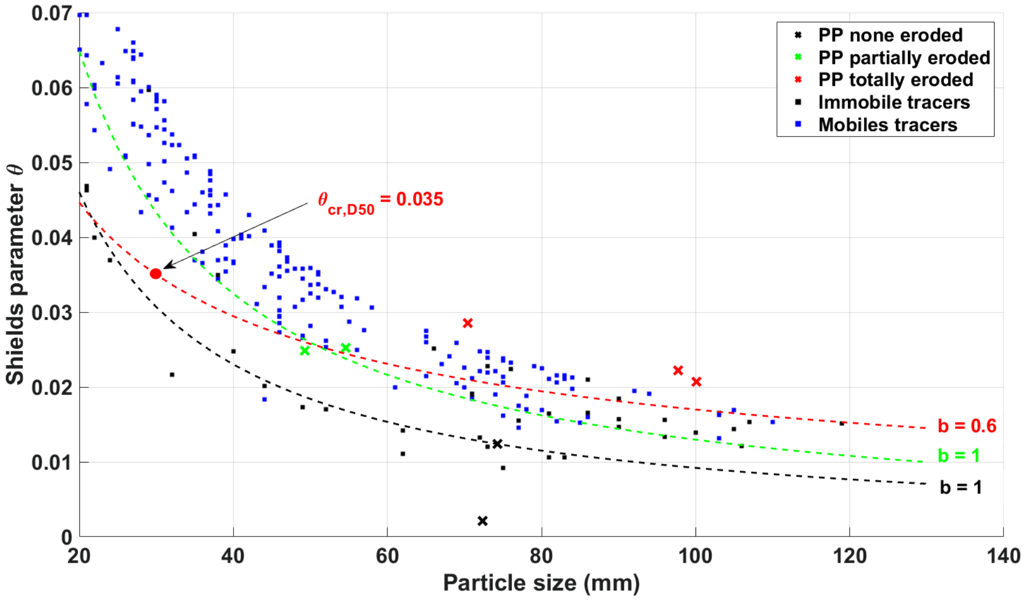

Figure 3.6: Shields parameter computed (equation 3.1) based on (i) the maximum grain shear stress modelled at each painted patch (denoted PP) or tracer location and to (ii) the size of the studied particles, whether they are mobile or immobile. The green dashed line represents an extrapolation of the critical Shields parameter estimated from partially eroded patches, assuming equal mobility ($b = 1$). The black dashed line represents an extrapolation of the Shields parameter estimated from uneroded patches, assuming equal mobility ($b = 1$). The red dashed line represents an extrapolation of the critical Shields parameter estimated from partially eroded patches, assuming size-selective transport ($b = 0.6$)

The Shields parameter estimated at the two painted patches where partial transport occurred, considered as critical, were plotted as a function to the D_{95} of the particles transported out of the patch (Figure 3.6). Results show a value of $\theta_{cr} = 0.025$ for grain sizes D of 4.9 and $5.5cm$. Considering the uncertainties in grain shear stress modelling and grain size measurements, it suggests that critical Shields parameter could be as constant ($b = 0$) as variable ($b > 0$). Plotting Shields parameters estimated from painted patches, where total transport occurred, results indicates that coarser particles were mobilized for values lower than 0.025, which disproves the hypothesis of a constant critical Shields parameter. To match with our results, the critical Shields parameter should vary according to the particles relative size, computed (equation 3.6) as a function to a reference size of $30mm$, corresponding to the bed surface D_{50}. The resulting curve must pass (i) between values of critical Shields parameter determined from partial transport, (ii) below values determined from total transport transport, where the threshold was largely exceeded and (iii) above values where no sediment transport were observed. In the latter case, as none of the different particle sizes were transported at a grain shear stress of $14.3N/m^2$, the values of the Shields parameter under which no sediment transport occurred was computed for all particle sizes. The curve of equal mobility being located above this curve, the value of the hiding factor b could reach 1, even if it is unlikely, since partial sediment transport was observed.

The Shields parameter was computed (equation 3.1) at each tracers location, according to their size and the maximum bed shear stress modelled where they were recovered (at S_0 for mobile and at S_1 for immobile). By adding to figure 3.6 the values estimated for immobile tracers, the results show two different tendencies varying as a function of the tracer sizes. Most values obtained for immobile tracers finer than 70 mm were very close to the curve under which no sediment transport occurred, thereby validating the previous result. Furthermore, a large number of values obtained for coarser immobile tracers were above the curve of b equal 1, which confirms that entrainment of particles occurs in a size-selective way ($b < 1$) rather than by equal mobility ($b = 1$). Therefore, the curve of critical Shields parameter should pass above values obtained for both finer and coarser immobile tracers, while respecting recommendations made earlier. To meet all these criteria, an agreement has been reached by setting a hiding factor of 0.6, which allowed to rotate the curve of the critical Shields parameter around the reference particle size of $30mm$. The critical Shields parameter $\theta_{cr,D50}$ estimated for this particle size of $30mm$, corresponding to the bed surface D_{50} was 0.035, which allowed to express the following law:

$$\theta_{cr,i} = 0.035 \left(\frac{D_i}{0.03} \right)^{-0.6} \tag{3.16}$$

In order to confirm the validity of this law, the value of Shields parameter estimated for mobile tracers were added to the figure 3.6. As we can see, almost all of them were above the curve from equation 3.16, except some tracers between $70 - 90mm$ that were transported for a Shields parameter lower than the estimated critical value. As some of these tracers were also below the curve of equal mobility, we supposed that these particles may have protruded from riverbed after their injection and thus were more easily entrained.

The critical Shields parameter $\theta_{cr} := 0.035$ estimated in this study with a medium grain size of $D_{50} = 30mm$, falls within the classical range of 0.02 to 0.065 reported in the literature for rough turbulent flow (Buffington and Montgomery, 1997). This value is much lower than the value of 0.06 predicted for a median grain size of $30mm$, by the classical Shields-Yalin diagram (Yalin, 1992), computed using the Soulsby and Whitehouse (1997) formula. This higher value, however, is unrealistic for our case study as shown by our results, since the tracers moved above a value of 0.04. Our results are much closer to the threshold of 0.03 predicted by the Shields-Parker diagram (Parker et al., 2003). Considering the influence of the river slope, a value of 0.024 was obtained using the law proposed by (Recking, 2009), based on an average slope of 1.2‰. This lower value compared to our results seems to be an underestimation since no sediment transport was observed below a value of 0.03. As most of the bedload transport laws involve a threshold value (cf. equation 3.2), using a critical Shields parameter estimated from flume experiments would result to underestimated the sediment transport, while using a critical Shields parameter estimated from the river slope would result to overestimate the bedload transport. The exponent of 0.6 found in this study, for hiding/exposure effects (equation 3.6), falls within the range of 0.5 to 0.7 estimated from the largest particle size moving under different flow conditions (Komar, 1987; Ashworth and Ferguson, 1989). Our results closely align with the empirical law proposed by Komar (1987), were $b = 0.68$ (Figure 3.7), which was also determined from flow competence estimation. The method proposed in this article, combining the survey of both patches erosion and tracer mobility, appears to be highly accurate for calibrating both the critical Shields parameter and the hiding and exposure exponent b in a 2D hydro-sedimentary model.

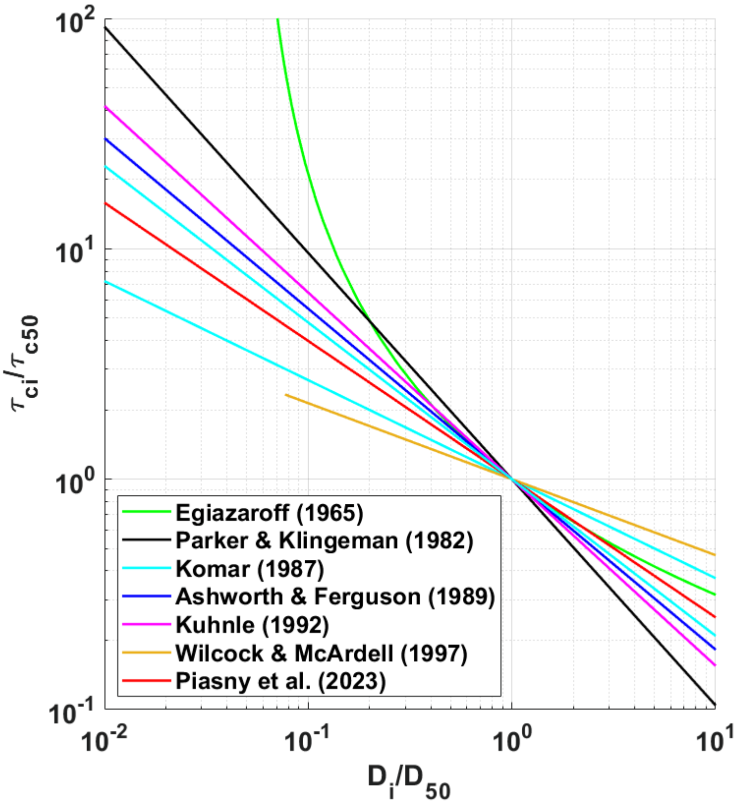

Figure 3.7: Comparison of different hiding functions : in all studies $\theta_{ci} = \theta_{cr}\left(\frac{D_i}{D_r}\right)^{-b}$ with $b \in [0.33; 0.98]$ except in Egiazaroff (1965) where $\theta_{ci} = \left(\log(19)/\log(19\frac{D_i}{D_r})\right)^2$.

3.4.3 Assessment of the critical shear stress estimation

The ability of the 2D hydro-sedimentary model to predict the sediment motion, using the threshold value estimated in this study, was assessed at the scale of the “Wild Moselle River“, by comparing (i) the maximum Shields parameter modeled over eroded areas to (ii) the critical Shields parameter $\theta_{cr,D50}$ estimated for the bed surface D_{50}. The eroded areas were identified by calculating differences in elevation Z between 2018 and 2019 DEMs, over the 88% of riverbed surfaces, being covered during both topo-bathymetric LiDAR surveys A_1 and A_2. Over this $62ha$ study area, sediment deposit ($\Delta Z \geq 10cm$) and bed erosion ($\Delta Z \leq -10cm$) occurred on 28% and 7% of the riverbed, respectively, while remaining surfaces were considered stable. The proportion of eroded areas is significantly lower than the proportion of deposition areas, as surfaces of eroded banks are not considered in this computation. Out of the $4.4ha$ where bed erosion was observed, only $3.6ha$ were studied, excluding very localized eroded areas that are sparely distributed along the river and considered as epiphenomena. This surface gathers 143 spatial entities, ranging from a few square meter to thousands of square meters with a median size of $30m^2$. These areas are mainly distributed in the meandering part of the river located between the dam of Bainville and Bayon (Figure 3.1 b). The thickness of observed eroded bed ranged from -10 to $-50cm$.

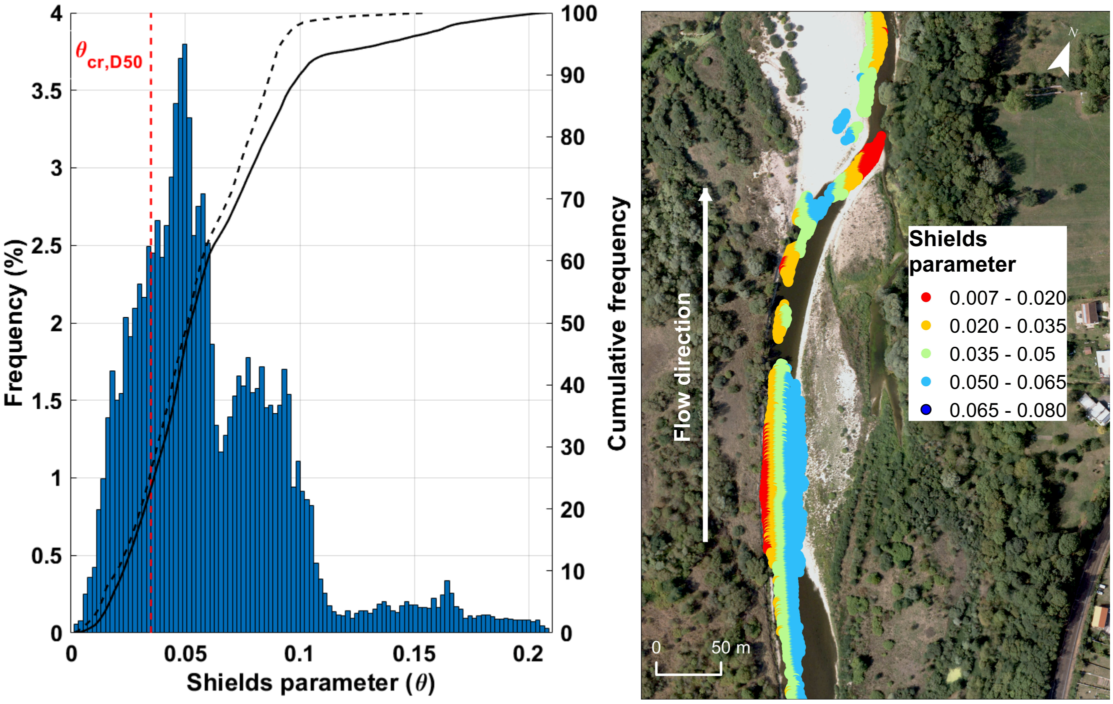

Figure 3.8: Statistical distribution of the Shields parameter computed over all areas eroded ($\Delta Z \leq -10cm$) between LiDAR surveys A_1 and A_2, compared to the critical Shields parameter estimated in this study $\theta_{cr} := 0.035$. An example of the spatial distribution of the maximum Shields parameter modeled over eroded areas distributed along a reach located at the downstream part of the study site.

The frequency distribution of the Shields parameter computed over eroded areas using a unique grain size of $30mm$ and the maximum grain shear stress modelled with the DEM of 2018 are presented in figure 3.8. Computed values vary between 0.005 and 0.2 within three main classes : 0.005 - 0 065, 0.065 - 0.012 and above 0.12. An analysis of the spatial distribution of the values shows that usually a patch of erosion gathered values from a unique group. Values above 0.12 are all located downstream of the points where the river meets hillside, at L10 and upstream to L11, where the bedrock is locally outcropping. Values between 0.065 and 0.012 are mainly located on the upstream parts of the convex bar, where grain sizes are supposed to be coarser, and along runs where field measurements show finer grain sizes. Values below 0.065 were located on many patches, generally of a smaller size and distributed along the river close to curved sections, where bank erosion or sediment deposit occurred. In most of these patches, the proportion of values below 0.035 varies between one quarter and one third of the surface, according to the location of the patch. These values of θ are laterally distributed within the patches, values higher than θ_{cr} were closer to the central part of the river, while values lower than θ_{cr} were always near the convex bank (Figure 3.8). This implies that, using this hydraulic simulation and the estimated critical values, we would not have been able to predict the sediment transport that occurred near the riverbank in these curved sections.

Assuming that the critical Shields parameter was well estimated and that grain size are relatively constant across river sections, one explanation could be that the bed shear stress is underestimated close to concave banks. This may arise from two modelling choices that influence the lateral distribution of velocities: (i) the absence of secondary currents which are classically used to redistribute the flow momentum towards concave banks and (ii) the fixed bed which prevents from modification of the river section or lateral migration acting in the flow distribution. The first hypothesis of neglecting secondary currents stems from the fact that it is a complex parameterization, and default parameters Bernard and Schneider (1992) for production/dissipation of vorticity seems not adapted to our case - their estimation requiring very detailled flow velocity profiles as shown in Piasny et al. in prep. In order to verify the second hypothesis, we ran hydraulic simulations using both DEMs of 2018 and 2019. For each of these simulations, the cumulative frequency of Shields parameter value computed over areas which were eroded are presented in figure 3.8. Results show that the critical Shields parameter was not exceeded over 22% and 25% of eroded areas, using DEMs of 2018 and 2019, respectively. This means that underestimations of the bed shear stress observed close to bank are not related to changes in flow distribution caused by bed migration during floods. The modelling of secondary currents could therefore improve the prediction of the sediment motion in curved section, as well as the consideration of the slope effects on sediment motion and the spatio-temporal evolution of the bed surface grain size distribution. However, our model is still able to predict sediment mobilization in 78% of the areas where erosion was observed. As sediment mobilization is not always indicative of bed erosion, a more in-depth study would require modeling the morphological evolution the river.

3.5 Conclusion

The new method proposed in this article enables to accurately determine the critical shields parameter and the coefficient b for hiding and exposure effects. On the one hand, it relies on painted places that advantageously enable to estimate very locally flow competence under real conditions while considering natural imbrication of sediments. From the mobility of particles from each of the 6 painted places over the 8 km of the studied reach, we found masking and surexposition effects indicating that the hiding coefficient might be higher than 0.

On the other hand, the proposed method also uses RFID tracers that advantageously provide a large amount of information with tracers covering a large range of particle diameters and flow conditions, despite lower position accuracy. In addition, the use of a 2D hydraulic model, the spatialized friction of which is finely calibrated on *in situ* data, crucially gives access to an accurate bed shear stress cartography. From this size based mobility, the hiding coefficient has been determined precisely ($b = -0.6$) and consequently the critical Shields value $\theta_{c,D50} = 0.035$ for median grain size $D_{50} = 30mm$.

The critical Shields parameter estimated in this study could not be predicted using classical approaches based on the particle Reynolds number, or the dimensionless diameter, or on the river slope, leading to either under or over estimations, which shows the importance of spatialized *in situ* measurements to accurately estimate this parameter.

Thanks to precise LiDAR acquisitions performed both before and after floods, eroded areas have been accurately identified. The fine 2D hydraulic model provides a map of the maximal shear stress observed between each LiDAR survey, hence indicating exceedance of estimated critical shields parameter ($\theta_{cr,D50} = 0.035$ for $D_{50} = 30mm$) in eroded zones.

Our result show that for more than 80% of observed eroded zones they are determined as transport zones, which show that the critical Shields estimated with the proposed method is physically meaningful. Note that the remaining 20% unpredicted but observed eroded zones are located close to river banks, which could potentially be related to difficulties in estimating lateral velocity distribution.

Our estimation of the critical Shields parameter, that is site specific, enables to compute sediment transport flux. It is often the only and most important parameter of common empirical formulas, in more or less complex hydraulic models (0D to 2D). The proposed rigorous method leads to meaningful estimation of the critical Shields value as shown by accurate solid discharges found in Piasny et al. (2023c).

The method is transposable to other rivers, ideally building the 2D hydrodynamic model first in order to potentially formulate recommendations for the location of the field surveys.

Chapter 4

Flood scale dynamic bedload transport estimation through acoustic measurements compared to 2D hydro-sedimentary modeling

Ce chapitre porte sur l'estimation du flux de transport sédimentaire à partir de mesures directes (prélèvements), indirectes (acoustiques) et d'un modèle hydro-sédimentaire 2D au droit du pont de Bainville. Cette méthodologie originale combine à la fois (i) le calage du modèle numérique et acoustique à l'aide des mesures directes de transport solide, et (ii) la comparaison des deux estimations des débits de charriage variables dans le temps, estimés lors d'une inondation modérée.

4.1 Introduction

Two-dimensional numerical modelling of sediment transport and river morphodynamic has been increasingly used for river management, engineering works, restoration projects or research purposes (Brousse et al., 2022; El Kadi Abderrezzak et al., 2016; Yu et al., 2022; Iwasaki et al., 2016; Nelson et al., 2015). These numerical simulations are usually based on bedload transport laws expressed as $q_s \propto \alpha\left(\tau-\tau_{cr}\right)^{3/2}$where the bedload transport rate q_s is a power-law function of the shear stress τ and the critical shear stress for sediment motion τ_{cr}, affected by an empirical coefficient α (Meyer-Peter and Müller, 1948; Wong and Parker, 2006). τ_{cr} and α are constant variables generally established from flume experiments performed under steady state conditions with a relative uniform grain size distribution, but the grain size distribution of natural gravel-bed rivers is rarely uniform and sediment transport mostly occurs under unsteady flows.

Flume experiments conducted under unsteady flows, using a narrow grain size distribution and a proportional feeding system, demonstrated that for a given shear stress above τ_{cr} a considerable variability in q_s is observed, suggesting a non-linear relation between τ and q_s during flood events (Phillips et al., 2018). When flow changes rapidly, higher q_s were observed during the falling limb than during rising limb of an hydrograph, resulting in counterclockwise hysteresis in the bedload flux. Other flume experiments conducted under unsteady flows using a bimodal grain size distribution and a recirculating feeding system, demonstrated a significant increase of τ_{cr} between the rising limb and the falling limb of the hydrograph, resulting in clockwise hysteresis in the bedload fluxes (Mao, 2012). This increase of τ_{cr} is attributed to temporal changes in the degree of organization and complexity of the bed surface, indicating the influence of the flow history in sediment mobility as shown by Paphitis and Collins (2005).

In natural gravel-bed rivers, Pretzlav et al. (2020) show that τ_{cr} progressively increases with cumulative shear stress until a sufficiently large flood event occurred to disrupt the bed surface and "reset" the flow history, as suggested by Masteller et al. (2019). The cumulative stress tends to increase the bed stability though various mechanisms such as surface armoring (Pfeiffer et al., 2017), bed compaction (Marquis and Roy, 2012), grain size changes (selective erosion) (Humphries et al., 2012), sediment supply (Recking, 2012b), clustering (Strom et al., 2004) and interlocking of grains (Yager et al., 2018). These bed organizations induces a variety of hysteresis loops between flow and sediment flux (Gunsolus and Binns, 2018) making it difficult to model the instantaneous fluxes, using bedload laws developed under steady steady conditions with uniform grain size and a constant critical shear stress.

Given these complex physical processes acting in bedload transport, its modeling remains challenging and *in situ* measurement remain a reliable mean to estimate bedload fluxes. To monitor the bedload fluxes, direct *in situ* measurement using bedload sampler are traditionally performed, but sampling with such devices is an expensive and time-consuming operation. Thus, new methods were developed to monitor indirectly the bedload fluxes using vibration sensors on impacted objects(Mizuyama et al., 2010; Rickenmann and Fritschi, 2017), the record of bedload self-generated noises using hydrophones (Marineau et al., 2016; Geay et al., 2020), seismic observations (Tsai et al., 2012; Bakker et al., 2020) or apparent bedload velocity measured with acoustic Doppler current profilers (aDcp) (Rennie et al., 2017). Recently, Nasr (2023) used the global calibration curve proposed by Geay et al. (2020) to convert continuous acoustic measurement performed from a bank into time series of bedload fluxes and founds encouraging results.

Despite the advances in acoustic bedload fluxes monitoring, acoustic measurement are currently only performed at a given time and compared to direct bedload measurement (Geay et al., 2020) or at longer time scales but compared with integrative sediment budgets (Nasr, 2023). Analyzing continuous bedload fluxes estimation at flood time scale from acoustic measurements, would give access to the dynamics of sediment transport, but has seldom been investigated. Moreover, comparing such dynamics estimates of bedload fluxes at flood time scale to bedload fluxes estimated with a 2D hydro-sedimentary dynamic model has never been done. This yet enables, as studied here, to (i) compare the temporal variations of simulated and measured bedload fluxes, while (ii) relating these variations to the simulated flow dynamics in space an time.

Therefore, this article proposes an original combination of direct *in situ* bedload measurements, passive and continuous acoustic measurements, and of a fine 2D hydro-sedimentary model, enabling to finely depict and better apprehend the bedload transport dynamics at the flood scale in a gravel-bed river. The study is based on an unprecendently fine and diverse dataset on which is applied an original methodology combining: (i) the calibration of both numerical and acoustic methods using bedload samples and (ii) the comparison of both estimates of time-varying bedload discharges estimated during a moderate flood event.

The remainder of this article is organized as follows: section 2 presents the site and the general context of this study, section 3 details the methods employed to estimate the bedload fluxes using both an acoustic-based approach and an hydraulic-based approach, section 4 compares the cumulative and instantaneous bedload fluxes estimated using both methods and discusses the complementary of these data to gain a better understanding of the bedload transport dynamics in a gravel-bed river.

4.2 Study site

The Moselle river is $560km$ long from its source at the pass of Bussang in the northeast of France to its confluence with the Rhine river at Koblenz in Germany (Figure 4.1 a). The upper part of the Moselle river drains a catchment area of $1,976\,\mathrm{km}^2$ from the western side of the southern Vosges Mountains to the gauging station of Tonnoy on the Lorraine plateau. The geology of the Vosges Mountains consists mainly in crystalline (granites) and metamorphic (gneiss) rocks originating from the Hercynian basement, while the substratum of the Lorraine plateau is composed by a superposition of limestone and marl sedimentary layers (Maire and Corbonnois, 2000). The longitudinal profile of the Moselle river is characterized by a main slope of 10% at the upstream extremity, which decrease rapidly to 0.4% at Remiremont and attain an average value of 1.7‰ further downstream. The predominance of impermeable rocks and steep sectors contributes to propagate rapidly the flows to Epinal, while the physiography of the catchment contributes to the flood peaks concomitance, which generates major hydrological events downstream.

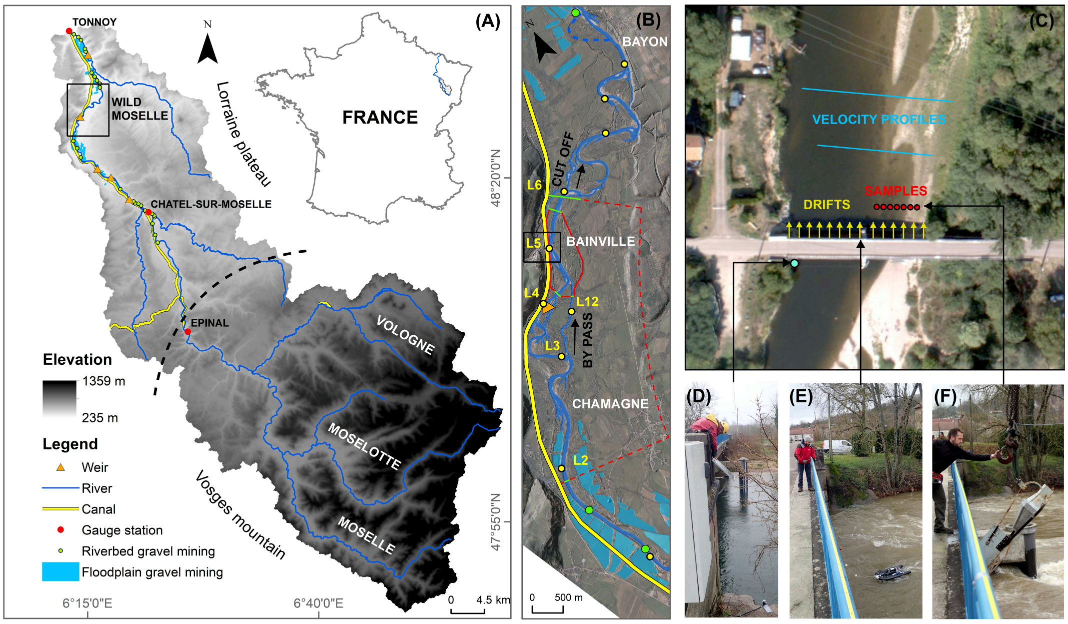

Figure 4.1: (A) location of the "Wild Moselle river" in the Moselle Basin, (B) longitudinal extension of the 2D hydraulic model $\mathcal{M}_{f,h}$ (red dashed line) and the 2D hydro-sedimentary model $\mathcal{M}_{f,s}$ (red solid line) into the natural regional reserve (C) area of bedload fluxes measurement and modelling, velocity and acoustic measurements, (D) hydrophone fixed at the left bank, (E) acoustic mapping, (F) bedload sampling.

The precipitation are unevenly distributed with a mean annual values of $800mm$ over the Lorraine plateau versus $1100mm$ over the Vosges Mountains, where import variations are observed with locally more than $2000mm$ on the crest (Beck and Corbonnois, 2003). Precipitations occurs mainly during the winter (November-February) with monthly more than $200mm$ over the Vosges Mountains. The river hydrological regime is pluvial with high flows in winter-spring (2- and 10-year floods are $405m^3/s$ and $651m^3/s$ respectively) and low flow in summer, while the mean interannual flow is of $42m^3/s$ at the gauging station of Châtel-sur-Moselle.

The sediment supply of the Moselle river arises mainly from the remobilization of Holocene alluvial deposits composed of gravel and sand carried by the river from the Vosges Mountains (Maire and Lasserre, 1991). This sediment redistribution occurs primarily though bed and/or bank erosion, where the lateral mobility is strongly influenced by the valley width that varies according to the nature of the eroded substratum. The river morphodynamic was altered by (i) the construction of a canal which reduced laterally the flood expansion area and concentrates the flow into the river bed, (ii) the construction of dams which locally modify the river competence and interrupt the sediment transport and (iii) the massive sediment extraction which occurred in the river bed ($1950-1980$) and thereafter in the floodplain (Figure 4.1 a). The destabilization of the river morphodynamic equilibrium conducted to morphological adjustments that result into river bed incision which induced locally an emptying of the river bed sediment stock (Beck and Corbonnois, 2003).

The study zone is a $12km$ long meandering reach of the Moselle River located between Gripport and Bayon at the western foothills of the Vosges Mountains and yet was relatively unaffected by human activities (Figure 4.1 a). This section was classified in 2006 as regional natural reserve (the “Wild Moselle”) in order to protect the water resources as well as the biodiversity (Figure 4.1 b). This reach of moderate energy, with an average specific stream power of $50W/m^2$, represents one of the most dynamic section of large rivers in the northeast of France. It is characterized by a catchment area of $1,758\,km^2$, a sinuosity of 1.4, an average slope of 1.2, a bankfull width (resp. discharge) of about $60m$ (resp. $250m^3/s$) and a surface (resp. subsurface) D_{50} of $30mm$ (resp. $13mm$).

Although this sector was protected, the propagation of morphodynamic adjustments (regressive and progressive erosion) initiated by actions carried out at the edge of the natural reserve converges towards the central part of the reach. This trajectory, towards a new dynamic equilibrium, could induce a river avulsion which may destabilize infrastructures. A capture of the river by two floodplain gravel pits is also possible. The present research work is performed in the context of a project of the “Wild Moselle” River reach, lead by the Rhin-Meuse Water Agency and Strasbourg University, in view to protect and/or restore the lateral mobility of the “Wild Moselle” river. In addition to document accurately hydromorphosedimentary processes, the estimation of a bedload transport law is also a crucial issue to constrain morpho-sedimentary models that will be used to investigate management/restoration scenarios.

4.3 Methods

The methodology proposed aims the estimation of bedload fluxes temporal variations at flood scale, by combining an acoustic-based approach and a 2D hydraulic-morphodynamic model-based approach, using a unprecedented dataset. The comparison of bedload fluxes estimated from acoustic and numerical methods is carried out over the river section located at the Bainville-aux-Miroirs bridge (Figure 4.1 b) for a one year return period flood that occurred in early March 2020 (Figure 4.2). This flood lasted around 87 hours and discharges ranged between 75 and $279m^3/s$ according to the Châtel-sur-Moselle gauge station. Many field monitoring (bedload sampling, passive acoustic monitoring and lateral profile of flow velocity) were performed during and before this flood (Figure 4.2) in order to construct and calibrate both acoustic and numerical models. All these steps are presented in the next sections.

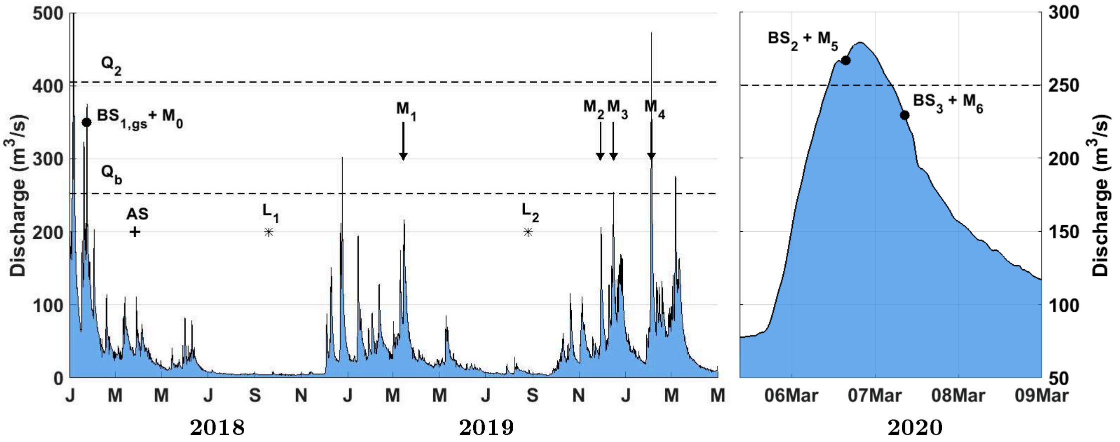

Figure 4.2: Monitoring framework related to the flow hydrograph of the Moselle river at the Châtel-sur-Moselle gauging station with a focus on the studied flood F. BS_n indicates the dates of bedload sampling with gs signifying that bedload samples were sieved, AS indicates the date of the installation of the acoustic monitoring station at the bridge, L_n indicates the dates of the LiDAR topo-bathymetric acquisition, M_n indicates the date of acoustic maps.

4.3.1 Acoustic-based estimation of the bedload transport

The acoustic-based method uses the power of acoustic signal resulting from the bedload Self-Generated Noise (SGN) continuously recorded by two hydrophones fixed at the bridge piers. Bedload flux law is estimated from acoustic power with a power law model calibrated on *in situ* data as proposed by Geay et al. (2020). This power law relates cross-section averaged bedload fluxes to cross-section averaged acoustic powers measured during several field campaigns carried out in various French rivers, and has been recalibrated in this study including the three field campaigns on the Moselle river. The bedload fluxes and acoustic powers were measured from the Bainville-aux-Miroirs bridge for different river discharges, with direct bedload sampling and passive acoustic monitoring, following the method of Geay et al. (2018). The acquisition and integration of these data for the power law calibration are described in the next subsections as well as the use of this law to convert recorded acoustic chronicle into bedload fluxes.

4.3.1.1 Acquisition and integration of bedload monitoring into the acoustic model

Three campaigns of synchronized bedload monitoring with both direct and indirect methods were performed on the Moselle river (Figure 4.2). The first campaign BS_1 occurred on January 23, at $360m^3/s$, during the falling limb of a flood event that peaked at $375m^3/s$. The second BS_2 and third BS_3 campaigns were conducted on March 6 and 7, at $268m^3/s$ and $233m^3/s$ respectively, before and after the peak of a flood that reached $279m^3/s$. Sampled discharge ranges between 65 and 102% of the bankfull discharge estimated at the bridge ($350m^3/s$), as recommended by Bakke et al. (1999) to characterize rivers bedload transport. The measurements were preferentially performed during falling limb of hydrographs in order to reduce probability of collision with log jams carried by the river during the rising limb of floods. The flow velocities and water depths were measured using a Surface Velocity Radar (SVR) and an echo sounder during the first campaign BS_1 and a acoustic Doppler current profiler (ADCP) during the other campaigns BS_2 and BS_3.

Bedload sampling

The bedload sample were collected using a cable suspended Helley-Smith pressure-difference sampler with an intake size of $152-mm$ and a collection bag with a mesh size of $0.5mm$, which enable to avoid sampling particles in suspension (Figure 4.1 f). This portable device of approximately $75kg$ was deployed along the bridge using a mobile crane, but samples were only able to be collected at the right half of the channel bottom, because surface flow velocities ($> 2.5m/s$) and water depths ($> 3.5m$) were too high at the left side. The samples were collected at 7 verticals distributed with an equal-width-increment (Edwards and Glysson, 1999) of $2m$ between the central pier ($x = 24m$) and the right bank ($x = 40m$). The measurements were repeated at least 3 times per vertical profile with sampling durations varying between 30 seconds and 5 minutes, determined in order that the sampled volume does not exceed 40% of the sampler capacity (Edwards and Glysson, 1999). As Helley and Smith (1971) observed that the sampler tends to scoop additional material when it is placed or lifted from the riverbed, a sampling of a few seconds was also carried out to verify and, if so, quantify this amount of sediment.

All samples were dried and weighed on the field to estimate the specific bedload flux q_s ($g.m^{-1}.s^{-1}$) which corresponds to the instantaneous unit bedload rates. The specific bedload flux of a sample i writes as:

$$q_{s,i} = k\frac{M_i}{d_i W_{sampler}} \tag{4.1}$$

where k is the sampler efficiency, $W_{sampler}$ is the sampler intake width (m),M_i and d_i are respectively the mass (g) and duration (s) of the sample i. The specific bedload flux $q_{s,i}$ was averaged at each vertical distributed along the bridge at location x_j

$$q_s\left(x_j\right) = \frac{1}{N}\sum_i q_{s,i} \tag{4.2}$$

where q_s is the average specific bedload flux ($g.m^{-1}.s^{-1}$) computed at location x_j (m) using N the number of samples i collected at this vertical. The average-specific bedload flux was computed by averaging q_s between the central pier and the right bank of the bridge.

$$\overline{q_s} = \frac{\sum q_s(x_j)}{M} \tag{4.3}$$

where M is the number of verticals distributed along the bridge.

As sieving multiple sediment samples at the field is labor-intensive, the grain size distribution (GSD) of bedload samples was only measured during the first campaign BS_1. The samples were sieved using round-holes sieves, ranging from -2ϕ ($4mm$) to -7ϕ ($128mm$) with a standard increment of 0.5ϕ and weighed using an accurate digital scale. The results were compared to GSD of surface and subsurface samples collected after the flood of 10-year return period (Figure 4.2), on the closest emerged bar located upstream of the bridge, according to the method presented in the appendix A. The size of the largest particle collected is compared to the maximum size able to be transported in order to asses the sampler efficiency (equation 4.1), which may decrease as grain size and bedload rates increase (Vericat et al., 2006). Water samples were also collected during the first campaign BS_1 to quantify the suspended load and determine its composition in laboratory using laser diffraction spectroscopy.

Passive acoustic monitoring

The bedload Self-Generated Noises (SGN) was recorded using a HTI-96 hydrophone installed under a river board at $0.4m$ depth and plugged into a Song Meter SM3BAT distributed by Wildlife acoustics (Figure 4.1 E). The hydrophone was deployed from the bridge by an operator and left drifting at flow velocity in order to reduce hydraulic-induced noise and therefore optimize the signal to noise ratio of bedload. The acoustic measurements were performed along the bridge at $2m$ interval and repeated at least 3 times during the bedload sampling, starting at $x = 6m$ because of the presence of a recirculation area at the left bank. The drifts duration varied between 10 and 20 seconds, which corresponds to acoustic longitudinal profiles of approximately 40 to $50m$, according to the local flow velocity. The total duration of each acoustic maps therefore varies between 1h and 1h30, which is shorter than the bedload sampling duration and thus enables to perform several acoustic measurements during each campaign.

The raw acoustic signals were stored in wav files with a sampling frequency of $192kHz$ and converted into pressure fluctuation (µPa) according to the parameters of the measurement chain (device sensibility of $-190.2V/\mu Pa$ and gain factor of 1) as described by Geay (2013). For each acoustic signal, a short-term Fourier transform algorithm is first applied. Then, a spectral probability density (SPD), which is the empirical probability density of the PSD, was computed using the Merchant et al. (2013) algorithm. This algorithm allows to detect persistent tonal components and insufficient dynamic, which may be undetected by conventional techniques. Next, the median Power Spectral Density (PSD) of each acoustic signal was computed using windows of approximately 20 milliseconds with a recovery rate of 50%. As proposed by Geay et al. (2017), the median PSD was preferred to the mean PSD (Welch, 1967) since it allows to filter outlier acoustic signals resulting for example from the collision of the hydrophone with the riverbed.

The power P (μPa^2) of acoustic signal recorded during each drift i was computed by integrating the median PSD ($\mu Pa^2 Hz^{-1}$) of the sampled acoustic signal over a range of frequencies comprised between $f_1 = 2kHz$ and $f_2 = 50kHz$. The power of each drift signal i is obtained by integrating the median PSD over the range of frequencies:

$$P_i = \int_{f1}^{f2} PSD_i(f)df \tag{4.4}$$

This range of frequencies was determined according to a quantitative analyses of PSD indicating that below $2kHz$ the acoustic measurements could be affected by hydraulic noises, while the signal is fully dominated by bedload noise up to $50kHz$. The acoustic power P_i computed at cross-sectional location x_j was averaged, as for the bedload fluxes, such that:

$$P_i(x_j) = \frac{1}{N} \sum_i P_i \tag{4.5}$$

where N is the number of drifts carried out at each location x_j.

The average-specific acoustic power was computed by averaging P_i estimated at bedload sampling locations in order to be compared to the average-specific bedload flux.

$$\overline{P} = \frac{\sum_j P(x_j)}{M} \tag{4.6}$$

where M is the number of drifts location distributed between the central pier and the right bank of the bridge.

The cross-sectional profiles of bedload flux and acoustic power were compared, but the relation between paired direct and indirect measurements carried out at the same locations was not investigated. Indeed, bedload sampling are local while passive acoustic measurements are integrative and provide information on bedload flux over a large and unknown area of the riverbed (Geay, 2013). To overcome this difference in measurement spatial representativity, as proposed by Geay et al. (2018) the cross-section averaged bedload fluxes $\overline{q_s}$ ($g.m^{-1}.s^{-1}$) were related to the cross-section averaged acoustic power $\overline{P}$ (μPa^2). The cross-section averaged values of acoustic power and bedload flux estimated from the first field campaign (BS_1) carried out on the Moselle river was added to the 24 value obtained by Geay et al. (2020). Thus value were estimated applying the same experimental protocol using different types of bedload samplers on 14 rivers located in France with various hydraulic conditions (flow discharge and water depth), bedload (rate and grain size distribution) and slopes. By plotting the cross-section averaged values of acoustic power against bedload flux and fitting a power law, the authors found the following relationship were 60 of bedload flux was estimated within a factor of 2.

$$\overline{P} = a\overline{q_s}^b \tag{4.7}$$

with $a = 9.08 \times 10^{10}$ and $b = 1.28$.

As part of the present study, the cross-section averaged values of acoustic power and bedload flux estimated from the second (BS_2) and third (BS_3) sampling campaigns are added to this dataset of Geay et al. (2020) and the coefficient and exponent of equation 4.7 have been readjusted considering those additional measurements. The position of our 3 values is compared to the readjusted global calibration curve of Geay et al. (2020) in order to asses the ability of this relationship to estimate bedload fluxes on the Moselle river with an hydrophone.

4.3.1.2 Calibration and conversion of continuous acoustic monitoring in bedload fluxes

A continuous monitoring of bedload Self-Generated Noise (SGN) was performed between march 2018 and august 2020 using two HTI-96 hydrophones deployed in fixed position at the bridge (Figure 4.1 d). The first was installed between sheet piles of the left abutment, while the second was installed behind a flow deflector specially added on the central round pier in order to protect the sensor from collision with flowing objects. The hydrophones protrudes from rigid plastique tubes vertically positioned about $0.2m$ above the riverbed which protect cables up to a Song Meter SM3BAT (Wildlife acoustic) located at left bank. This device is powered by a solar panel and records sounds during 30 seconds every 10 minutes with a sampling frequency of $19.2kHz$ and stores raw acoustic signal in wav files on SD memory cards. As for drifting measurements, the acoustic power (μPa^2) was computed by integrating the median PSD of each records (equation 4.4), but over a narrower range of frequency $2 - 19.2kHz$ due to an error in parametrization of sampling frequency when the station was installed. Unfortunately, for discharges exceeding approximately $200m^3/s$ the flow deflector installed at the bridge vibrates strongly against the central pier which makes records from the second hydrophone unusable.

The acoustic power monitored by the hydrophone located at the left abutment is the integral of the power generated by bedload transport over the river bed and propagated from their points of emission (Geay et al., 2020):

$$P_{fixed}(X_h) = \int P_{SGN}(X_S) \bigotimes G(X_h, X_s) dX_s \tag{4.8}$$

where $\bigotimes$ is the convolution operator, $P_{fix}(\mu Pa^2)$ is the acoustic power monitored by the hydrophone fixed at position X_h and G is the Green function of the environment propagating the acoustic waves generated at position X_s to X_h. The listing distance of bedload impacts toward this hydrophone is however unknown (e.g $5 - 10m$ in Geay et al. (2017)) because propagation laws vary in function of rivers (Geay et al., 2019) or of water depth (Rigby et al., 2016). To assess the spatio-temporal representativity of sounds recorded by this hydrophone in relation to bedload sounds generated across the section, the acoustic power measured at the bank was compared to the cross-sectional average acoustic power. The sound was spatially mapped across the river section with passive acoustic profiles (Geay et al., 2020) carried out at the same spatial resolution and using the same material than for bedload flux quantification (see 4.3.1.1). These acoustic maps M_n were performed at 6 different discharges given that propagation effects may vary with water depths and that bedload transport may vary in space and time depending on flow distribution or morphological evolutions. The passive acoustic monitoring was performed between March 2019 and February 2020 (Figure 4.2) at discharges ranging between 158 and $350m^3/s$, in rising and falling phases as well as at flood peak (Table 4.1). The 2 acoustic maps M_5 and M_6 carried out during the bedload sampling of March 2020 were added to this dataset, but results from the campaign M_0 of January 2019 could not be used since hydrophones were not yet installed at the bridge. The acoustic power was computed for each longitudinal profile (equation 4.4), values were averaged at each measurements location (equation 4.5) and missing cross-sectional values were linearly interpolated at $1m$ interval. The cross-sectional averaged power ($\overline{P_{XS}}$) was computed for each acoustic map (equation 4.6) and plotted against the averaged acoustic power ($\overline{P_F}$) recorded during this monitoring by the hydrophone installed at the bridge.

$$\overline{P_F} = \frac{\sum P_{hydrophone}(t_i)}{N} \tag{4.9}$$

where $P_{hydrophone}$ is the acoustic power (μPa^2) recorded at the time t by the hydrophone fixed at the bridge and N is the number of records i performed during the acquisition of acoustic maps. The number of records used to compute the averaged acoustic power measured from the bank varies from 6 to 9 files according to the duration of each acoustic profiles. A rating curve was established between acoustic power measured from the bank ($\overline{P_F}$) and from acoustic map ($\overline{P_{XS}}$) by fitting a power law to this 6 field monitoring. This rating curve writes:

$$\overline{P_F}\,(Q) = \alpha \overline{P_{XS}}^{\beta}\,(Q) \tag{4.10}$$

The value of the coefficient of correlation (R^2 Pearson of the adjustment of polynomial 10 on data) as well as the dispersion of values around this curve allows to assess if the representativity of the bank measurements in relation to acoustic maps varies with discharge or morphological evolution. This rating curve is used to extrapolate the acoustic power continuously measured by the hydrophone installed at the bridge though the entire cross-section. The time series of cross-sectional average acoustic power are converted into bedload flux using equation 4.7 and applied to the active channel which width of $40m$ corresponds to the distance between the left abutment and the right pier of the bridge. The continuous bedload fluxes estimated across the river section are compared to the time series of flow discharges and bedload fluxes estimated using a 2D hydro-sedimentary model.

Monitoring	Date	Duration	Discharge (m^3/s)	Hydrograph phase
M_1	15/03/2019 13:45	1h45	167	Rising limb
M_2	29/11/2019 15:15	1h	158	Rising limb
M_3	16/12/2019 15:00	2h	235	Peak
M_4	04/02/2020 16:30	1h30	350	Falling limb
M_5	06/03/2020 15:00	2h	268	Plateau
M_6	07/03/2020 8:00	1h30	233	Falling limb

Table 4.1: Summarize of hydrodynamic conditions during acoustic maps

4.3.2 Hydraulic model-based estimation of the bedload transport

The bedload transport is estimated using a 2D hydraulic model Telemac-2D, internally coupled to a sediment transport and bed evolution module Sisyphe of the TELEMAC-MASCARET modeling system. An hydraulic model $\mathcal{M}$ was previously built along the "Wild Moselle" river (Piasny et al., 2023b) based on an accurate DEM and calibrated using water surface elevation records and velocity measurements. This model allowed to estimate the critical bed shear stress for particle motion based on the river flow competence which was determined using painted bed patches and pit-tags. As part of this study, the bedload fluxes are computed using several bedload laws, based on the bed shear stress simulated at the bedload sampling location and the critical bed shear stress for particle motion determined in Piasny et al. (2023b). The predicted bedload fluxes are compared to the *in situ* measurements performed from the bridge, in order to select and calibrate the sediment transport laws used to compute the bedload fluxes during the studied flood F. This computation is simply done with successive short steady state simulations performed using the hydro-sedimentary model $\mathcal{M}_{f,s}$ run with a unique grain size and varying hydrodynamic conditions. This is some how a simple prediction of sediment transport capacity, as classically done in space and time, based via the functionality of the 2D model. The advantage of this short time simulation is to avoid unrealistic morphological evolution derived from simplification of riverbed grain size distribution or unknown inflow sediment discharge which may modify the hydrodynamic condition or the sediment supply at the bridge.

4.3.2.1 Numerical model description

The TELEMAC-MASCARET modeling system is an open-source well-tested and widely-used package employed in many fields of application which was developed by the French Electricity Board (EDF). All modules of this suites of solvers are based on unstructured mesh and finite-element or finite volume algorithms that allow to run parallel computations (Hervouet, 2007). The components of the hydrodynamic (shallow water equations) and sediment transport (bed shear stress partitioning and bedload transport formulas) module used is this study are described below. The module of bed evolution (Exner equation) and other additional sediment transport processes (secondary current, slope effect...) are excluded from this description since only the sediment transport capacity at the scale of the cross-section is of interest.

Hydrodynamic model

Telemac-2D model solves the shallow water equations (SWE) in their conservative forms (momentum and continuity) which are derived from the full 3D Navier-Stokes equations (Villaret et al., 2013; Ancey, 2016; Dingman, 1984). These equations were simplified in the vertical direction assuming hydrostatic pressure distribution and negligible vertical acceleration wherein turbulence effects are taken into account using a constant viscosity model.

The first term on the right hand side of the two equations of momentum is the pressure gradient, the second is the bottom friction and the third is the horizontal diffusion.

$$\frac{\partial H}{\partial t} + \frac{\partial (UH)}{\partial x} + \frac{\partial (VH)}{\partial y} = 0 \tag{4.11}$$

$$\frac{\partial U}{\partial t} + U\frac{\partial U}{\partial x} + V\frac{\partial U}{\partial y} = -g\frac{\partial Z_s}{\partial x} + \frac{\tau_x}{h} + \frac{1}{h}div(h\nu.grad(U)) \tag{4.12}$$

$$\frac{\partial V}{\partial t} + U\frac{\partial V}{\partial x} + V\frac{\partial V}{\partial y} = -g\frac{\partial Z_s}{\partial y} + \frac{\tau_y}{h} + \frac{1}{h}div(h\nu.grad(V)) \tag{4.13}$$

where h is the water depth (m), U and V are horizontal mean velocity components (m/s), g is the gravity acceleration (m/s^2), Z_s is the free surface elevation (m), t is the time (s), x and y are horizontal space coordinates (m), ν is the depth-averaged eddy viscosity (m^2/s) and τ_x (resp. τ_y) is the bed shear stress (N/m^2) along the Cartesian x-axis (resp. y-axis) as

$$\tau_b = \sqrt{\tau_x^2 + \tau_y^2} = \sqrt{\left(\frac{1}{2}\rho C_f U^2\right) + \left(\frac{1}{2}\rho C_f V^2\right)} \tag{4.14}$$

where ρ is the water density (kg/m^3) and C_f is a dimensionless quadratic friction coefficient calculated as

$$C_f = \frac{2g}{K_s^2 h^{1/3}} \tag{4.15}$$

where $K_s\,(x,y)$ is the Strickler coefficient ($m^{1/3}/s$) that generally needs to be calibrated to fit flow observations. This hydraulic friction coefficient is considered spatialized which is affordable with our dense dataset, in order to finely compensate data-model errors.

Sediment transport model

Sisyphe model corrects the total bed shear stress τ_b (N/m^2) issued from the hydrodynamic model (equation 4.14) using a factor μ to express the grain shear stress τ' (N/m^2) which is the only component acting on the bedload transport (Mendoza et al., 2017).

$$\tau' = \mu \tau_b \tag{4.16}$$

where the correction factor $\mu = C'_f/C_f$ corresponds to the ratio between friction coefficient C_f issued by hydrodynamic model, and friction coefficient C'_f only due to the skin friction given by:

$$C'_f = 2\left(\frac{\kappa}{log(12h/h'_s)}\right)^2 \tag{4.17}$$

where κ is the von Karman coefficient, h the water level (m) and h'_s the roughness height (m) defined as

$$h'_s = \alpha_{h'_s} d_{50} \tag{4.18}$$

where $\alpha_{h'_s}$ is a calibration parameter (3 by default; Tassi and Villaret (2014)) and d_{50} (m) is the sediment mean diameter.

The bedload transport formulas are computed as function of the Shields parameter θ which is the dimensionless shear stress given by

$$\theta = \frac{\tau'}{(\rho_s - \rho)gd} \tag{4.19}$$

where τ' is the grain shear stress (N/m^2), g is the gravitational acceleration (m/s^2), d is the grain size diameter (m) and ρ andρ_s (2650 kg/m^3 by default) which are respectively the fluid and sediment densities (kg/m^3). The dimensionless current-induced bedload transport rate Φ_b can be computed using several bedload transport formulas available in Sisyphe model such as the most widely used Meyer-Peter and Müller (MPM) equation (1948). This formula was developed from flume experiments performed using uniform sediments, under plane bed conditions and validated for grain size of $0.4 < d_{50} < 29mm$ and slope of $0.4 < S < 2.4‰$. It is a simple excess shear stress relationship where no sediment transport is predicted under a given threshold value

$$\Phi_{b,MPM} = \alpha_{MPM}(\theta - \theta_{cr})^{3/2} \tag{4.20}$$

where θ is the Shields parameter, θ_{cr} is the critical Shields parameter for sediment motion and α_{MPM} is an empirical coefficient. MPM found values of $\theta_{cr} = 0.047$ and $\alpha_{MPM} = 8$, but Wong and Parker (2006, noted WP) reanalyzed their data set and proposed values of 0.0495 and 3.97 respectively, arguing that bedload transport was over-predicted due to an unnecessary bed roughness correction. Adding this data set to other flume experiments and field measurements, Camenen and Larson (2005, noted CL) shows that MPM formula also slightly overestimates Φ_b when $\theta < \theta_{cr} < 5\theta_{cr}$ and that low sediment transport is often observed even when $\theta \lesssim \theta_{cr}$. To avoid such errors, CL introduced a continuous function without threshold for inception of bedload transport following the probabilistic approach suggested by Einstein (1950, noted E-B), which allows low sediment transport when $\theta \approx \theta_{cr}$. This formula was developed for coastal transport, with grain sizes of $0.1 < d_{50} < 200mm$, but was also validated for steady, uni-directional flows. Its simplest form using an exponential relationship for the effect of θ_{cr} is given by

$$\Phi_{b,CL} = 12\theta^{3/2} exp\left(-4.5\frac{\theta_{cr}}{\theta}\right) \tag{4.21}$$

where θ is the Shields parameter, θ_{cr} is the critical Shields parameter for sediment motion. As sediment transport in natural river generally occurs close to θ_{cr} and that this value is marked by uncertainties, the CL formula was implemented into Sisyphe and tested during this study. The volumetric bed load sediment transport rate per unit time and width q_s (m^2/s) is computed as

$$q_{s,\square} = \Phi_{b,\square}\sqrt{(s-1)gd_{50}^3} \tag{4.22}$$

where s is the relative density ρ_s/ρ, g is the gravitational acceleration (m/s^2), d_{50} is the median grain size (m) and Φ_b dimensionless bedload transport rate and $\square$ correspond to MPM or CL formulas.

4.3.2.2 Model construction and calibration

A 2D hydraulic model $\mathcal{M}$ was previously built along the entire “Wild Moselle” river (Piasny et al., 2023b) based on an accurate DEM and calibrated using a large data set of field measurements. From this 2D hydraulic model of the whole zone, we built two submodels: an hydraulic model ($\mathcal{M}_{f,h}$) of the large domain and an hydro-sedimentary ($\mathcal{M}_{f,s}$) on the bridge measurement area.

The studied flood F was simulated using the existing model $\mathcal{M}$ but resulting water surface elevations (WSE) were significantly higher than observed ones at the upstream of the meander cutoff and at the Bainville-aux-miroirs bridge (Figure 4.1 b). This difference is due to the deepening ($> 1m$) and enlargement ($\sim 20m$) of the meander cutoff that occurred between the DEM acquisition and the studied flood F (Figure 4.2) which was not considered into the model $\mathcal{M}$. In order to avoid this downstream bias, a new 2D hydraulic model $\mathcal{M}_{f,h}$ was built along the Moselle river up to the meander cutoff and WSE recorded by a limnimeter located there were used as downstream boundary condition. The results of this hydraulic model $\mathcal{M}_{f,h}$ were used as boundary condition for the hydro-sedimentary model $\mathcal{M}_{f,s}$ which was spatially reduced to exclude from computational domain the Bainville-aux-miroirs dam where simulation of bedload transport is complex. The hydraulic component of this submodel $\mathcal{M}_{f,s}$ was calibrated using WSE records and velocity measurements carried out during the studied flood F, while the sedimentary component was calibrated using *in situ* bedload measurements. The construction and calibration of both large hydraulic model $\mathcal{M}_{f,h}$ and reduced hydro-sedimentary model $\mathcal{M}_{f,s}$ are described below.

Hydraulic model of the large domain

The computational domain of the hydraulic model $\mathcal{M}_{f,h}$ extends over a 6 km-long section of the Moselle river located between Gripport and Bainville-aux-miroirs (Figure 4.1 b). The domain starts far upstream from the bridge in order to set the boundary condition into a channelized reach located at the beginning of the natural reserve where the river did not overflow. The downstream limit of the domain was set right at the diffluence between the historical channel and the meander cutoff in order to be as close as possible of the limnimeter used as boundary condition. The lateral border of the domain was set over a canal dike at the left side and over a road embankment at the right side since both civil engineering structures were not submerged for a 10-years flood. This domain was discretized into a computational grid composed of 438692 triangular elements and 220296 nodes generated using Bluekenue software. This grid is composed of structured submeshes into the riverbed and unstructured mesh into the floodplain with mesh sizes of 3.5 and $5m$ respectively. The size of the mesh was locally refined at diffluences and confluences or in narrow river sections such as in the dam bypass channel ($2.7m$) or in the diversion canal of the dam ($2m$). The mesh nodes elevations were interpolated from an accurate DEM of $1m$ resolution generated from an airborne LiDAR topo-bathymetric acquisition performed at low flow during the summer 2019. This aerial acquisition was completed by a bathymetric campaign carried out over uncovered areas ($depth > 2.4m$) as for example at the upstream and under to the bridge of Bainville, more details are presented in Appendix B.

The large hydraulic model $\mathcal{M}_{f,h}$ has 3 boundary conditions distributed along the Moselle river: one upstream at Gripport, one lateral at the diversion canal of the dam and one downstream at the bridge of Bainville.

- At the upstream boundary condition, we imposed an hydrograph derived from WSE recorded by the limnimeter L2 which were converted into discharges using a stage-discharge relation. This relationship was built from results of successive steady state simulations performed between 40 and 500 m^3/s at 10 m^3/s interval using the 2D hydraulic model $\mathcal{M}$ calibrated over the entire reserve. This hydrograph was smoothed using wavelets (Matlab) and compared for validation to hourly discharges recorded by the gauge station of Châtel-sur-Moselle located $12km$ upstream of the limnimeter. As expected, estimated discharges are slightly higher than observed ones ($\approx 5m^3/s$ overstimation at the peak) which is in agreement with the results obtained in Piasny et al. (2023b).

- At the lateral boundary condition, we imposed a constant output discharge of $3.2m^3/s$ which corresponds to the diversion canal discharge measured using an ADCP ($5m^3/s$) minus the estimated lateral inflows from the "Wild Moselle" tributaries ($1.8m^3/s$).

- At the downstream boundary condition, we imposed the WSE recorded by the limnimeter L6 adding a constant value of $5cm$ in order to take into account the difference of altitude reference between the location of the boundary condition and the limnimeter. This difference was estimated by comparing WSE recorded by the limnimeter and WSE simulated at the boundary condition of $\mathcal{M}_{f,h}$ using the hydraulic model $\mathcal{M}$ previously built along the entire "Wild Moselle" river.

The friction coefficients calibrated independently of the mesh size, for model $\mathcal{M}$, were mapped onto the submodel $\mathcal{M}_{f,h}$ domain with for different friction zones: $K_s := 47\ m^{1/3}/s$ in the main channel riverbed, $K_s := 33\ m^{1/3}/s$ at the upstream part of bypass channel, $K_s := 8\ m^{1/3}/s$ at the downstream face of the dam and $K_s := 8\ m^{1/3}/s$ in the floodplain. The validity of those Strickler coefficient values (calibrated in Piasny et al. (2023b) on the flood event of 2018) in $\mathcal{M}_{f,h}$, was verified by comparing simulations results to the WSE recorded during the studied flood F by the limnimeter L3, L4, L5 and L12 (Figure 4.1 b). This hydraulic simulations were performed using the finite-element numerical solver of Telemac-2D (version 8.1) run on 42 parallel processors with a constant time-step of 0.5 which enables to respect a CFL value of 1 on the studied cases.

Hydro-sedimentary model on the bridge measurement area

The longitudinal extension of the hydro-sedimentary model $\mathcal{M}_{f,s}$ was reduced to a $1.5km$ long reach centered around the bridge in order to exclude the dam from the computational domain (Figure 4.1 b). The abutments and piers located at the left (2 round piers of $0.9m$ diameter) and at the right side (1 oblong pier of $1m$ large) of the bridge were excluded from the meshed domain to take into account their influences in flow distribution/acceleration. The computational grid composed of 188835 triangular elements and 95001 nodes was refined at pier walls ($\approx 10cm$) which allows a mesh size of approximately $1m$ at location of bedload measurements. The hydraulic boundary conditions implemented into the hydro-sedimentary model $\mathcal{M}_{f,s}$ were extracted at 5 minutes interval time step, from outputs of the hydraulic simulation performed using the large model $\mathcal{M}_{f,h}$. At the two upstream boundary conditions we imposed flow hydrographs computed using control sections, while at the downstream boundary condition we imposed a stage hydrograph extracted at a point located in the middle of the river. The influence of this downstream boundary condition on WSE simulated at the bridge was assessed by modifying the stage hydrograph by $\pm 50cm$. The friction coefficients from the large hydraulic model $\mathcal{M}_{f,h}$ ($47m^{1/3}/s$ in the riverbed and $8m^{1/3}/s$ in the floodplain) were applied into the hydro-sedimentary model $\mathcal{M}_{f,s}$ and the calibration of this submodel was verified at the bridge by comparing simulated and observed WSE. The value of the Strickler coefficient was laterally adjusted under the bridge in order to calibrate the distribution of flows between the bridge piers (Figure 4.1). This calibration was carried out by comparing, at steady state, simulated and observed velocity profiles measured during both bedload sampling campaigns BS_2 and BS_3 (Figure 4.2). These velocity profiles were measured using an Acoustic doppler Current Profiler (ADCP) deployed from the bridge along transects located further downstream avoiding turbulence induced by piers. In order to be able to compare these field measurements to simulated depth-average flow velocity, the data had to be post-processed (beam filtering, projection of velocity vectors, vertical velocity profile extrapolation...), all these steps are described in Appendix C. A sensitivity analysis was carried out in order to ensure that flow distribution between bridge piers is mesh independent.

The results of this calibration were used to run at steady state the hydro-sedimentary model $\mathcal{M}_{f,s}$ without bedload transport in order to compute during both sampling campaign (i) τ_b the total bed shear stress and (ii) μ the ratio of the skin friction to the total friction. As part of these simulations, the roughness height (equation 4.18) involved into the computation of the skin friction was computed using the median diameter of the bed surface ($D_{50} = 30mm$) estimated along the "Wild Moselle" reach. The calibration parameter $\alpha hs'$ which determines the ratio between the skin friction and the median diameter was set to 3 (default value) considering flat bed conditions during the studied flood (Villaret et al., 2013). The value of the total bed shear stress τ_b and the correction factor μ were extracted from simulation results at each verticals where bedload samples were collected during each campaign (Figure 4.1). This values were used to calculate the grain shear stress τ' (equation 4.16) which is the only component of the total bed shear stress acting on the bedload transport. The results were adimentionalized according to the D_{50} of the bed surface in order to expressed the Shields parameter θ (equation 4.19) used to compute the dimensionless bedload transport rate Φ_b in the sediment transport laws. The averaged specific bedload flux q_s (in $m^3.s^{-1}.m^{-1}$) computed at each verticals (equation 4.2) were plotted against values of θ in order to assess the relationship between simulated shear stresses and observed sediment transport.

The bedload transport rates $q_{s,\square}$ (equation 4.22) predicted from the laws available in Sisyphe and applicable to our study site were added to the plot in order to identify which laws are most suitable to our results. These laws (Meyer-Peter and Muller, Camenen and Larson and Einstein-Brown) were selected according to their field of validity which should correspond to the physical properties (median grain size and slope) of the Moselle river. Two different values of critical Shields parameter, $\theta_{cr} = 0.047$ as proposed by MPM (1948) and $\theta_{cr} = 0.035$ as found by Piasny et al. (2023b) for the Moselle river, were used in both MPM (equation 4.20) and CL (equation 4.21) laws in order to study the influence of this parameter. The coefficient α_{MPM} used in the MPM laws (equation 4.20) was calibrated by comparing simulated $Q_{s,mod}$ and observed $Q_{s,obs}$ bedload discharge computed (equation 4.23) between the central pier ($27m$) and the right pier of the bridge ($39m$).

$$Q_{s,\square} = \int q_{s,\square}(x)d(x) \tag{4.23}$$

where q_s is the bedload transport rate at each vertical and $\square$ stands for simulated or observed data. The sum of absolute differences between $Q_{s,mod}$ and $Q_{s,obs}$ was computed for different value of α_{MPM} and the best coefficient for the MPM law (equation 4.20) was determined according to the lowest result. This value was compared to other empirical values proposed by MPM (1948) $\alpha_{MPM} = 8$ or by Wong and Parker (2006) $\alpha_{MPM} = 3.97$ in order to discuss about the validity of our result. The cross-sectional profiles of bedload transport rates computed using the different calibrated laws were superimposed to bedload transport rates measured during each sampling campaign in order to compare results between laws and determine which laws are the most adapted to our study site.

The selected laws were implemented into the hydro-sedimentary model $\mathcal{M}_{f,s}$ to predict the bedload fluxes during the studied flood and the obtained results were compared to the values estimated using the hydrophone. The bedload discharge was predicted by running successive short steady state simulations based on (i) a unique riverbed morphology measured before the flood, (ii) a unique grain size ($D = 30mm$) considered as representative of the bed surface and (iii) varying hydrodynamic conditions extracted from results of the calibrated hydraulic model $\mathcal{M}_{f,h}$.

The short duration of each independent simulations avoided the development of unrealistic morphological evolutions, which may change the hydrodynamic conditions previously calibrated and therefore modify the predicted bedload discharges. These unrealistic morphological evolutions may stem from simplifications of the hydrodynamics (neglected vertical processes at the bridge piers) and sedimentary (horizontal and vertical uniform grain size) components on which relies the 2D hydro-sedimentary model. These successive short steady state simulations were performed (i) at 10 minutes interval in order to match the measurement frequency of the hydrophone and (ii) during 3 seconds in order to reach the equilibrium between hydrodynamic conditions and bedload transport.

These hydrodynamic conditions which vary during the flood were implemented into the hydro-sedimentary model using a different hot-start file per steady state simulation. These 401 hot-start were automatically built using Telemac Tools developed in Matlab to extract from previous hydraulic results the hydrodynamic conditions applied in each simulation. These simulations were run using the hydro-sedimentary model $\mathcal{M}_{f,s}$ parameterized in order to computed the main sediment transport processes (transport mechanisms) without adding other uncalibrated processes (secondary currents, slope effect, sediment slide...). The bedload discharge across the river section was computed into Sisyphe during each simulation using a control section located $8m$ downstream of the bridge. The time series of predicted and observed bedload discharge were compared as well as the total mass carried during the flood.

4.4 Results and discussion

This section presents the results of (i) the large dataset obtained from the numerous field measurements performed during this study, (ii) the calibration of the acoustic and numerical models for bedload transport estimation, performed using this dataset and (iii) the time-varying bedload discharges estimated during the studied flood F using both of these models. All these results are finely analyzed in the light of direct measurements of bedload transport available and compared between each other in order to discuss about the advantages, disadvantages and complementary of each of these indirect methods to estimate the sediment discharge on the Moselle river. This section first presents the calibration of the acoustic model, next the calibration of the numerical 2D hydraulic $\mathcal{M}_{f,h}$ and hydro-sedimentary model $\mathcal{M}_{f,s}$ and then the comparison of bedload transport estimated using both acoustic and numerical approach.

4.4.1 Acoustic model calibration

In this part, we compare the largest particles sampled during measurements to the maximum particle size that can be transported by the river in order to assess the efficiency of the sampler used to measure the bedload flux. Then, we compare cross-section averaged acoustic powers measured in function of specific bedload fluxes to the global calibration curve of Geay et al. (2020) in order to assess the suitability of this curve to predict the bedload fluxes on the Moselle river. Finally, we compare the acoustic powers measured from the bank to the acoustic powers measured from acoustic maps in order to assess the suitability of bank measurement to predict the acoustic power over the entire cross-section. According to both results, the continuous monitoring of acoustic power recorded by the hydrophone fixed at the bridge would be extrapolated to the entire cross-section and converted into bedload fluxes.

4.4.1.1 Relationship between acoustic power and bedload fluxes

The results of the sieving of the bedload samples collected between the central ($23m$) and the right piers ($42m$) of the bridge during the first campaign BS_1 are presented in figure 4.3. The cross-sectional profile of the median diameter (D_{50}) of the bedload samples (Figure 4.3 a) shows that the bedload median grain-size increases from the bridge piers ($D_{50} \simeq 10mm$) to the middle of the section ($D_{50} \simeq 30mm$). This cross-sectional grain-sizes sorting is coherent with the lateral distribution of flow velocities (1.5 to $2.5m/s$) measured downstream of the bridge during the second (BS_2) and third (BS_3) campaigns (Figure 4.7). The higher variability of bedload median grain-sizes (10 to $37mm$) measured between samples collected close to the left pier (27 and $29m$) may be due to the flow perturbation induced by this pier which is located in the middle of the riverbed.

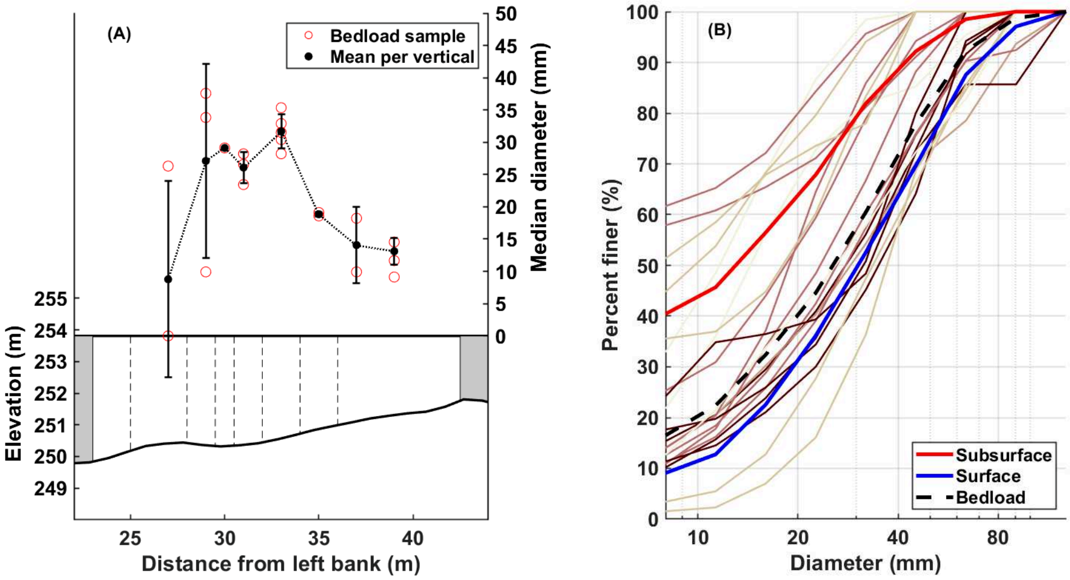

Figure 4.3: Results of the sieving of the bedload samples collected during the first campaign (BS_1) represented as (A) Cross-sectional profile of the bedload samples D_{50} and the mean D_{50} per verticals, along with its standard deviation (B) Cumulative grain size distribution of each bedload sample (solid brown line, which becomes darker as sample is collected close to the center of the section located at $33m$). The GSD of all bedload samples combined (dashed black line) is compared to the GSD of the bed surface (solid blue line) and bed subsurface (solid red line).

The cumulative grain size distribution (GSD) of bedload samples (Figure 4.3 b) is in average much closer to the surface material than to the subsurface material of the river. The gravels may be dominant in bedload GSD due to the suspension of sand (Torok et al., 2019), but measurements in water samples show that the suspended load is insignificant ($0.07g/L$) with a low fraction of sand (22%). The good correspondence between the D_{50} of the bedload samples collected, where flow velocities are the highest and the D_{50} of the bed surface tends to indicate the presence of an armored layer during measurement. Indeed, when the armored layer is disrupted, finer particles that are largely present in the subsurface material are released, thus the D_{90} of the bedload samples is often closer to the D_{50} of the subsurface riverbed (Petit et al., 2015).

This assumption is reinforced by the fact that the D_{90} of these bedload samples ($\simeq 60mm$) is slightly lower than the D_{90} of the bed surface ($\simeq 70mm$), which indicates that coarse sediments of the armored layer are effectively only partially transported by the river. The propensity for these coarse sediments to be sampled however decreases as the ratio between the particle size and the sampler intake increases (Vericat et al., 2006), which means that the estimation of the flow competence as well as the bedload fluxes may be affected. The efficiency of the sampler is difficult to assess, but as three bedload samples collected particles that are as coarse than the D_{max} of the bed surface, we assumed that the sampler efficiency approximated 100% for the three campaigns performed on the Moselle river.

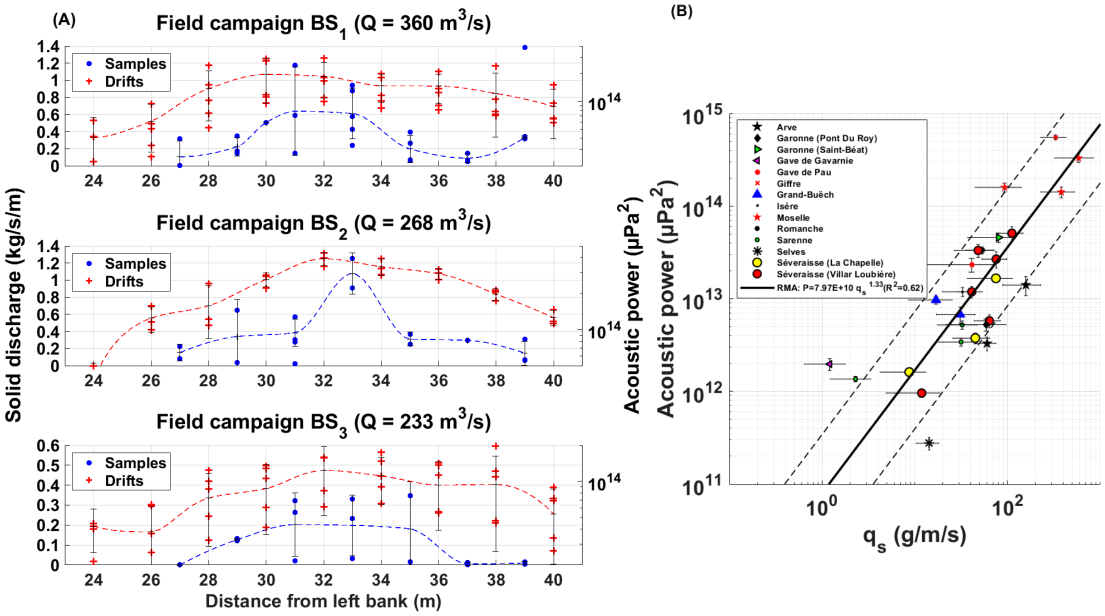

Figure 4.4: (A) Cross-sectional profiles of bedload flux (samples) and acoustic power (drifts) monitored at each field campaign. (B) Relationship between cross-sectional averaged values of acoustic power and specific bedload flux integrated into the model proposed by Geay et al. (2020)

The results of the direct bedload measurements performed between the central ($23m$) and the right pier ($42m$) of the bridge during the three campaigns BS_1, BS_2 and BS_3, expressed in specific bedload flux (equation 4.1) using a sampler efficiency of 1, are presented in figure 4.4 a. The total number of samples collected during each campaign varies according to the measurement duration: first campaign BS_1, 22 samples (4 hours); second campaign BS_2, 17 samples (2 hours); and third campaign BS_3, 19 samples (3 hours). The specific bedload flux ranges between 0 and $1.382kg/s/m$; a higher value of $6.352kg/s/m$ was also found at $33m$ during the last measurement of the second campaign BS_2, but this result was considered as unrealistic and was therefore excluded from the dataset. The value progressively increases from the bridge piers to the middle of the section, except (i) during the first campaign BS_1 where the highest value was found at $39m$ and (ii) during the second campaign BS_2 where the lowest value was at $31m$. Both values were also considered as outliers and excluded from computation of averaged specific bedload flux (equation 4.2) performed at each vertical and interpolated along cross-section.

These results show that average specific bedload flux reach a plateau in the central part of the section ($31m - 35m$), which gradually decreases according to the discharge ($0.6kg/s/m$ at $360m^3/s$, 0.4 kg/s/m at $268m^3/s$ and 0.2 kg/s/m at $233m^3/s$), except during the second campaign BS_2 where a peak higher than $1kg/s/m$ was observed at $33m$. This trend of gradual decrease of averaged specific bedload flux according to the discharge was less observed at the extremity of the cross-section ($27m$, $37m$ and $39m$) where bedload transport was rather measured (BS_1 and BS_2) or not (BS_3). The standard deviation between bedload flux measured at the same vertical was generally higher in the central part of the section ($31m - 35m$), especially at the lowest discharge where values range from $0.015kg/s/m$ to $0.347kg/s/m$ in 10 minutes.

The presence of these sediment pulses highlights the spatial and temporal variability of the bedload transport and demonstrates the importance to collect several samples in order to define accurate mean bedload flux. The comparison of the lateral distributions and standard deviations of bedload fluxes measured during each campaign indicates that results from the second campaign BS_2 were different (presence of a peak of transport in the center, lateral extension of the plateau and lower variability between paired samples) from the others. This differences may be due to the fact that the second campaign BS_2 was performed at almost steady state conditions during a shorter period, between two phases of rising limb, while the other campaigns were performed during a phase of falling limb. This reason may also explain why the averaged-specific bedload at the second campaign BS_2 ($583g/m/s$) was 35 higher than at the first campaign BS_1 ($379g/m/s$), while during the flood discharge was 10 lower.

The results of the passive acoustic measurements of bedload self-generated noise performed during each field campaign BS_n, expressed in acoustic power (equation 4.4) recorded above $2kHz$, are presented in figure 4.4 a. The averaged acoustic power (equation 4.6) varies from 4.10^{13} to $4.10^{14}\mu Pa^2$, and values are higher in the middle of the river section than close to the bridge piers, which is coherent to the bedload sampling measurements. The maximum of averaged acoustic power ($4.10^{14}\mu Pa^2$) and bedload flux ($1kg/s/m$) are similarly located during the second campaign BS_2 ($32m$), but the peaks are more diffuse in the acoustic than in the sampling profiles. This variation is due to the fact that bedload sampling measurements are local, while hydrophone measurements are integrative of a larger and unknown area, which depends on the propagation of the acoustic signal. The bedload SGN can propagate further than $5m$ from the location of the bedload transport (Geay et al., 2017), which explains why the hydrophone recorded an acoustic activity during the third campaign BS_3, where no bedload transports were measured (27, 37 and $39m$). This inconsistency in the spatial representativity of both methods of measurement justified the use of the cross-section averaged acoustic power as a proxy for quantifying the cross-section averaged bedload flux.

The average-specific acoustic power $\bar{P}$ (equation 4.6) recorded in function of averaged-specific bedload flux $\bar{q}$ (equation 4.3) measured during the second (BS_2) and third (BS_3) campaigns were added to the plot of Geay et al. (2020). The results (Figure 4.4 b) shows that acoustic power recorded on the Moselle river during the three campaigns ($1.4\times10^{14}, 3.3\times10^{14}$ and $1.6\times10^{14}\mu Pa^2$ respectively) are among the highest values obtained applying this protocol on different gravel-bed rivers. Therefore, the power law established by Geay et al. (2020) between average acoustic power and specific bedload flux was readjusted considering these additional measurements when fitting the power law (equation 4.7) to the log values of $\bar{P}$ and $\bar{q}$. The results show that the coefficient (7.97) and exponent (1.33) of this relationship are slightly higher than values proposed by Geay et al. (2020), which allows to slightly improve the Pearson correlation coefficient from 0.57 to 0.62.

This relationship enables a good estimation of bedload flux measured on the Moselle river, the result of the first ($BS_1 = 379g/m/s$) and the second ($BS_2 = 583g/m/s$) campaign are within a factor 1, but the result of the third ($BS_3 = 92g/m/s$) campaign is close to a factor 3. The specific-averaged acoustic power of this last measurements may be overestimated, because the value obtained during this campaign ($BS_3 = 3.3 \times 10^{14}$µ$Pa^2$) is slightly higher than during the first campaign ($BS_1 = 1.4 \times 10^{14}$µ$Pa^2$), while solid and liquid discharges were much lower. This overestimation may be related to the use of acoustic records performed before and after the bedload sampling rather than during direct measurement (lack of available operator during third campaign BS_3) for the computation of averaged values. By using only the data recorded after the campaign (two lowest values per verticals) the value of $\bar{P}$ decreased to 6.2×10^{13}µPa^2, which allows an estimation of the bedload flux measured during this campaign using the calibration curve, within a factor 1. This results show that the data recorded after the bedload sampling may be more representative of the acoustic power during the flood than the data recorded before, which may be explained by a reduction of the falling limb during this period (Figure 4.2). The good agreement between this calibration curve and our results indicates that it is possible to use the equation 4.7 to estimate bedload specific flux from averaged acoustic power measurements on the Moselle river.

4.4.1.2 Relationship between bank and cross-sectional acoustic power

The results of the 6 acoustic maps M_n performed between March 2019 and February 2020 for flow discharges varying from 158 to $350m^3/s$, expressed in acoustic power (equation 4.4) recorded above $2kHz$, are presented in figure 4.5 a. The averaged acoustic powers computed (equation 4.5) at each measurement location and linearly interpolated at $1m$ interval, increase from the bridge piers (0, 22.5 and $40m$) to the middle of both sections of the bridge (12 and $32m$). The acoustic profiles are globally symmetric at the right side ($0 - 23m$), but asymmetric at the left side ($23 - 40m$) with the maximum averaged acoustic powers ($16 - 18m$) that are closer to the central pier than to the left abutment. This asymmetry is due to enrockments located along the left bank (Figure 4.1), which directs flows and sediments to the right side of the channel, creating a recirculation zone downstream of the bridge ($0 - 7m$). The acoustic profiles are more diffuse at higher flow discharges, because bedload self generated noises are less attenuated across the section, when water level increases (Geay et al., 2017). The highest averaged acoustic powers are always recorded at the right side of the profile ($32m$), except during the acoustic map measurement performed at the lowest water levels ($18m$), incomplete due to a technical issue. The bedload transport therefore begins ($Q < 180m^3/s$) in the scour located along the left concave bank and thereafter ($Q \geq 200m^3/s$) mostly occurs downstream of the convex bank, where the riverbed is relatively flat (Figure 4.1).

The results of the specific-averaged acoustic powers $\overline{P_{XS}}$ computed (equation 4.6) between 7 and $40m$, show that value increases with flow discharge from $158m^3/s$ (9.0×10^{11}µPa^2) to $167m^3/s$ (3.2×10^{12}µPa^2). Two very different values (1.4×10^{14} and 2.6×10^{13}µPa^2) are however recorded around $235m^3/s$. This difference comes from clockwise hysteresis in bedload transport observed at the Moselle river (see part 4.4.3), where for a given flow discharge the specific-acoustic power is higher at rising limb than at falling limb. Therefore, the value of $\overline{P_{XS}}$ is much higher during the campaign M_3 (1.4×10^{14}µPa^2) performed at the flood peak, than during the campaign M_6 (2.6×10^{13}µPa^2) performed at falling limb (Table 4.1). The value recorded during campaign M_3 (1.4×10^{14}µPa^2) is also higher than that recorded during the campaign M_4 (9.7×10^{13}µPa^2), which was conducted at a flow discharge of $350m^3/s$ during the falling limb of a flood event exceeding a two-year return period. This higher $\overline{P_{XS}}$ is due to higher averaged acoustic powers recorded at the left section of the bridge ($2 \times 10^{14} \mu Pa^2$), which are almost as high than at the right section ($3 \times 10^{14} \mu Pa^2$). The highest averaged acoustic power ($4.10^{14} \mu Pa^2$) monitored during this study is however recorded during campaign M_5 at a flow discharge of $268 m^3/s$, in the middle of the bedload sampling area (Figure 4.5 a), when the flood hydrograph reached a plateau (Figure 4.2).

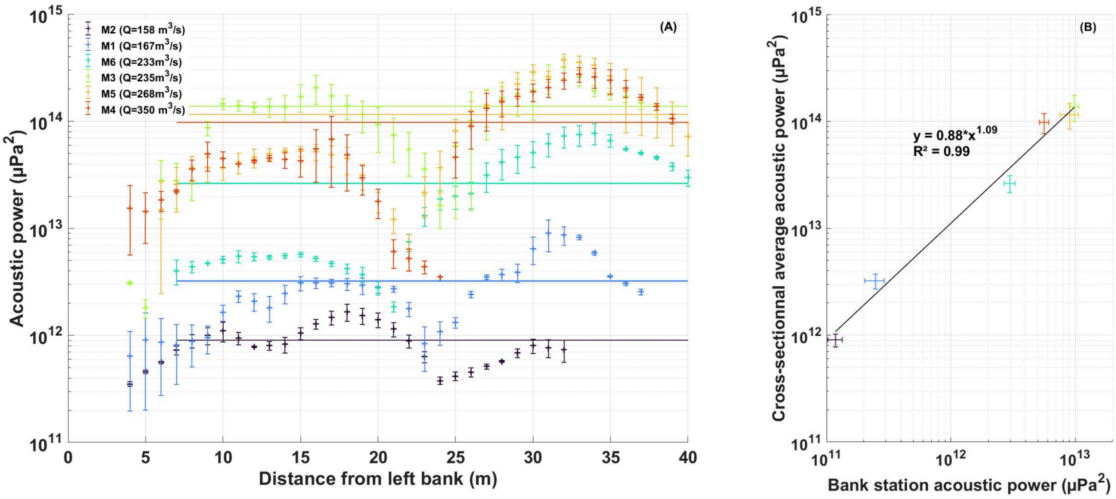

Figure 4.5: (A) Results of acoustics maps performed at different discharge and (B) relationship between bank and cross-section averaged measurements

The specific-averaged acoustic powers $\overline{P_{XS}}$ are plotted (Figure 4.5 b) against the averaged acoustic power $\overline{P_F}$ (equation 4.9) recorded during each acoustic profile by the hydrophone fixed at the bridge. The results show an excellent linear relationship between acoustic powers measured from the bank and from acoustic maps, with a Pearson correlation coefficient computed to log values of 0.99. The power of the signal recorded at the bank is approximately 10 times lower than that recorded across the river section ($\alpha = 0.88$), a difference that remains relatively constant throughout the various campaign ($\beta = 1.09$). The acoustic powers recorded at the bank are therefore proportional (equation 4.10) to bedload sounds generated across the section regardless to bedload discharges or morphological evolutions. The continuous bank measurement can thus be extrapolated to the entire cross-section using this rating curve (equation 4.10) and converted into bedload flux using the adjusted (equation 4.7) calibration curve of Geay et al. (2020). By combining equation 4.10 and equation 4.7, the total bedload discharge q_s across the Moselle River can then be computed at the bridge from the acoustic power $\overline{P_F}$ measured at the bank using:

$$q_s = 10^{\log\left(\frac{0.87\overline{P_F}^{1.09}}{7.97\mathrm{E}+10}\right)\times\frac{1}{1.33}} \times W \tag{4.24}$$

where W is the river width at the bridge. The time series of acoustic power monitored from the bank will be converted to bedload flux using equation 4.24 and compared to bedload fluxes estimated using the 2D hydro-sedimentary model.

4.4.2 Numerical model calibration

This part presents the results of the calibration of the 2D hydro-sedimentary model $\mathcal{M}_{f,s}$ (Figure 4.1) used to predict the bedload transport at the bridge. The results of the calibration of the large hydraulic model $\mathcal{M}_{f,h}$, from which were determined the boundary conditions for the hydro-sedimentary model $\mathcal{M}_{f,s}$, are presented in appendix D. First, we show the results of the calibration of the friction coefficient of the hydrodynamic module, in order to assess the ability of the model to predict the bed shear stress on the sampling area during the bedload measurements. Then, we represent, in function of these bed shear stresses, the bedload fluxes measured on the field and predicted using bedload transport equations, in order to determine which laws are the most suitable. Finally, we show the results of the calibration of the selected laws and the ability of the hydro-sedimentary model $\mathcal{M}_{f,s}$ to predict the Moselle river bedload transport.

4.4.2.1 Hydrodynamic model

The calibration of the friction coefficient of the hydrodynamic module of the hydro-sedimentary model $\mathcal{M}_{f,s}$ is based on : (i) a time series of WSE measured during the flood by the limnimeter located upstream of the bridge and (ii) a velocity profile performed during each bedload sampling campaign (BS_2 and BS_3) using an ADCP deployed from the bridge. The results of this calibration presented below are independent of the mesh size ($1m$ resolution at the bedload sampling area) according to a sensitivity analysis performed by refining the mesh from $2m$ to $0.5m$ around bridge piers, excluded from the computational domain.

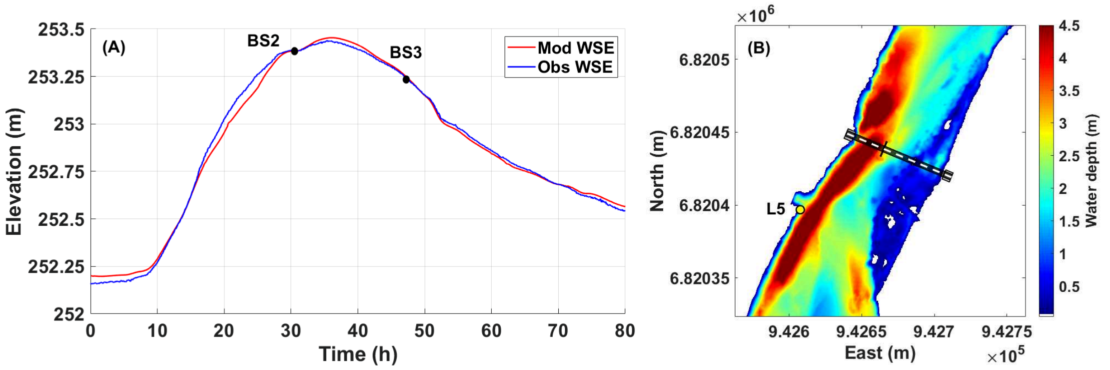

Figure 4.6: (A) Comparison between the WSE recorded by the limnimeter located upstream of the bridge (yellow point in B) and the WSE modeled during the studied flood F from unsteady simulations performed with the submodel $\mathcal{M}_{f,s}$ (B) Map of the water depth predicted at steady state ($Q = 268m^3/s$) by the submodel $\mathcal{M}_{f,s}$ during the bedload sampling campaign BS_2.

Calibration of water surface elevation

The comparison between simulated and observed WSE (Figure 4.6), shows that the hydro-sedimentary submodel $\mathcal{M}_{f,s}$ is well calibrated at the bridge, especially during the two bedload sampling campaigns (BS_2 and BS_3), for which both WSE curves are superimposed. The simulated WSE are slightly underestimated compared to observed ones during the rising limb of the flood, but this difference is also observed in calibration results for the large hydraulic model $\mathcal{M}_{f,h}$. The WSE are therefore well predicted on the bedload sampling area using a Strickler friction coefficient of $47m^{1/3}/s$ in the riverbed and of $8m^{1/3}/s$ in the floodplain (Figure 4.1).

Calibration of flow distribution

The comparison between simulated and observed velocities (Figure 4.7 a), shows that the model overestimated flows at the left section of the bridge and underestimated them at the right section. The velocities measured during the second campaign BS_2 are equal ($2m/s$) in the middle of the left and right sections, while the simulation results are much higher in the left ($2.7m/s$) than in the right section ($1.4m/s$). During the first campaign BS_1, the velocity in the middle of the left section are unknown because of too turbulent flows, but simulated results are also lower ($1.5m/s$) than observed ($2.2m/s$) at the right section. The simulation results intersect the field measurements downstream velocities of the central piers of the bridge, where velocities decrease ($1.8m/s$).

The distribution of flows between each section is calibrated by applying a friction coefficient of $15m^{1/3}/s$ under the left section of the bridge and of $10m^{1/3}/s$ around the central piers (Figure 4.7 b). This higher friction at the left section may be due to the enrockments located at the abutment (and probably on the bottom of a part of the left section), but the wrong distribution of flows may also be related to the variation of the river section between the LiDAR survey L_2 (August 2019) and the bedload monitoring BS_2 and BS_3 (March 2020). Indeed, the erosion of the convex bank observed during this period as well as the erosion of the river bed measured during the flood in the middle of the right section may favor flows in this section. This calibration enables however to balance velocities between each section of the bridge during both studied campaigns, which allows to predict accurately the flow velocities and therefore the grain shear stress τ' at the bedload sampling areas.

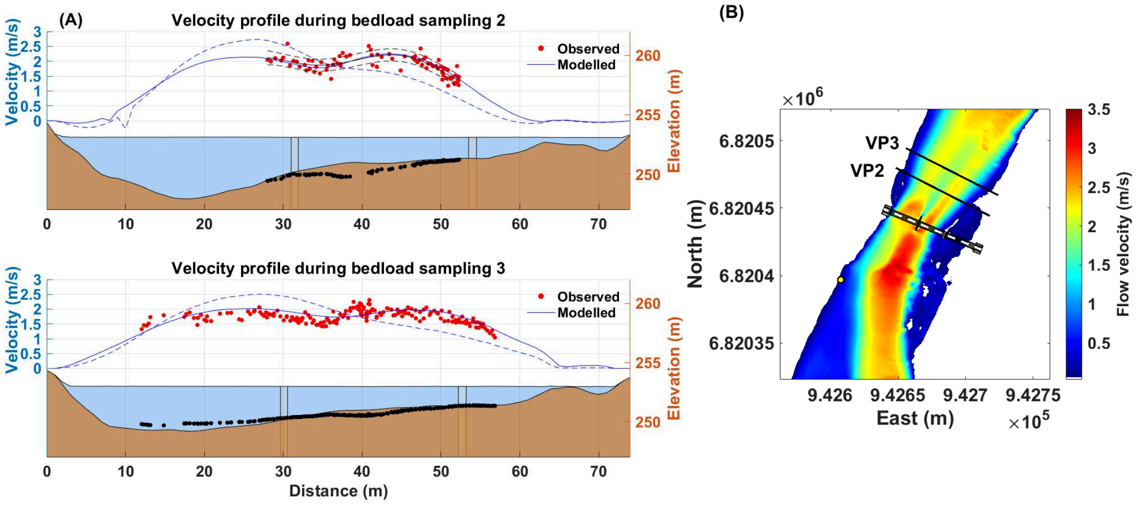

Figure 4.7: (A) Comparison between observed (red points) and modeled depth-averaged flow velocities, during the bedload sampling BS_2 ($Q = 268m^3/s$) and BS_3 ($Q = 233m^3/s$), before (solid blue line) and after (dashed blue line) calibration of the friction coefficient. (B) Map of the depth-averaged flow velocities predicted at steady state ($Q = 268m^3/s$) by the model $\mathcal{M}_{f,s}$ during the bedload sampling campaign BS_2.

4.4.2.2 Hydro-sedimentary model

The bedload transport laws used in the 2D hydro-sedimentary model $\mathcal{M}_{f,s}$ were selected based on a comparison between the predicted and observed relationships between the specific bedload fluxes q and the Shields parameter θ. These relationships were computed using the critical Shields parameter θ_{cr} suggested by the authors of each law and estimated for the Moselle river by Piasny et al. (2023b) to establish the optimal threshold value. The selected laws with empirical coefficients were calibrated based on a comparison between the predicted q_s and observed bedload fluxes $\overline{q}$, integrated across the sampled section of the river.

Selection of bedload transport laws

The Shields parameter θ was extracted at each vertical x (Figure 4.8 b) where bedload samples were collected and then plotted against averaged specific bedload fluxes $\overline{q}$ measured at those locations during both sampling campaigns. The results (Figure 4.8 a) exhibit a strong positive correlation between $\overline{q}$ and θ, when θ exceeds the critical Shields parameter θ_{cr} of 0.035, with values of $\overline{q}$ ranging from $5.8E-5m^3/s/m$ at 0.04 to $1.4E-4m^3/s/m$ at 0.06. The data exhibit a wider scatter when $\theta \lesssim \theta_{cr}$, as (i) $\overline{q}$ measured during BS_3 are significantly lower than during BS_2 and (ii) $\overline{q}$ drops sharply below θ_{cr} during BS_3, while $\overline{q}$ gradually decreases during BS_2. This scatter may be explained by the increasing influence of local bedload fluctuations and uncertainties in estimating $\overline{q}$ and θ, as bedload tends to zero. The local bedload fluctuations are related to the chaotic nature of the flow turbulence (Ancey, 2016) and of the sediment transport motion (Einstein, 1950). The uncertainties in estimating $\overline{q}$ arise from the sampler's measurement accuracy, while the uncertainties in estimating θ stem from the sampler's XY position accuracy. These results therefore do not clearly indicate whether sediment transport is initiated at a threshold value or not, which means that laws with and without threshold values can potentially be used to estimate sediment transport.

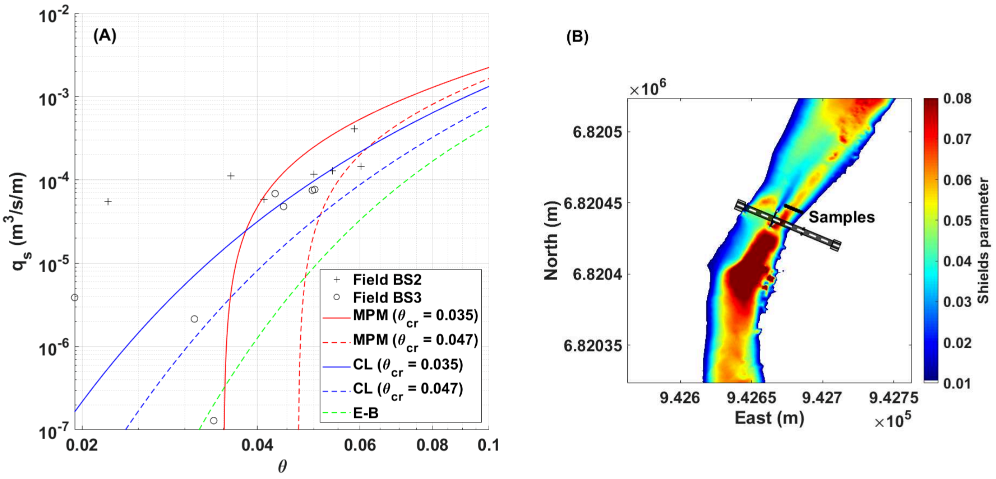

Figure 4.8: (A) Local bedload transport measured during sampling BS_2 and BS_3 as a function of the local Shields parameter modelled at steady state for the corresponding discharge using $\mathcal{M}_{f,s}$ (MPM : Meyer-Peter & Müller laws, CL : Camenen & Larson laws, E-B : Einstein-Brown laws) (B) Map of the Shields parameter predicted at steady state ($Q = 268m^3/s$) by the model $\mathcal{M}_{f,s}$ during the bedload sampling campaign BS_2.

The bedload fluxes $\overline{q}$, measured as a function of θ, were compared to the bedload fluxes q_s predicted using the sediment transport laws implemented into Sisyphe and applicable to our study site: Meyer-Peter and Müller (1947, noted MPM), Camenen and Larson (2005, noted CL) and Einstein-Brown (1950, noted EB). The bedload fluxes q_s were computed using a critical Shields parameter θ_{cr} of 0.047, as suggested by the authors of the laws and of 0.035 as determined by Piasny et al. (2023b) for the Moselle river. The comparison (Figure 4.8 a) indicates that (i) the EB law consistently underestimated q_s, (ii) the MPM law underestimated the threshold for the inception of bedload transport using $\theta_{cr} = 0.047$, but overestimated q_s using $\theta_{cr} = 0.035$ and (iii) the CL law underestimated q_s using $\theta_{cr} = 0.047$, but is in good agreements with the field measurements ($\theta > 0.04$) using $\theta_{cr} = 0.035$. Based on these results, the estimation of $\theta_{cr} = 0.035$ was validated and both CL and MPM laws were selected to predict the bedload transport of the Moselle river, as scatter in $\overline{q}$ measurements do not clearly indicate whether sediment transport initiates at a threshold value or not. The empirical coefficient of the MPM laws had however to be calibrated, contrarily to CL law, in order to accurately predict the bedload discharges.

Calibration of bedload transport laws

The calibration of MPM law consists in determining α_{MPM} as follows. The bedload transport computed using the MPM law and a coefficient α_{MPM} varying from 2 to 6 by steps of 0.1, was integrated between the central ($27m$) and right ($39m$) piers of the bridge and compared to the cross-sectional bedload discharge measured during the BS_2 ($5.1kg/s$) and BS_3 ($1.4kg/s$) campaigns. The sum of absolute differences between predicted $Q_{s,mod}$ and observed $Q_{s,obs}$ cross-sectional bedload discharges (Figure 4.9 a) indicate that the best α_{MPM} coefficient is 3.40. The value of this coefficient is much lower that the value proposed by MPM of 8, as bedload transport computed using MPM coefficient were significantly overestimated compared to field measurements (Figure 4.8 a). This overestimation of the bedload transport, using MPM coefficient, was also observed by Wong and Parker (2006) who reanalyzed MPM data and proposed a coefficient of 3.97, computed without an unnecessary bed roughness correction. The coefficients determined in the present study, being close to the values proposed by Wong and Parker, it gives us confidence in the results of our calibration, despite reduced number of data and measurement uncertainties.

The bedload transport rates computed across the sampling section, using the CL and MPM laws, were superimposed to the bedload transport rates measured during both bedload sampling campaigns BS_2 and BS_3. The results (Figure 4.9 b) highlight that each law underestimated the sediment transport close to the bridge piers ($0.15kg/s/m$ between $27m-29m$ and $37m-39m$) and in the middle of the section ($0.32kg/s/m$ between $32m-34m$) during BS_2. The bedload transport was underestimated at the section extremities, because the transport of fine sediments measured in the field at those locations (Figure 4.3), could not be predicted by the model, using a unique grain size corresponding to the bed surface D_{50}. The bedload transport was underestimated in the middle of the section, due to a peak of q which occurred during the field measurements BS_2 (Figure 4.10), where sediment transport was no longer correlated to flow discharge (see also part 4.4.3), that could therefore not be predicted by the model. Results (Figure 4.9 b) indicate that each law relatively well predicted q, along the entire cross-section during BS_3, with respect to measurement variability, when compared to the maximum bedload fluxes measured at each vertical. The bedload transport was however, overestimated when compared to the averaged specific bedload fluxes computed at each vertical, as the 2D model is not able to predict the sediment pulses, which occurred during the bedload samplings, when computing successive steady state simulations. The model may therefore slightly overestimate q at the beginning and at the end of the bedload transport when sediment pulses highly influence the transport, but this amount of sediment is insignificant at the scale of an entire flood event. Globally our result shows that, when the critical Shields parameter is well calibrated, bedload transport can be accurately predicted either by the CL law (without requiring additional calibration) or by the MPM law using the coefficient proposed by Wong and Parker (in case where calibration data are unavailable). The CL law better predicts the lateral distribution of bedload transport compared to the MPM law.

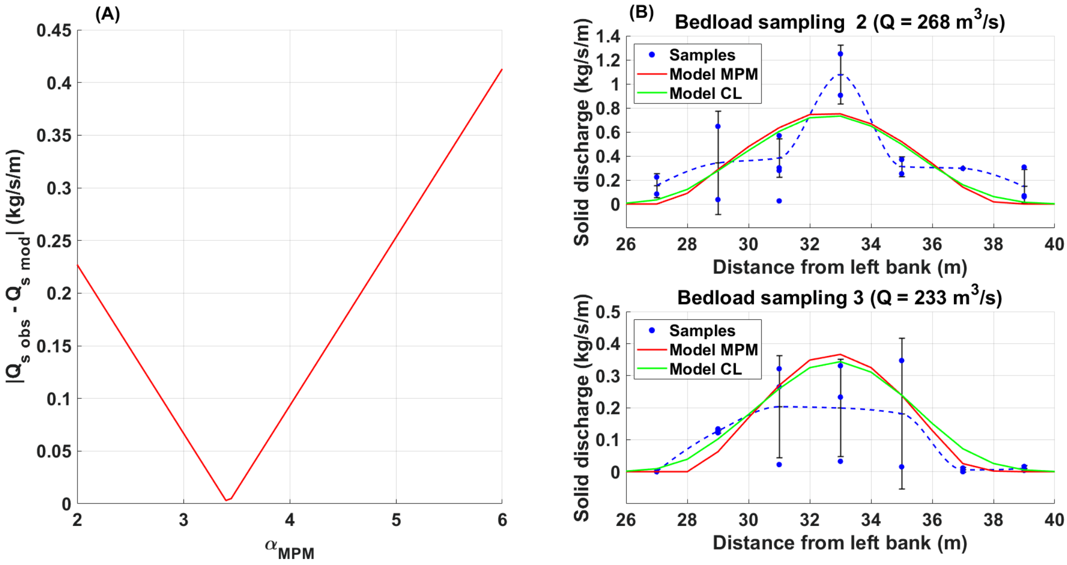

Figure 4.9: (A) Calibration of α_{MPM} and (B) Comparison between observed and predicted cross-sectional bedload transport rates during bedload sampling campaigns BS_2 and BS_3.

4.4.3 Comparison of bedload fluxes estimated using acoustic and numerical models

The cross-sectional instantaneous and cumulative bedload fluxes estimated during the flood, using the acoustic and numerical models, were compared in order to highlight the similarities, differences and potential complementary between both methods.

4.4.3.1 Comparison of dynamic bedload fluxes

The time series of acoustic power recorded from the left bank was extrapolated (equation 4.10) to the active width of the channel ($40m$) and compared to the flow hydrograph estimated using the 2D hydro-sedimentary model $\mathcal{M}_{f,s}$. The results (Figure 4.10) indicate that the cross-sectional average acoustic power varies by a factor of 2, ranging from $10^{12}\mu Pa^2$ at$75m^3/s$ to $10^{14}\mu Pa^2$ at $275m^3/s$. The shapes of both curves are comparable, except when the flow discharge reached a plateau at $260m^3/s$, where the acoustic power continued to increase until reaching a peak of $1.5\times10^{14}\mu Pa^2$ at the end of the plateau and then decreased when the flow discharge raised again. The time series of cross-sectional averaged acoustic power was converted (equation 4.7) into bedload fluxes and compared to the bedload fluxes predicted using the selected bedload transport laws (Figure 4.10). This analysis is performed following four phases in the hydrograph: at the beginning, during the rising limb, during the falling limb and the end of the flood event.

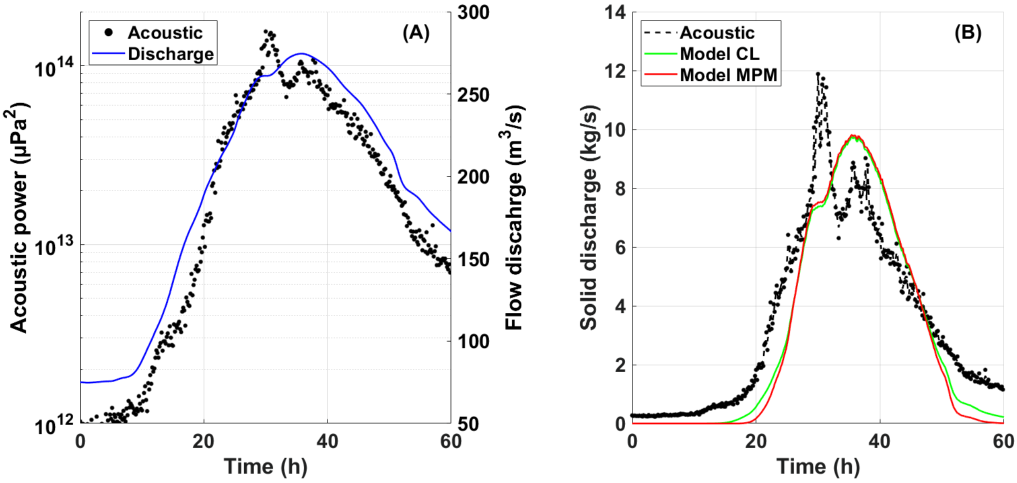

Figure 4.10: Comparison between chronicles of (A) acoustic power and flow discharge and (B) bedload fluxes estimated using acoustic measurements and numerical simulations during the studied flood F of March 2020.

At the begging of the flood, the results of acoustic measurements (Figure 4.11) show a baseline sediment discharge of $0.3kg/s$, when flow discharges ranged between $75-90m^3/s$. The sediment discharge slightly increased to $0.6kg/s$ when the flow discharge reached $110m^3/s$ at 13h and then increased rapidly when the flow discharge exceeded $160m^3/s$ after 17h. The results of the numerical simulations predict that the sediment transport began at 13h, using the CL laws and at 17h using the MPM law. The comparison between acoustic and numerical results may indicate that transport of particles finer than the bed surface D_{50} is recorded above $1.7\times10^{12}\mu Pa^2$, while the transport of particles of this size is recorded above $5.2\times10^{1}2\mu Pa^2$. At the beginning of the flood, the bedload transport predicted using each law is, however, consistently lower (0.6 kg/s) than that estimated using acoustic measurements due to the existence of a baseline sediment discharge.

During the first rising limb of the flood, the bedload discharge predicted by the numerical simulations is lower ($2kg/s$) than that estimated by the acoustic measurements, indicating that the threshold of motion θ_{cr} used in the model may be overestimated. This overestimation may be attributed to the temporal evolution of θ_{cr} in response to flow history which occurred between its calibration in December 2018 and the flood event F studied in March 2020. Indeed, Masteller et al. (2019) demonstrated that θ_{cr} tends to progressively increase over seasonal timescales in response to small to intermediate high-flow events and then decrease after major flood events. Given that, θ_{cr} was calibrated (Piasny et al., 2023b) during an intermediate flood of $303m^3/s$ (25/12/2018), which occurred after nearly a year of successive small flood events (Figure 4.2), while the studied flood occurred a few weeks after a high-flow event of $470m^3/s$ (04/02/2020). Thus, according to Masteller et al. (2019), the threshold value may have been overestimated.

At the plateau of the hydrograph (30h), the bedload discharge estimated by the acoustic measurements reached a maximum peak of $12 kg/s$, whereas the bedload transport predicted by the numerical simulations reached a plateau of $7.5 kg/s$. Although, *in situ* measurements of bedload transport performed at the plateau of the hydrograph (Figure 4.2 b) were only conducted at the left half of the cross-section. The result of $5 kg/s$ measured between $26 - 40 m$ (Figure 4.9), with a maximum specific bedload discharge of $1.1 kg/s/m$ at $33 m$ and an excluded value of $6.3 kg/s/m$ (see section 4.4.1.1), tends to confirm the occurrence of this high peak of bedload transport. During the second rising limb of the discharge, the bedload discharge estimated by the acoustic measurements first decreased to $7 kg/s$ (34h) and then increased again to a lower peak of $9 kg/s$ at the maximum flow discharge (35h), while the bedload transport predicted by the numerical simulations only increased from $7.5 kg/s$ (30h) to $10 kg/s$ (35h). These two distinct peaks of bedload discharge, one before and one at the maximum discharge, was also experimentally observed by Phillips et al. (2018) when they studied the effects of flood hydrograph duration, magnitude and slope on bedload sediment fluxes. This experiment was conducted in a 30m by 0.5m sediment and water feed flume, using a trapezoidal hydrograph of a shape similar to the one observed in this study, with adjusted sediment feed rates to keep a constant slope of the bed. To isolate the influence of the hydrograph on the sediment dynamics, the experiment was performed using a narrow unimodal grain size distribution and during short durations of competent flows. This setup reduced the textural, morphological and granular adjustments and prevented the formation of longer-term morphological structures that could affect the sediment dynamics (Wilcock and McArdell, 1997; Ferrer-Boix and Hassan, 2014). According the results of Phillips et al. (2018), the shape of the curve of sediment fluxes estimated by the acoustic measurements (Figure 4.10), with two distinct peaks of sediment transport, were primarily controlled by the trapezoidal shape of the observed flood hydrograph. As Phillips et al. (2018) found within the flood event a considerable variability between bedload fluxes and Shields parameters, it may also explain why the model used in this study, based on a unique relationship between bedload flux and Shields parameter (equation 4.20 and 4.21) was unable to reproduce the shape of observed sediment fluxes.

At the peak and during the falling limb of the flood ($<$ 45h), the bedload discharges predicted by the numerical simulations were higher ($\sim 2 kg/s$) than those estimated by the acoustic measurements, which contrasts with the results observed during the rising limb. This contrast is due to the lower ($2 kg/s$) bedload discharges estimated by the acoustic measurements during the falling limb than during the rising limb of the flood event (Figure 4.11), indicating a bedload clockwise hysteresis. This phenomena is generally attributed to a gradual decrease in upstream sediment supply (Recking, 2012b; Singer, 2010) or to a progressive decrease in the sediment mobility, through a structural arrangement of the river bed (Church et al., 1998; Houssais et al., 2015; Strom et al., 2004). In our case, the sediment supply may be controlled by a weir located $1.2 km$ upstream, but given the bedload velocity ($< 10 m/h$; Piasny et al., 2023a), its influence could not be propagated up to the study area within the 60-hour duration of the studied flood. The river banks also supply sediments, but riverbank failures most frequently occur during the falling limb than the rising limb of the hydrograph (Rinaldi et al., 2004; Periketi et al., 2007), which would have resulted in a counterclockwise hysteresis. Based on those considerations, the observed bedload clockwise hysteresis is attributed to a progressive decrease of the sediment mobility though increase of the bed stability. This increase could occur through different mechanisms such as bed compaction (Marquis and Roy, 2012), surface sorting/grain size changes (Humphries et al., 2012), changes in bed surface roughness (Venditti et al., 2010; Wilcock and Crowe, 2003), evolution of grain interlocking (Yager et al., 2018), coarse grain clustering (Hassan et al., 2020) or degree of armoring (Mao, 2012). In our case, we assumed that bed stability increased progressively during the rising limb of the flood, possibly due to one or more of these mechanisms, after having been disrupted by the previous flood event exceeding a two-years returns period (Figure 4.2). This progressive stabilization of the bed bottom gradually increased the threshold of motion θ_{cr} up to the peak of solid discharge (Pretzlav et al., 2020), leading to the bedload clockwise hysteresis. The increase of θ_{cr} can be observed by the convergence between the observed and predicted bedload transport curves at the end of the first rising limb (30h). The numerical model was unable to reproduce this clockwise hysteresis without modelling the grain size sorting and with a constant critical Shields parameter (Figure 4.11). Note that the 2D model simulated an hysteresis, which can be due to classical hydraulic hysteresis as predicted by classical shallow water equations (submersion and rarefaction waves do not have the same speeds) and to the downstream boundary conditions imposed consisting in water depth time series. The lattes, may contain local total hysteresis, hydraulic plus morphological one. Pretzlav et al. (2020) proposed to improve the numerical modelling by increasing the critical Shields parameter as a function to the cumulative shear stress, in order to consider the progressive stabilization of the river bed.

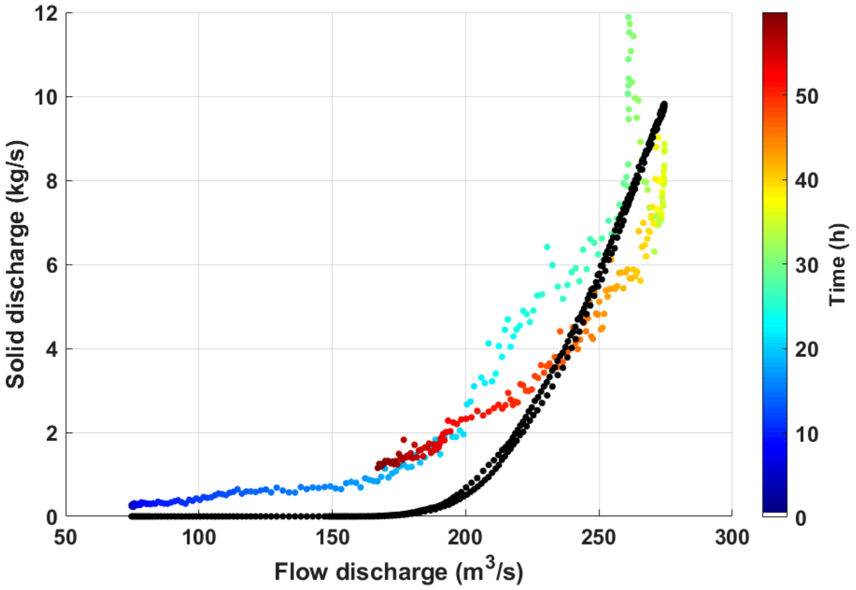

Figure 4.11: Comparison between observed (colored points) and modeled (black points using MPM law) bedload hysteresis during the studied flood F of March 2020.

At the end of the flood, the acoustic measurements were slightly higher ($\sim 0.4 kg/s$ at $167 m^3/s$) than at the beginning of the flood event (Figure 4.11). This slight difference may be related to morphological evolutions of the river bed that could have occurred during the flood, locally changing the hydrodynamic conditions, and therefore the bedload fluxes. The river morphological evolution being not considered into the model, the bedload transport predicted at the end of the event was then lower (~ 0.4 kg/s considering the baseline sediment discharge of the acoustic measurement) and shorter than observed.

4.4.3.2 Comparison of cumulative bedload fluxes

The predicted and estimated bedload fluxes were cumulated and compared. The results show that even if predicted and estimated instantaneously, bedload discharge varies though time, the cumulative values at the flood scale are comparable: 743 tons with acoustic, 661 tons with CL law and 640 tons MPM law. Model derived estimates compared to acoustic estimates, both with calibrated bedload laws, are in rather good relative agreement of more than 85%.

4.5 Conclusion

This study is based on an unprecedented dataset of direct (sampling) and indirect (acoustic) measurement of bedload transport coupled with a 2D hydro-sedimentary model. It shows that the bedload fluxes can be estimated at the scale of a flood event using (i) continuous acoustic measurement recorded from the river bank, calibrated by acoustic maps performed at different discharges, and converted using the global calibration curve proposed by Geay et al. (2020) and (ii) a fine description of hydrodynamic conditions, especially bed shear stress in space and time, thanks to a 2D hydro-sedimentary model, along with the CL and MPM laws, both calibrated using a very rich *in situ* dataset. The bedload fluxes estimated by the continuous acoustic measurements were compared to the bedload fluxes predicted by each law throughout the entire duration of a moderate flood event.

From the obtained result, on a gravel-bed river with a relatively low slope and a non-uniform sediment grain size distribution, the following conclusions can be raised:

- The shape of both chronicles of bedload fluxes varies significantly, with two distinct peaks of bedload transport estimated by the acoustic measurements and only one predicted by the numerical simulations. The origin of these two distinct peaks of bedload transport was attributed to the shape of the flood hydrograph, following the results of laboratory experiments performed by Phillips et al. (2018).

- The temporal evolution of the sediment fluxes in relation to discharge varies significantly, the acoustic measurements shows a higher bedload transport during the rising limb than during the falling limb of the hydrograph, indicating a clockwise hysteresis of bedload transport, while the numerical simulations shows a discharge-dependent bedload transport. The origin of this hysteresis was attributed to a progressive decrease of the sediment mobility due to an increase of the bed stability though the rearrangement of the bed surface particles during the flood. This gradual stabilization of the river bed increased the threshold of motion θ_{cr}, whereas the model assumed it to be constant, which explained the difference between field and numerical estimation of the bedload fluxes.

- The cumulative bedload fluxes estimated during the entire flood events were similar using each method, indicating that despite the model's limitations in computing instantaneous transport, it can provide reasonable predictions of the total fluxes during whole floods.

This comparison demonstrates that both methods for estimating the bedload fluxes are complementary and allow a better understanding of the bedload dynamics in a gravel-bed river. The continuous acoustic measurements could be used to determine the temporal evolution of the threshold for motion, which, in turn, could be incorporated into the model to enhance the prediction of the instantaneous bedload transport.

Appendix A

The subsurface GSD was determined by sieving a volumetric sample of sediments deposited during a 10-year flood on the closest emerged bar located upstream to the bridge (Figure 4.2). The sampled volume of 346 kg was sufficiently large to exceed the minimum sample-mass criteria proposed by Church et al. (1987) and computed according to the bed surface D_{max}. The surface GSD was determined by a grid-by-number pebble counts of 1200 particles collected in the riverbed on 6 homogeneous patches distributed along the upstream reach of the Moselle river. The sampling procedure was a variant of the method of Wolman (1954) proposed by Bunte and Abt (2001) using a frame and a template, more details are presented in Piasny et al. (2023b).

Appendix B

The acquisition of the topo-bathymetric LiDAR was achieved with an Optech Titan sensor using both near-infrared and green lasers to measure respectively the topography and the shallow bathymetry (Lague and Feldmann, 2020). The flights were conducted at an elevation of $450m$ which allows a ground resolution of $38pts/m^2$ and $7pts/m^2$ for emerged and submerged areas receptively. The relative low density of underwater measurements is due to a sensor malfunctioning, all discrete returns were not recorded, which conduct to use full-waveform data whose recording frequency is divided by two. The point cloud density were however sufficient to build digital elevation models (DEM) of $1m$ resolution were 95% of the river submerged areas (depth$> 2.4m$) were covered. To complete the DEM on submerged uncovered areas a bathymetric campaign was done from a boat using an ADCP coupled with a centimetric-accuracy DGPS. The water depths were recorded each seconds and associated to DGPS coordinates during the post-processing by synchronizing both devices. The boat trajectory followed a zigzag path from one river side to the other in order to optimize the riverbed mapping and simplify bathymetric transects interpolation. The ADCP vertical beams were interpolated using the Triangular Irregular Networks tools (TIN) of ArcGIS software and edges were manually adjusted to map the riverbed as observed in the field. The TIN which elevation accuracy was estimated at $\pm 5cm$ were rasterized into $1m$ cells and vertically shifted in order to overlap with the LiDAR DEM throughout merging process.

Appendix C

The flow velocity profiles were upload from ADCP and imported in Qrev 4, a computer program developed by the USGS providing information about measurements quality. The Signal-to-Noise (SNR) filter enabled us to identify invalid beams, but filtered data being not exportable from Qrev, identified points were manually deleted thanks to Matlab. Cleaned profiles were imported in the Velocity Mapping Toolbox (VMT) developed by Parsons et al. (2013) in order to project data of repeated transects into a single cross-section plane and then calculate depth-average flow velocity of each vertical beams. For this purpose, VMT source code had to be modified to (i) stop the VMT transect-averaging procedure after the steps of transects data projection (ii) integrate flow direction in calculation of depth-average velocity and (iii) extrapolate unmeasured top and bottom parts of the ADCP profiles according to the methods proposed by Mueller (2016). Hence, each vertical beam was projected to a predefined cross section using an orthogonal translation, velocity vector of each cell was projected onto a line orthogonal to this cross-section and a power law was fitted to the measured vertical velocity profiles. If the R^2 coefficient is higher than 0.8, the power law is used to calculate the depth-average flow velocity, if not the velocity of top cells are extrapolated to the surface and a power law is fitted to the last one third cells of the velocity profile and extrapolated to the bottom (most cases). Finally the depth-average velocity are calculated by dividing the area of the velocity profile by the water depth.

Appendix D

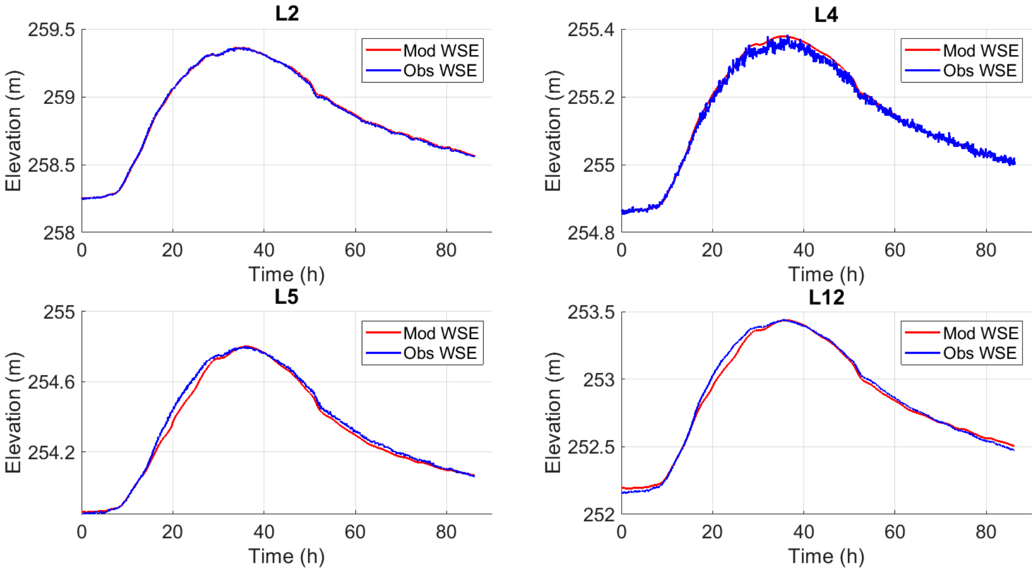

Figure 4.12: Comparison between the WSE recorded by limnimeter L_n and the WSE modeled during the studied flood F from unsteady simulations performed with the submodel $\mathcal{M}_{f,h}$.

Chapter 5

Calibration of non-uniform bedload transport 2D model using particle tracing

Ce chapitre vise à améliorer la prédiction de la composition de la charge de fond modélisée dans le cadre d'une granulométrie non uniforme. Une méthode est proposée pour caler successivement, pour chaque taille de particule à l'aide de données indépendantes, un coefficient lié à la mise en mouvement des sédiments ainsi qu'un second coefficient lié à la dynamique de transport. L'entraînement des particules est estimé à partir de la mobilité des traceurs, tandis que le transport des particules est estimé à l'aide de la vitesse virtuelle des traceurs. Un modèle hydro-sédimentaire 2D est utilisé pour simuler finement les conditions hydrodynamiques et, en particulier, la contrainte de cisaillement du lit ainsi que le transport multi-classes.

5.1 Introduction

Two-dimensional numerical modelling of sediment transport and river morphodynamics has been increasingly used for river management, engineering works, restoration projects or research purposes (Brousse et al., 2022; El Kadi Abderrezzak et al., 2016; Yu et al., 2022; Iwasaki et al., 2016; Nelson et al., 2015). The discretization of riverbeds into several layers composed of multiple sediment classes in a 2D morphodynamic numerical model (Cordier et al., 2019) enables to better represent sediment transport in poorly sorted graved-bed rivers. Such hydro-sedimentary models generally use semi-empirical laws (Meyer-Peter and Müller, 1948; Einstein, 1950; Engelund and Hansen, 1967; van Rijn, 1984) to compute separately the bedload transport rates of each class of sediments available in the uppermost bed layer, to determine the total bedload. These semi-empirical laws are however usually valid for uniform grain size and has to be calibrated for non-uniform sediment transport in order to consider interactions between particles of different sizes (Wu, 2007; Einstein, 1950).

Several authors proposed various calibration factors based on flume experiments, to modify the critical sediment motion threshold (Einstein, 1950; Egiazaroff, 1965; Day, 1980) or the sediment transport rates (Einstein, 1950; Karim and Kennedy, 1982; Shen and Lu, 1983) of each size class. Nevertheless, predicting an accurate composition of bedload transport in poorly sorted gravel-bed rivers remains challenging due to (i) the spatio-temporal complexity of flow physics (ii) and the impact of the surrounding sediments on the initiation of motion and the dynamics of motion. While those two phenomena might be indiscernible in a classical bedload transport measurement (Church and Hassan, 1992), one can use complementary measurements to estimate the effect of surrounding particles on (i) the initiation of motion with painted places, and (ii) the particle motion dynamics with bedload tracers survey. Moreover, the increasing availability of fine topo-bathymetric DEM of river bed morphology (Lague and Feldmann, 2020) and flow measurements enables to constrain accurate 2D hydraulic models, hence fine spatio-temporal estimation of the bed shear stress, which is a crucial hydrodynamic parameter for sediment transport (Chien and Wan, 1999). Using the above-mentioned complementary measurements combined with a 2D hydraulic model, which enables to separately account for hiding exposure effects and trapping effects in the estimation of bedload transport composition, has not yet been addressed.

So, this contribution presents a new method for calibration of the bedload transport rates of a 2D hydro-sedimentary model with non-uniform sediments, based on the dimentionless virtual velocity of a large number of tracers of different sizes.

The grain size distribution of natural gravel-bed rivers is rarely uniform (Cudden and Hoey, 2003; Mosselman, 2012; Parker and Klingeman, 1982). Indeed, the geometric standard deviation of the bed material tends to increase ($\sigma > 5$) with the median grain size ($d_{50} > 1cm$; Basile, 2001). The spatio-temporal variation of hydrodynamic forcing induces an horizontal (Nelson et al., 2009) and vertical (Bacchi et al., 2014) sorting of grain sizes, influencing bed roughness (van Rijn, 1984) and bed erodability, for example when armoring with coarser sediments occurs (Wang et al., 2020). Therefore, it is of paramount importance to account for horizontal and vertical grain size distribution for predicting bedload transport and associated morphological evolutions.

The most common method used to consider the effect of non-uniform sediments sizes into such models is to discretize :

- the bed-material grain size distribution curve into K sediment size classes with boundaries $[D'_k, D'_{k+1}]$. This number of size classes K, needed to predict bedload transport of non-uniform sediment mixtures, varies according to the standard deviation and the asymmetry of the grain size distribution curve. Optimum number of size classes ranges between 5 and 10 for natural gravel-bed rivers (Basile, 2001), with intervals between classes following a factor 2 assuming a log-normal distribution of grain sizes. Each size classe $k \in 1..K$ is caracterized by a representative diameter D_k which corresponds to the class center and a percentage p_k which corresponds to the volume of the class divided by the total volume of the bed-material;
- the river bed into an active (or mixing) layer in contact with the flow and substrate layer. The active layer acts as an interface between the flow and the river bed. It supplies sediments that can be transported or receive deposited sediments and then exchange materials with the substrate layer in order to keep a given thickness (Hirano, 1971). The composition and the thickness of the active layer thus influence the transport rate as well as the grain size distribution of the bedload. The thickness of this layer depends on the flow and sediment characteristics. So it can be proportional to morphological evolution (erodable depth or deposit thickness; Benett and Nordin, 1977; Borah et al., 1982), bed forms height (0.2 dune; Karim and Kennedy, 1982) or to the layer composition (D_{90} or $3D_{50}$; Garcia, 2008).

In classical formulas, bedload transport is generally calculated as a function of the dimensionless bed shear stress parameter θ proposed by Shields (1936), which corresponds to the ratio between the hydrodynamic forces to the sediment relative weight.

It is written here for a sediment class $k \in 1..K$:

$$\theta_k = \frac{\tau'}{(\rho_s - \rho) g D_k} \tag{5.1}$$

where τ' is the grain shear stress (see total bed shear stress definition in section 5.3.2.1), the only component of the bed shear stress acting on sediment transport (Mendoza et al., 2017), g is the gravitational acceleration, D_k is the representative diameter of the class k and ρ and ρ_s are the fluid and sediment volume weight, respectively.

The dimensionless bedload transport rate Φ_k, is usually computed as a function of the Shields parameter θ_k relative to the critical Shields parameter θ_{cr} which is the dimensionless critical shear stress for incipient motion of particles.

$$\Phi_k = \alpha \left(\theta_k - \theta_{cr}\right)^{\beta} \tag{5.2}$$

where α and β are empirical coefficients usually determined, as well as the critical Shields parameter θ_{cr}, from tables of the literature (Meyer-Peter and Müller, 1948; Wang et al., 2020). Semi-empirical laws (Meyer-Peter and Müller, 1948; Einstein, 1950; van Rijn, 1984; Wong and Parker, 2006) used in hydro-sedimentary models are generally determined and validated from flume experiments, using relatively uniform grain size distributions ($\sigma < 1.3$ where σ is the geometric standard deviation of the grain size distribution). In a sediment mixture, finer particles can however be hidden between or behind coarser particles, while coarser particles can protrude from the bed surface. Finer (resp. coarser) particles may therefore be more protected (resp. exposed) from flows and become less (reps. more) mobile than in a uniform grain size distribution (Einstein, 1950). To consider these hiding-exposure effects, on bedload transport rate of each size class k, the semi-empirical laws (5.2) can be corrected using hiding/exposure factors ζ_k (Wu, 2007).

This correction factor is usually computed according to the relative size of the particle D_k representative of the class k (logarithmic mean of the class limits sizes here) compared to a reference particle size D_r.

$$\zeta_k = \left(\frac{D_k}{D_r}\right)^{b} \tag{5.3}$$

where b is an empirical coefficient and D_r is the particle size that is not affected by the hiding/exposure effects, which is often considered to be the median grain size of the bed surface (Komar, 1987). This correction factor can be applied to the dimensionless critical threshold for particle motion θ_{cr} or to the dimensionless bedload transport rate Φ_k of each size class k;

- correction applied to the critical threshold for particle motion. This correction allows to reduce (resp. increase) the critical threshold for particle motion θ_{cr}, for size classes k coarser (resp. finer) than the reference particle sizes D_r, which tends to standardize the behavior of each particle size. The corrected dimensionless bedload transport rate $\Phi_k^{*,\theta}$ of the size class k is expressed as below with the tuning parameter denoted $\zeta_{k,\theta}$:

  $$\Phi_k^{*,\theta} := p_k \alpha \left(\theta_k - \zeta_{k,\theta}\theta_{cr}\right)^{\beta} \tag{5.4}$$

  where α and β are tunable coefficients, and p_k the fraction of size class k available in the active layer. The hiding factor exponent used to compute $\zeta_{k,\theta}$ (equation 5.3) is denoted b_θ varies from 0 (particles have no influence on each other so the value of τ_{cr} is almost proportional to the particle weight) to -1 (difference in particle exposure and friction angle completely compensates differences in particle weight so the value of τ_{cr} is the same for all particle sizes). The value of b_θ indicates if the entrainment of particles of different sizes occurs in a size-selective way ($b_\theta > -1$) rather than in equal mobility ($b_\theta \approx$ -1) (Parker and Klingeman, 1982; Andrews, 1983). Flume and field measurements suggest that the value of b_θ ranges between -0.6 and -1, but this estimations depends on the method employed to determine the motion of a particle and on the magnitude of the flood (Ashworth and Ferguson, 1989);

- correction directly applied to the bedload transport rate. This correction allows to increase (resp. reduce) the bedload transport rate Φ_k computed using semi-empirical laws (5.2), for size classes k coarser (resp. finer) than the reference particle sizes D_r, which tends to coarsening the bedload composition. The corrected bedload transport rate $\Phi_k^{*,\Phi}$ of the size class k is expressed as below when the tuning parameter is $\zeta_{k,\phi}$:

  $$\Phi_k^{*,\Phi} := p_k \zeta_{k,\phi} \Phi_k \tag{5.5}$$

  where p_k is the fraction of size class k available in the active layer.
  The hiding factor exponent used to compute $\zeta_{k,\phi}$ (equation 5.3) is denoted b_Φ. Karim and Kennedy (1982) found a value of $b_\Phi = 0.85$, therefore contrarily to the coefficient of correction applied to the critical threshold for particle motion, this coefficient of correction is an increasing function of the relative particle size D_k/D_r.

The volumetric bedload transport rate per units of time and of width $q_{s,k}$ for a class $k \in 1..K$, is then computed as a function of the sediment properties:

$$q_{s,k} = \Phi_k^{\square} \sqrt{(s-1) g D_k^3} \tag{5.6}$$

where $\Phi_k^{\square}$ stems for dimensionless bedload transport with (equation 5.4 or 5.5) or without correction (equation 5.2), $s = \rho_s/\rho$ is the relative density with ρ_s and ρ are respective volumetric weight of sediment and water, g is the gravitational acceleration, D_k is the representative diameter of sediment size class k. The total bedload transport rate $q_{s,t}$ is computed by adding bedload transport rates $q_{s,k}$ computed separately for each class k (equation 5.6), affected by a coefficient p_k representing the fraction of size class k available in the active layer.

$$q_{s,t} = \sum_k p_k q_{s,k} \tag{5.7}$$

The idea of the new method proposed in this article is to use successively calibrated, with independent data $\zeta_{k,\theta}$ and $\zeta_{k,\phi}$, applied to critical threshold of motion (in equation 5.4) and to the bedload transport rates (in equation 5.5), respectively, in order to improve the prediction of the bedload composition in a poorly sorted gravel-bed river. These successive calibrations allow to consider the influence of the surrounding particles sizes on both entrainment through $\zeta_{k,\theta}$ (hiding-exposure effects) and transport through $\zeta_{k,\phi}$ (trapping effects) of each particle size, when computing the bedload transport rates of non-uniform sediment. To distinguish each effect, independent datasets are utilized. The particle entrainment is estimated based on tracers mobility, while the particle transport is estimated based on tracer virtual velocities. As tracers mobility allows to determine size-based flow competence, virtual velocities are rarely studied using size-based competence duration, expect in the study of Milan (2013) with a very simple water surface slope to discharge relation as modelling approach.

In the present study, a novel method is proposed, introducing two factors of correction of hiding-exposure and trapping effects for more realistic multi-class bedload transport modelling, taking advantage of (i) independent measurements of tracers mobility and virtual velocity to calibrate them, (ii) of a 2D hydro-sedimentary model to finely simulate hydrodynamic conditions and especially bed shear stress as well as multi-class transport. The remainder of this article is organized as follows: section 2 presents the site and the context of this study, section 3 details the method employed to estimate the tracers dimensionless virtual velocity and explains how this information can be used to calibrate non-uniform bedload transport, section 4 describes the results and discusses about the improvements in the bedload gain size prediction achieved through the developed calibration factor.

5.2 Study site

The Moselle river is $560km$ long from its source at the pass of Bussang in the northeast of France to its confluence with the Rhine river at Koblenz in Germany (Figure 5.1 a). The upper part of the Moselle river drains a catchment area of $1,976\,\text{km}^2$ from the western side of the southern Vosges Mountains to the gauging station of Tonnoy on the Lorraine plateau. The geology of the Vosges Mountains consists mainly in crystalline (granites) and metamorphic (gneiss) rocks originating from the Hercynian basement, while the substratum of the Lorraine plateau is composed by a superposition of limestone and marl sedimentary layers (Maire and Corbonnois, 2000). The longitudinal profile of the Moselle river is characterized by a slope of 10% at its upstream extremity, rapidly decreasing to 0.4% at Remiremont and reaching an average value of 1.7‰ further downstream. The predominance of impermeable rocks and steep sectors contributes to propagate rapidly the flows to Epinal, while the physiography of the catchment contributes to the flood peaks concomitance, which generates major hydrological events downstream (Maire and Lasserre, 1991).

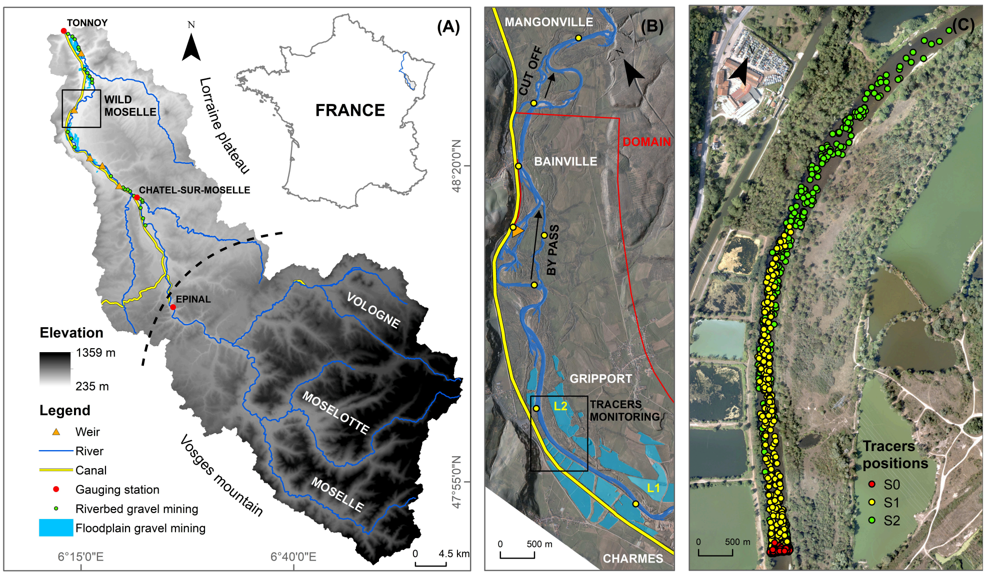

Figure 5.1: Study site (A) location of the "Wild Moselle river" in the Moselle Basin, (B) longitudinal extension of the 2D hydro-sedimentary model $\mathcal{M}_{f,p}$ (C) position of tracers over time.

The precipitation are unevenly distributed with a mean annual values of $800mm$ over the Lorraine plateau versus $1100mm$ over the Vosges mountains, where important variations are observed with locally more than $2000mm$ on the crest (Beck and Corbonnois, 2003). Precipitations occurs mainly during the winter (November-February) with monthly more than $200mm$ over the Vosges Mountains. The river hydrological regime is pluvial with high flows in the winter-spring (2- and 10-year floods are $405m^3/s$ and $651m^3/s$ respectively) and low flow in the summer, while the mean interannual flow is of $42m^3/s$ at the gauging station of Châtel-sur-Moselle.

The sediment supply of the Moselle river arises mainly from the remobilization of Holocene alluvial deposits composed of gravel and sand carried by the river from the Vosges Mountains (Maire and Lasserre, 1991). This sediment redistribution occurs primarily though bed and/or bank erosion, where the lateral mobility is strongly influenced by the valley width that varies according to the nature of the eroded substratum. The river morphodynamic was altered by (i) the construction of a canal which reduced laterally the flood expansion area and concentrates the flow into the river bed, (ii) the construction of dams which locally modify the river competence and interrupt the sediment transport and (iii) the massive sediment extraction which occurred in the river bed ($1950-1980$) and thereafter in the floodplain (Figure 5.1 a). The destabilization of the river morphodynamic equilibrium conducted to morphological adjustments that result into the river bed incision which induced locally an emptying of the river bed sediment stock (Beck and Corbonnois, 2003).

A meandering reach of $12km$ length, located between Gripport and Bayon at the western foothills of the Vosges Mountains, was however relatively less affected by human activities (Figure 5.1 a). This section was classified in 2006 as regional natural reserve (the "Wild Moselle") in order to protect the water resources as well as the biodiversity (Figure 5.1 b). This reach of moderate energy, with an average specific stream power of $50W/m^2$, represents one of the most dynamic section of large rivers in the northeast of France. It is characterized by a catchment area of $1,758\,km^2$, a sinuosity of 1.4, an average slope of 1.2, a bankfull width (resp. discharge) of about $60m$ (resp. $250m^3/s$) and a surface (resp. subsurface) D_{50} of $30mm$ (resp. $13mm$).

Although this sector was protected, the propagation of morphodynamic adjustments (regressive and progressive erosion) initiated by actions carried out at the edge of the natural reserve converge towards the central part of the reach. This trajectory, towards a new dynamic equilibrium, could induce a river avulsion which may destabilize infrastructures. The present research is part of a project aiming to study different scenarios of management/restoration of the lateral mobility of the "Wild Moselle" river, based on 2D morpho-sedimentary simulations. The calibration of non-uniform sediment transport presented in this article is therefore crucial, since spatio-temporal evolutions of the riverbed grain size distribution resulting from sediment transport, may strongly influences the river morphodynamic.

5.3 Methods

The aim of this new method is to calibrate the grain size distribution (GSD) of the bedload transport predicted by an hydro-sedimentary model. This calibration was started by Piasny et al. (2023b), by estimating a hiding-exposure factor $\zeta_{k,\theta}$, which was applied to the critical Shields parameter θ_{cr}. The GSD of the bedload transport predicted by the model, when applying $\zeta_{k,\theta}$, was however finer than observed which lead us to apply also, a hiding-exposure factor $\zeta_{k,\Phi}$ (called "trapping factor") to correct the bedload transport rate $\Phi^{*,\theta}$.

The bedload transport rate $\Phi_k^{*,\theta,\Phi}$ corrected for hiding-exposure and trapping effects is expressed as follows:

$$\Phi_k^{*,\theta,\Phi} := \alpha p_k \zeta_{\Phi,k}(\theta_k - \zeta_{\theta,k}\theta_{cr})^{3/2} \tag{5.8}$$

where p_k is the fraction of class k available in the active layer, $\alpha = 3.4$ is empirical coefficients and $\theta_{cr} = 0.035$ is the critical Shields parameter which were estimated in Piasny et al. (2023c).

Given that $\zeta_{k,\theta}$ is computed as $\theta_{cr,Dk}/\theta_{cr,Dr}$ where $\theta_{cr,\square}$ is the critical Shields parameter for particle motion estimated from tracers (colored particles and pit-tags) entrainment, we propose to compute $\zeta_{k,\Phi}$ as $V^*_{D_k}/V^*_{D_r}$ where $V^*_{\square}$ is the particle dimensionless virtual velocity, associated to a particle diameter, estimated from bedload tracers (pit-tags) survey.

The virtual velocity V_i (Hassan et al., 1992; Haschenburger and Church, 1998) of each tracer i is computed as:

$$V_i = \frac{L_i}{T_i} \tag{5.9}$$

and expressed in its dimensionless form as:

$$V_i^* = \frac{V_i}{\sqrt{gD_i}} \tag{5.10}$$

where L_i is the distance traveled by the tracer and T_i is the duration of the flow competent to transport this tracer, D_i is the tracer size and g the gravitational acceleration.

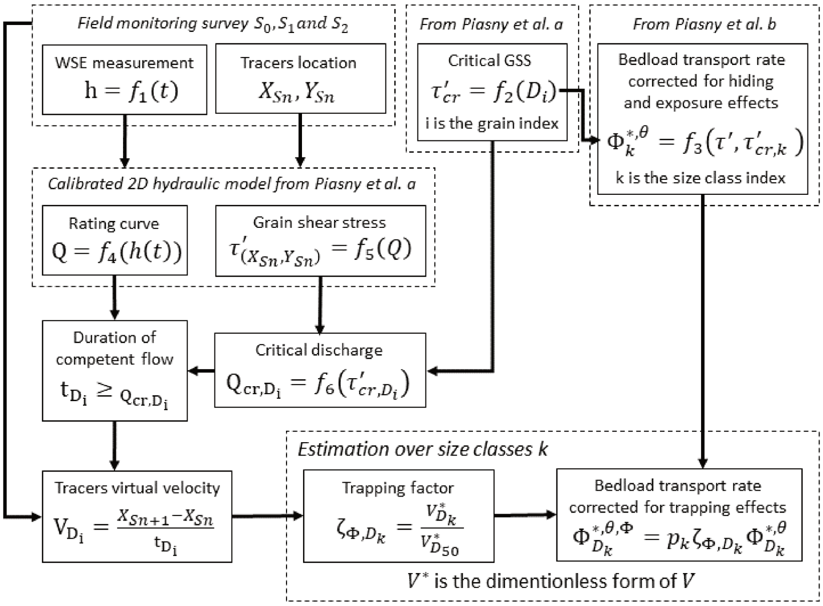

Figure 5.2: Flowchart of the main components of the method for calibrating the bedload transport composition for a 2D hydro-sedimentary model using complementary data on particle mobility and dynamics.

This distance is estimated by subtracting the tracer final longitudinal position $X_{i,s+n}$ from the tracer initial longitudinal position $X_{i,s}$. The duration of the flow competent to transport the tracer is computed by integrating the time $t_{>Q_{c,i}}$, during which the river discharge Q is greater or equal to the critical discharge $Q_{c,i}$ for the tracer motion. The river discharge is estimated by converting a time-series of water surface elevation (WSE) measurement into a discharge hydrograph, using a rating curve derived from the outputs of a calibrated 2D hydraulic model. The critical discharge for the tracer motion $Q_{c,i}$ is estimated by determining the discharge at which the grain shear stress τ' computed with the 2D hydraulic model at the tracer location X_i, Y_i, equals the critical grain shear stress for the tracer motion $\tau'_{cr,i}$ established in Piasny et al. (2023b). All these steps are summarized in the flowchart presented below (Figure 5.2) and detailed in the following subsections.

5.3.1 Tracer travel distance estimation

The distance L_i traveled by each tracer i, which was used to compute their virtual velocity (equation 5.9), was estimated from a field monitoring of the tracer's positions, performed once a year during three years. The method employed to (i) equip and inject these tracers, (ii) detect their positions and (iii) compute their travel distance and characterize their mobility, are presented in following subsections.

5.3.1.1 Tracer equipment and injection

The study was performed using a large number of tracers ($n = 450$) of different sizes, in order to overcome the uncertain recovery rates (Chardon et al., 2021b). Particles were equipped with low-frequency Passive Integrated Transponders (PIT- tags, Lamarre et al., 2005) distributed by Texas Instruments (2001). Transponders of 32 mm-long were used rather than 23 mm-long, within the limit of particle size, and preferentially inserted in the shortest particle axis to improve detection (Arnaud et al., 2015). Tracers diameter are representative of the riverbed grain size ($16 - 128mm$), measured along the reach of injection (Figure 5.4 and 5.3), using a grid-by-number pebble counts ($n_{tot} = 1200$). Samples were collected during summer 2018, following a variant of the Wolman method (1954) proposed by Bunte and Abt (2001), with a frame and a round-hole template to reduce the bias in particle selection on submerged areas. Tracer grain size distribution was slightly different from bed surface (Figure 5.3), because particles were equally distributed into 5 classes, in order that each grain size has the same probability to be recovered (Arnaud et al., 2017).

Tracers were injected along a large straight reach located at the upstream part of the study site (Figure 5.1), with high banks, a flat bed, trapezoidal cross-sections and where no significant morphological evolutions were observed over time. This reach was selected in order to ensure (i) that the hydrodynamic conditions were relatively constant along the paths of the tracers (no spatio-temporal variation of the river longitudinal profile or of the river cross-sections shape) and (ii) that the tracers move only in the longitudinal direction (no secondary flows). Tracers were injected (I) across the river section in spring 2018, when the riverbed was wadeable (Figure 5.4). They were seeded around 18 injection points (25 tracers/point with 5 tracers/class) laterally distributed at $5m$ intervals along 2 transects separated by $10m$, in order to minimize particle hiding effects during detection.

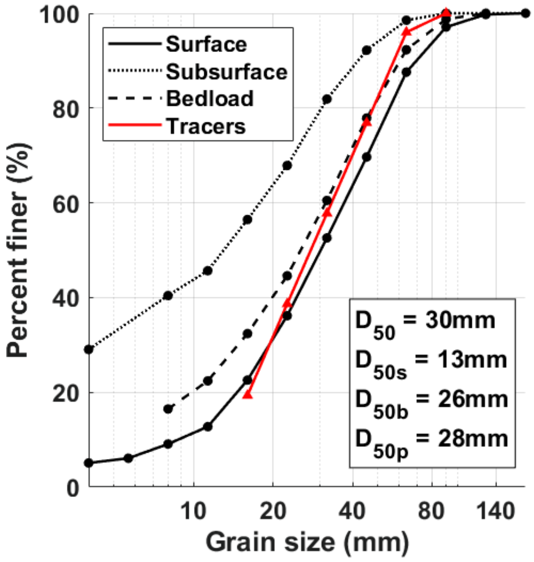

Figure 5.3: Cumulative grain size distribution of (i) the bed surface material, estimated from 6 samples collected along the reach of injection by grid-by-number pebble counts ($n_{tot} = 1200$), (ii) the bed subsurface material, estimated from a volumetric sample collected on a bar located in the middle of the study area ($m_{tot} = 346kg$), (iii) the bedload material, estimated from bedload samples collected in the middle of the study area during a flood of bankfull discharge using a Helley-Smith sampler ($m_{tot} = 245kg/s$) and (iv) the injected pit-tags ($n = 450$) with corresponding median diameter of the bed surface (D_{50}), the bed subsurface (D_{50s}), the bedload (D_{50b}), the pit-tags (D_{50p}).

5.3.1.2 Tracer detection

The Radio Frequency Identification (RFID) technology enables to detect tracers, using a antenna of $1.2m$ long and $0.5m$ width connected to a RFID reader, developed by the CIPAM Corporation. The reading distance of this rectangular antenna allowed to detect tracers over a section of $1.5m$ width and an air thickness of $0.9m$. The control box of the RFID reader was connected to a computer recording the tracers IDs with the date and time of their detection, using the ComTools software (V2.4.4.0). The electronic devices were placed on a board traversed by a steel pin fixed to the center of the antenna in order to keep the board vertical to the antenna regardless to the depths. The antenna of a centimeter accuracy differential GPS (DGPS) set in tracking mode was fixed at the top of the steel pin to record every second the position of the detection antenna. The tracer coordinates are determined during post-processing by time synchronizing the computer records and GPS tracks with one second accuracy, using the Matlab software (R2018a). The coordinates of tracers recovered multiple times during a survey, were automatically averaged, in order to improve the accuracy of the tracers localization. This original setup (Figure 5.1) allowed to (i) reduce the number of operators (no need to hand write tracers ID and GPS positions), reduce physical effort (no need to carry heavy equipment), (iii) reduce the time of post-processing (no transcription of field data) and (iv) increase the horizontal precision of the tracer localization (no discrepancy between antenna and GPS position), which is estimated at $3m$ in XY.

The surveys were performed by two persons, in summer 2018 (S_0), 2019 (S_1) and 2020 (S_2), when the riverbed was wadeable (Figure 5.1). The tracers were detected through pedestrian searches, with the antenna being pulled manually, except in deeper areas ($d > 1.5m$) located along the concave bank of the curved reach, where the antenna was towed by a boat. This rectangular antenna was pulled between two string of $50m$ long spaced by $1.8m$ (maximum lateral reading distance), successively shifted across the river section, in order to limit recovering between passages and optimize the field monitoring. The surveys were ended in the downstream direction, when the number of tracers found along a reach of $50m$ was less than or equal to 3. The tracking area, and thus the field survey duration, increased as tracers propagated downstream, from a 40-m-long reach of $0.2ha$ covered in 1/2 day (S_0), to an 750-m-long reach of $2.5ha$, covered in 3 days (S_1) and a 1.4-km-long reach of $5ha$, covered in 6 days (S_2).

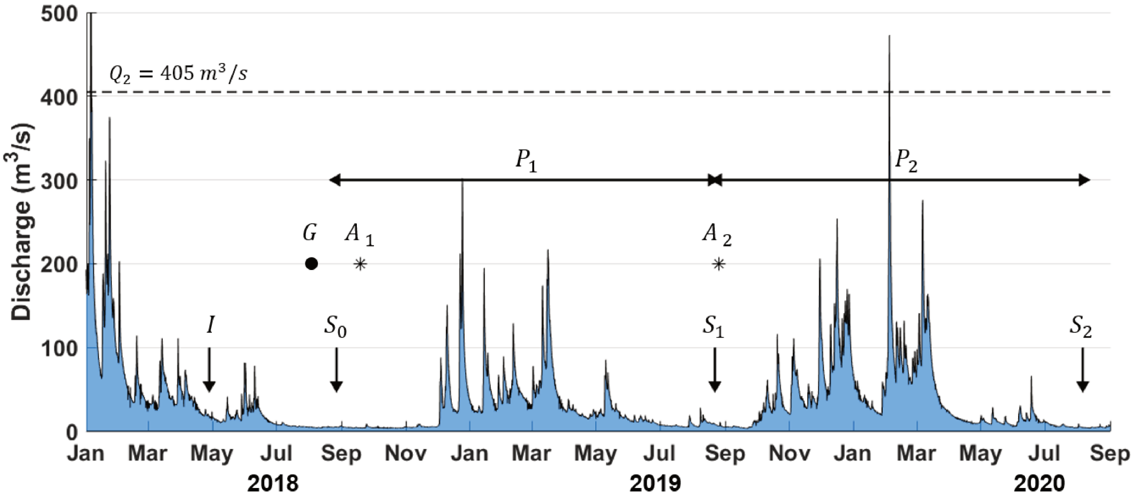

Figure 5.4: Monitoring framework related to the flow hydrograph of the Moselle river at the Châtel-sur-Moselle gauging station. A_n indicates the dates of aerial topo-bathymetric acquisitions, G indicates the date of surface and subsurface material grain size measurements, I indicates the date of tracer injection, S_n indicates the dates of tracer surveys and P_n is the monitoring periods between two tracer surveys.

5.3.1.3 Tracer travel distance

The tracers positions were projected onto the channel centerline, using the linear referencing tool available in ArcMap (v10.6), in order to only consider the tracers longitudinal displacement and take into account the channel curvature (Figure 5.1). The tracer's longitudinal position $X_{i,Sn-1}$ found at survey S_{n-1} was subtracted from the tracer's longitudinal position $X_{i,Sn}$ found at survey S_n, in order to compute the distance traveled by each tracer i during both periods P_n.

$$L_{i,P_n} = X_{i,Sn} - X_{i,Sn-1} \tag{5.11}$$

The tracers missing at S_0 but recovered at S_1 were set by default at injection position, considering that they remained immobile after injection and were not found because of hiding effects. The tracers having travel distances of less than $5m$ were considered as immobile, according to geolocation accuracy, as well as tracers recovered at less than $15m$ from transect of injection. The mean distance $\overline{L_{k,Pn}}$ traveled by each size class k was computed in order to identify if the mode of sediment transport was rather partial or full during P_n.

$$\overline{L_{k,P_n}} = \frac{\sum L_{i,P_n}}{n_i} \tag{5.12}$$

were $L_{i,Pn}$ is the distance travelled by a mobile tracer i from size class k during P_n and n_i is the total number of mobile tracers from this size class founded in both S_{n-1} and S_n. The travel distance L_{i,P_n} and size D_i of each mobile tracers i were scaled (equation 5.13 and 5.14), in order to compare the relative travel distance of tracers from the Moselle river to tracers from other studies Church and Hassan (1992).

$$L^*_{i,P_n} = \frac{L_{i,P_n}}{\overline{L_{k_{D50},Pn}}} \tag{5.13}$$

$$D^*_i = \frac{D_i}{D_{50s}} \tag{5.14}$$

were $L^*_{i,Pn}$ is the scaled traveled distance, D^*_i is the scaled tracer size, $\overline{L_{k_{D50},Pn}}$ is the mean distance traveled by the size class k containing the median surface grain size D_{50} and D_{50s} is the median subsurface grain size. The D_{50s} was estimated from a volumetric sample (Figure 5.3) collected during summer 2018 (Figure 5.4) on a emerged a bar located in the middle of the study site. The mass of the sample (m = 346kg) was sufficiently important to exceed the minimum sample-mass (mmw) suggested by Church et al. (1987) and computed as follow:

$$mmw = 2.882D_{max} - 47.6 \tag{5.15}$$

where D_{max} is maximum diameter of the bed surface, which was estimated by averaging the diameter of the 30 coarsest particles observed on the surface of the bar.

5.3.2 Duration of competent flow

The duration T_i of the flows competent to transport each tracer i, used to compute their virtual velocity (equation 5.9), was estimated from results of numerical simulations, performed under steady state conditions (Q ranging from 50 to $500m^3/s$ at $10m^3/s$ intervals) without bedload transport. The choice of using 2D hydraulic steady state simulations to produce bed shear stress maps related to an inflow discharge value stems from the following reasons: (i) it is a reasonable hypothesis given the low temporal variability of spatially distributed quantities of interest, over a short river reach; (ii) to save computational time and storage since writing such output could be heavy and require software modifications; (iii) overall, we believe it makes our method more easily transposable to other zones with a limited hydraulic modeling effort.

The following subsections describe (i) the employed modeling system, (ii) the construction and parametrization of the hydro-sedimentary model used to estimate hydrodynamics condition along the study reach and (iii) the methodology used to estimate the duration of the competent flow.

5.3.2.1 Numerical model description

Numerical simulations were performed using the hydraulic solver Telemac-2D, internally coupled to the morphodynamic module Sisyphe of the TELEMAC-MASCARET modeling system. This modeling system is an open-source well-tested and widely-used software employed in many fields of application, that is developed by the French Electricity Board (EDF). All modules of this suite of solvers enable parallel computations on unstructured meshes with finite-element or finite volume algorithms (Hervouet, 2007). The components of the hydrodynamic (2D shallow water equations) and sediment transport (bed shear stress partitioning) module used to estimate the duration of competent flows are described below.

Hydrodynamic module

Telemac-2D model solves the shallow water equations (SWE) in their conservative forms (momentum and continuity) which are derived from the full 3D Navier-Stokes equations (Villaret et al., 2013; Ancey, 2016; Dingman, 1984). These equations were simplified in the vertical direction assuming hydrostatic pressure distribution and negligible vertical acceleration wherein turbulence effects are taken into account using a constant viscosity model. The first term on the right hand-side of the two equations of momentum is the pressure gradient, the second is the bottom friction, and the third is the horizontal diffusion.

$$\frac{\partial H}{\partial t} + \frac{\partial (UH)}{\partial x} + \frac{\partial (VH)}{\partial y} = 0 \tag{5.16}$$

$$\frac{\partial U}{\partial t} + U\frac{\partial U}{\partial x} + V\frac{\partial U}{\partial y} = -g\frac{\partial Z_s}{\partial x} + \frac{\tau_x}{h} + \frac{1}{h}div(h\nu.grad(U)) \tag{5.17}$$

$$\frac{\partial V}{\partial t} + U\frac{\partial V}{\partial x} + V\frac{\partial V}{\partial y} = -g\frac{\partial Z_s}{\partial y} + \frac{\tau_y}{h} + \frac{1}{h}div(h\nu.grad(V)) \tag{5.18}$$

where h is the water depth (m), U and V are horizontal depth averaged velocity components (m/s), g is the gravity acceleration (m/s^2), Z_s is the free surface elevation (m), t is the time (s), x and y are horizontal space coordinates (m), ν is the depth-averaged eddy viscosity (m^2/s) and τ_x (resp. τ_y) is the bed shear stress (N/m^2) along the Cartesian x-axis (resp. y-axis) as:

$$\tau_b = \sqrt{\tau_x^2 + \tau_y^2} = \sqrt{\left(\frac{1}{2}\rho C_f U^2\right) + \left(\frac{1}{2}\rho C_f V^2\right)} \tag{5.19}$$

where ρ is the water density (kg/m^3) and C_f is a dimensionless quadratic friction coefficient calculated as

$$C_f = \frac{2g}{K_s^2 h^{1/3}} \tag{5.20}$$

where $K_s\,(x, y)$ is the Strickler coefficient ($m^{1/3}/s$) that generally needs to be calibrated to fit flow observations. This hydraulic friction coefficient is considered, spatialized which is affordable with our dense dataset, in order to finely compensate data-model errors.

Morphodynamic module

Sisyphe model corrects the total bed shear stress τ_b (N/m^2) issued from the hydrodynamic model (equation 5.19) using a factor μ to express the grain shear stress τ' (N/m^2), which is the only component acting on the bedload transport (Mendoza et al., 2017):

$$\tau' = \mu \tau_b \tag{5.21}$$

where the correction factor $\mu = C'_f/C_f$ corresponds to the ratio between friction coefficient C_f issue from hydrodynamic model and friction coefficient C'_f only due to the grain friction as:

$$C'_f = 2\left(\frac{\kappa}{log(12h/h'_s)}\right)^2 \tag{5.22}$$

where κ is the von Karman coefficient, h the water level (m) and $h_s^{'}$ the roughness height (m) defined as:

$$h_s^{'} = \alpha_{h'_s} d_{50} \tag{5.23}$$

where $\alpha_{h'_s}$ is a calibration parameter (3 by default; Tassi and Villaret 2014) and d_{50} (m) is the sediment mean diameter. This parameter of calibration varies according to the presence of bedforms, Mendoza et al. (2017) found $\alpha_{h'_s} = 37$ for dunes and $\alpha_{h'_s} = 3.6$ for bars.

5.3.2.2 Numerical hydro-sedimentary model construction and calibration

The numerical model $\mathcal{M}_{f,p}$ used in this study is a submodel (Figure 5.1) of a 2D hydro-sedimentary model of the study site $\mathcal{M}$, built by Piasny et al. (2023b) from an accurate digital elevation model (Lidar DEM from 2018) and calibrated over the highest flood events observed in 2018 ($Q = 300m^3/s$), using a large field dataset. This submodel $\mathcal{M}_{f,p}$, while having a similar resolution in terms of mesh cells size than the large extent model $\mathcal{M}$, enables to save computational resources.

The spatially distributed friction coefficients of $\mathcal{M}$ were calibrated using relatively dense water surface elevation time series recorded by 12 limnimeters distributed along the $12km$ long river reach, and discharge gauging carried out in the bypass channel. The dimensionless critical bed shear stress for particle motion was calibrated by Piasny et al. (2023b) from flow competence, estimated during the highest flood event observed in 2018, using painted bed patches and pit-tags. The sediment transport equations were selected and calibrated in Piasny et al. (2023b) using *in situ* bedload measurements performed during a moderate flood event, that occurred in March 2020.

Model construction

The longitudinal extension of the model $\mathcal{M}$ previously built in Piasny et al. (2023b) along the entire study site was reduced for $\mathcal{M}_{f,p}$ submodel to the upstream part of the reserve, between Charmes and Mangonville, again, to reduce computational times (Figure 5.1). The submodel downstream limit was placed between the bridge and the meander cutoff, where the Moselle river is not bypassed by secondary channels, to avoid setting multiple downstream boundary conditions. The lateral extension of this submodel follows the limits of the previous model, from the hill summits to the canal dikes, since simulated inundation extent is contained within this area. The submodel domain, covering a 11 km-long section of the Moselle river, was discretized into a computational grid composed of 653767 triangular elements and 328278 nodes generated using

Bluekenue software. This grid is composed of structured submeshes located into the riverbed and unstructured mesh located into the floodplain with mesh sizes of $3.5m$ and $5m$, respectively. The size of the mesh was locally refined at diffluences and confluences or in narrow river sections such as in the dam bypass channel ($2.7m$) or in the diversion canal of the dam ($2m$). The mesh node elevation were interpolated from accurate digital elevation models (DEMs) of $1m$ resolution generated from airborne LiDAR topo-bathymetric acquisition, completed by bathymetric campaigns carried out over unobservable deepest flow areas (depth $> 2.4m$). The DEM from September 2018 (A_1) was used to model the hydrodynamic conditions of period P_1, while the DEM from August 2019 (A_2) was used to model hydrodynamic conditions of period P_2. This submodel has 3 boundary conditions distributed along the Moselle river: one upstream at Charmes, one lateral at the diversion canal of the dam and one downstream at Mangonville.

Model parametrization and calibration

At the upstream boundary condition of submodel $\mathcal{M}_{f,p}$, we imposed constant inflows discharges Q, from 40 to $500m^3/s$ at $10m^3/s$ intervals, in order to build a catalog of all hydrodynamic conditions which occurred during the studied periods (Figure 5.4). At the lateral boundary condition, we imposed a constant output discharge of $3.2m^3/s$ which corresponds to the discharge measured into the diversion canal minus the estimation of lateral inflows from the tributaries of the study reach. At the downstream boundary condition of submodel $\mathcal{M}_{f,p}$, we imposed a model derived rating curve built from results of successive steady state simulations, which was performed using the 2D hydro-sedimentary model $\mathcal{M}$ of the whole study zone calibrated by Piasny et al. (2023b). The influence of this downstream boundary condition on hydrodynamic conditions modelled at the tracers locations was assessed by modifying the rating curve by $\pm 1m$.

The friction coefficients calibrated independently of the mesh size, for model $\mathcal{M}$ in previous studies, were mapped onto the submodel $\mathcal{M}_{f,p}$ domain with for different friction zones: $K_s := 47$ $m^{1/3}/s$ in the main channel riverbed, $K_s := 30$ $m^{1/3}/s$ at the upstream part of bypass channel, $K_s := 8$ $m^{1/3}/s$ at the downstream face of the dam and $K_s := 8$ $m^{1/3}/s$ in the floodplain. The validity of those Strickler coefficients (calibrated in Piasny et al. (2023b) on the flood event of 2018) in $\mathcal{M}_{f,p}$, was verified for each studied period (with different DEM and friction zones delimitation than in calibration). By comparing the WSE simulated during the highest flood event of each period ($300m^3/s$ and $470m^3/s$) to the WSE recorded by the limnimeter L1 and L2 located on either sides of the tracer locations (Figure 5.1 b). These unsteady simulations were performed using the finite-element numerical solver of Telemac-2D (version 8.1) run on 42 parallel processors with a constant time-step of 0.5, which enables to respect a CFL value of 1 in studied cases. The total bed shear stress τ and the correction factor μ were computed for each discharge, using Sisyphe (version 8p1) run without bedload transport, in order to avoid simulating unrealistic morphological evolutions. The correction factor was derived from a roughness height computed (equation 5.23), using the median diameter D_{50} of the bed surface of $30mm$ (Figure 5.3) considered constant along the river reach, and with the calibration parameter $\alpha_{h'_s}$ set to 3 considering flat bed conditions during the studied flood (Villaret et al., 2013).

5.3.2.3 Duration of competent flow

The duration T_i of flow competent to transport each tracer i was computed by integrating the time $t_{>Q_{c,i}}$during which the river discharge Q was greater or equal to the critical discharge $Q_{c,i}$ for the tracer i motion. As explained below, both Q and $Q_{c,i}$ were estimated from results of numerical simulations performed using the hydro-sedimentary model built along the study reach.

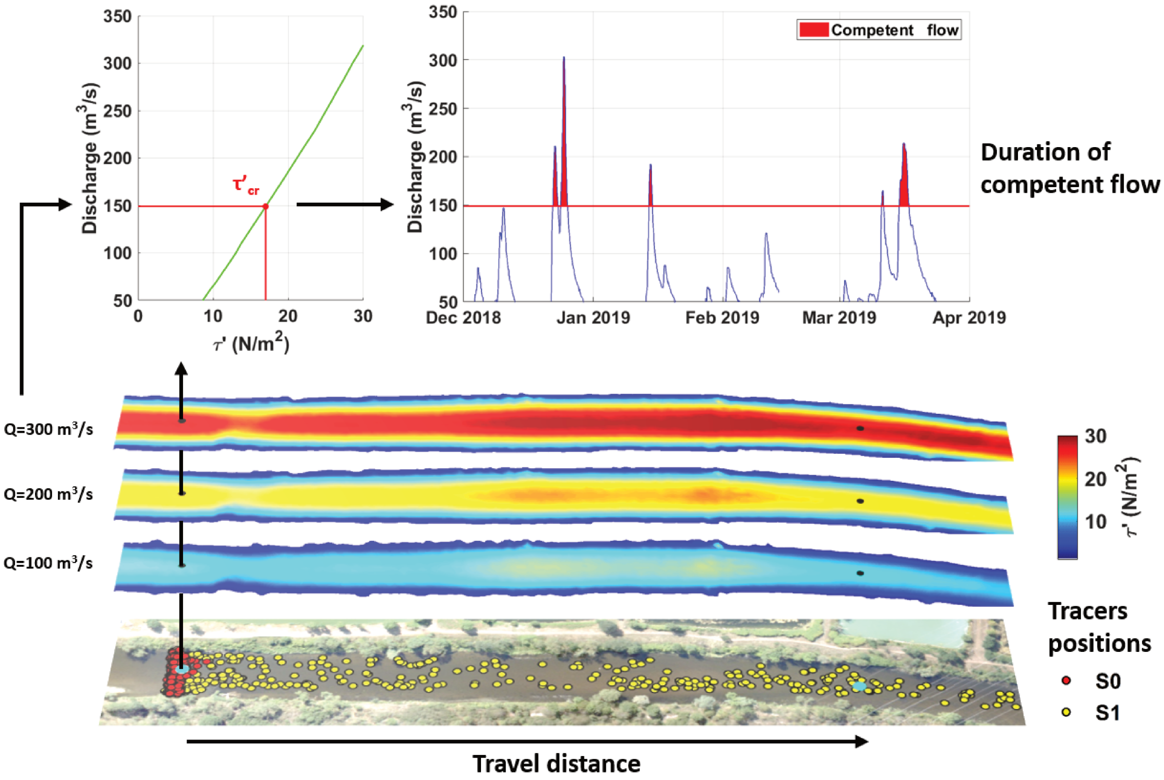

Figure 5.5: Flowchart of the methods employed to estimate the distances traveled by the tracers and the duration of the flow competent to transport these tracers. These methods are based on the results of field surveys (S_n) and of the catalog of 2D hydro-sedimentary model outputs for different inflow discharge.

River discharge estimation

The river discharge was estimated along the study reach by converting the time series of water surface elevation (WSE) recorded by the limnimeter L2 (Figure 5.1) into a discharge hydrograph, using a model derived stage-discharge relation. The WSE was measured by a 5 min interval with a Leveloggers Edge M10 inserted in a strainer tube sank into the riverbed near to the bank and leveled using a centimetric-accuracy Leica Viva GNSS. The device elevation was readjusted by comparing the WSE records to the free surface elevation measured by the topo-bathymetric LiDAR which allows a vertical accuracy estimated at $\pm 3cm$. The stage-discharge relation $z = f(Q_i)$ was established by extracting the free surface elevations, from the catalog of model outputs for different inflow discharge Q defined in section 5.3.2.2, at the location of the limnimeter L2. The obtained hydrograph was smoothed using wavelets (Matlab, R2018) and the cumulative flows were calculated for each period to be compared for validation to the value recorded by the gauge stations located upstream and downstream from the study site (Figure 5.1 a).

Critical discharge for tracers motion

For each tracer i, at its $X_{i,Sn}, Y_{i,Sn}$ (Figure 5.5) position at the beginning of each study period defined above, the catalog of model outputs for different inflow discharge Q_i defined in section 5.3.2.2, enables to estimate an array of corresponding local grain shear stress $\tau'(X_{i,Sn}, Y_{i,Sn}, Q_i) = \mu\tau_b(X_{i,Sn}, Y_{i,Sn}, Q_i) = f(U, V, h; X_{i,Sn}, Y_{i,Sn}, Q_i)$. Hence, a relation between τ'_i and Q_i can be built, by extracting τ'_i from each results of steady state simulations. These relations were built from simulation results based on the DEM of 2018 (A_1) for tracers located at S_0 and from simulation results based on the DEM of 2019 (A_2) for tracers located at S_1 and S_2, in order to take into account the river morphological evolutions. From each $\tau'_i - Q$ relation associated to each tracer i, a critical discharge $Q_{c,i}$ was estimated using a linear interpolation to determine the discharge Q at which, the critical grain shear stress $\tau'_{cr,i}$ for the tracer i motion is reached. This critical threshold was computed as follows:

$$\tau'_{cr,i} = \theta_{cr,i} g \left(\rho_s - \rho\right) D_i \tag{5.24}$$

where $\tau'_{cr,i}$ is the critical grain shear stress for tracer motion, g is the gravitational acceleration, D_i is the size of the tracer, ρ and ρ_s are respectively the fluid and sediment volume weight and $\theta_{cr,i}$ is the critical Shields parameter, computed as follow, according to Piasny et al. (2023b). The critical Shields parameter for tracer i writes, by injecting $D_{50} = 0.03$ and $\theta_{cr,D50} = 0.035$ into equation 5.25:

$$\theta_{cr,i} = 0.035 \left(\frac{D_i}{0.03}\right)^{-0.6} \tag{5.25}$$

The discharges for which each tracer is transported were compared between surveys $S_{n=0..2}$, by plotting the critical discharge $Q_{c,i}$ estimated at S_n against the critical discharge $Q_{c,i}$ estimated at S_{n+1}, in order to study if these results vary over time, as tracers propagate towards the downstream direction. The flow competence duration was calculated for each studied period P_n, by cumulating time $t_{\geq Q_c}$, between each survey S_n, during which the river discharge Q, estimated at 5 minutes interval, was greater than or equal to the critical discharge Q_c for tracer motion. These durations were compared as a function of the tracers size and of the tracers lateral position into the channel. These analyses were only performed using mobile tracers that were recovered during all the surveys, in order to study the spatio-temporal variation of the critical discharge of the same tracer.

5.3.3 Calibration of the non-uniform sediment transport

The composition of the bedload predicted by a model depends on the proportion of each size class transported, which varies according to the capacity of the flow to transport each size class and to the availability of each size class. The sediment transport capacity is predicted using bedload transport laws, which can be corrected to consider effects of non-uniform grain size distribution, on particles motion (hiding-exposure effect) and on particles transport (the proposed trapping effect). The volume of available sediments is determined by the proportion of each size class implemented into the active layer and to the active layer thickness. The following subsections presents (i) the discretization into the model of the bed structure and bed material and (ii) the calibration of the predicted bedload grain distribution using a specific coefficient of correction for the hiding-exposure and trapping effects.

5.3.3.1 Discretization of the bed material and bed structure

The river bed was discretized into an active and a substrate layer. The active layer thickness was estimated from measurements of the total scour and fill occurring during flow events. These measurements were conducted using 20 scour chains (Laronne et al., 1994) installed across the river at 6 easily accessible emerged gravel bars distributed along the Moselle river. The scour chains of $50cm$ long, composed of links of $7cm$ long to correspond to the bed surface D_{90}, were fixed to a snap hook, which could vertically slide along a concrete bar driven into the riverbed. This bar of $1cm$ diameter and $1m$ long protrudes slightly from the bed surface, with an orange steel cap welded on the top, in order to make them easier to find. This configuration allowed to measure the bed erosion (variation in distance between the chain top and the steel cap bottom) and the sediment deposits (thickness of the sediment deposited over the chain) by placing a metal square on the top of the chain. The total scour and fill were monitored after 3 morphological floods ($Qmax = 303m^3/s$; $214m^3/s$ and $254m^3/s$) and the most frequently measured sediment thickness (3 times) was of $7cm$ (Figure 5.6). This thickness approximately corresponds to the D_{90} of the bed surface, as estimated by Parker (1992). The active layer was then set to constant thickness of 7cm.

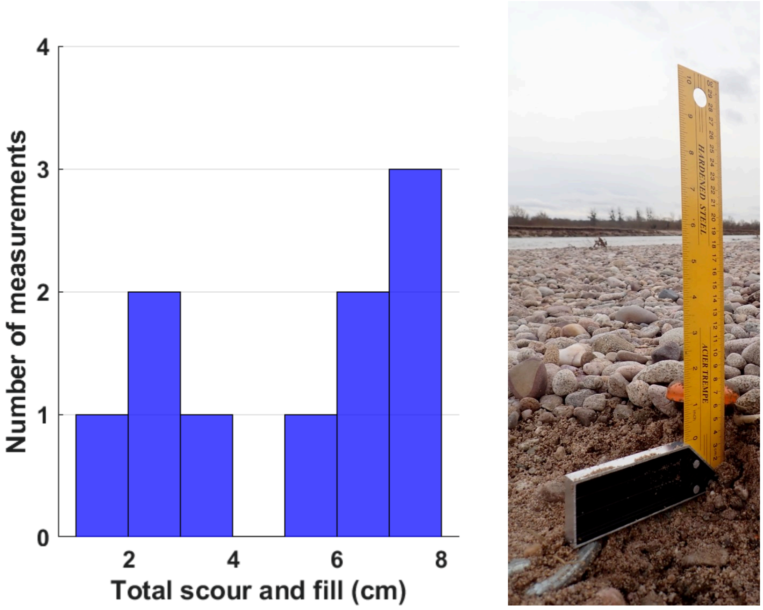

Figure 5.6: Distribution of total scour and fill measured during 3 flow events ($Qmax = 303m^3/s$; $214m^3/s$ and $254m^3/s$) by 20 chains ($n_{tot} = 60$) installed across the river at 6 easily accessible emerged gravel bars of the Moselle river (left). Results excludes cases of (i) no morphological evolutions ($n = 29$), (ii) river incision ($n = 3$), (iii) lost chains ($n = 4$) and (iv) stolen chains ($n = 14$). Measurement of total scour and fill using a scour chain (right).

The grain size distribution of the bed surface material was set into the active layer, while the grain size distribution of the subsurface material was set into the substrate layer (Figure 5.3). The granulometric curve of the bed surface material was discretized into 1 to 6 size classes of varying sizes (Figure 5.7), and short steady state simulations were performed in order to identify when the predicted bedload becomes independent of the number of classes used in the model.

The size classes were implemented in the model based on a representative diameter D_k (logarithmic mean of the class limits) and a percentage p_k (volume of the class k divided by the total volume of sediments). The simulations were carried out using the 2D hydro-sedimentary model built to estimate the duration of competent flow (see section 5.3.2.2), re-parameterized in order to compute the sediment transport. The roughness height was set as constant ($h_s^{'} = 90mm$) in order to avoid that the variations in riverbed composition (Figure 5.7) changes the hydrodynamic conditions (equation 5.22) and thus the bedload transport between simulations.

The bedload transport was computed using equation 5.2 with a critical Shields parameter θ_{cr} of 0.035 estimated for the D_{50} by Piasny et al. (2023b), a coefficient α of 3.4 estimated by Piasny et al. (2023c) and the coefficient β of 3/2 proposed by Meyer-Peter and Müller (1948). The simulations were run at a constant discharge of $300m^3/s$ ($Q_{max,P1}$) as the hydrodynamic conditions at this discharge ($\overline{\theta_{d50}} \approx 0.05$) were very close to the conditions observed during *in situ* bedload measurements. These measurements were conducted in the middle of the study area (Figure 5.1), using a Helley-Smith sampler deployed from a bridge (Piasny et al., 2023c). The GSD of the bedload samples (Figure 5.3), were then used as reference to calibrate the bedload composition in the hydro-sedimentary model. The runs were performed during 3 seconds, in order to reach an equilibrium between hydrodynamic conditions and sediment transport, and the bedload was extracted at the cross-section located at the site of tracers injection. The results were compared to determine when the predicted bedload is independent of the number of size classes implemented into the model and this sensitivity analysis was completed by a simulation run with 10 size classes.

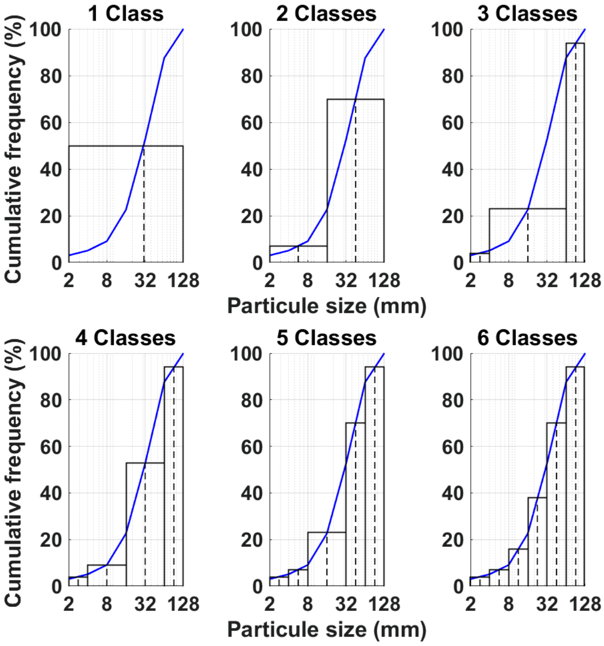

Figure 5.7: Discretization of the granulometric curve of the bed surface material into different numbers of size classes with corresponding representative diameters. This curve was determined from Wolman pebble counts performed along the injection reach.

5.3.3.2 Calibration of the bedload grain size distribution

The bedload grain size distribution was predicted (i) using first a correction factor $\zeta_{\theta,k}$ for hiding-exposure effects, applied to the critical Shields parameter θ_{cr} (equation 5.4) and then (ii) adding a correction factor $\zeta_{\Phi,k}$ for trapping effects, applied to the bedload transport rates Φ_k^* (equation 5.5). Both results, as well as results obtained without coefficient of corrections, were compared to the grain size distribution of bedload samples, collected under similar hydrodynamic conditions (Figure 5.3). This made possible to assess improvements on prediction of bedload grain size distribution. Each simulation was performed with the parametrization presented in 5.3.3.1, using the optimum number of size classes determined in that section.

The factor of correction $\zeta_{\theta,k}$ for hiding and exposure effects was estimated by Piasny et al. (2023b) as follows:

$$\zeta_{\theta,k} = \left(\frac{D_k}{D_{50}}\right)^{b_\theta} \approx \frac{\theta_{cr,Dk}}{\theta_{cr,D50}} \tag{5.26}$$

recalling that $\theta_{cr,Dk}$ is the critical Shields parameter of the representative diameter D_k of the size class k, $\theta_{cr,D50}$ is the critical Shields parameter of the median diameter D_{50} of bed surface and b_θ is the hiding-exposure exponent. Both $\theta_{cr,Dk}$ and $\theta_{cr,D50}$ were determined from flow competence estimated using painted bed patches and pit-tags. The resulting hiding-exposure factor b_θ , was found to be -0.6.

The factor of correction $\zeta_{\Phi,k}$ for trapping effects was estimated in this study such as follows, having remarked on our data the following relation to virtual velocity:

$$\zeta_{\Phi,k} = \left(\frac{D_k}{D_{50}}\right)^{b_\Phi} \approx \frac{V_{Dk}^*}{V_{D50}^*} \tag{5.27}$$

were V_{Dk}^* is the median dimensionless virtual velocity of selected tracers i (recovered at all S_n,$L_{i,Pn} \geq 5m$ and $t_{i,Pn} > 0$) contained in this class and V_{D50}^* is the dimensionless virtual velocity of the size class containing the D_{50} of the bed surface. The dimensionless virtual velocity V_i^* of each tracer i was computed using equation 5.10. Where the tracers virtual velocity V_i was computed (equation 5.9), by dividing the tracers traveled distance L_i measured from field surveys (see section 5.3.1.3), by the duration of the flow competent to transport the tracers $t_{>Qc,i}$ estimated from numerical simulations (see section 5.3.2.3). The median dimensionless virtual velocity V_{Dk}^* of tracers i contained in each size class k was plotted in a log-log plane as a function to the relative median diameter $D_k^* = D_k/D_{50}$ of tracers i contained in each of the size class. A simple simple polynomial fit enables to determine the exponent b_Φ in equation 5.27 hence $\zeta_{\Phi,k}$. This exponent b_Φ was estimated for each period P_n in order to investigate the influences of the frequency and magnitude of the flood events, as well as the tracers dispersion or burial, on tracers dimensionless virtual velocities, and consequently on the trapping factor $\zeta_{\Phi,k}$. The relation between D_k^* and V_{Dk}^* was compared to the curve found by Milan (2013), who also investigated the virtual velocity of tracers using a size-based competence duration.

5.4 Results and discussion

5.4.1 Tracer travel distance estimation

5.4.1.1 Tracer recovery rates

The tracer recovery rates exceeds 80% for all of the three monitoring (Table 5.1), with more than $n = 360$ tracers recovered during each survey, which is a very high rate compared to other studies conducted in large rivers, e.g., Lamarre et al. (2005; n = 177 to 196), Liébault et al. (2012; $n = 203$ to 401), Gaeuman (2013; $n = 90$ to 277), Phillips et al. (2013; $n = 93$ to 150), Chapuis et al. (2015; $n = 95$), Stähly et al. (2019; $n = 277$) or Chardon et al. (2021; $n = 157$ to 644). The recovery rate of smaller tracers ($16 - 32mm$) was relatively lower ($\approx 10\%$) than for other tracers, probably because they were equipped with 23 mm-long tags, whose detection distances is shorter. The recovery rates was relatively constant over time, but recovery rate of each size class varied between the surveys (Table 5.1). The number of large tracers recovered increased from S_0 to S_2, while the number of small tracers recovered increased between S_0 and S_1 and then decreased at S_2. This variation is due to the tracers dispersion (Figure 5.8). Indeed, when all tracers were grouped around the injection points, collisions of tracer signals reduced recovery rates of each size class (S_0). When tracers were transported in the downstream direction this effects became negligible and recovery rates of each size class increased (S_1 - S_2), except for small tracers which may have traveled too far to be found (S_2). This small unrecovered tracers were unlikely buried, as topo-bathymetric surveys show that few morphological evolutions occurred along the reach during the studied periods, and that thickness of sediment deposits ($< 60cm$) did not exceed the antenna distance of detection ($\approx 90cm$).

Class (mm)		N_s	S_0	S_1	S_2	S_0 and S_1	S_0 and S_2	S_0 to S_2	$\overline{L_{S0-S1}}$	$\overline{L_{S0-S2}}$
[1]	$16 - 22.6$	87	63	67	52	55 (53)	40 (40)	36 (34)	350±218	753±294
[2]	$22.6 - 32$	87	69	72	65	61 (57)	51 (50)	45 (42)	357±190	748±345
[3]	$32 - 45.3$	86	75	78	75	67 (60)	64 (62)	58 (51)	310±178	686±335
[4]	$45.3 - 64$	86	75	76	78	68 (60)	69 (69)	62 (56)	224±162	576±331
[5]	$64 - 90.5$	86	75	79	81	69 (45)	70 (65)	64 (42)	104±96	378±240
[6]	$90.5 - 128$	18	15	16	17	15 (6)	15 (13)	15 (6)	27±21	227±184
Total number		450	372	388	368	335 (281)	309 (299)	280 (231)		
Recovery rate		100%	83%	86%	82%	74% (62%)	69% (66%)	62% (51%)		

Table 5.1: Statistical parameters for each particle tracking survey, indicating the total number N_S of tracers injected and recovered at survey S_n with the number of mobile tracers among recovered ones as well as the corresponding recovery rates mentioned in brackets

The recovery rate between survey S_0 and S_n of same tracers approximates 70% for both surveys (Table 5.1), which is around 10% lower than respective recovery rates S_n. This lowering is relatively evenly distributed between size classes, therefore as for individual surveys, less small tracers (CL1 63% at S_1 and 46% at S_2) were found between surveys than large pit-tags (CL5 80% at S_1 and 81% at S_2). The proportion of mobile tracers among recovered ones decreases as a function of the tracers sizes, from 96% (CL1) to 65% (CL5) at S_1 and from 100% (CL1) to 93% (CL5) at S_2, because of size-selective sediment transport. The small immobile tracers were preferentially located close to the river banks ($< 7m$), while large immobile tracers were distributed across the whole river section, which is coherent with the flow velocities lateral distribution.

The variation between surveys of tracers mobility, 84% at S_1 and 97% at S_2, is due to the flow competence (Figure 5.4), which was higher during P_2 ($Q_{max} = 470m^3/s$) than during P_1 ($Q_{max} = 303m^3/s$). The recovery rate of mobile tracers found between surveys S_0 and S_n therefore increased from CL1 (60% at S_1 and 45% at S_2) to CL4 (70% at S_1 and 80% at S_2), and then decreased at CL5 (52% at S_1 and 75% at S_2). The recovery rate of mobile tracers found at S_0, S_1 and S_2 followed this trend (Table 5.1), with a lower ratio of mobile tracers among recovered (CL1 39% and CL4 65%), but there are at least 30 pit-tags per class (except CL6 excluded from further analyzes with only 6 tracers). Despite the reduced number of tracers recovered during the three surveys, our tracer sample size ($n = 231$) was much higher than that of Milan (2013) ($n = 23$), who also investigated the virtual velocity of tracers using the size-based competence duration.

5.4.1.2 Tracer longitudinal travel and dispersion

The longitudinal distance traveled by tracers ($\overline{L_{S0-S1}} = 270m$ and $\overline{L_{S0-S2}} = 593m$) and their dispersion ($\sigma_{S0-S1} = 197m$ and $\sigma_{S0-S2} = 343m$) increased over time (Figure 5.8 a), indicating that tracers traveled through a clear translation-dispersion mode (Chardon et al., 2021b). The tracers located in the middle of the channel (Figure 5.1) traveled further downstream ($L_{max,S1} = 732m$ and $L_{max,S2}= 1296m$) than tracers placed close to the banks ($< 75m$ at S_2), causing a heavy-tailed distribution. These tracers traveled less far than the others or were immobile, because of the lateral distribution of flow velocities, but also because some of them were trapped between blocks located at the bank toe (left bank) or within a scour created around a log-jam (right bank). This heavy-tailed distribution is also due to the longitudinal sorting of tracers, resulting from size-selective sediment transport, which occurred during both monitored periods (Figure 5.8 b and c). The mean travel distance decreased as function of the size class (Table 5.1), from $357m$ (CL2) to $104m$ (CL5) at S_1 and from $753m$ (CL1) to $378m$ (CL5) at S_2, except for size class CL1. Nevertheless, the travel distance ($350m$) of CL1 was only $7m$ lower than CL2 at S_1.

This discrepancy may be due to an underestimation of the mean distance traveled by this class, calculated using a reduced number of tracers compared to the others size classes (Table 5.1). The longitudinal sorting of tracers increased as a function to the size class, and over time, resulting of the additive effect of multiple size selective flow events. The flood that exceeds a two-years return period ($470m^3/s$), which occurred during period P_2, did therefore not disturb the sorting trend observed during period P_1, even if almost all size classes were transported during this event. The increased mean distance traveled by each size class between S_1 and S_2 also suggests that flow were more longer competent during P_1 than P_2, but these metrics may be affected by the tracers dispersion (σ), which increased as a function of the travel distance ($\overline{L}$) ($\sigma = 2.03\overline{L} - 62.62$ with $R^2 = 0.96$). The longitudinal distribution of tracers (Figure 5.8) shows that during survey S_1, a high proportion (29%) of tracers were recovered between $285m$ and $485m$, along the only riffle-pool sequence of the reach. These tracers were relatively evenly distributed between the two geomorphological units, with a cluster of 8 tracers observed in the riffle ($305m$), in the run ($435m$) and in the pool ($515m$). The tracers were therefore not preferentially stored on the riffle, where the bed shear stress is lower than in pools during floods (Lisle, 1979; Petit, 1987), as observed in other studies (Sear, 1996). The river bed morphology thus has a relative influence on the tracers locations. As observed during survey S_2, where a cluster of 10 tracers was found in shallow ($695m$) and deep ($765m$) parts of the river. This conclusion allows to consider only hydrodynamic conditions when studying the tracers displacement.

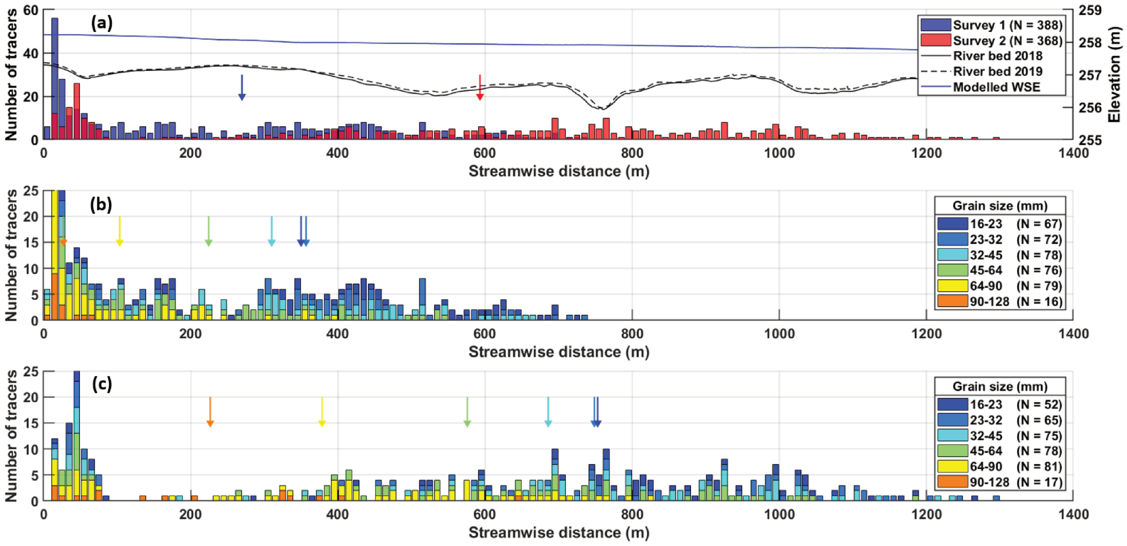

Figure 5.8: Longitudinal distribution of (a) all tracers recovered at S_n and the longitudinal profile of the river bed extracted at the centerline from the DEM of 2018 and 2019 with the water surface elevation modelled at $Q = 40m^3/s$ using the DEM of 2018, (b) all tracers recovered at S_1 and (c) all tracers recovered at S_2. Arrows indicate the mean distance traveled by all mobile tracers recovered at $S_n - S_{n+1}$ in (a), the mean distance traveled by each size class k, based on mobile tracers recovered at $S_0 - S_1$ in (b) and at $S_1 - S_2$ in (c).

5.4.1.3 Tracer relative travel distances

The tracer relative traveled distances L_i^* were computed (equation 5.13) by scaling the distance L_i traveled by each tracer i by the mean distance $\overline{L_k}$ traveled by the size class k containing the bed surface D_{50} of $30mm$ (Figure 5.3). This scaling was therefore computed using the mean traveled distance of the size class CL2 ($22.6 - 32mm$), which correspond to $357m$ during the period P_1 and to $748m$ during the period P_2 (Table 5.1). L_i^* were plotted as function of the relative tracers size D_i^*, computed (equation 5.14) by scaling the size D_i of each tracer i by the subsurface D_{s50} of $13mm$ (Figure 5.3). This scaling was performed using the D_{s50} rather than D_{50}, as proposed by Church and Hassan (1992), who argues that the bedload D_{b50} is similar to subsurfaceD_{s50} (even if our results show the contrary figure 5.3), in order to be able to compare our results to their curve. This comparison (Figure 5.9) shows that our results are similar to the results of Church and Hassan (1992) and Milan (2013). This demonstrates that tracer traveled distances drop off rapidly as $D_i > D_{s50}$, while tracers traveled distances increased progressively as $D_i < D_{s50}$. Our curve may slightly deviate from the others curves, at finer and coarser extremities, because we were not able to equip with tags the particles as small as the D_{s50}, and because the number of tracers within the coarser size class is very low (Table 5.1). Despite these difficulties inherent to the Moselle river granulometry, the similarities with existing results allowed to be confident about our data.

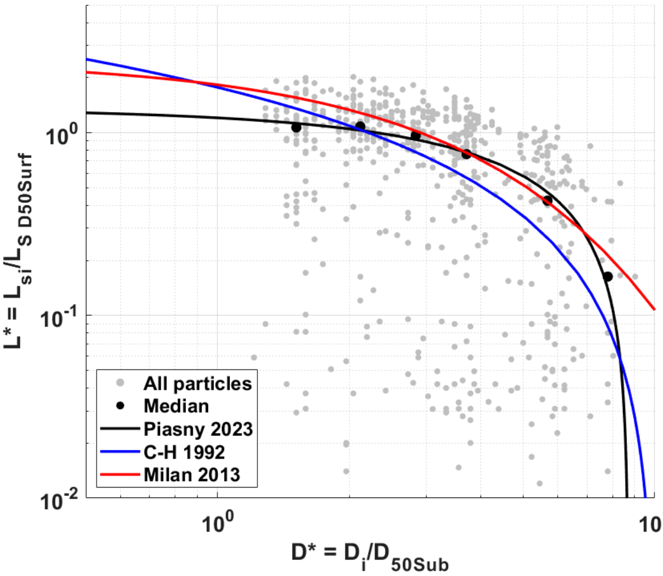

Figure 5.9: Relative travel distances of all tracers recovered during $S_n - S_{n+1}$ as a function to their relative size and median relative travel distances of tracers contained in each size class as a function of the median relative size of those tracers contained in each size class. Polynominal curve fitted to our median value compared to the curve found by Church and Hassan (1992) (noted C-H) and Milan (2013).

5.4.2 Duration of competent flow

5.4.2.1 Hydraulic model calibration and river discharge estimation

The numerical model used in this study is a submodel of the 2D hydro-sedimentary model of the Moselle river, built from a high resolution DEM leveled in summer 2018 (A_1) and calibrated using time series of WSE recorded during the largest flood event ($Q_{max} = 303m^3/s$), occurred during the period P_1. The validity of the calibration of this submodel, over the entire studied periods (Figure 5.4), was assessed (i) by modelling the largest flood event ($Q_{max} = 470m^3/s$) occurred during the period P_2, using the DEM leveled in summer 2019 (A_2) and (ii) by comparing simulation results to time series of WSE recorded by two limnimeters (L1 and L2) located on either side of the tracers injection site. This simulation was performed by injecting into the model the hourly discharge data recorded by the gauging station of Châtel-sur-Moselle (Figure 5.1). The comparison of the results (Figure 5.10) shows that the model is well calibrated at L1 and L2, even if modelled WSE are slightly underestimated ($\sim 10cm$) at rising limb ($\sim 20h$), while slightly overestimated ($\sim 5cm$) at falling limb ($\sim 100h$–$120h$) compared to the observed WSE. The good correspondence of modelled and observed WSE at the flood peak ($\sim 40h$) and plateau ($\sim 50h$), where discharges are relatively constant over time, indicates that the 2D model enables a good modelling of hydrodynamic conditions. The successive steady state simulations performed with this model to build a catalog of model outputs for different inflow discharges Q can therefore be used to (i) build stage-discharge relations at L2 and (ii) estimate the bed shear stress at each tracer location, assuming that hydrodynamic conditions are also well predicted along the straight reach located between both limnimeters.

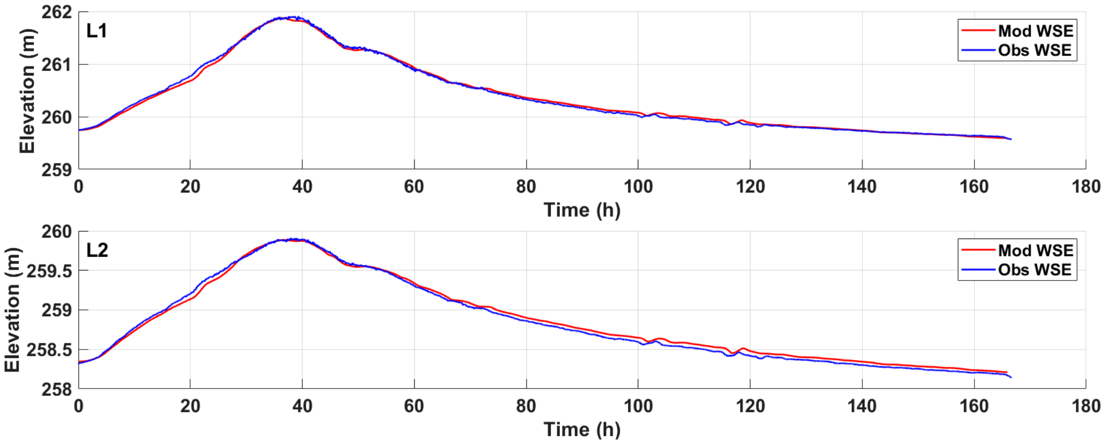

Figure 5.10: Comparison between the WSE recorded by the limnimeter L1 and L2, located on either side of the injection site, and the WSE modeled during the peak flood of period P_1 ($Q = 303 m^3/s$), obtained from unsteady simulations performed using the submodel $\mathcal{M}_{f,p}$.

The two stage-discharge relations, built using simulation results based on DEMs of 2018 and of 2019, were used to convert time series of WSE recorded at 5 minutes interval by the limnimeter L2, during the period P_1 and P_2, into flow hydrographs. The sum of the discharge estimated using this limnimeter, located at Gripport (Figure 5.1), was compared to the sum of the discharge measured by the gauging station of Châtel-sur-Moselle located $12km$ upstream and by the gauging station of Velle-sur-Moselle located $21km$ downstream. Comparison (Appendix A) shows that the cumulative discharge estimated at Gripport (L2), lies between the cumulative discharge measured by the upstream and downstream gauging stations during both periods P_1 and P_2. The cumulative discharge estimated at Gripport are very close to the cumulative discharge estimated at Châtel-sur-Moselle, which validates previous assumption that contributions of upstream tributaries are insignificant. The flow hydrographs computed during this study can therefore be used to estimate accurately the river discharge during both periods.

5.4.2.2 Estimation of critical discharge for tracer motion

The critical discharge $Q_{c,i}$ was estimated for all tracers i, mobilized during P_1 and P_2 and recovered from S_0 to S_2, according to their position at each survey, in order to study the variation of $Q_{c,i}$ as a function of the lateral position of the tracers i. The results (Figure 5.11) show that the values of $Q_{c,i}$ increased (i) as a function of the tracers size, which is consistent with the size-selective transport, observed previously, and (ii) as a function that tracers lateral positions from the channel centerline, which is consistent with the cross-sectional distribution of flow velocities (Figure 5.5). Few mobile tracers were recovered above $20m$ from the centerline, because flow velocities drop rapidly when getting close of the banks ($\sim 25m$) and thus tracers remained immobile at the lateral extremities of the injection transects. This distance decreased to $17m$ for coarser tracers, because the critical threshold for tracers motion increased as a function to the tracer size and therefore coarser tracers remained immobile over a wider portion of the injection transect. These discrepancies between results are also due to the longitudinal variation of $Q_{c,i}$ (Figure 5.5).

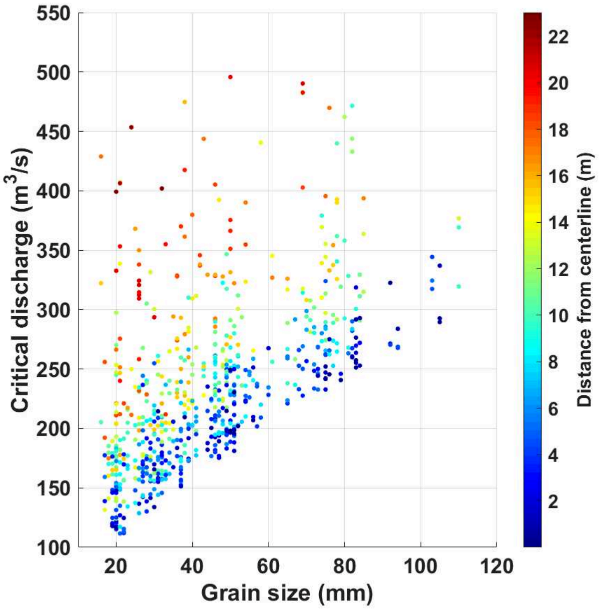

Figure 5.11: Critical discharge for tracers motion as a function to the tracers size and lateral position according to the river centerline.

The critical discharge $Q_{c,i}$ for tracer motion, estimated at surveys S_n and S_{n+1}, were compared in order to study the temporal and thus the longitudinal variations of $Q_{c,i}$ along the river reach. Results show (Figure 5.12) that the values of $Q_{c,i}$ were relatively constant between survey S_0 and S_1, as indicated by the trendline connecting both datasets ($Q_{S1} = 1.03Q_{S0} + 2.89$), which is closely aligned with the 1:1 line, exhibiting a high coefficient of determination ($R^2 = 0.71$). The hydrodynamic conditions being comparable before (S_0) and after (S_1) mobilisation, the duration of the flow competent to transport each tracer, during the period P_1, can therefore be computed similarly using the value of $Q_{c,i}$ estimated either at the beginning or at the end of this monitoring. The comparison between the critical discharge estimated at S_1 and S_2 (Figure 5.12) reveals significant differences, so there is no longer a discernible correlation between the two datasets ($R^2 = 0.14$). This variation is observed because the values of $Q_{c,i}$ significantly increased ($> 50\%$) for roughly a third of the small tracers ($16 - 45mm$), while the values of $Q_{c,i}$ experienced a slight decrease ($< 25\%$) for approximately a half of the large tracers ($> 70mm$). These changes may be explained by the longitudinal variation of the bed shear stress θ (Figure 5.8), small tracers that traveled far downstream ($> 700m$) are now located where the values of θ are lower than at the injection transect, while some coarse tracers are now located over the riffle ($\sim 300m$) where the values of θ are higher than at the transect of injection. The hydrodynamic conditions varying between the tracers motions (S_1) and deposits (S_2), the duration T_i of the flow competent to transport each tracer, during the period P_2, can therefore change according to the values of $Q_{c,i}$ (S_1 or S_2) selected. As part of this study, we will use the values of $Q_{c,i}$ estimated at S_1 to compute T_i, because the majority of the tracers are close to the 1:1 line, but remembering that the value of $t_{>Qc}$ can be overestimated for some of the small tracers and underestimated for some of coarse tracers.

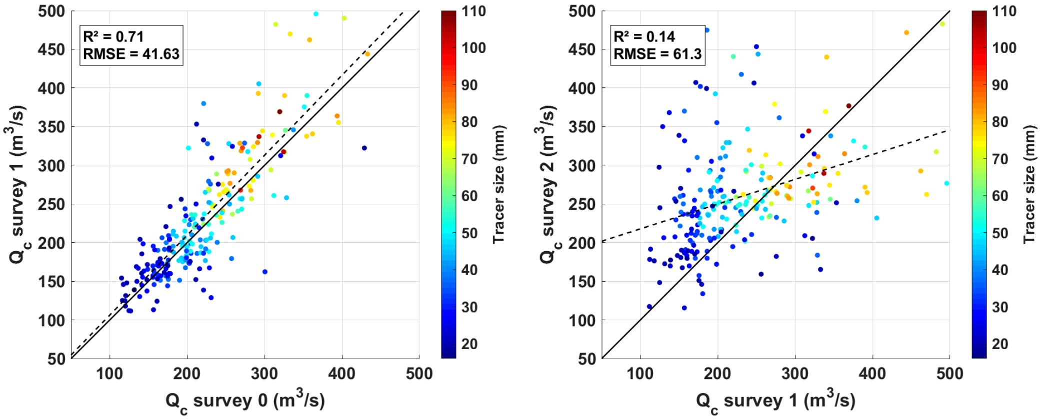

Figure 5.12: Comparison of the critical discharge for tracers motion between $S_0 - S_1$ (left plot) and $S_1 - S_2$ (right plot). The solid line corresponds to the 1:1 relationship and the dotted line represent the trendline based on our data.

5.4.2.3 Duration of competent flow

The flow competence duration T_i was computed for each tracers i, during periods P_1 and P_2, according to the hydrodynamic conditions estimated at each tracers location at S_0 and S_1, respectively. The results (Figure 5.13 a) show that this duration (i) decreases as a function of the tracers size ($T_i \coloneqq 10days$ and $T_i \coloneqq 2days$ for respectively tracers 20 and $50mm$ located in the middle of the river), due to the size-selective sediment transport and (ii) as tracers location is distant from the river centerline ($T_i \coloneqq 3days$ and $T \coloneqq 0.5days$ for respectively tracers 20 and $50mm$ located at $16m$ from the centerline), due to lateral variation of the flow velocities. The comparison of the values of T_i estimated at P_1 and P_2 (Figure 5.13 b) indicates, that almost all tracers were transported over a longer period in winter 2020 than in winter 2019, especially tracers of medium size, whose duration of transport increased significantly ($T_{P1} = 1day$ and $T_{P2} = 3.5days$ for tracers of $55mm$).

The flow competence duration was equal to 0 for 27 tracers (22 during $P_1$and 5 during P_2) of relatively coarse size ($45 - 90mm$), mostly located at the lateral extremities of the riverbed (distance from centerline $> 10m$). According to the simulation results (Figure 5.11), the critical discharge for their motion was not reached during the respective periods, but field surveys showed that these tracers moved over relatively short distances ($10 - 30m$). This difference between predicted and observed tracers mobility may be due to the fact that (i) tracers protruded from the river bed and were thus transported at a lower discharge than predicted, (ii) the flow velocities were locally higher than predicted because of the presence of a log-jam, (iii) the tracer lateral positions were inaccurate due the geolocation accuracy ($\pm 3m$) which may have led to underestimate the hydrodynamic conditions and (iv) the hydraulic model underestimates the bed shear stress along the river banks. This last assumption was privileged, as the results of the comparison between predicted and observed bed erosion performed by Piasny et al. (2023b) show that modelled bed shear stress tends to be underestimated near the river banks. These 27 pit-tags were therefore excluded from the dataset for the computation of the tracers virtual velocity.

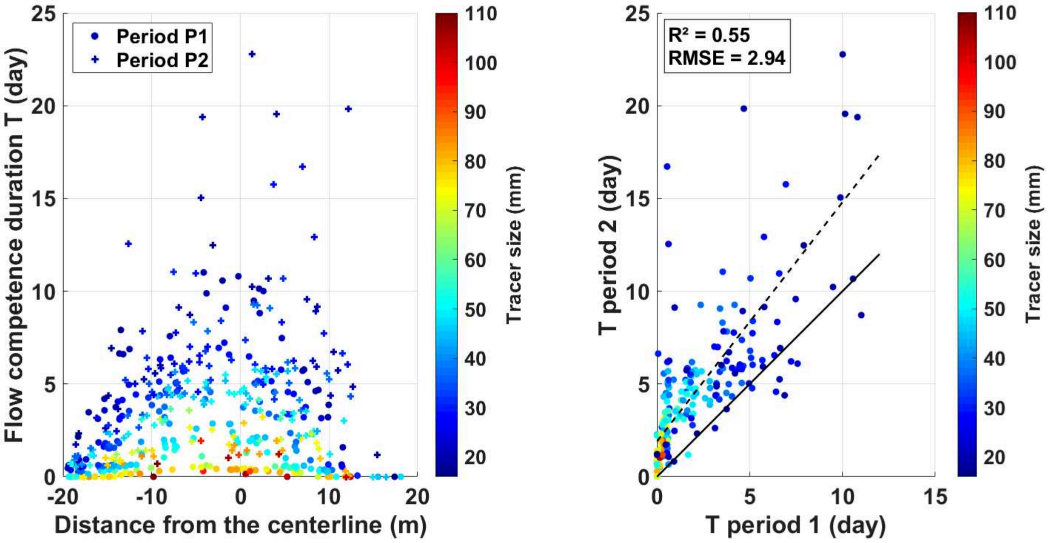

Figure 5.13: Duration of competent flow as a function to the tracer lateral position and size for each period P_n (left plot) and comparison of the flow competence duration between periods $P_1 - P_2$ (right plot). The solid line corresponds to the 1:1 relationship and the dotted line represents the trendline based on our data.

5.4.3 Calibration of non-uniform sediment transport

5.4.3.1 Tracers virtual velocity

The median virtual velocity V_k of tracers i within size class k was calculated and plotted as a function to median diameter D_k of tracers i within size class k, in order to study the variation of virtual velocity according to the tracer size. Despite the scattered distribution of the data within each size class, the results (Figure 5.14) show a strong positive log-log relationship between V_k and D_k, with a coefficient of determination of 0.98 for P_1 and P_2. The tracers virtual velocities V_k slightly decreased over time ($a := -3.13$ over P_1 and $a := -3.20$ over P_2), which can be explained by (i) an overestimation of V_k during P_1 as tracer might still protrude from the riverbed after the minor floods which occurred between the tracers injection and the first survey (Figure 5.4) and/or (ii) an underestimation of V_k during P_2 as tracers could be progressively buried after successive flood events (Ferguson et al., 2002; Chardon et al., 2021b; Houbrechts et al., 2015). The rate at which the tracer's virtual velocity V_k increases according to their size D_k, however, remains constant over time ($b := 1.32$ over P_1 and $b := 1.29$ over P_2), indicating that this rate is independent to the number and magnitude of the flood events (Figure 5.4 b) which occurred as well as to the downstream dispersion of the tracers (Figure 5.1). A power law was fitted to all the median values of V_k and D_k estimated during each period P_n, which gives the following equation, where V_i is the virtual velocity expressed in m/h and D_i is the particle size expressed in millimeter.

$$V_i = exp(-3.07) D_i^{1.27} \tag{5.28}$$

This law has been fitted on $n = 428$ data pairs with a pearson correlation coefficient of $R^2 = 0.99$ and an $RMSE = 0.04$.

This relationship demonstrates that the tracer virtual velocity increased as a function of the tracers size, from $2m/h$ for the smallest particle size ($D_i = 20mm$) to $11.7m/h$ for the largest particle size ($D_i = 75mm$). This result contrasts with observations from previous studies (Ferguson and Wathen, 1998), who indicate that tracers virtual velocities decrease, when the grain size increase. Those studies find as well that finer tracers travel further downstream than coarser tracers, but the flow competence duration was considered as invariant for all particle sizes, therefore virtual velocities (equation 5.9) inversely increased with the tracer size. This latter assumption was made from bedload measurements (Ashworth and Ferguson, 1989; Wathen et al., 1995), showing that all grain sizes were transported over a similar threshold shear stress and consequently for an equal duration. The field measurements performed on the Moselle river, to estimate the critical threshold for particle motion θ_{cr} (Piasny et al., 2023b) however show that the value of θ_{cr} progressively increases relatively to the median grain size of the bed surface (equation 5.25). As the assumption of a unique threshold shear stress for all grain sizes is not valid for our study site, the duration of the flow is competent to transport each tracer is then computed according to the tracers size. This duration decreases rapidly as a function of the tracers size (Figure 5.13), since coarser tracers require a higher discharge to be transported (Figure 5.11), which was exceeded over significantly shorter periods (Figure 5.4). By considering a size-based flow competence duration, small tracers has then lower virtual velocity than coarse tracers (equation 5.28), because of the much longer duration of competent flow relative to the traveled distance (Figure 5.28).

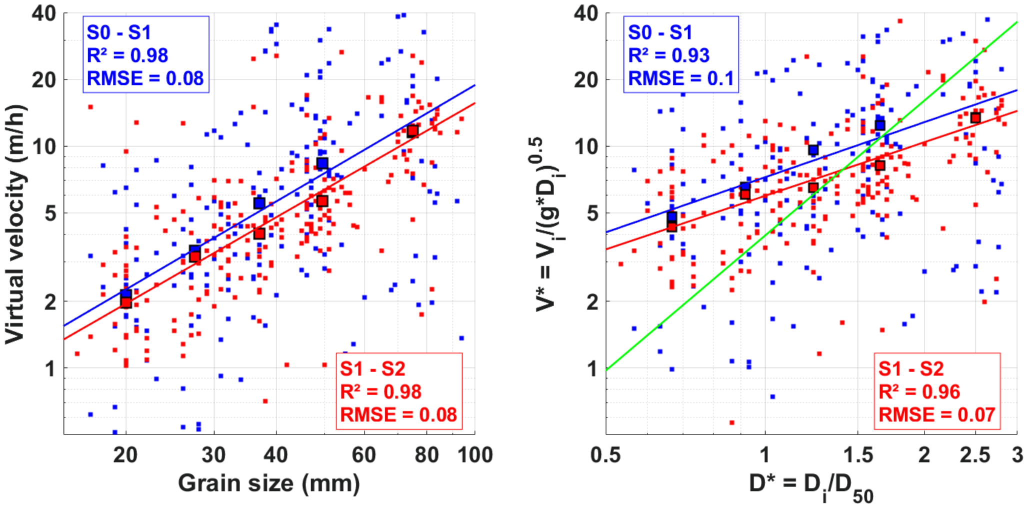

Figure 5.14: Virtual velocity of tracers as a function to their size during each period P_n (left plot) and dimensionless virtual velocity of tracers as a function to their relative size during each period P_n (right plot). Large squares indicates the median velocity as a function of the median size of tracers within each size class and green line represents the results obtained by Milan (2013).

Our data were adimentionalized (equation 5.10) and the median dimensionless virtual velocity V_k^* of tracers i within size class k was calculated and plotted as a function to median relative diameter D_k^* of tracers i within the size class k. As for the tracer virtual velocity, the results (Figure 5.14) show a strong positive log-log relationship between V_k^* and D_k^*, with a coefficient of determination of 0.93 for P_1 and 0.96 for P_2. The tracers dimensionless virtual velocities V_k^* also slightly decreased over time ($a \coloneqq 1.97$ over P_1 and $a \coloneqq 1.78$ over P_2), while the rate at which

V_k^* increase according to D_k^* remains almost constant between P_1 ($b \coloneqq 0.82$) and P_2 ($b \coloneqq 0.80$). A power law was fitted to all the medians values of V_k^* and D_k^* estimated during each period P_n, which gives the following equation, where V_i^* is the dimensionless virtual velocity and D_i^* is the relative size of particle i.

$$V_{D_i^*}^* = exp(1.87)D_i^{*0.78} \tag{5.29}$$

This law has been fitted on $n = 428$ data pairs with a pearson correlation coefficient of $R^2 = 0.99$ and an $RMSE = 0.02$.

This relation was compared to the relation found by Milan (2013), who also investigated the virtual velocity of painted tracers in the Rede River using as well a size-based flow competence duration. The results of this comparison (Figure 5.14) show that tracers smaller than 1.5 times the bed surface D_{50} traveled at a higher V^*on the Moselle river ($V_{0.5}^* = 4m/h$) than on the River Rede ($V_{0.5}^* = 1m/h$), while coarser tracers traveled at a lower V^*on the Moselle river ($V_3^* = 15m/h$) than on the Rede River ($V_3^* = 40m/h$). This discrepancy may be explained by the consideration or not of hiding and exposure effects in the computation of the size-based flow competence duration. In fact, in poorly sorted gravel-beds, the relative smaller particles are more likely hidden from flow by their larger neighbors and then have a higher θ_{cr}, whereas relatively larger particles have more chances to be exposed to flow and then have a lower θ_{cr} (Andrews, 1983). By considering these effects on particle entrainment, the discharge at which small particles are mobilized increases, while the discharge at which large particles are mobilized decreases. So, the influence of hiding and exposure effects tends to decrease the duration during which small particles are transported and increase the duration during which large particles are transported. These effects were however not considered by Milan (2013) which may explain an underestimation of virtual velocity for relative small tracers and inversely for relatively coarse tracers.

In our study, these effects were considered, but as the tracers from the Moselle river experienced less selective mobility than the tracers from the River Rede (Figure 5.9), these effects were also more pronounced, which may enhance differences between results of the two studies. As the hiding and exposure effects acting on particles entrainment were considered in the computation of the size-based flow competence duration, the other factor which may explain that dimensionless virtual velocities increased as a function of the particle size, is that small tracers experienced longer periods of rest during their transport than coarser tracers (Schmidt and Ergenzinger, 1992). The smaller tracers may have experienced longer periods of rest during their transport than coarser tracers, due to a higher probability of being trapped among other particles during their motion (Church and Hassan, 1992). This size-based resting duration are considered in the computation of the bedload transport rates (equation 5.4), (i) when $\zeta_{k,\theta}$ is calibrated using bedload sampler or sediment traps, since both hiding/exposure and trapping effects act during bedload transport, but not (ii) when $\zeta_{k,\theta}$ is calibrated using painted bed patches or tracers mobilization, as only hiding/exposure effects act during particle entrainment. A correction factor should therefore be applied to the bedload transport rates (equation 5.5), computed based on the relative dimensionless virtual velocity (V_{Dk}^*/V_{D50}^*), to take into account of the decreasing probability of particles to be trapped during their transport, according to their relative size (D_k/D_{50}). Since it was found that V_{Dk}^*/V_{D50}^* can be approximated (equation 5.27) by $(D_k/D_{50})^{b_\Phi}$ were b_Φ correspond to the exponent b of the relationship between V_{Dk}^* and D_k^* (equation 5.29), the trapping factor $\zeta_{k,\Phi}$ is computed as $(D_k/D_{50})^{0.78}$.

5.4.3.2 Improvement of the prediction of the bedload composition

The bedload transport was modeled (see section 5.3.3.1) along the studied reach ($Q = 303m^3/s$) and extracted at the transect of tracers injection (Figure 5.1), in order to compare its composition to field measurements (Figure 5.3), according to (i) the number of size classes used in the model (Figure 5.7) and (ii) to the coefficient of correction $\zeta_{\theta,k}$ applied to the dimensionless critical shear stress for particle motion θ_{cr} (equation 5.4) and (iii) to the coefficient of correction $\zeta_{\Phi,k}$ applied to the corrected bedload transport rates $\Phi_k^{*,\theta}$ (equation 5.5). The result (Table 5.2) shows that using a constant θ_{cr} of 0.035 for all size classes, the bedload discharge Q_s across the river section significantly varies according to the number of classes, up to 4 classes, and then stabilizes at $0.0083m^2/s$ using 6 classes and more. The granulometric curve of the bed surface material (Figure 5.3) was then discretized in the model, into 6 classes (Figure 5.7), so that the bedload transport predicted by the model is independent of the number of classes used. This number of classes falls within the range of 5 to 10 classes proposed by Basile (2001) for natural gravel-bed rivers.

Number of size classes	Bedload transport (m^3/s)
1	0.0054
2	0.0061
3	0.0140
4	0.0085
5	0.0093
6	0.0083
10	0.0083

Table 5.2: Variation of the cross-sectional bedload discharge according to the number of size classes implemented into the hydro-sedimentary model $\mathcal{M}_{f,p}$.

The composition of the bedload predicted using a constant θ_{cr} of 0.035 for all size classes was compared to the GSD of a bedload sample collected under similar hydrodynamic conditions. Unlike results from other studies (Parker and Klingeman, 1982), the GSD of this sample was much closer to the GSD of the surface material than the subsurface material (Figure 5.3). The results of this comparison (Figure 5.15) shows that bedload GSD predicted by the model ($D_{50m} = 13.2mm$) is much finer than observed ($D_{50b} = 26mm$) and corresponds more closely to the GSD of the subsurface material ($D_{50s} = 12.8mm$). The proportion of fine sediment transported is therefore overestimated, while the proportion of coarse sediment transported is underestimated, which can be explained by the hiding and exposure effects acting on particle entrainment, that are not considered in the model using a constant $\theta_{cr,k}$. To consider these effects a factor of correction $\zeta_{\theta,k}$ computed (equation 5.3) according to the relative particle size (D_i/D_{50}) and a hiding factor exponent b of -0.6, was applied to θ_{cr} (equation 5.4), in order to increase $\theta_{cr,k}$ of small particles and decrease $\theta_{cr,k}$ of coarse particles. By applying these factors of correction, the D_{25m} increased from $6mm$ to $8mm$, while the D_{85m} increased from $26mm$ to $38mm$ and sediments of the coarser size classes were this time transported. The changes in proportions of each size class contributed to the coarsening of the bedload GSD (Figure 5.3), but the D_{50} predicted by the model ($17.2mm$) remained significantly lower than observed ($26mm$). Although, hiding and exposure effects acting at particle entrainment were considered in the computation of the bedload transport rates (equation 5.4), trapping effects observed in the field and acting during particle motion, were not accounted for.

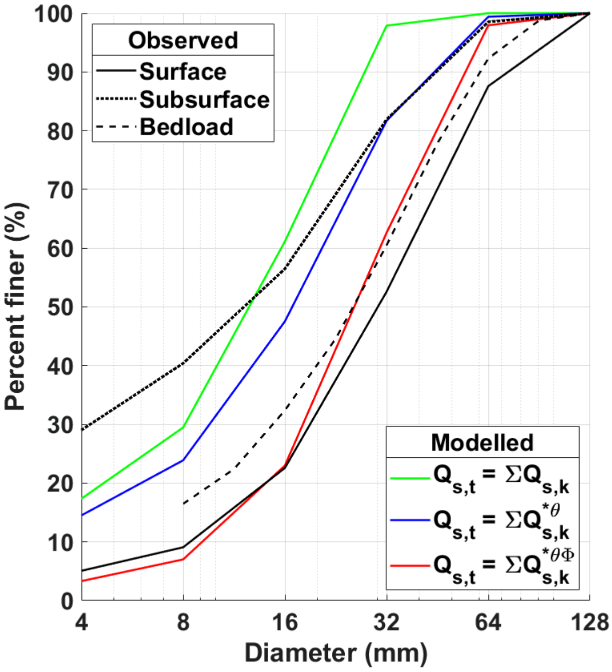

Figure 5.15: Comparison of the grain size distribution of the observed bedload and modelled bedload using 6 size classes, without a correction factor ($Q_{s,k}$), with a corrector factor ζ_θ for hiding-exposure effects ($Q^{*,\theta}_{s,k}$) and with a correction factor for hiding-exposure effects ζ_θ and a correction factor ζ_Φ for trapping effects ($Q^{*,\theta,\Phi}_{s,k}$).

To consider these trapping effects, a correction factor $\zeta_{\Phi,k}$ was applied to the bedload transport rates $\Phi^{*,\theta}_k$ of each size class k (equation 5.5), which was computed (equation 5.27) according to their relative size (D_i/D_{50}) and a trapping factor exponent b. This exponent b of 0.78 corresponds to the rate at which the dimensionless tracer's virtual velocity increase according to their relative size (equation 5.29), as the variations in tracer dimensionless virtual velocities was assumed to depend on the trapping effects. By applying this factor of correction, the D_{25m} increased from $8mm$ to $17mm$, the D_{50m} increased from $17mm$ to $27mm$ and the D_{85m} increase from $38mm$ to $52mm$. These changes in proportions of each size class led to the coarsening of the bedload GSD (Figure 5.3), so that the D_{50} predicted by the model ($27mm$) is similar to the D_{50} of the bedload measurements ($26mm$). The coarse tail of the bedload GSD predicted by the model ($D_{85} = 52mm$) fits also very well to observed ($D_{85} = 54mm$), whereas the fine tail of the bedload GSD predicted by the model ($D_{25} = 16mm$) was slightly finer than observed ($D_{25} = 12mm$). The discrepancy between predicted and observed GSD increased as particles become finer than $22.6mm$, which corresponds to the median diameter of the finest size class equipped with tags (Table 5.1). The finest particle sizes may therefore experience during their transport an other behavior than predicted, which could not be assessed in this study, due to the relatively coarser lowest bound of GSD of tracers.

This study demonstrates that despite fine particles are transported under a lower bed shear stress and thus for a longer duration, their transport is slower than that of coarse particles, minimizing the size-selective transport, towards conditions where particles have an equal mobility (Andrews and Parker, 1987). This results indicate that the bedload transport laws have to be calibrated to consider size-selective entrainment, but also size-selective transport. To consider both phenomena, bedload transport laws were calibrated using (i) a hiding factor $\zeta_{k,\theta}$ estimated from tracers mobility and (ii) a trapping factor $\zeta_{k,\Phi}$ estimated from tracers virtual velocities. By applying both factors, the prediction of the bedload D_{50} and D_{85} was greatly improved, but the prediction of the D_{25} was slightly underestimated. This underestimation shows the limits of the method of calibration $\zeta_{k,\theta}$ and $\zeta_{k,\Phi}$ using a limited range of particle size ($> 0.5D^*$) compared to the bed grain size distribution and suggests, as proposed by Egiazaroff (1965), to estimate an exponent b different above and below $0.4D^*$.

The trapping factor exponent b of 0.78 estimated in this study is however remarkably similar to the exponent of 0.85 proposed by Karim and Kennedy (1982) for correcting the bedload transport rate Φ_k^* to accounting for hiding-exposure effects (equation 5.5). This close correspondence gives us confidence in the estimation of this exponent using tracer's virtual velocity. As well, the fact that the exponent b estimated during both P_1 and P_2 is similar, despite the significantly different hydrodynamic conditions observed during each period, instills confidence in the robustness of this exponent. A robust estimation of this exponent, however, involves to determine the bed shear stress at the tracers X_i,Y_i location when estimating the critical discharge for the tracers i motion. Indeed, when estimating a critical discharge for tracers motion i, using a reach averaged bed shear stress, as it is classically done in geomorphological studies, we observed that the value of b decreased from 1.44 at $P1$ to 0.84 at P_2. This latter result shows the importance of considering the hydrodynamic conditions at the scale of the tracers when studying the temporal evolution of tracers virtual velocity and thus highlights the need of coupling such studies with an accurate 2D hydro-sedimentary model.

5.5 Conclusions

The mode of bedload transport of a large gravel-bed river, the Moselle, was studied during two years, using tracers of different sizes, injected into a straight reach of high banks and a relatively flat bed. Despite the large dispersion of tracers, the recovery rates of annual surveys were very high, thanks to an original setup, that allowed to reduce the number of operators, minimize physical effort, shorten post-processing time and improve the accuracy of tracers geolocation. The longitudinal sorting of tracers show, that the sediment transport was size-selective, and that in-channel geomorphological units have a limited influence on tracers distribution. The duration of the flow competent to transport the tracers was computed according to the tracers size and location, using results of numerical simulations to determine when the critical discharge for each tracers motion was exceeded.

This critical discharge was estimated by taking into account the hiding and protrusion effects, reducing the size-selective entrainment of tracers which was determined in a previous study. Surprisingly, the tracers virtual velocities increased according to their size, at a consistent rate during both studied periods, indicating that these results are independent of flood intensity. The relatively lower virtual velocity of fine tracers was attributed to their higher probability of being trapped, between other coarser particles during transport. To consider these trapping effects into a 2D hydro-sedimentary model, we introduced a trapping factor $\zeta_{\Phi,k}$ computed according to the relative grain size D_k/D_{50} and an exponent b of 0.78. This exponent corresponds to the rate at which the tracer virtual velocities increases according to their size. The trapping factor $\zeta_{\Phi,k}$was applied the bedload transport rates $\Phi_k^{*,\theta}$ of each size class k, computed into the model, resulting in a reduction (resp. increase) of the proportion of relatively fine (resp. coarse) size classes transported.

This correction improved significantly the prediction of the bedload grain size distribution, which accurately matched to *in-situ* measurements conducted under similar hydrodynamic conditions. The non-uniform sediment transport can therefore be accurately predicted into a 2D hydro-sedimentary model, using (i) the tracers size-selective entrainment (flow competence) to calibrate the hiding factor ζ_θ and (ii) the tracers size-selective motion (virtual velocity) to calibrate the trapping factor ζ_Φ. The method proposed in this article, to estimate both calibration factors could be easily transposed to other rivers, where an accurate 2D hydro-sedimentary is built and well calibrated and accurate bedload grain size data are available or can be collected.

Appendix A

Period	Q_{tot} Châtel	Q_{tot} Gripport	Q_{tot} Velle
P1	1.49	1.53	1.63
P2	2.84	2.90	3.40

Table 5.3: Comparison of the total discharge ($Q > 40m^3/s$) estimated during P_1 at Gripport, at Châtel upstream and at Velle downstream gauging stations, expressed in millions of cubic meters.

Chapitre 6

General conclusions and perspectives

6.1 Conclusion Générale

Ce travail de thèse a porté sur la compréhension et la modélisation de la dynamique du transport sédimentaire sur un tronçon sinueux de la Moselle entre Gripport et Bayon, le tronçon de grande rivière le plus dynamique du nord-est de la France (réserve naturelle régionale de la «Moselle Sauvage»). Bien que ce secteur soit relativement épargné d'actions anthropiques passées directes (endiguements, extractions de granulats en lit mineur...), la propagation de réajustements morphodynamiques initiés par des actions effectuées en amont et en aval de ce secteur impacte le fonctionnement actuel de la réserve : érosions régressive et progressive, contraction du lit mineur... Les fronts d'érosion convergent aujourd'hui vers le secteur central de la réserve, marquée par la présence d'un seuil, et pourraient entraîner dans le futur une défluviation du lit mineur avec des risques significatifs pour des infrastructures.

En vue d'apprécier et d'anticiper ces impacts potentiels, une étude morphodynamique détaillée et des modélisations numériques fines ont été réalisées. Les processus physiques ont été abordés à différentes échelles emboitées, dans leurs dimensions longitudinales, latérales, et temporelles sur la base (i) d'une analyse historique, (ii) d'une importante instrumentation *in situ* et d'un suivi de l'évolution morphologique du site (iii) de modélisations de complexité adaptée aux données collectées. Ces recherches s'inscrivent dans une volonté de compréhension de la dynamique du transport sédimentaire sur ce cours d'eau sinueux graveleux et à sa modélisation. Une des originalités de ce travail réside dans l'élaboration conjointe et la mise en œuvre d'une approche complète combinant suivi de terrain multi-sources de la zone d'étude et modélisation hydro-sédimentaires 2D.

Le suivi de terrain sur quatre ans a permis de suivre l'évolution de la morphologie du cours d'eau (3 survols LIDAR topo-bathymétriques), l'hydrodynamique (12 limnimètres, profils de vitesse ADCP), la distribution spatio-temporelle de la granulométrie des sédiments de surface et de subsurface, la dynamique longitudinale (2500 traceurs RFID avec au moins 80% de taux de retour) et verticale (20 chaînes d'érosion) du transport de la charge de fond et le flux charrié (mesures directes Helley-Smith, mesures indirectes acoustiques). Ces mesures hétérogènes et complémentaires, documentant plusieurs événements de crues morphogènes, ont permis de constituer un jeu de données particulièrement varié et volumineux.

A partir de ces données, une méthodologie de complexité adaptée a été mise en place pour la détermination successive de paramètres hydro-sédimentaires clés pour des modélisations morphodynamiques. Les différentes étapes ont porté sur (i) la détermination de la contrainte critique de mise en mouvement des sédiments, (ii) l'estimation dynamique du flux de sédiments et du transport cumulé de la charge de fond et (iii) le calage d'un modèle de transport multi-classes. Pour chaque partie, des méthodes originales et novatrices ont été proposées sur la base de combinaisons d'un modèle numérique 2D avec des données multi-sources pertinentes adaptées aux objectifs. Une attention particulière a été portée à l'élaboration d'une modélisation hydraulique 2D fine, sur la base de bathymétries LIDAR et *in situ* très détaillées et de données de calage issues d'un réseau de mesures déployé spécifiquement pour le projet. Les principales conclusions sont détaillées par parties.

Tout d'abord, concernant la détermination de la contrainte critique de mise en mouvement de la charge de fond, une méthode simple a été proposée basée sur l'estimation de la compétence de transport, à partir de placettes peintes et de traceurs RFID. Les placettes donnant une information locale, permettent une estimation précise de la compétence en prenant en compte l'imbrication naturelle des sédiments. Les traceurs RFID, quant à eux, permettent ici de travailler sur une distribution granulométrique plus grossière. L'utilisation du modèle hydraulique 2D calé permet d'avoir accès à une estimation spatialisée de la contrainte de cisaillement basale pour n'importe quel débit. Cela a permis d'estimer la contrainte critique à partir de la compétence du cours d'eau. Des effets de masquage et de surexposition pour la mise en mouvement des sédiments ont été mis en évidence, dont la prise en compte a permis d'améliorer la modélisation des conditions critiques par l'ajout d'un nouveau coefficient.

La contrainte critique ainsi déterminée a permis de tester plusieurs modèles empiriques de transport de la charge de fond. La dynamique au cours d'une crue du flux sédimentaire a été étudiée à partir de mesures directes et indirectes du transport de la charge de fond. Des mesures acoustiques "continues en temps" réalisées depuis le pied de berge ont permis d'estimer les flux sédimentaires sur la section. Les flux estimés et modélisés par une approche hydro-sédimentaire 2D sont en bon accord pour le transport cumulé. Des différences de flux instantanés ont été relevées, particulièrement au niveau d'un double-pics de transport solide lors des débits de crue maximaux. Cela pourrait être attribué à la forme de l'hydrogramme, comme cela a été montré récemment dans une expérimentation en laboratoire sur les effets instationnaires du transport de sédiments en lien avec la forme de l'hydrogramme de crue (Phillips et al., 2018). Nos résultats montrent une forte hystérésis horaire pour la relation débit solide - débit liquide, qui pourrait être attribuée à une diminution de la disponibilité en sédiments et/ou à une stabilisation du lit au cours du temps.

Enfin, l'information apportée par les traceurs RFID a pu être utilisée pour caler un second coefficient prenant en compte les différences de vitesses de transport selon la taille des particules. La relation inverse entre la vitesse virtuelle de transport et la taille des traceurs, qui est contraire aux résultats de la majorité des études, est interprétée comme étant la conséquence du piégeage des particules les plus fines lors du transport. Cela nous a permis d'estimer un second coefficient d'ajustement du modèle de transport. Ce second coefficient, calé à partir de mesures complémentaires et indépendantes des placettes peintes, a permis d'améliorer la prédiction de la granulométrie de la charge de fond par le modèle de transport. Dans ces travaux, l'utilisation couplée et la mise en cohérence de données variées et de modélisations fines ont permis d'améliorer la connaissance des processus physiques, tant en termes d'hydrodynamique que de transport sédimentaire et d'évolutions géomorphologiques.

La richesse du jeu de données de terrain, systématiquement mise en lien avec la démarche de modélisation, a permis d'établir des modélisations hydrauliques et hydro-sédimentaires fines de la zone d'étude complète, mais aussi de faire des zooms sur des portions d'intérêt. Parmi ces dernières, un méandre très actif a fait l'objet d'un suivi spécifique en vue d'intégrer la dimension latérale de l'évolution du cours d'eau. Les résultats encourageants de modélisation du transport sédimentaire obtenus sur des biefs rectilignes rendent ainsi possible, en perspective, l'étude de la dynamique latérale de la rivière.

6.2 Perspectives de travail

La combinaison fine des résultats de suivis hydrauliques et morpho-sédimentaires de terrain avec des modélisations hydrauliques et morpho-sédimentaires 2D, sur des questionnements scientifiques variés (conditions critiques de mise en mouvement, estimation du débit solide à l'échelle d'une crue, modélisation multi-classes granulométriques de la charge de fond), a permis de proposer de nouvelles approches. Il semble extrêmement porteur de poursuivre et approfondir dans cette voie. Comme annoncé en 1.4, cela pourra concerner la mobilité latérale de la Moselle et pourra par la suite être transposé à d'autres rivières à forts enjeux, si possible ayant déjà fait l'objet d'acquisitions de données, voire de modélisations, hydrologiques, hydrauliques, morphodynamiques et sédimentaires.

Des perspectives de travail sont données ici à partir de travaux déjà débutés pour la plupart. En outre un data paper est prévu pour favoriser la diffusion et l'utilisation du jeu de données de la thèse en modélisation, voire en apprentissage machine appliqué au transport solide.

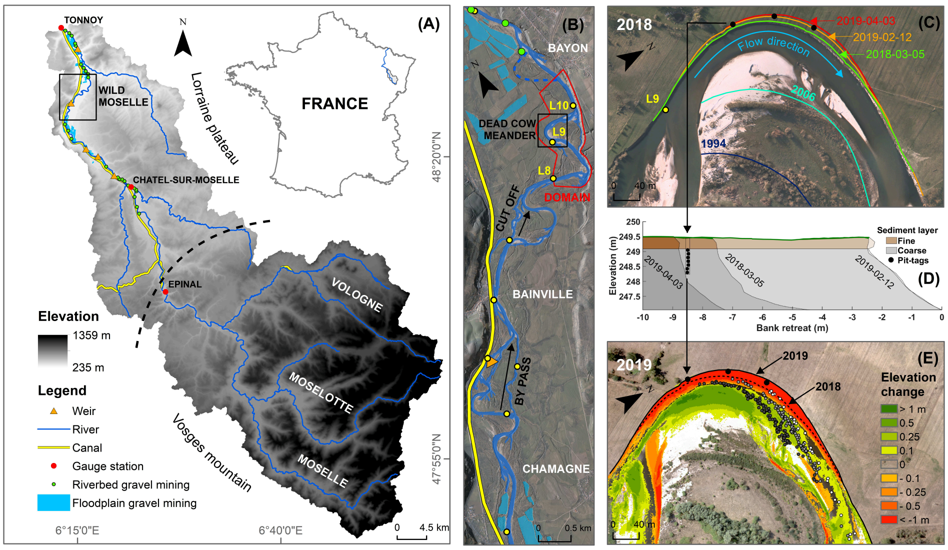

FIGURE 6.1 : (A) localisation du tronçon de la "Moselle sauvage" au sein du bassin versant de la Moselle, (B) extension longitudinale du modèle hydro-sédimentaire 2D "sto", (C) suivi du recul de la berge concave du méandre de "la vache morte", (D) profil en travers du recul de berge, (E) suivi du déplacement de traceurs placés dans la berge.

6.2.1 Modélisation de la mobilité latérale

Grâce au calage des principaux paramètres hydrodynamiques et de transport sédimentaire au niveau de tronçons relativement rectilignes. Cela permettent désormais de s'intéresser à la dynamique latérale du cours d'eau, dont l'étude a été débutée avec le suivi d'un méandre (Figure 6.1 c) dont l'évolution a été finement étudiée au cours de la thèse (4 campagnes de mesures de la topographie de la berge par photogrammétrie effectuée à l'aide d'un drone). Un modèle hydrodynamique 2D local nommé "sto" a également été mis en place (Figure 6.2 b), avec à nouveau un calage fin de l'hydrodynamique, en particulier de la répartition latérale des vitesses à partir d'une correction de vorticité. Ce calage a été réalisé à partir des profils en travers de vitesse (ADCP) réalisés en bateau le long du méandre pour un débit significatif de période de retour d'un an ($Q = 180\,m^3/s$). Les résultats de calage sont très bons en terme de reproduction des hauteurs d'eau aux endroits d'intérêt, mais aussi de profils de vitesses (Figure 6.2).

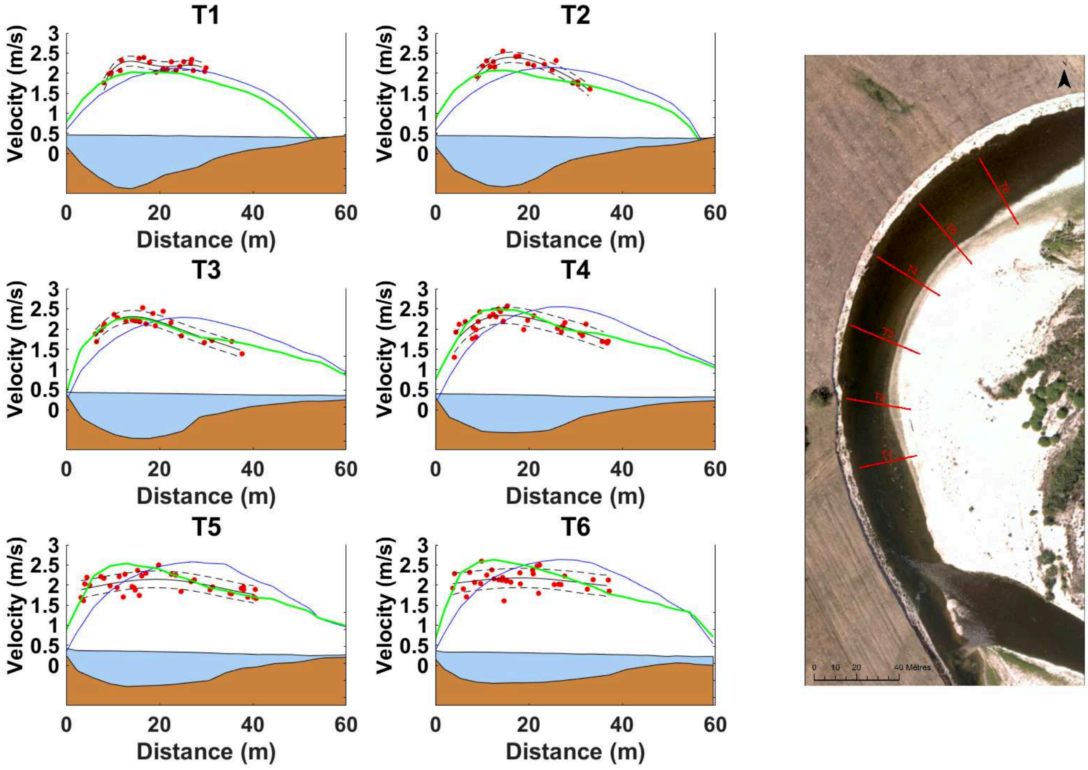

FIGURE 6.2 : Comparaison de profils de vitesse $T_{n=1..6}$ mesurés par ADCP (points rouge) et modélisés avec (lignes vertes) ou sans (lignes bleues) correction, le long du méandre de "la vache morte", lors d'une crue de période de retour d'un an ($Q = 180\,m^3/s$).

Une modélisation hydraulique, en régime permanent (débit correspondant aux mesures ADCP) a été confrontée aux résultats de suivis de traceurs RFID mis en place le long de la berge érodée. Une attention particulière a été portée à la direction du transport sédimentaire dans la courbure par rapport à la direction de l'écoulement (Figure 6.3), permettant de caler le paramètre angulaire entre la direction principale de l'écoulement et celle du transport sédimentaire.

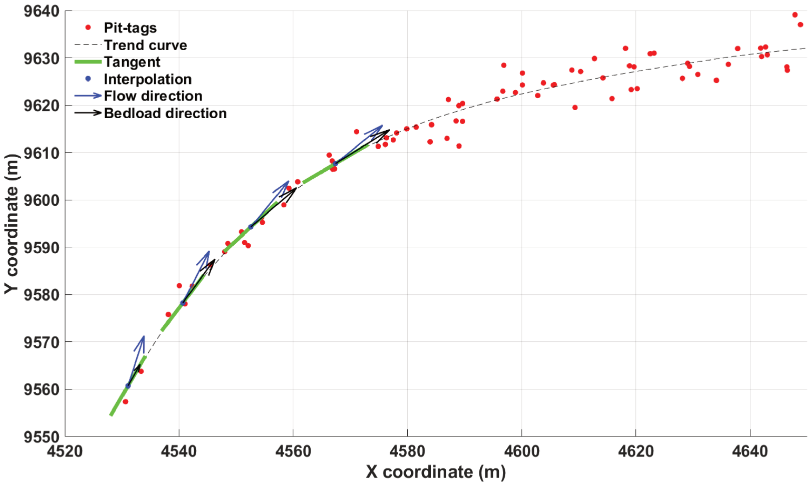

FIGURE 6.3 : Comparaison de la direction du transport sédimentaire modélisé le long du méandre de “la vache morte”, lors d’une crue de période de retour d’un an ($Q = 180\,m^3/s$) par rapport à la trajectoire de traceurs provenant de l’érosion de la berge concave.

Une fois tous ces paramètres calés, une modélisation hydro-sédimentaire dynamique a été menée à l’échelle de la crue d’intérêt. Les résultats préliminaires sont présentés dans la Figure 6.4. Des investigations numériques supplémentaires sont nécessaires ainsi que des analyses plus poussées afin de pouvoir améliorer la prédiction de l’érosion de berge sur la partie amont du méandre. La rédaction d’un article a débuté présentant et discutant l’ensemble des résultats, combinés, des suivis de terrain et de modélisés.

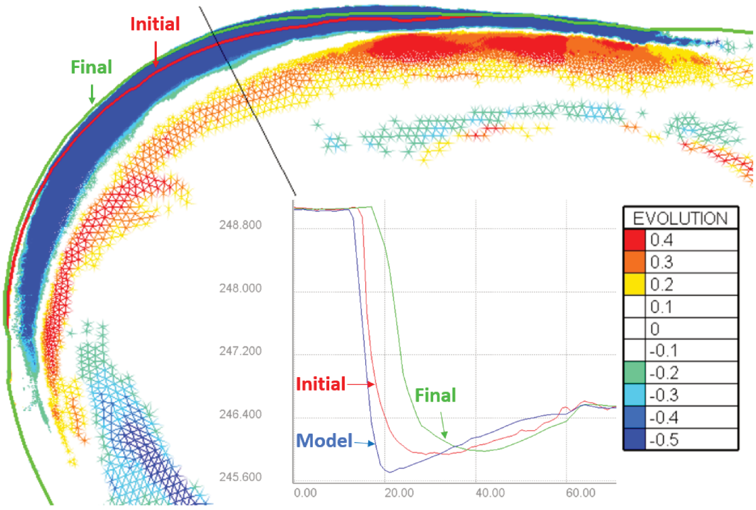

FIGURE 6.4 : Résultat préliminaire de la modélisation de l’érosion de la berge concave du méandre de “la vache morte”, simulée par le modèle hydro-morphologique “sto”, pour une crue de période de retour d’un an ($Q = 180\,m^3/s$).

6.2.2 Modélisation d'un recoupement de méandre

Le recoupement du méandre de Mangonville, qui s'est produit en 2018 suite à la crue décennale de Janvier 2018 permet d'étudier la dynamique d'un chenal nouvellement crée dans une plaine graveleuse. Le levé LiDAR topo-bathymétrique effectué chaque année à la suite de ce recoupement (et pas avant la crue, profils en travers *in situ* disponibles cependant) permet de caractériser l'évolution longitudinale et latérale de la morphologie de ce tronçon (cf. Figure 6.5).

Les MNT successifs permettent de caractériser l'évolution morphologique de ce nouveau chenal de recoupement (approfondissement, élargissement, etc.). La signature hydraulique temporelle de cet ajustement morphologique, donnée par le limnimigraphe L7 situé à l'amont immédiat du recoupement, tend à montrer un abaissement probablement liée à une érosion régressive.

Des traceurs RFID injectés au niveau du pont, *i.e.* environ $800m$ en amont du recoupement, ont permis de montrer que la majorité de la charge de fond amont se dépose dans la partie recoupée (ancienne boucle de méandre). Sur la base de ces différentes données, une modélisation morpho-dynamique visant à reproduire ce recoupement est possible. Elle pourra être entreprise sur une période relativement longue, notamment en essayant d'utiliser les données acoustiques pour estimer les conditions limites amont du flux solide.

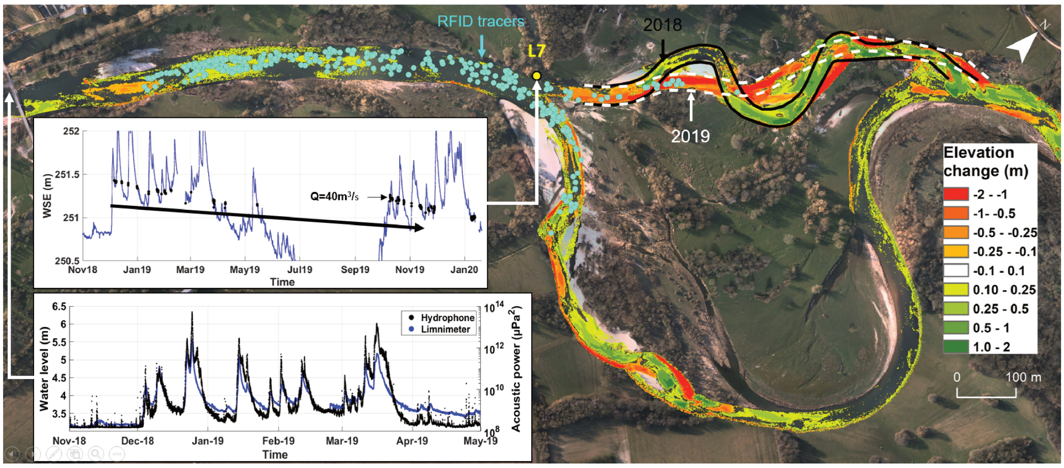

FIGURE 6.5 : Jeu de données sur le méandre recoupé : évolution bathymétriques issues des relevés LiDAR 2018 et 2019 ; Chronique temporelle de niveau d'eau mesurée par le limnimètre L7 à l'amont du recoupement (niveau d'eau en trait bleu et en points noirs niveaux d'eau pour une valeur de débit égale au module de $40m^3/s$) ; Chronique temporelle de la puissance acoustique enregistrée par l'hydrophone fixé à la pile du pont.

6.2.3 Approfondissement des résultats des suivis morpho-sédimentaires

Le traitement et l'interprétation des nombreux résultats hydro-géomorphologiques de terrain pourront être poursuivis, en intégrant également, selon les types de données, les résultats des données pluri-décennaux (données issues des travaux de Beck and Corbonnois (2016) et de Chardon (2014)).

Ces analyses porteront principalement sur :

- l'évolution verticale du thalweg ;
- la dynamique latérale de la bande active et du thalweg (superficie, taux de migration des méandres selon forçages) ;
- des budgets sédimentaires à divers pas de temps ;
- la dynamique de la charge de fonds à partir des traceurs RFID ;
- etc.

Ces analyses seront menées de façon à répondre également aux attentes opérationnelles.

6.2.4 Co-construction de scénarios de gestion durable de la mobilité latérale de la Moselle sauvage

Sur la base des diverses modélisations hydrauliques et morpho-sédimentaires, et des résultats des suivis de terrain, des scénarios de gestion durable de la mobilité latérale et verticale de la Moselle sauvage pourront être co-construits avec les gestionnaires, notamment l'Agence de l'eau Rhin-Meuse et le CEN Lorraine. L'objectif général est de préserver - voire si possible renforcer - la mobilité latérale de la rivière tout en maîtrisant les risques liés à celle-ci. Les modélisations seront assorties d'estimations des incertitudes.

Les tests concerneront :

- divers forçages hydrologiques : crues annuelle, décennale, centennale ;
- diverses options opérationnelles ou liées à l'évolution propre de la rivière : (i) arasement du seuil de Bainville-aux-miroirs (effets sur la ligne d'eau et les ajustements verticaux et latéraux), (ii) défluviation du lit de la Moselle court-circuitant le seuil et (iii) déroctages de berges locaux ;

Ces modélisations pourront approfondir les modélisations préliminaires du TFE ENGEES de Zafra-Gomez (2021) qui ont porté sur (i) l'érosion régressive de la Moselle en cas de défluviation (grand court-circuit du barrage de Bainville-aux-miroirs) et (ii) sur le risque de capture de la Moselle par les gravières de Gripport.

Notons que l'important jeu de données pourra également être enrichi, selon les évolutions futures (fortes crues, importants déplacements latéraux, etc.), au travers de nouvelles campagnes d'acquisition de données (LIDAR topo-bathymétriques, suivis des traceurs RFID, etc.) et de nouvelles modélisations, pour réactualiser le diagnostic fonctionnel et l'appui aux prises de décision.

List of Tables

2.1 Plus fort débit journalier (QJX) et plus fort débit instantané (QIX) avec les périodes de retour associées pour la Moselle à Epinal, calculés sur 58 ans (Banque hydro). . 38

2.2 Plus fort débit journalier (QJX) et plus fort débit instantané (QIX) avec les périodes de retour associées pour la Moselle à Tonnoy calculées sur 39 ans (Banque hydro) . 39

2.3 Débits caractéristiques interpolés pour la station de Châtel-sur-Moselle 40

3.1 Evolution of the painted bed patches PP_n at each survey (E_n). Erosion indicates that the patch was totally eroded, Partial indicates that the patch was partially eroded, Deposits indicates that the patch was covered by sediments deposits and none indicate that no evolution was observed. The patch D_{95} corresponds to the averaged diameter of the ten largest particles measured in pictures taken at the installation of the patch. The D_{95} mobilized corresponds to (i) 0 when no evolution was observed, (ii) the patch D_{95} when it was totally eroded or to (iii) the average diameter of the ten largest particles measured out of the patch when it was partially eroded. The Shields parameter is computed (equation 3.1) according to (i) the maximum grain shear stress (GSS) modelled at each patch during F_n and to (ii) either the patch D_{95} when no evolution was observed or to the mobilized D_{95} when the patch was totally or partially eroded. 77

3.2 Statistical parameters for each particle tracking survey, indicating the total number N_s of tracers injected and recovered at survey S_n or S_n and S_{n+1} (*denoting that tracers located at less than 7m from the left bank were excluded from data), with the number of mobile and immobile tracers among recovered ones. 79

4.1 Summarize of hydrodynamic conditions during acoustic maps 98

5.1 Statistical parameters for each particle tracking survey, indicating the total number N_S of tracers injected and recovered at survey S_n with the number of mobile tracers among recovered ones as well as the corresponding recovery rates mentioned in brackets 140

5.2 Variation of the cross-sectional bedload discharge according to the number of size classes implemented into the hydro-sedimentary model $\mathcal{M}_{f,p}$. 150

5.3 Comparison of the total discharge ($Q > 40m^3/s$) estimated during P_1 at Gripport, at Châtel upstream and at Velle downstream gauging stations, expressed in millions of cubic meters. 153

List of Figures

1.1 Les quatre dimensions de l'hydrosystème fluvial d'après Amoros and Petts (1993). . 9
1.2 Modèle conceptuel hiérarchique des liens fonctionnels entre les principales composantes du système fluviale, d'après Schmitt (2010). 11
1.3 Vue longitudinale et en plan des formes et processus fluviaux et des facteurs de contrôle associés, d'après Brierley and Fryirs (2013). 13
1.4 Echelles temporelles et spatiales de l'ajustement des différentes composantes morphologiques du chenal. Les longueurs, indicatives, sont appliquées à un cours d'eau tempérés, d'après Knighton (1998). 14
1.5 Bilan des forces s'exerçant sur un volume d'eau en écoulement uniforme et répartition verticale des vitesses d'écoulement sur la colonne d'eau. 16
1.6 Bilan des forces s'exerçant sur une particule au sein d'un écoulement, d'après Lamb et al. (2008). 17
1.7 Diagramme de Shields dans Garcia et al. (2000). 18
1.8 Compilation de données montrant la variation du paramètre critique de Shields en fonction de la pente moyenne du fond, d'après Lamb et al. (2008). 18
1.9 Compilation de 8700 mesures collectées sur plus de 100 cours d'eau (pente $0.0001 < S < 0.1$) et de 1317 mesures issues du laboratoire (matériaux quasi-uniformes) avec la courbe rouge représentant la relation de Meyer-Peter and Müller (1948), modifié d'après Recking (2012a) et Recking (2006). 21
1.10 Exemples de formules de transport de la charge de fond applicables aux cours d'eau graveleux, avec leur plage de validité, d'après Carrillo et al. (2021). 22
1.11 Zone d'étude et emprises des différents modèles hydrauliques emboités, modèles de zooms en gris. 29

2.1 Topographie du bassin versant de la Moselle en amont de Tonnoy 32
2.2 Carte géologique simplifiée du bassin versant de la Moselle en amont de Tonnoy . . 33
2.3 Profil en long de la Moselle, d'après AERM (1992) 34
2.4 Linéaire d'étude de la Moselle entre Charmes et Bayon 35
2.5 Précipitations moyennes annuelles (en mm) dans le bassin versant de la Moselle (période de référence $1971 - 1990$), d'après Beck and Corbonnois (2003) 36
2.6 Ecoulements mensuels à Epinal calculés sur 60 ans (Banque hydro) 37
2.7 Ecoulements mensuels à Tonnoy calculés sur 40 ans (Banque hydro) 38
2.8 Apports des affluents, d'après CEGUM (2006) 39
2.9 Hydrogramme de la Moselle au cours de l'hiver 2017-2018 (Banque hydro) 41
2.10 Alternance de tronçons à méandrage et à tressage dans le secteur Charmes-Bainville aux XVIIIe siècle (extrait de la carte Naudins env. 1730) 42
2.11 Réseau d'irrigation des prairies aux environs de Bainville en 1878 (Archives 54) . . . 43
2.12 Implantation du Canal de l'Est et son rôle dans la dynamique latérale de la Moselle, d'après Maire and Lasserre (1991) 44

2.13 Profil en long de la Moselle en 1932 et 1979, d'après Maire and Lasserre (1991) . . . 45
2.14 Extraction de granulats en lit mineur et modification du cours d'eau, d'après Beck and Corbonnois (2016) . . . 47
2.15 Evolution de la dynamique de la Moselle à la suite de l'arrêt des extractions en lit mineur, d'après Beck and Corbonnois (2016) . . . 48
2.16 Evolution des aires d'extraction de granulats en lit majeur entre 1975 et 2002, d'après Beck and Corbonnois (2003) . . . 49
2.17 Modélisation des surfaces inondées pour une crue décennale dans le secteur de Gripport (Atlas Sogreah) . . . 50
2.18 Photographie aérienne de la capture de la Moselle par les gravières de Gripport en 1995 (Source IGN) . . . 51
2.19 Station de pompage de Virecourt (Photographie M. et Mme Tacail) . . . 52
2.20 Evolution du lit et du milieu riverain de la Moselle entre 1950 et 2000, d'après Maire and Corbonnois (2000) . . . 53
2.21 Evolution du lit à Charmes (gauche) et Bainville (droite) (BCEOM, 1981) . . . 54
2.22 Evolution du profil en long de la Moselle sur le secteur Gripport-Bayon, d'après Beck and Corbonnois (2016) . . . 55
2.23 Evolution des volumes charriés de 1979 à 2012 d'après, Beck and Corbonnois (2016) 56
2.24 Évolution de la bande active des méandres du grand travers, d'après Corbonnois et al. (2006) . . . 57
2.25 Lit de la Moselle avec les principales structures du fond de vallée entre Charmes et Bainville en 2000, d'après Maire and Corbonnois (2000). . . . 58
2.26 Lit de la Moselle avec les principales structures du fond de vallée entre Bainville et Bayon en 2000, d'après Maire and Corbonnois (2000). . . . 59
2.27 Photographie aérienne de la Moselle en crue dans le secteur de Mangonville . . . 60

3.1 Study site (A) location of the "Wild Moselle river" in the Moselle Basin, (B) longitudinal extension of the natural regional reserve with orange points indicating the positions of painted bed patches PP_n and the green points indicating the initial positions of the tracers, (C) longitudinal extension of the 2D hydro-sedimentary model (red solid line), spatial distribution of the Strickler coefficients, with yellow points indicating the positions of the limnimeters L_n, (D) spatial extent of flood areas simulated during the peak of the flood event F_1 ($Q = 300m^3/s$). . . . 67
3.2 Monitoring framework related to the flow hydrograph of the Moselle river at the Châtel-sur-Moselle gauging station. A_n indicates the dates of the aerial topo-bathymetric acquisitions, E_n indicates the dates of the painted bed patches surveys, PI indicates the patches installation and TI the tracers injection, F_n indicates the floods for which the flow competence is estimated and S_n indicates the dates of the tracer surveys. . 70
3.3 Example of (A) an orthophoto mosaic built from pictures taken at PP_6 during survey E_1, when partial transport was observed. Orange circles indicate the diameters, measured on the orthophoto, of particles recovered out of the patch, (B) a cumulative frequency distribution of mobile particles size measured on the orthophoto and of particles measured in the field at riverbed surface, (C) picture showing a digitalization of the ten largest particle observed on the patch PP_1 set at PI. . . . 78
3.4 Grain shear stress τ' modelled at the peak of the flood F_1 ($Q = 303m^3/s$) over tracers injection site. Points indicate mobile (white), immobile (black), and excluded (red) tracers. . . . 79

3.5 Comparison between observed and modelled WSE during the flood event F_1 (discharges ranging from 40 to $303m^3/s$). Blue solid line indicate the WSE recorded by the limnimeter L_n distributed along the Moselle river (Figure 3.1 D). Red and green solid line indicates the WSE modelled using the DEM of 2018, with a Strickler coefficient in the floodplain of $47m^{1/3}/s$ and $8m^{1/3}/s$, respectively. Dashed black line indicates, at L7 and L10, the WSE modelled using the DEM of 2019 with a Strickler coefficient in the floodplain of $8m^{1/3}/s$. 81
3.6 Shields parameter computed (equation 3.1) based on (i) the maximum grain shear stress modelled at each painted patch (denoted PP) or tracer location and to (ii) the size of the studied particles, whether they are mobile or immobile. The green dashed line represents an extrapolation of the critical Shields parameter estimated from partially eroded patches, assuming equal mobility ($b = 1$). The black dashed line represents an extrapolation of the Shields parameter estimated from uneroded patches, assuming equal mobility ($b = 1$). The red dashed line represents an extrapolation of the critical Shields parameter estimated from partially eroded patches, assuming size-selective transport ($b = 0.6$) 83
3.7 Comparison of different hiding functions : in all studies $\theta_{ci} = \theta_{cr} \left(\frac{D_i}{D_r}\right)^{-b}$ with $b \in [0.33; 0.98]$ except in Egiazaroff (1965) where $\theta_{ci} = \left(\log(19)/\log(19\frac{D_i}{D_r})\right)^2$. 85
3.8 Statistical distribution of the Shields parameter computed over all areas eroded ($\Delta Z \leq -10cm$) between LiDAR surveys A_1 and A_2, compared to the critical Shields parameter estimated in this study $\theta_{cr} \coloneqq 0.035$. An example of the spatial distribution of the maximum Shields parameter modeled over eroded areas distributed along a reach located at the downstream part of the study site. 86

4.1 (A) location of the "Wild Moselle river" in the Moselle Basin, (B) longitudinal extension of the 2D hydraulic model $\mathcal{M}_{f,h}$ (red dashed line) and the 2D hydro-sedimentary model $\mathcal{M}_{f,s}$ (red solid line) into the natural regional reserve (C) area of bedload fluxes measurement and modelling, velocity and acoustic measurements, (D) hydrophone fixed at the left bank, (E) acoustic mapping, (F) bedload sampling. 91
4.2 Monitoring framework related to the flow hydrograph of the Moselle river at the Châtel-sur-Moselle gauging station with a focus on the studied flood F. BS_n indicates the dates of bedload sampling with gs signifying that bedload samples were sieved, AS indicates the date of the installation of the acoustic monitoring station at the bridge, L_n indicates the dates of the LiDAR topo-bathymetric acquisition, M_n indicates the date of acoustic maps. 93
4.3 Results of the sieving of the bedload samples collected during the first campaign (BS_1) represented as (A) Cross-sectional profile of the bedload samples D_{50} and the mean D_{50} per verticals, along with its standard deviation (B) Cumulative grain size distribution of each bedload sample (solid brown line, which becomes darker as sample is collected close to the center of the section located at $33m$). The GSD of all bedload samples combined (dashed black line) is compared to the GSD of the bed surface (solid blue line) and bed subsurface (solid red line). 105
4.4 (A) Cross-sectional profiles of bedload flux (samples) and acoustic power (drifts) monitored at each field campaign. (B) Relationship between cross-sectional averaged values of acoustic power and specific bedload flux integrated into the model proposed by Geay et al. (2020) 106
4.5 (A) Results of acoustics maps performed at different discharge and (B) relationship between bank and cross-section averaged measurements 109

4.6 (A) Comparison between the WSE recorded by the limnimeter located upstream of the bridge (yellow point in B) and the WSE modeled during the studied flood F from unsteady simulations performed with the submodel $\mathcal{M}_{f,s}$ (B) Map of the water depth predicted at steady state ($Q = 268m^3/s$) by the submodel $\mathcal{M}_{f,s}$ during the bedload sampling campaign BS_2. 110

4.7 (A) Comparison between observed (red points) and modeled depth-averaged flow velocities, during the bedload sampling BS_2 ($Q = 268m^3/s$) and BS_3 ($Q = 233m^3/s$), before (solid blue line) and after (dashed blue line) calibration of the friction coefficient. (B) Map of the depth-averaged flow velocities predicted at steady state ($Q = 268m^3/s$) by the model $\mathcal{M}_{f,s}$ during the bedload sampling campaign BS_2. . . 111

4.8 (A) Local bedload transport measured during sampling BS_2 and BS_3 as a function of the local Shields parameter modelled at steady state for the corresponding discharge using $\mathcal{M}_{f,s}$ (MPM : Meyer-Peter & Müller laws, CL : Camenen & Larson laws, E-B : Einstein-Brown laws) (B) Map of the Shields parameter predicted at steady state ($Q = 268m^3/s$) by the model $\mathcal{M}_{f,s}$ during the bedload sampling campaign BS_2. . . 112

4.9 (A) Calibration of α_{MPM} and (B) Comparison between observed and predicted cross-sectional bedload transport rates during bedload sampling campaigns BS_2 and BS_3. 114

4.10 Comparison between chronicles of (A) acoustic power and flow discharge and (B) bedload fluxes estimated using acoustic measurements and numerical simulations during the studied flood F of March 2020. 115

4.11 Comparison between observed (colored points) and modeled (black points using MPM law) bedload hysteresis during the studied flood F of March 2020. 117

4.12 Comparison between the WSE recorded by limnimeter L_n and the WSE modeled during the studied flood F from unsteady simulations performed with the submodel $\mathcal{M}_{f,h}$. 120

5.1 Study site (A) location of the "Wild Moselle river" in the Moselle Basin, (B) longitudinal extension of the 2D hydro-sedimentary model $\mathcal{M}_{f,p}$ (C) position of tracers over time. 125

5.2 Flowchart of the main components of the method for calibrating the bedload transport composition for a 2D hydro-sedimentary model using complementary data on particle mobility and dynamics. 127

5.3 Cumulative grain size distribution of (i) the bed surface material, estimated from 6 samples collected along the reach of injection by grid-by-number pebble counts ($n_{tot} = 1200$), (ii) the bed subsurface material, estimated from a volumetric sample collected on a bar located in the middle of the study area ($m_{tot} = 346kg$), (iii) the bedload material, estimated from bedload samples collected in the middle of the study area during a flood of bankfull discharge using a Helley-Smith sampler ($m_{tot} = 245kg/s$) and (iv) the injected pit-tags ($n = 450$) with corresponding median diameter of the bed surface (D_{50}), the bed subsurface (D_{50s}), the bedload (D_{50b}), the pit-tags (D_{50p}). 129

5.4 Monitoring framework related to the flow hydrograph of the Moselle river at the Châtel-sur-Moselle gauging station. A_n indicates the dates of aerial topo-bathymetric acquisitions, G indicates the date of surface and subsurface material grain size measurements, I indicates the date of tracer injection, S_n indicates the dates of tracer surveys and P_n is the monitoring periods between two tracer surveys. 130

5.5 Flowchart of the methods employed to estimate the distances traveled by the tracers and the duration of the flow competent to transport these tracers. These methods are based on the results of field surveys (S_n) and of the catalog of 2D hydro-sedimentary model outputs for different inflow discharge. 135

5.6 Distribution of total scour and fill measured during 3 flow events ($Qmax = 303m^3/s$; $214m^3/s$ and $254m^3/s$) by 20 chains ($n_{tot} = 60$) installed across the river at 6 easily accessible emerged gravel bars of the Moselle river (left). Results excludes cases of (i) no morphological evolutions ($n = 29$), (ii) river incision ($n = 3$), (iii) lost chains ($n = 4$) and (iv) stolen chains ($n = 14$). Measurement of total scour and fill using a scour chain (right). 137

5.7 Discretization of the granulometric curve of the bed surface material into different numbers of size classes with corresponding representative diameters. This curve was determined from Wolman pebble counts performed along the injection reach. 138

5.8 Longitudinal distribution of (a) all tracers recovered at S_n and the longitudinal profile of the river bed extracted at the centerline from the DEM of 2018 and 2019 with the water surface elevation modelled at $Q = 40m^3/s$ using the DEM of 2018, (b) all tracers recovered at S_1 and (c) all tracers recovered at S_2. Arrows indicate the mean distance traveled by all mobile tracers recovered at $S_n - S_{n+1}$ in (a), the mean distance traveled by each size class k, based on mobile tracers recovered at $S_0 - S_1$ in (b) and at $S_1 - S_2$ in (c). 142

5.9 Relative travel distances of all tracers recovered during $S_n - S_{n+1}$ as a function to their relative size and median relative travel distances of tracers contained in each size class as a function of the median relative size of those tracers contained in each size class. Polynominal curve fitted to our median value compared to the curve found by Church and Hassan (1992) (noted C-H) and Milan (2013). 143

5.10 Comparison between the WSE recorded by the limnimeter L1 and L2, located on either side of the injection site, and the WSE modeled during the peak flood of period P_1 ($Q = 303m^3/s$), obtained from unsteady simulations performed using the submodel $\mathcal{M}_{f,p}$. 144

5.11 Critical discharge for tracers motion as a function to the tracers size and lateral position according to the river centerline. 145

5.12 Comparison of the critical discharge for tracers motion between $S_0 - S_1$ (left plot) and $S_1 - S_2$ (right plot). The solid line corresponds to the 1:1 relationship and the dotted line represent the trendline based on our data. 146

5.13 Duration of competent flow as a function to the tracer lateral position and size for each period P_n (left plot) and comparison of the flow competence duration between periods $P_1 - P_2$ (right plot). The solid line corresponds to the 1:1 relationship and the dotted line represents the trendline based on our data. 147

5.14 Virtual velocity of tracers as a function to their size during each period P_n (left plot) and dimensionless virtual velocity of tracers as a function to their relative size during each period P_n (right plot). Large squares indicates the median velocity as a function of the median size of tracers within each size class and green line represents the results obtained by Milan (2013). 148

5.15 Comparison of the grain size distribution of the observed bedload and modelled bedload using 6 size classes, without a correction factor ($Q_{s,k}$), with a corrector factor ζ_θ for hiding-exposure effects ($Q^{*,\theta}_{s,k}$) and with a correction factor for hiding-exposure effects ζ_θ and a correction factor ζ_Φ for trapping effects ($Q^{*,\theta,\Phi}_{s,k}$). 151

6.1 (A) localisation du tronçon de la “Moselle sauvage” au sein du bassin versant de la Moselle, (B) extension longitudinale du modèle hydro-sédimentaire 2D “sto”, (C) suivi du recul de la berge concave du méandre de “la vache morte”, (D) profil en travers du recul de berge, (E) suivi du déplacement de traceurs placés dans la berge. 157
6.2 Comparaison de profils de vitesse $T_{n=1..6}$ mesurés par ADCP (points rouge) et modélisés avec (lignes vertes) ou sans (lignes bleues) correction, le long du méandre de “la vache morte”, lors d’une crue de période de retour d’un an ($Q = 180\,m^3/s$). . . . 158
6.3 Comparaison de la direction du transport sédimentaire modélisé le long du méandre de “la vache morte”, lors d’une crue de période de retour d’un an ($Q = 180\,m^3/s$) par rapport à la trajectoire de traceurs provenant de l’érosion de la berge concave. . . . 159
6.4 Résultat préliminaire de la modélisation de l’érosion de la berge concave du méandre de “la vache morte”, simulée par le modèle hydro-morphologique “sto”, pour une crue de période de retour d’un an ($Q = 180\,m^3/s$). 159
6.5 Jeu de données sur le méandre recoupé : évolution bathymétriques issues des relevés LiDAR 2018 et 2019 ; Chronique temporelle de niveau d’eau mesurée par le limnimètre L7 à l’amont du recoupement (niveau d’eau en trait bleu et en points noirs niveaux d’eau pour une valeur de débit égale au module de $40m^3/s$) ; Chronique temporelle de la puissance acoustique enregistrée par l’hydrophone fixé à la pile du pont. . . . 160

Bibliography

Agence de l'Eau Rhin-Meuse, 1992. Définition et impact d'un avant-projet-sommaire d'aménagement de la Moselle entre Bayon et Gripport.

Agence de l'Eau Rhin-Meuse, 1998. Typologie des cours d'eau du bassin Rhin-Meuse.

Allen, J.R.L., 1984. Sedimentary structures: their character and physical basis. volume 11 of *Developments in sedimentology*. Elsevier, Amsterdam.

Amoros, C., Petts, G., 1993. Hydrosystèmes fluviaux. volume 24 of *Ecologie*. Masson, Paris.

Ancey, C., 2016. Mécanique des fluides une introdution à l'hydraulique pour les ingénieurs. EPFL, Lausanne, Switzerland.

Ancey, C., 2020. Bedload transport: a walk between randomness and determinism. part 2. challenges and prospects. Journal of Hydraulic Research 58, 18–33. doi:`10.1080/00221686.2019.1702595`.

Andrews, E., Parker, G., 1987. Formation of a coarse surface layer as the response to gravel mobility. john wiley and sons ed.. Chichester, UK. pp. 269–300.

Andrews, E.D., 1983. Entrainment of gravel from naturally sorted riverbed material. Geol Soc America Bull 94, 1225. doi:`10.1130/0016-7606(1983)94<1225:EOGFNS>2.0.CO;2`.

Arnaud, F., Piégay, H., Béal, D., Collery, P., Vaudor, L., Rollet, A.J., 2017. Monitoring gravel augmentation in a large regulated river and implications for process-based restoration. Earth Surf. Process. Landforms 42, 2147–2166. doi:`10.1002/esp.4161`.

Arnaud, F., Piégay, H., Vaudor, L., Bultingaire, L., Fantino, G., 2015. Technical specifications of low-frequency radio identification bedload tracking from field experiments: Differences in antennas, tags and operators. Geomorphology 238, 37–46. doi:`10.1016/j.geomorph.2015.02.029`.

Arnaud, F., Schmitt, L., . Carte à la une : reconstituer le rhin disparu. URL: `http://geoconfluences.ens-lyon.fr/informations-scientifiques/a-la-une/carte-a-la-une/reconstituer-rhin-disparu`.

Ashmore, P.E., 1991. How do gravel-bed rivers braid ? Can. J. Earth Sci. 28, 326–341. doi:`10.1139/e91-030`.

Ashworth, P.J., Ferguson, R.I., 1989. Size-selective entrainment of bed load in gravel bed streams. Water Resources Research 25, 627–634. doi:`10.1029/WR025i004p00627`.

Bacchi, V., Recking, A., Eckert, N., Frey, P., Piton, G., Naaim, M., 2014. The effects of kinetic sorting on sediment mobility on steep slopes. Earth Surface Processes and Landforms 39, 1075–1086. doi:`10.1002/esp.3564`.

Bagnold, R.A., 1966. An approach to the sediment transport problem from general physics. Professional Paper 422-I, U. S. Govt., USGS. doi:`10.3133/pp422I`.

Bagnold, R.A., 1980. An empirical correlation of bedload transport rates in flumes and natural rivers. Proc. R. Soc. Lond. A 372, 453–473. doi:`10.1098/rspa.1980.0122`.

Bakke, P.D., Basdekas, P.O., Dawdy, D.R., Klingeman, P.C., 1999. Calibrated parker-klingeman model for gravel transport. Journal of Hydraulic Engineering 125, 657–660. doi:`10.1061/(ASCE)0733-9429(1999)125:6(657)`.

Bakker, M., Gimbert, F., Geay, T., Misset, C., Zanker, S., Recking, A., 2020. Field application and validation of a seismic bedload transport model. Journal of Geophysical Research: Earth Surface 125. doi:`10.1029/2019JF005416`.

Barry, J.J., Buffington, J.M., King, J.G., 2004. A general power equation for predicting bed load transport rates in gravel bed rivers. Water Resources Research 40. doi:`10.1029/2004WR003190`.

Basile, P.A., 2001. On the number of fractions to compute transport of sediment mixtures. International Journal of Sediment Research 16, 399–407.

BCEOM, 1981. Stabilisation du lit de la Moselle entre Epinal et Neuves-Maisons. Rapport d'étude. AERM, Metz.

Beck, T., Corbonnois, J., 2003. Les différents états du lit mineur de la Moselle entre Epinal et Méréville, étapes de la reconstruction d'un nouvel équilibre. Actes du Colloque "le fil de l'eau", Nancy, 10-12 mars 2003.

Beck, T., Corbonnois, J., 2016. Analyse du temps de résilience d'un cours d eau à moyenne énergie (la moselle amont) suite aux importantes altérations anthropiques de la deuxième moitié du vingtième siècle. Bulletin de la Société Géographique de Liège 67, 195–208.

Beeson, C., Doyle, P., 1995. Comparison of bank erosion at vegetated and non-vegetated channel bends. Journal of the American Water Resources Association 31, 983–990. doi:`10.1111/j.1752-1688.1995.tb03414.x`.

Benett, J.P., Nordin, C.F., 1977. Simulation of sediment transport and armouring. Hydrological Sciences Bulletin 22, 555–569. doi:`10.1080/02626667709491760`.

Bernard, R.S., Schneider, M.L., 1992. Depth-Averaged Numerical Modeling for Curved Channels. Technical report, DTIC Document, Departement of the army.

Bonnefont, J.C., Carcaud, N., 1997. The morphodynamic behaviour of moselle river before its harnessings. Géomorphologie : relief, processus, environnement 3, 339–353. doi:`10.3406/morfo.1997.932`.

Borah, D.K., Alonso, C.V., Prasad, S.N., 1982. Routing graded sediments in streams: Formulations. Journal of the Hydraulics Division 108, 1486–1503. doi:`10.1061/JYCEAJ.0005955`.

Brandt, S.A., 2000. Classification of geomorphological effects downstream of dams. CATENA 40, 375–401. doi:`10.1016/S0341-8162(00)00093-X`.

Bravard, J.P., 1994. The incision of river beds : from a natural and reversible morphodynamic phenomenon to irreversible impacts. Revue de géographie de Lyon 69. doi:`10.3406/geoca.1994.4231`.

Bravard, J.P., Amoros, C., Pautou, G., Bornette, G., Bournaud, M., Creuzé Des Chatelliers, M., Gibert, J., Peiry, J.L., Perrin, J.F., Tachet, H., 1997. River incision in south-east france: morphological phenomena and ecological effects. Regul. Rivers: Res. Mgmt. 13, 75–90. doi:`10.1002/(SICI)1099-1646(199701)13:1<75::AID-RRR444>3.0.CO;2-6`.

Bravard, J.P., Peiry, J.L., 1993. La disparition du tressage fluvial dans les alpes françaises sous l'effet de l'aménagement des cours d'eau (19-20ème siècle). Zeitschrift Für Geomorphologie 88, 67–79.

Bravard, J.P., Petit, F., 1997. Les cours d'eau. Dynamique du système fluvial. Armand Colin, Paris, 222 p.

Brice, J., 1975. Airphoto interpretation of the form and behavior of alluvial rivers. Final report, Army Research Office, Durham, North Carolina .

Bridge, J.S., 2005. Rivers and floodplains: forms, processes, and sedimentary record. Blackwell, Oxford.

Brierley, G., Fryirs, K., 2013. Geomorphic analysis of river systems : an approach to reading the landscape. Wiley-Blackwell, Oxford, UK.

Brookes, A., 1988. Channelized Rivers: Perspectives for Environmental Management. John Wiley & Sons, New York.

Brousse, G., Claude, N., Cordier, F., Loire, R., Jodeau, M., 2022. 2d morphodynamic modelling as a predictive tool for gravel replenishment: the saint-sauveur dam case study. International Journal of River Basin Management , 1–14doi:`10.1080/15715124.2022.2153857`.

Brown, C., 1950. Sediments transportation. John Wiley and Sons, New York.

Brunner, G., 2010. HEC-RAS, River Analysis System Hydraulic Reference Manual. Version 4.1. US Army Corps of Engineers. Hydrologic Engineering Center, Davis, CA.

Buffington, J.M., Montgomery, D.R., 1997. A systematic analysis of eight decades of incipient motion studies, with special reference to gravel-bedded rivers. Water Resour. Res. 33, 1993–2029. doi:`10.1029/96WR03190`.

Bunte, K., Abt, S.R., 2001. Sampling frame for improving pebble count accuracy in coarse gravel-bed streams. Journal of the American Water Resources Association 37, 1001–1014. doi:`10.1111/j.1752-1688.2001.tb05528.x`.

Camenen, B., Larson, M., 2005. A general formula for non-cohesive bed load sediment transport. Estuarine, Coastal and Shelf Science 63, 249–260. doi:`10.1016/j.ecss.2004.10.019`.

Camenen, B., Melun, G., 2021. Guide technique pour la mesure et la modélisation du transport solide. Office français de la biodiversité.

Carcaud, N.N., 1992. Remplissages des fonds de vallées de la Moselle et de la Meurthe en Lorraine sédimentaire. Thèse de doctorat, Université de Nancy 2.

Carrillo, V., Petrie, J., Timbe, L., Pacheco, E., Astudillo, W., Padilla, C., Cisneros, F., 2021. Validation of an experimental procedure to determine bedload transport rates in steep channels with coarse sediment. Water 13, 672. doi:`10.3390/w13050672`.

Casado, A., 2013. Human impacts and fluvial metamorphosis : the effects of flow regulation on the hydrology, morphology and water temperature of the Sauce Grande River, Argentina. Thèse de doctorat, Université Blaise Pascal, Clermont-Ferrand 2.

Champalbert Expertises, hydro expertise, 2008. Capture de plan d'eau. Application au site de Gripport. Rapport d'étude 07-14-V1a.

Chapuis, M., Dufour, S., Provansal, M., Couvert, B., de Linares, M., 2015. Coupling channel evolution monitoring and RFID tracking in a large, wandering, gravel-bed river: Insights into sediment routing on geomorphic continuity through a riffle-pool sequence. Geomorphology 231, 258–269. doi:`10.1016/j.geomorph.2014.12.013`.

Chardon, V., 2014. Etude de l'évolution morphologique de la Moselle sauvage et de zones à forte mobilité. Mémoire de Master 2, Université de Strasbourg.

Chardon, V., Piasny, G., Schmitt, L., 2021a. Comparison of software accuracy to estimate the bed grain size distribution from digital images: A test performed along the rhine river. River Research and Applications doi:`10.1002/rra.3910`.

Chardon, V., Schmitt, L., Arnaud, F., Piégay, H., Clutier, A., 2021b. Efficiency and sustainability of gravel augmentation to restore large regulated rivers: Insights from three experiments on the rhine river (france/germany). Geomorphology 380, 107639. doi:`10.1016/j.geomorph.2021.107639`.

Chassaing, P., 1997. Fluid mechanics. Elements of a first course; Mécanique des fluides. Éléments d'un premier parcours.

Chien, N., Wan, Z., 1999. Mechanics of Sediment Transport. American society of civil engineers ed., Reston, VA.

Chiew, Y.M., Parker, G., 1994. Incipient sediment motion on non-horizontal slopes. Journal of Hydraulic Research 32, 649–660. doi:`10.1080/00221689409498706`.

Chow, V., 1959. Open-channel Hydraulics. Mc Graw-Hill, New-York, USA.

Church, M., 1983. Pattern of instability in a wandering gravel bed channel, in: Modern and Ancient Fluvial Systems. John Wiley & Sons, Ltd, pp. 169–180. doi:`10.1002/9781444303773.ch13`.

Church, M., 2002. Geomorphic thresholds in riverine landscapes. Freshwater Biology 47, 541–557. doi:`10.1046/j.1365-2427.2002.00919.x`.

Church, M., Hassan, M.A., 1992. Size and distance of travel of unconstrained clasts on a streambed. Water Resour. Res. 28, 299–303. doi:`10.1029/91WR02523`.

Church, M., Hassan, M.A., Wolcott, J.F., 1998. Stabilizing self-organized structures in gravel-bed stream channels: Field and experimental observations. Water Resources Research 34, 3169–3179. doi:`10.1029/98WR00484`.

Church, M., McLean, D., Walcott, J., 1987. River bed gravels: sampling and analysis. john wiley and sons ed.. Chichester. pp. 43 – 88.

Cipriani, T., Toilliez, T., Sauquet, E., 2012. Caractérisation du régime des crues en France métropolitaine. Rapport final, irstea.

Corbonnois, J., Beck, T., Giovannacci, L., Jacquemot, T., Winkel, B., 2006. L'érosion fluviale de cours d'eau lorrains, d'origine vosgienne : Moselle, Meurthe, Vezouze, Mortagne, Sarre. Rapport final, Centre d'Etudes Géographiques de l'Université de Metz, Metz.

Cordier, F., Tassi, P., Claude, N., Crosato, A., Rodrigues, S., Pham Van Bang, D., 2019. Numerical study of alternate bars in alluvial channels with nonuniform sediment. Water Resources Research 55, 2976–3003. doi:`10.1029/2017WR022420`.

Couvert, B., Lefebvre, B., Lefort, P., Morin, E., 1991. Etude générale sur les seuils de correction torrentielle et les plages de dépots. La Houille Blanche 77, 449–456. doi:`10.1051/lhb/1991043`.

Cudden, J.R., Hoey, T.B., 2003. The causes of bedload pulses in a gravel channel: the implications of bedload grain-size distributions. Earth Surface Processes and Landforms 28, 1411–1428. doi:`10.1002/esp.521`.

Davies, T.R.H., Sutherland, A.J., 1983. Extremal hypotheses for river behavior. Water Resources Research 19, 141–148. doi:`10.1029/WR019i001p00141`.

Day, T., 1980. A study of the transport of graded sediments. IT 190, HRS wallingford.

Degoutte, G., 2006. Diagnostic, aménagement et gestion des rivières : hydraulique et morphologie fluviale appliquées. Tec et Doc, Lavoisier.

Dinger, F., Fischesser, B., Centre national du machinisme agricole, d.g.r., 1982. L'étude d'impact des aménagements des cours d'eau. CEMAGREF, Grenoble.

Dingman, S.L., 1984. Fluvial Hydrology. W H Freeman & Co, New York.

Dingman, S.L., 2009. Fluvial hydraulics. Oxford university press.

Doering, M., Uehlinger, U., Rotach, A., Schlaepfer, D., Tockner, K., 2007. Ecosystem expansion and contraction dynamics along a large alpine alluvial corridor (tagliamento river, northeast italy). Earth Surface Processes and Landforms 32, 1693–1704. doi:`10.1002/esp.1594`.

Dufresne, M., Isenmann, G., 2020. Transport solide. ENGEES, Strasbourg.

Edelblutte, S., 2000. Exploitation or protection in the middle moselle valley ? the landscape as an indicator of spatial conflicts linked to gravel extradion. Géocarrefour 75, 293–304. doi:`10.3406/geoca.2000.2481`.

Edwards, T., Glysson, G., 1999. Field methods for measurement of fluvial sediment. Technical report, U.S Geological Survey, Reston, VA.

Egiazaroff, I.V., 1965. Calculation of nonuniform sediment concentrations. Journal of the Hydraulics Division 91, 225–247. doi:`10.1061/JYCEAJ.0001277`.

Einstein, H.A., 1950. The Bed-Load Function for Sediment Transportation in Open Channel Flows. Technical Bulletin. doi:`10.22004/ag.econ.156389`.

El Kadi Abderrezzak, K., Die Moran, A., Tassi, P., Ata, R., Hervouet, J.M., 2016. Modelling river bank erosion using a 2d depth-averaged numerical model of flow and non-cohesive, non-uniform sediment transport. Advances in Water Resources 93, 75–88. doi:`10.1016/j.advwatres.2015.11.004`.

Engelund, F., Hansen, E., 1967. A monograph on sediment transport in alluvial streams. Technical Press, University of Denmark, Copenhagen.

Ferguson, R.I., Bloomer, D.J., Hoey, T.B., Werritty, A., 2002. Mobility of river tracer pebbles over different timescales: mobility of river tracer pebbles. Water Resour. Res. 38, 3–1–3–8. doi:`10.1029/2001WR000254`.

Ferguson, R.I., Wathen, S.J., 1998. Tracer-pebble movement along a concave river profile: Virtual velocity in relation to grain size and shear stress. Water Resour. Res. 34, 2031–2038. doi:`10.1029/98WR01283`.

Ferguson, R.I., Werritty, A., 1983. Bar development and channel changes in the gravelly river feshie, scotland, in: Collinson, J.D., Lewin, J. (Eds.), Modern and Ancient Fluvial Systems. 1 ed.. Wiley, pp. 181–193. doi:`10.1002/9781444303773.ch14`.

Ferrer-Boix, C., Hassan, M.A., 2014. Influence of the sediment supply texture on morphological adjustments in gravel-bed rivers. Water Resources Research 50, 8868–8890. doi:`10.1002/2013WR015117`.

FLUVIAL.IS, 2015. Expertise sur les conséquences probables d'un recoupement de méandre de la Moselle sauvage par déversement - Commune de Mangonville. Rapport d'étude.

Frécaut, R., 1972. La Moselle et son bassin : contribution à l'hydrologie et à la dynamique fluviale en milieu tempéré océanique. Thése Doctorat d'Etat, Nancy.

Gaeuman, D., 2013. Monitoring the Effectiveness of Gravel Augmentations for Salmonid Habitat Improvement Downstream from Dams. Completion Report, Project 0295, US Bureau of Reclamation Science and Technology, Washington, DC.

Garcia, M., 2008. Sedimentation Engineering: Processes, Measurements, Modeling, and Practice. American Society of Civil Engineers, Reston, VA. doi:`10.1061/9780784408148`.

Garcia, M.H., Laursen, E.M., Michel, C., Buffington, J.M., 2000. The legend of a. f. shields. Journal of Hydraulic Engineering 126, 718–723. doi:`10.1061/(ASCE)0733-9429(2000)126:9(718)`.

Geay, T., 2013. Mesure acoustique passive du transport par charriage dans les rivières. Thèse de doctorat, Université Joseph Fourier, Grenoble.

Geay, T., Belleudy, P., Gervaise, C., Habersack, H., Aigner, J., Kreisler, A., Seitz, H., Laronne, J.B., 2017. Passive acoustic monitoring of bed load discharge in a large gravel bed river. JGR Earth Surface 122, 528–545. doi:`10.1002/2016JF004112`.

Geay, T., Michel, L., Zanker, S., Rigby, J.R., 2019. Acoustic wave propagation in rivers: an experimental study. Earth Surface Dynamics 7, 537–548. doi:`10.5194/esurf-7-537-2019`. publisher: Copernicus GmbH.

Geay, T., Zanker, S., Misset, C., Recking, A., 2020. Passive acoustic measurement of bedload transport: Toward a global calibration curve? JGR Earth Surface 125, e2019JF005242. doi:`10.1029/2019JF005242`.

Geay, T., Zanker, S., Petrut, T., Recking, A., 2018. Measuring bedload grain-size distributions with passive acoustic measurements. E3S Web Conf. 40, 04010. doi:`10.1051/e3sconf/20184004010`.

Gessler, J., 1971. Beginning and ceasing of sediment motion. volume 1 of *River Mechanics*. H.w. shen ed., Fort Collins.

Graf, W., Altinakar, M., 2000. Hydraulique fluviale: écoulement et phénomènes de transport dans les canaux à géométrie simple. volume 16. PPUR presses polytechniques.

Grospretre, L., 2011. Etude et gestion des impacts hydrogéomorphologiques de la périurbanisation. l'exemple du bassin de l'yzeron dans l'ouest lyonnais .

Gunsolus, E.H., Binns, A.D., 2018. Effect of morphologic and hydraulic factors on hysteresis of sediment transport rates in alluvial streams. River Research & Apps 34, 183–192. doi:`10.1002/rra.3184`.

Haschenburger, J.K., Church, M., 1998. Bed material transport estimated from the virtual velocity of sediment. Earth Surf. Process. Landforms 23, 791–808. doi:`10.1002/(SICI)1096-9837(199809)23:9<791::AID-ESP888>3.0.CO;2-X`.

Hassan, M.A., Church, M., Ashworth, P.J., 1992. Virtual rate and mean distance of travel of individual clasts in gravel-bed channels. Earth Surface Processes and Landforms 17, 617–627. doi:`10.1002/esp.3290170607`.

Hassan, M.A., Saletti, M., Zhang, C., Ferrer-Boix, C., Johnson, J.P., Müller, T., von Flotow, C., 2020. Co-evolution of coarse grain structuring and bed roughness in response to episodic sediment supply in an experimental aggrading channel. Earth Surface Processes and Landforms 45, 948–961. doi:`10.1002/esp.4788`.

Helley, E.J., Smith, W., 1971. Development and calibration of a pressure-difference bedload sampler. Open-File Report 73-108 doi:`10.3133/ofr73108`.

Hervouet, J.M., 2007. Hydrodynamics of free surface flows. Modelling with the finite element method. John wiley & sons, ltd, ed., West Sussex, England.

Hey, R.D., 1988. Bar form resistance in gravel-bed rivers. Journal of Hydraulic Engineering 114, 1498–1508. doi:`10.1061/(ASCE)0733-9429(1988)114:12(1498)`.

Hirano, M., 1971. River bed degradation with armoring. Civil Eng 3(2), 55–65.

Houbrechts, G., Levecq, Y., Peeters, A., Hallot, E., Van Campenhout, J., Denis, A.C., Petit, F., 2015. Evaluation of long-term bedload virtual velocity in gravel-bed rivers (ardenne, belgium). Geomorphology 251, 6–19. doi:`10.1016/j.geomorph.2015.05.012`.

Houbrechts, G., Levecq, Y., Vanderheyden, V., Petit, F., 2011. Long-term bedload mobility in gravel-bed rivers using iron slag as a tracer. Geomorphology 126, 233–244. doi:`10.1016/j.geomorph.2010.11.006`.

Houbrechts, G., Van Campenhout, J., Levecq, Y., Hallot, E., Peeters, A., Petit, F., 2012. Comparison of methods for quantifying active layer dynamics and bedload discharge in armoured gravel-bed rivers. Earth Surface Processes and Landforms 37, 1501–1517. doi:`10.1002/esp.3258`.

Houssais, M., Ortiz, C.P., Durian, D.J., Jerolmack, D.J., 2015. Onset of sediment transport is a continuous transition driven by fluid shear and granular creep. Nat Commun 6, 6527. doi:`10.1038/ncomms7527`.

Humphries, R., Venditti, J.G., Sklar, L.S., Wooster, J.K., 2012. Experimental evidence for the effect of hydrographs on sediment pulse dynamics in gravel-bedded rivers. Water Resources Research 48. doi:`10.1029/2011WR010419`.

Hygelund, B., Manga, M., 2003. Field measurements of drag coefficients for model large woody debris. Geomorphology 51, 175–185. doi:`10.1016/S0169-555X(02)00335-5`.

Iwasaki, T., Shimizu, Y., Kimura, I., 2016. Numerical simulation of bar and bank erosion in a vegetated floodplain: A case study in the otofuke river. Advances in Water Resources 93, 118–134. doi:`10.1016/j.advwatres.2015.02.001`.

Jackson, R.G., 1976. Depositional model of point bars in the lower wabash river. J Sediment Petrol 46, 579–594.

Karim, M., Kennedy, J., 1982. A computer based flow and sediment routing. IIH report 250, University of Iowa, Iowa City, USA.

Knighton, D., 1998. Fluvial Forms and Processes: A New Perspective. 2 ed., Routledge, London. doi:`10.4324/9780203784662`.

Koehl, M., Piasny, G., Thomine, V., Garambois, P.A., Finaud-Guyot, P., Guillemin, S., Schmitt, L., 2020. 4d GIS for monitoring river bank erosion at meander bend scale: case of moselle river. The International Archives of the Photogrammetry, Remote Sensing and Spatial Information Sciences XLIV-4-W1-2020, 63–70. doi:`10.5194/isprs-archives-XLIV-4-W1-2020-63-2020`.

Komar, P.D., 1987. Selective gravel entrainment and the empirical evaluation of flow competence. Sedimentology 34, 1165–1176. doi:`10.1111/j.1365-3091.1987.tb00599.x`.

Komar, P.D., Carling, P.A., 1991. Grain sorting in gravel-bed streams and the choice of particle sizes for flow-competence evaluations. Sedimentology 38, 489–502. doi:`10.1111/j.1365-3091.1991.tb00363.x`.

Lague, D., Feldmann, B., 2020. Topo-bathymetric airborne LiDAR for fluvial-geomorphology analysis, in: Developments in Earth Surface Processes. Elsevier. volume 23, pp. 25–54. doi:`10.1016/B978-0-444-64177-9.00002-3`.

Lamarre, H., MacVicar, B., Roy, A.G., 2005. Using passive integrated transponder (PIT) tags to investigate sediment transport in gravel-bed rivers. Journal of Sedimentary Research 75, 736–741. doi:`10.2110/jsr.2005.059`.

Lamb, M.P., Dietrich, W.E., Venditti, J.G., 2008. Is the critical shields stress for incipient sediment motion dependent on channel-bed slope? J. Geophys. Res. 113, F02008. doi:`10.1029/2007JF000831`.

Landon, N., 2007. Du constat d'enfoncement du lit fluvial aux actions de recharge sédimentaire : quelles solutions pour une gestion raisonnée de nos cours d'eau ?, in: Guide de gestion de l'eau en territoire de montagne. PNR du queyras, ONEMA et MEDR ed.. PNR du Queyras, ONEMA et MEDR, pp. 28 – 39.

Lane, E.W., 1955. Design of stable channels. Transactions of the American Society of Civil Engineers 120, 1234–1260. doi:`10.1061/TACEAT.0007188`.

Laronne, J.B., Outhet, D.N., Carling, P.A., McCabe, T.J., 1994. Scour chain employment in gravel bed rivers. CATENA 22, 299–306. doi:`10.1016/0341-8162(94)90040-X`.

Lefort, P., 2007. Une formule semi-empirique pour le calcul du transport solide des rivières et torrents., Lyon.

Leopold, L.B., Wolman, M.G., 1957. River channel patterns: Braided, meandering, and straight. Professional Paper 282-B, U.S. Government Printing Office. doi:`10.3133/pp282B`.

Leopold, L.B., Wolman, M.G., Miller, J.P., 1964. Fluvial processes in geomorphology. Freeman press ed., San Francisco.

Lesser, G., Roelvink, J., van Kester, J., Stelling, G., 2004. Development and validation of a three-dimensional morphological model. Coastal Engineering 51, 883–915. doi:`https://doi.org/10.1016/j.coastaleng.2004.07.014`.

L'Hommedieu, W., Tullos, D., Jones, J., 2020. Effects of an engineered log jam on spatial variability of the flow field across submergence depths. River Research & Apps 36, 383–397. doi:`10.1002/rra.3555`.

Liébault, F., Bellot, H., Chapuis, M., Klotz, S., Deschâtres, M., 2012. Bedload tracing in a high-sediment-load mountain stream: bedload tracing in a high-sediment-load mountain stream. Earth Surf. Process. Landforms 37, 385–399. doi:`10.1002/esp.2245`.

Lisle, T., 1979. A sorting mechanism for a riffle-pool sequence. GSA Bulletin 90, 1142–1157. doi:`10.1130/GSAB-P2-90-1142`.

Maire, G., Corbonnois, J., 2000. The recent morphodynamic development of the moselle between charmes and bayon. an audit of the present state of the river bed and the choice of an appropriate management system for the fluvial area. geoca 75, 305–315. doi:`10.3406/geoca.2000.2482`.

Maire, G., Lasserre, S., 1981. Stabilisation du lit de la Moselle entre Epinal et Neuves-Maisons. Cartographie morphodynamique du lit et du fond de vallée : secteurs représentatifs au 1/50000. Rapport CGA-ULP pour le compte du BCEOM.

Maire, G., Lasserre, S., 1991. Structure et fonctionnement d'un systeme fluvial déséquilibré par l'intervention anthropique : La moselle non canalisée à la sortie du massif vosgien. Mosella XVIII, 39–81.

Malavoi, J.R., Bravard, J.P., 2010. Eléments d'hydromorphologie fluviale appliquée. Onema.

Malou, T., 2022. Modélisations des écoulements fluviaux adaptées aux observations spatiales et assimilations de données altimétriques. Thèse de doctorat, Univérsite de Toulouse.

Mao, L., 2012. The effect of hydrographs on bed load transport and bed sediment spatial arrangement. J. Geophys. Res. 117. doi:`10.1029/2012JF002428`.

Mao, L., Uyttendaele, G.P., Iroumé, A., Lenzi, M.A., 2008. Field based analysis of sediment entrainment in two high gradient streams located in alpine and andine environments. Geomorphology 93, 368–383. doi:`10.1016/j.geomorph.2007.03.008`.

Marineau, M., Wright, S., Gaeuman, D., 2016. Calibration of sediment-generated noise measured using hydrophones to bedload transport in the trinity river, california, USA, in: River Flow 2016, CRC Press, St. Louis, USA. pp. 1519–1525. doi:`10.1201/9781315644479-239`.

Marquis, G.A., Roy, A.G., 2012. Using multiple bed load measurements: Toward the identification of bed dilation and contraction in gravel-bed rivers. J. Geophys. Res. 117. doi:`10.1029/2011JF002120`.

Masteller, C.C., Finnegan, N.J., Turowski, J.M., Yager, E.M., Rickenmann, D., 2019. History-dependent threshold for motion revealed by continuous bedload transport measurements in a steep mountain stream. Geophysical Research Letters 46, 2583–2591. doi:`10.1029/2018GL081325`.

Mendoza, A., Abad, J.D., Langendoen, E.J., Wang, D., Tassi, P., Abderrezzak, K.E.K., 2017. Effect of sediment transport boundary conditions on the numerical modeling of bed morphodynamics. J. Hydraul. Eng. 143, 04016099. doi:`10.1061/(ASCE)HY.1943-7900.0001208`.

Merchant, N.D., Barton, T.R., Thompson, P.M., Pirotta, E., Dakin, D.T., Dorocicz, J., 2013. Spectral probability density as a tool for ambient noise analysis. The Journal of the Acoustical Society of America 133, EL262–EL267. doi:`10.1121/1.4794934`.

Meyer-Peter, E., Müller, R., 1948. Formulas for Bed-Load transport. In Proc.2nd IAHR Congress, Stockholm, Sweden.

Milan, D.J., 2013. Virtual velocity of tracers in a gravel-bed river using size-based competence duration. Geomorphology 198, 107–114. doi:`10.1016/j.geomorph.2013.05.018`.

Miller, M.C., McCAVE, I.N., Komar, P.D., 1977. Threshold of sediment motion under unidirectional currents. Sedimentology 24, 507–527. doi:`10.1111/j.1365-3091.1977.tb00136.x`.

Mizuyama, T., Laronne, J.B., Nonaka, M., Sawada, T., Satofuka, Y., Yamashita, S., Sako, Y., Tamaki, S., Watari, M., Yamaguchi, S., 2010. Calibration of a passive acoustic bedload monitoring system in japanese mountain rivers .

Montgomery, D.R., Buffington, J.M., 1997. Channel-reach morphology in mountain drainage basins. Geological Society of America Bulletin 109, 596–611. doi:`10.1130/0016-7606(1997)109<0596:CRMIMD>2.3.CO;2`. number: 5.

Mosley, M.P., 1981. Semi-determinate hydraulic geometry of river channels, south island, new zealand. Earth Surf. Process. Landforms 6, 127–137. doi:`10.1002/esp.3290060206`.

Mosselman, E., 2012. Modelling sediment transport and morphodynamics of gravel-bed rivers, in: Gravel-Bed Rivers. John Wiley & Sons, Ltd, pp. 101–115. doi:`10.1002/9781119952497.ch9`.

Mouradi, R.S., Audouin, Y., Goeury, C., Claude, N., Tassi, P., 2016. Sensitivity analysis and uncertainty quantification in 2D morphodynamic models using a newly implemented API for TELEMAC2D/SISYPHE. 23rd TELEMAC-MASCARET User Conference, Paris, 11-13 october 2016.

Mueller, D.S., 2016. QRev-Software for computation and quality assurance of acoustic doppler current profiler moving-boat streamflow measurements-User's manual for version 2.8. Open-File Report 2016-1052, U.S. Geological Survey. doi:`10.3133/ofr20161052`.

Nasr, M., 2023. Development of an acoustic method for bedload transport measurement in rivers. Thèse de doctorat, Université de Grenoble Alpes.

Nelson, P.A., McDonald, R.R., Nelson, J.M., Dietrich, W.E., 2015. Coevolution of bed surface patchiness and channel morphology: 2. numerical experiments. JGR Earth Surface 120, 1708–1723. doi:`10.1002/2014JF003429`.

Nelson, P.A., Venditti, J.G., Dietrich, W.E., Kirchner, J.W., Ikeda, H., Iseya, F., Sklar, L.S., 2009. Response of bed surface patchiness to reductions in sediment supply. Journal of Geophysical Research: Earth Surface 114. doi:`10.1029/2008JF001144`.

Nikora, V., Koll, K., McEwan, I., McLean, S., Dittrich, A., 2004. Velocity distribution in the roughness layer of rough-bed flows. Journal of Hydraulic Engineering 130, 1036–1042. doi:`10.1061/(ASCE)0733-9429(2004)130:10(1036)`.

Paintal, A.S., 1971. Concept of critical shear stress in loose boundary open channels. Journal of Hydraulic Research 9, 91–113. doi:`10.1080/00221687109500339`.

Paphitis, D., Collins, M.B., 2005. Sand grain threshold, in relation to bed "stress history": an experimental study. Sedimentology 52, 827–838. doi:`10.1111/j.1365-3091.2005.00710.x`.

Parker, G., 1992. Some random notes on grain sorting, International Seminar on Grain Sorting, Ascona, Switzerland. pp. 19–76.

Parker, G., Klingeman, P.C., 1982. On why gravel bed streams are paved. Water Resources Research 18, 1409–1423. doi:`10.1029/WR018i005p01409`.

Parker, G., Klingeman, P.C., McLean, D.G., 1982. Bedload and size distribution in paved gravel-bed streams. Journal of the Hydraulics Division 108, 544–571. doi:`10.1061/JYCEAJ.0005854`.

Parker, G., Toro-Escobar, C.M., Ramey, M., Beck, S., 2003. Effect of floodwater extraction on mountain stream morphology. Journal of Hydraulic Engineering 129, 885–895. doi:`10.1061/(ASCE)0733-9429(2003)129:11(885)`.

Parsons, D.R., Jackson, P.R., Czuba, J.A., Engel, F.L., Rhoads, B.L., Oberg, K.A., Best, J.L., Mueller, D.S., Johnson, K.K., Riley, J.D., 2013. Velocity mapping toolbox (VMT): a processing and visualization suite for moving-vessel ADCP measurements. Earth Surface Processes and Landforms 38, 1244–1260. doi:`10.1002/esp.3367`.

Peiry, J., 1989. L'utilisation du cadastre sarde de 1730 pour l'étude des riviéres savoyardes : l'exemple de la vallée de l'arve (haute-savoie). Revue de géographie de Lyon 64, 197–203.

Periketi, R., Fox, G., Dabney, S., Shields Jr, F., Cullum, R., 2007. Seepage erosion properties contributing to streambank failure. Earth Surface Processes and Landforms 32, 447–459. doi:`10.1002/esp.1405`.

Petit, F., 1987. The relationship between shear stress and the shaping of the bed of a pebble-loaded river la rulles-ardenne. CATENA 14, 453–468. doi:`10.1016/0341-8162(87)90015-4`.

Petit, F., Gob, F., Houbrechts, G., Assani, A., 2005. Critical specific stream power in gravel-bed rivers. Geomorphology 69, 92–101. doi:`10.1016/j.geomorph.2004.12.004`.

Petit, F., Houbrechts, G., Peeters, A., Hallot, E., Van Campenhout, J., Denis, A.C., 2015. Dimensionless critical shear stress in gravel-bed rivers. Geomorphology 250, 308–320. doi:`10.1016/j.geomorph.2015.09.008`.

Petts, G.E., 1984. Impounded rivers: perspectives for ecological management. Wiley, Chichester.

Pfeiffer, A.M., Finnegan, N.J., Willenbring, J.K., 2017. Sediment supply controls equilibrium channel geometry in gravel rivers. Proceedings of the National Academy of Sciences 114, 3346–3351. doi:`10.1073/pnas.1612907114`.

Phillips, C.B., Hill, K.M., Paola, C., Singer, M.B., Jerolmack, D.J., 2018. Effect of flood hydrograph duration, magnitude, and shape on bed load transport dynamics. Geophysical Research Letters 45, 8264–8271. doi:`10.1029/2018GL078976`.

Phillips, C.B., Martin, R.L., Jerolmack, D.J., 2013. Impulse framework for unsteady flows reveals superdiffusive bed load transport. Geophysical Research Letters 40, 1328–1333. doi:`10.1002/grl.50323`.

Piasny, G., Garambois, P., Finaud-Guyot, P., Schmitt, L., 2023a. Calibration of non-uniform sediment transport 2D model using particle tracing. Draft to be submitted.

Piasny, G., Garambois, P.A., Finaud-Guyot, P., Schmitt, L., 2023b. Effective determination of critical bed shear stress from multi-source measurement of flow competence for 2D hydro-sedimentary modelling. Draft to be submitted.

Piasny, G., Garambois, P.A., Geay, T., Zanker, S., Finaud-Guyot, P., Schmitt, L., 2023c. Flood scale dynamic bedload transport estimation through acoustic measurements compared to 2D hydro-sedimentary modeling. Draft to be submitted.

Piton, G., 2014. Méthode de transfert de bassin. MOOC, Grenoble INP.

Pretzlav, K.L.G., Johnson, J.P.L., Bradley, D.N., 2020. Smartrock transport in a mountain stream: Bedload hysteresis and changing thresholds of motion. Water Resources Research 56, e2020WR028150. doi:`10.1029/2020WR028150`.

Pujol, L., 2022. Optimal synergy of multi-source data and hydraulic-hydrological models for the cartographic modeling of complex hydrosystems. Thèse de doctorat, Universite de Strasbourg.

Recking, A., 2006. Etude expérimentale de l'influence du tri granulométrique sur le transport solide par charriage. Thèse de doctorat, Institut National des Sciences Appliquées, Lyon.

Recking, A., 2009. Theoretical development on the effects of changing flow hydraulics on incipient bed load motion. Water Resources Research 45, 2008WR006826. doi:`10.1029/2008WR006826`.

Recking, A., 2012a. Cours d'hydraulique et de transport solide. Master II, Paris 6.

Recking, A., 2012b. Influence of sediment supply on mountain streams bedload transport. Geomorphology 175-176, 139–150. doi:`10.1016/j.geomorph.2012.07.005`.

Remy, G., 2009. Recensement des témoins historiques et actuels de la rivière Moselle et redéfinition du fuseau de mobilité sur le secteur de la Réserve Naturelle Régionale. Mémoire de Master 2, Université de Metz.

Rennie, C.D., Vericat, D., Williams, R.D., Brasington, J., Hicks, M., 2017. Calibration of acoustic doppler current profiler apparent bedload velocity to bedload transport rate, in: Gravel-Bed Rivers. John Wiley & Sons, Ltd, pp. 209–233. doi:`10.1002/9781118971437.ch8`.

Rice, S.P., Church, M., Wooldridge, C.L., Hickin, E.J., 2009. Morphology and evolution of bars in a wandering gravel-bed river; lower fraser river, british columbia, canada. Sedimentology 56, 709–736. doi:`10.1111/j.1365-3091.2008.00994.x`.

Rice, S.P., Rhoads, B.L., Roy, A.G., 2008. Introduction: River confluences, tributaries and the fluvial network, in: River Confluences, Tributaries and the Fluvial Network. John Wiley & Sons, Ltd, pp. 1–9. doi:`10.1002/9780470760383.ch1`.

Richards, K., 1982. Rivers: Form and Process in Alluvial Channels. Routledge, London ; New York.

Rickenmann, D., 1990. Bedload transport capacity of slurry flows at steep slopes. Doctoral Thesis, Swiss federal institute of technology, Zurich.

Rickenmann, D., Fritschi, B., 2017. Bedload transport measurements with impact plate geophones in two austrian mountain streams (fischbach and ruetz): system calibration, grain size estimation, and environmental signal pick-up. Earth Surf. Dynam. 5, 669–687. doi:`10.5194/esurf-5-669-2017`.

Rickenmann, D., Recking, A., 2011. Evaluation of flow resistance in gravel-bed rivers through a large field data set. Water Resources Research 47, 2010WR009793. doi:`10.1029/2010WR009793`.

Rigby, J., Wren, D., Kuhnle, R., 2016. Passive acoustic monitoring of bed load for fluvial applications. Journal of Hydraulic Engineering 142, 02516003. doi:`10.1061/(ASCE)HY.1943-7900.0001122`.

van Rijn, L.C., 1984. Sediment transport, part i: Bed load transport. J. Hydraul. Eng. 110, 1431–1456. doi:`10.1061/(ASCE)0733-9429(1984)110:10(1431)`.

Rinaldi, M., Casagli, N., Dapporto, S., Gargini, A., 2004. Monitoring and modelling of pore water pressure changes and riverbank stability during flow events. Earth Surface Processes and Landforms 29, 237–254. doi:`10.1002/esp.1042`.

Rosgen, D.L., 1994. A classification of natural rivers. CATENA 22, 169–199. doi:`10.1016/0341-8162(94)90001-9`.

Roux, H., 2004. Estimation de paramètres en hydraulique fluviale, à partir de données caractéristiques de l'imagerie aérienne.

Schmidt, K.H., Ergenzinger, P., 1992. Bedload entrainment, travel lengths, step lengths, rest periods-studied with passive (iron, magnetic) and active (radio) tracer techniques. Earth Surface Processes and Landforms 17, 147–165. doi:`10.1002/esp.3290170204`.

Schmitt, L., 2010. Dynamique fluviale et gestion environnementale durable des hydrosystèmes. Application à une grande plaine alluviale (Rhin-Ill, Alsace) et à un hydrosystème périurbain (Yzeron, Ouest lyonnais). Habilitation à Diriger des Recherches, Université Lumière Lyon 2.

Schoklitsch, A., 1962. Handbuch des Wasserbaues : Zweiter Band. 3 ed., Springer Verlag, Wien.

Schumm, S.A., 1963. Sinuosity of alluvial rivers on the great plains. Geol Soc America Bull 74, 1089. doi:`10.1130/0016-7606(1963)74[1089:SOAROT]2.0.CO;2`.

Schumm, S.A., 1973. Geomorphic thresholds and complex response of drainage systems., in: Morisawa, M. (Ed.), Fluvial geomorphology. State University of New York, Binghamton, N.Y.. Geomorphology, pp. 299–310.

Schumm, S.A., 1977. The Fluvial System. John Wiley & Sons, New-York.

Sear, D.A., 1996. Sediment transport processes in pool-riffle sequences. Earth Surface Processes and Landforms 21, 241–262. doi:`10.1002/(SICI)1096-9837(199603)21:3<241::AID-ESP623>3.0.CO;2-1`.

Shen, H.W., Lu, J.Y., 1983. Development and prediction of bed armoring. Journal of Hydraulic Engineering 109, 611–629. doi:`10.1061/(ASCE)0733-9429(1983)109:4(611)`.

Shields, A., 1936. Application of similarity principles and turbulence research to bed-load movement. CalTech library 26.

Shvidchenko, A.B., Pender, G., Hoey, T.B., 2001. Critical shear stress for incipient motion of sand/gravel streambeds. Water Resour. Res. 37, 2273–2283. doi:`10.1029/2000WR000036`.

Sinbio, 2010. Etude - bilan sur la dynamique de la Moselle dans le secteur Chamagne - Bayon. Rapport d'étude EP / CE 230 / B.

Singer, M.B., 2010. Transient response in longitudinal grain size to reduced gravel supply in a large river. Geophys. Res. Lett. 37. doi:`10.1029/2010GL044381`.

Sogreah, 2006. Projet d'extension de carrière en lit majeur de la Moselle: etude hydraulique.

Soulsby, R.L., Whitehouse, R.J., 1997. Threshold of sediment motion in coastal environments. Pacific Coasts and Ports '97: Proceedings of the 13th Australasian Coastal and Ocean Engineering Conference and the 6th Australasian Port and Harbour Conference; Volume 1 , 145–150doi:`10.3316/informit.929741720399033`.

Stähly, S., Franca, M.J., Robinson, C.T., Schleiss, A.J., 2019. Sediment replenishment combined with an artificial flood improves river habitats downstream of a dam. Sci Rep 9, 5176. doi:`10.1038/s41598-019-41575-6`.

Strom, K., Papanicolaou, A.N., Evangelopoulos, N., Odeh, M., 2004. Microforms in gravel bed rivers: Formation, disintegration, and effects on bedload transport. Journal of Hydraulic Engineering 130, 554–567. doi:`10.1061/(ASCE)0733-9429(2004)130:6(554)`.

Tal, M., Paola, C., 2010. Effects of vegetation on channel morphodynamics: Results and insights from laboratory experiments. Earth Surface Processes and Landforms 35, 1014–1028. doi:`10.1002/esp.1908`.

Tassi, P., Villaret, C., 2014. Sisyphe v6.3 User's Manual. Internal Report H-P74-2012-02004-EN, EDF R&D.

Thompson, C., Croke, J., 2008. Channel flow competence and sediment transport in upland streams in southeast australia. Earth Surface Processes and Landforms 33, 329–352. doi:`10.1002/esp.1558`.

Thual, O., 2010. Hydrodynamique de l'environnement. Ecole polytechnique.

Torok, G.T., Jozsa, J., Baranya, S., 2019. Validation of a novel, shear reynolds number based bed load transport calculation method for mixed sediments against field measurements. Water 11, 2051. doi:`10.3390/w11102051`.

Tsai, V.C., Minchew, B., Lamb, M.P., Ampuero, J.P., 2012. A physical model for seismic noise generation from sediment transport in rivers. Geophys. Res. Lett. 39. doi:`10.1029/2011GL050255`.

Venditti, J.G., Dietrich, W.E., Nelson, P.A., Wydzga, M.A., Fadde, J., Sklar, L., 2010. Mobilization of coarse surface layers in gravel-bedded rivers by finer gravel bed load. Water Resour. Res. 46. doi:`10.1029/2009WR008329`.

Vericat, D., Church, M., Batalla, R.J., 2006. Bed load bias: Comparison of measurements obtained using two (76 and 152 mm) helley-smith samplers in a gravel bed river. Water Resources Research 42. doi:`10.1029/2005WR004025`.

Villaret, C., Hervouet, J.M., Kopmann, R., Merkel, U., Davies, A.G., 2013. Morphodynamic modeling using the telemac finite-element system. Computers & Geosciences 53, 105–113. doi:`10.1016/j.cageo.2011.10.004`.

Wang, Q., Pan, Y., Yang, K., Nie, R., 2020. Structural properties of the static armor during formation and reestablishment in gravel-bed rivers. Water 12, 1845. doi:`10.3390/w12071845`.

Warren, I., Bach, H., 1992. Mike 21: a modelling system for estuaries, coastal waters and seas. Environmental Software 7, 229–240. doi:`https://doi.org/10.1016/0266-9838(92)90006-P`.

Wasson, J.G., Malavoi, J.R., Maridet, L., Souchon, Y., Paulin, L., 1995. Impacts écologiques de la chenalisation des rivières. Rapport final, CEMAGREF, EPTEAU et Ministère de l'Environnment.

Wathen, S.J., Ferguson, R.I., Hoey, T.B., Werritty, A., 1995. Unequal mobility of gravel and sand in weakly bimodal river sediments. Water Resources Research 31, 2087–2096. doi:`10.1029/95WR01229`.

Welch, P., 1967. The use of fast fourier transform for the estimation of power spectra: A method based on time averaging over short, modified periodograms. IEEE Trans. Audio Electroacoust. 15, 70–73. doi:`10.1109/TAU.1967.1161901`.

Whitaker, A.C., Potts, D.F., 2007. Analysis of flow competence in an alluvial gravel bed stream, dupuyer creek, montana. Water Resources Research 43. doi:`10.1029/2006WR005289`.

White, W.R., Bettess, R., Paris, E., 1982. Analytical approach to river regime. Journal of the Hydraulics Division 108, 1179–1193. doi:`10.1061/JYCEAJ.0005914`.

Wiberg, P.L., Smith, J.D., 1987. Calculations of the critical shear stress for motion of uniform and heterogeneous sediments. Water Resour. Res. 23, 1471–1480. doi:`10.1029/WR023i008p01471`.

Wilcock, P.R., 1988. Methods for estimating the critical shear stress of individual fractions in mixed-size sediment. Water Resources Research 24, 9.

Wilcock, P.R., 1992. Flow competence: A criticism of a classic concept. Earth Surf. Process. Landforms 17, 289–298. doi:`10.1002/esp.3290170307`.

Wilcock, P.R., 2001. Toward a practical method for estimating sediment transport rates in gravel bed rivers. Earth Surf Processes Landf 26, 1395–1408. doi:`10.1002/esp.301`.

Wilcock, P.R., Crowe, J.C., 2003. Surface-based transport model for mixed-size sediment. J. Hydraul. Eng. 129, 120–128. doi:`10.1061/(ASCE)0733-9429(2003)129:2(120)`.

Wilcock, P.R., McArdell, B.W., 1997. Partial transport of a sand/gravel sediment. Water Resources Research 33, 235–245. doi:`10.1029/96WR02672`.

Wolman, M.G., 1954. A method of sampling coarse river-bed material. Trans. AGU 35, 951. doi:`10.1029/TR035i006p00951`.

Wong, M., Parker, G., 2006. Reanalysis and correction of bed-load relation of meyer-peter and müller using their own database. J. Hydraul. Eng. 132, 1159–1168. doi:`10.1061/(ASCE)0733-9429(2006)132:11(1159)`.

Wu, W., 2007. Computational River Dynamics. CRC Press, London. doi:`10.4324/9780203938485`.

Yager, E.M., Schmeeckle, M.W., Badoux, A., 2018. Resistance is not futile: Grain resistance controls on observed critical shields stress variations. Journal of Geophysical Research: Earth Surface 123, 3308–3322. doi:`10.1029/2018JF004817`.

Yalin, M.S., 1992. River Mechanics. Pergamon, Oxford ; New York.

Yang, C.T., Song, C.C.S., Woldenberg, M.J., 1981. Hydraulic geometry and minimum rate of energy dissipation. Water Resources Research 17, 1014–1018. doi:`10.1029/WR017i004p01014`.

Yu, Q., Rennie, C.D., Slaney, J.M., Parsapour-Moghaddam, P., 2022. Impact evaluation of instream bar management using morphodynamic modelling. Journal of Environmental Management 318, 115564. doi:`10.1016/j.jenvman.2022.115564`.

Zafra-Gomez, J., 2021. Elaboration de scénarios de gestion/restauration de la Moselle sauvage à partir de la combinaison d'une étude hydrogéomorphologique et d'une modélisation hydraulique 2D. TFE ENGEES, LIVE, Strasbourg.

Annexes

Contents

Annexe 1 : Article Chardon et al., 2021, RRA **189**

Annexe 2 : Conference paper 3DGeoInfo, 2020, Londre **201**

Annexe 3 : Abstract WLRI 4th Conference, 2021, Moscou **211**

Annexe 3 : Résumé colloque TSMR - CFBR, 2022, Paris **215**

Annexe 4 : Abstract AFEQ 13th Conference, 2022, Strasbourg **219**

Annexe 1 : Article Chardon et al., 2021, RRA

Received: 7 May 2021 | Revised: 8 November 2021 | Accepted: 10 November 2021
DOI: 10.1002/rra.3910

SHORT COMMUNICATION

WILEY

Comparison of software accuracy to estimate the bed grain size distribution from digital images: A test performed along the Rhine River

Valentin Chardon | **Guillaume Piasny** | **Laurent Schmitt**

CNRS UMR 7362 LIVE, University of Strasbourg, Strasbourg, France

Correspondence
Valentin Chardon, CNRS UMR 7362 LIVE, University of Strasbourg, 3 rue de l'Argonne, Strasbourg 67000, France.
Email: valentin.chardon@live-cnrs.unistra.fr

Abstract

The quantification of the bed grain size distribution (GSD) of river surfaces is primarily conducted through manual approaches in the field. These methods are time consuming and not able to accurately represent the spatial diversity of the grain size distribution of rivers. Recently, several software programs and procedures have been developed using semi-automatic and automatic methods to estimate bed GSD from digital imagery. The purpose of this study is to compare softwares accuracy between reference GSDs and estimated GSDs using geometric approaches (Basegrain software and a procedure developed on ImageJ), statistical approaches (digital grain size [DGS] and PebbleCounts softwares), and a machine learning framework (SediNet). This study evaluates ten digital images recorded along the Rhine River downstream of the city of Basel. The results showed that all software programs considerably underestimated the manually measured GSDs. Nevertheless, it is possible to significantly improve the estimation of bed GSD by applying calibration laws. Both DGS and Basegrain softwares are reliable to estimate the GSD, while the three others softwares are accurate for percentiles equal and higher than the D_{50}. After linear regression correction, the mean normalized root mean square error of percentile errors did not exceed 13% for DGS and Basegrain software, while the others did not exceed 22% for percentiles coarser than the D_{50}.

KEYWORDS
bed grain size, digital images, Rhine, river, software accuracy

1 | INTRODUCTION

Riverbed grain size is a key parameter in geomorphological and ecological studies of rivers. This parameter allows researchers to evaluate physical habitat quality, sediment transport dynamics, and restoration action effects. The quantification of the bed grain size distribution (GSD) of river surfaces is mostly conducted through manual approaches in the field, such as Wolman sampling, the paint-and-pick approach, or grid sampling (Bunte & Abt, 2001). These methods are time consuming, and the measurements are not representative of the spatial diversity of a river's grain size distribution (Graham, Rollet, Piégay, & Rice, 2010). Currently, new remote sensing methods have been developed to semi-automatically or automatically estimate the bed GSD of bar surfaces. These approaches are divided into two classes: (i) two-dimensional approaches using terrestrial and aerial imagery (Baptista, Cunha, Gama, & Bernardes, 2012; Chang & Chung, 2012; Chardon, Schmitt, Arnaud, Piégay, & Clutier, 2021; Graham, Reid, & Rice, 2005; Lejot, Piégay, Hunter, Moulin, & Gagnage, 2011; Purinton & Bookhagen, 2019; Rubin, 2004; Strom, Kuhns, & Lucas, 2010; Sulaiman, Sinnakaudan, Ng, & Strom, 2014; Turley et al., 2017) and (ii) three-dimensional approaches using photogrammetry, laser scanning, or LiDAR datasets by estimating roughness as a proxy of bed GSD (Brasington, Vericat, & Rychkov, 2012; Chardon, Schmitt, Piégay, & Lague, 2020; Heritage & Milan, 2009; Vázquez-Tarrío, Borgniet, Liébault, & Recking, 2017; Woodget, Fyffe, & Carbonneau, 2018). Although the photographic sampling method does not enable the mapping of surface GSD over a large area when compared with a three-dimensional approach, it requires only a simple camera and thus is less costly. Moreover, terrestrial photographic sampling requires fewer preprocessing steps for correcting raw data than three-dimensional approaches, which can be difficult and technical (e.g., cleaning and georeferencing of raw point clouds, roughness metric calculation, and calibration with the manually recorded GSD) (Brasington et al., 2012; Heritage & Milan, 2009; Vázquez-Tarrío et al., 2017; Woodget et al., 2018). However, the accuracy of two-dimensional approaches is extremely sensitive to environmental conditions such as such as natural light conditions, the presence of vegetation or biofilms, and sediment petrography or/and mineralogy. In addition, for two-dimensional approaches, bed sediment structures (burial, overlapping, and foreshortening) also influence the accuracy of the results obtained (Graham et al., 2010; Hodge, Brasington, & Richards, 2009).

Two methods were used to estimate the bed GSD from digital images via morphological approaches and statistical approaches (Buscombe, 2013). Morphological approaches use thresholding and segmentation processing to define the outline of each visible particle, while statistical approaches tend to estimate the grain size through image texture analysis from the semi-variance approach (Carbonneau, Lane, & Bergeron, 2004), autocorrelation approach (Warrick et al., 2009), the wavelength approach (Buscombe, 2013), and recently, following the k-means approach (Purinton & Bookhagen, 2019). Deep learning methods were also developed to automatically estimate the GSD using digital images such as SediNet (Buscombe, 2019) and GRAINet (Lang et al., 2021). Although Basegrain (morphological approach) and DGS (statistical approach) programs are frequently used to estimate the GSD from digital images, a question still remains: Which software provides the most accurate estimation of bed GSD from digital imagery using default parameters? The objective of this study is to compare the software accuracy of reference GSDs and estimated GSDs from DGS, Basegrain, SediNet, PebbleCounts software, and a procedure using ImageJ. The analysis was based on ten digital images sampled along the Rhine River downstream of the city of Basel.

2 | METHODOLOGY

2.1 | Study area

Photographic sampling was performed on the Old Rhine River between the cities of Kembs and Ottmarsheim over five above-water deposits. The Old Rhine River is a bypassed and regulated reach in the Alsacian Plain. An instream flow is maintained in the Old Rhine between 52 and 115 m^3/s from the Kembs disversion dam, depending on the natural hydrological regime of the Rhine River (Figure 1b). Spills occur on the Old Rhine River when the Rhine River discharge exceeds 1,400 m^3/s in Basel, which is the maximum discharge capacity of the Grand Canal d'Alsace (GCA). The channel bottom of the study reach is composed mainly of gravel and cobble (Arnaud et al., 2015). The mean slope and mean width are equal to 0.09% and 100 m, respectively (Figure 1b).

2.2 | Field data collection

Photographic sampling was performed on clean substrates without vegetation or a biofilm to avoid substantial estimation errors induced by these elements (Chardon et al., 2020). According to the recommendations of Barnard, Rubin, Harney, and Mustain (2007) and Chardon et al. (2020), all digital images were taken under an umbrella in order to control solar conditions which could influence GSD estimations (Figure 1). Moreover, all images were taken using a telescoping bar and a bubble level to capture sediment patches with on a horizontal plane of view. The camera used was an Olympus TG-4, and the image resolution was equal to 16 MP (4,608 × 3,456 pixel). A median filter was applied to reduce error in the estimation resulting from pepper and salt phenomena (Chardon et al., 2020). As recommended by Chardon et al. (2020), the median-sized filter used in this study was equal to 5% of the D_{max} value measured for each digital image.

2.3 | Image processing

2.3.1 | Manual digitalization

Following the recommendations of Barnard et al. (2007), the b-axes of 80 to 100 particles were digitized manually from each digital image using a sampling grid to obtain a reference distribution. This step, which was performed using ImageJ software, allows us to achieve a reference GSD.

2.3.2 | DGS software

The first software used to automatically estimate the grain size of 10 sediment patches was the DGS software developed by Buscombe and implemented in MATLAB (2013). This software is based on a statistical approach using the wavelength method, which automatically provides the GSD within the sample grid (Figure 2). Batch processing has been proposed to evaluate the GSD of a large number of digital images. No filter was applied, and the totality of the surfaces of the digital images was considered for GSD estimation.

2.3.3 | Basegrain software

The second software used in this study was Basegrain software (Detert & Weitbrecht, 2012), which was also developed for

FIGURE 1 Set of sediments deposits studied ($n = 10$). A median filter was applied before analysis following the recommendations of Chardon et al. (2020) [Color figure can be viewed at wileyonlinelibrary.com]

MATLAB software (Figure 3). The approach of Basegrain is based on a morphological method. Five preprocessing steps are available for the user to compute median filter options, the minimal size of a grain area (for watershed algorithm application), and the minimal number of pixels (to determine the minimal area), which is related to grain size (Detert & Weitbrecht, 2012). This study used the default options for each step to decrease the processing time of digital images and to compare the methods between them to not to favor

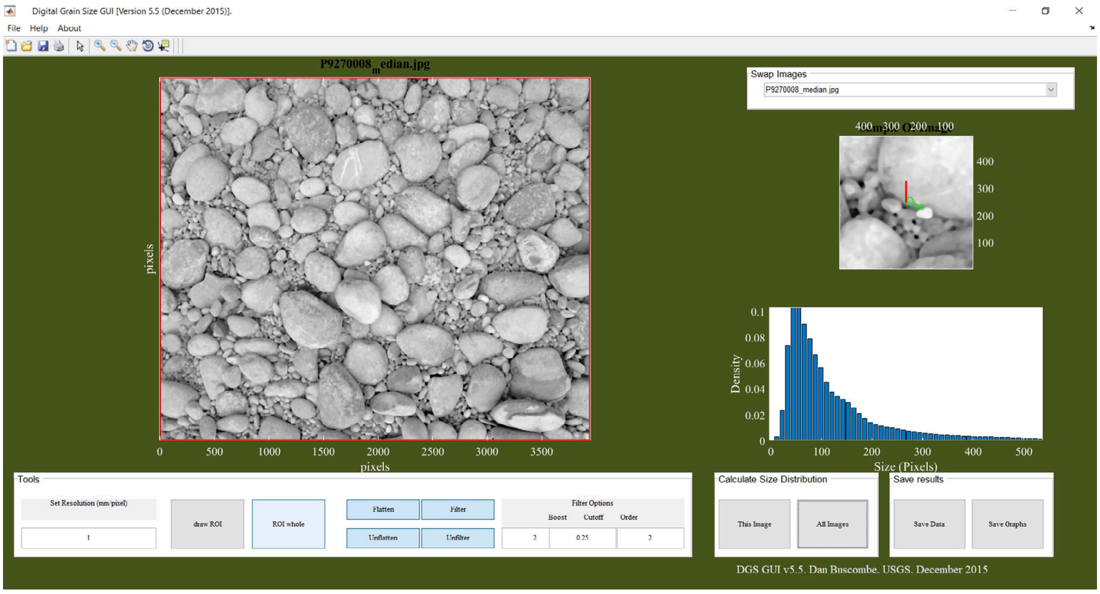

Set Resolution (mm/pixel): 1

Filter Options: Boost 2, Cutoff 0.25, Order 2

FIGURE 2 Example of image processing by the digital grain size (DGS) software package developed by Buscombe (2013) [Color figure can be viewed at wileyonlinelibrary.com]

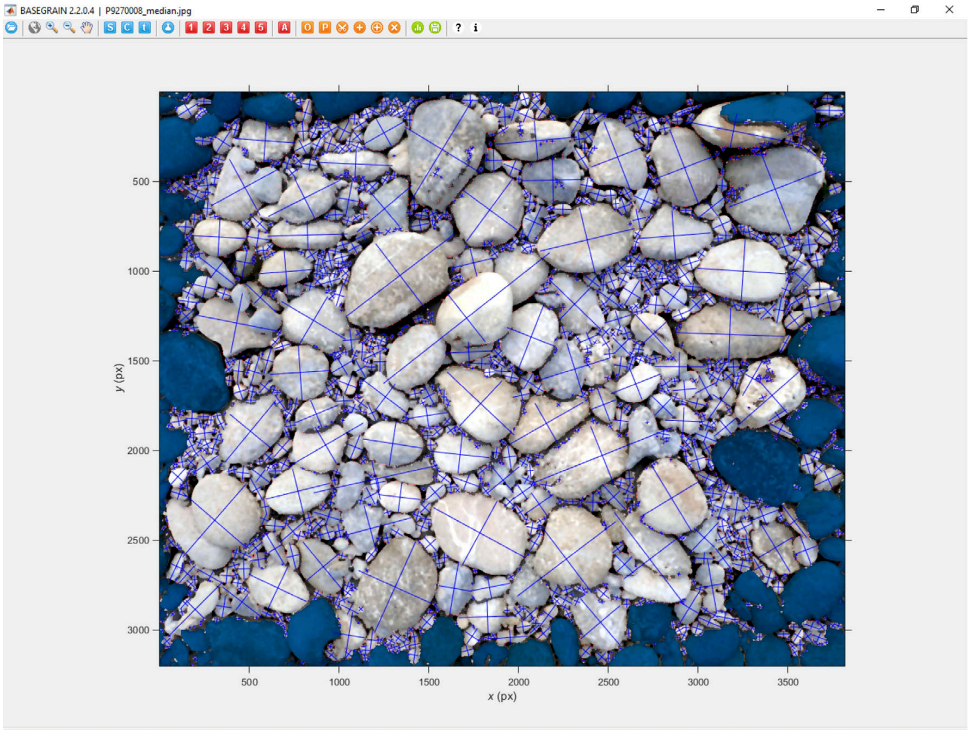

FIGURE 3 Example of image processing by the Basegrain software package developed by Detert and Weitbrecht (2012) [Color figure can be viewed at wileyonlinelibrary.com]

one method over another. The GSD can be obtained in a sample grid form.

2.3.4 | Procedure using ImageJ software

The method using ImageJ is based on a procedure established by (Sulaiman et al., 2014), which proposed a morphological approach to automatically extract the GSD by areal sampling. We slightly modified this protocol as follows: (i) the digital images were transformed in 8-bit format, (ii) the substrate background algorithm was applied with mobile windows equal to 50 pixels by default, (iii) an automatic threshold for black and white transformation was applied, (iv) the watershed algorithm was applied, and (v) the b-axis of all detected particles was determined via automatic measurement (Figure 4). To compare the GSD obtained with this method (areal sampling) with the two previous estimations from DGS and Basegrain software, we collected the b-axis of 60 to 100 particles detected using a grid built with QGIS software.

2.3.5 | PebbleCounts software

This software was developed in Python language and used initially to estimate the apparent GSD of above-water bar deposits using aerial imagery from a drone (Purinton & Bookhagen, 2019). This software was recently used to estimate the longitudinal bed grain size variations along 100 km of river length of the Toro watershed in Argentina (Purinton & Bookhagen, 2021). In this study, we used the automatic procedure called PebbleCountsAuto (AIF), which used edge detection and filter automatically suspect grains (Purinton & Bookhagen, 2019). Similarly to the procedure used in ImageJ software, we collected the b-axis of 60 to 100 particles detected using a grid built with QGIS software from X and Y coordinates provided by the output files of the software (Figure 5).

2.3.6 | SediNet software

This software was based on a machine learning framework developed by Buscombe (2019) using python language. It estimates quantitatively and automatically the measurements from digital images and given percentiles values directly as the output. In this study, we used the trainer developed only for gravel deposits related to our dataset.

2.4 | Estimation of the prediction accuracy

To evaluate and compare the prediction accuracy of each software, we compared percentile values estimated by each automatic processing approach with the reference distributions. The estimation errors by each software packages were quantified by two metrics, that is, the normalized root mean square error (NRMSE; Equation (1)) and normalized mean absolute error (NMAE; Equation (2)), which were calculated as follows:

$$\mathrm{NRMSE} = \frac{\sqrt{\sum_{i=1}^{n} (x_i - x)^2}}{x_{mean}} \tag{1}$$

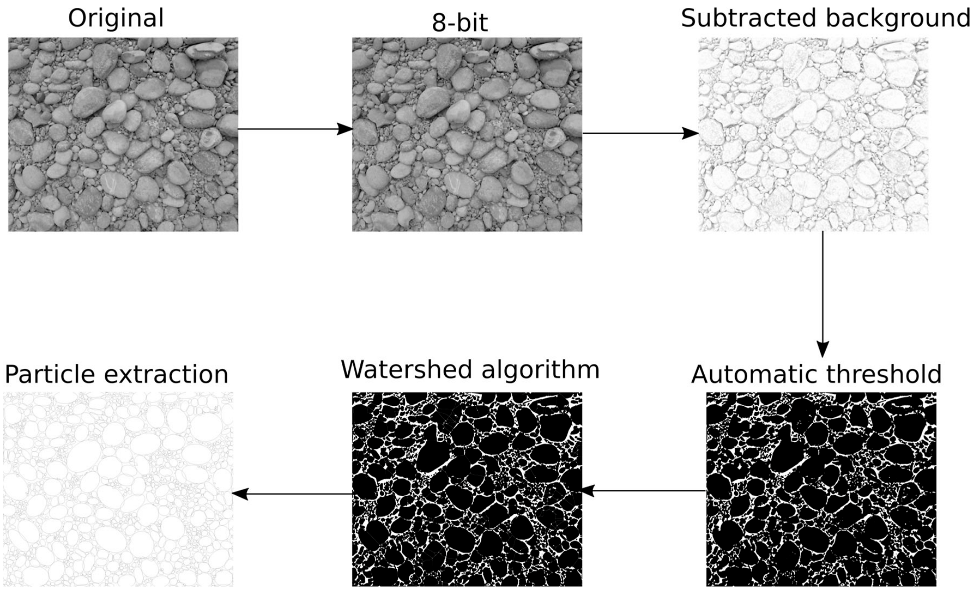

FIGURE 4 Example of image processing by the ImageJ software package, based on the protocol developed by Sulaiman et al. (2014)

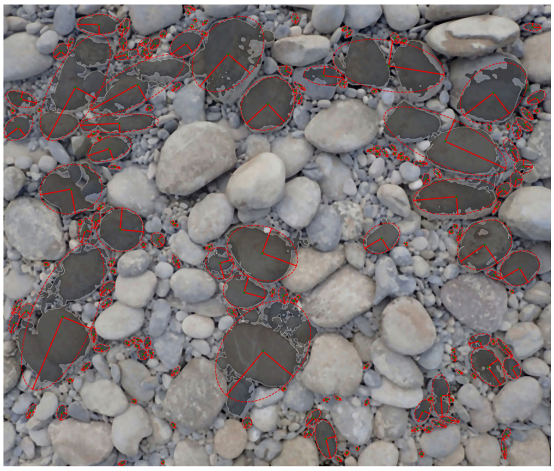

FIGURE 5 Example of image processing by the PebbleCounts software package developed by Purinton and Bookhagen (2019) [Color figure can be viewed at wileyonlinelibrary.com]

$$\mathrm{NMAE}=\frac{\left(\frac{\sum_{i=1}^{n}\left|(x_i-x)\right|}{n}\right)}{x_{mean}} \quad (2)$$

where x_i is equal to the value of the predicted percentile and x is the value of the manually measured percentile. X_{mean} corresponds to the mean value of the percentile manually measured for the digital image dataset.

3 | RESULTS

3.1 | Software accuracy before calibration

All of the software packages tested underestimated all percentiles (Figure 6). The results are quite similar for Basegrain software from D_{10} to $D_{50,}$ with a net underestimation of these percentiles (Table 1). In contrast, from D_{75} to D_{95}, an overestimation occurred using Basegrain (Table 1). Globally, for all software programmes, the NRMSE and NMAE decrease according to the increase in the estimated percentile (Figure 7). However, the values of these parameters differed considerably between programmes. For DGS software, the maximal NRMSE and NMAE values of percentile errors were equal to 56 and 47%, respectively. For Basegrain software, the maximal NRMSE and NMAE values were equal to 97 and 90%, respectively (Figure 7). For the ImageJ procedure, the maximal RMSE and NMAE values were equal to 88 and 79%, respectively. For SediNet, the maximal RMSE and NMAE values were equal to 67 and 58%, respectively. For PebbleCounts, the maximal RMSE and NMAE values were equal to 71 and 59%, respectively.

3.2 | Software accuracy after calibration

Significant linear associations were found between the manually measured and predicted percentiles by DGS and Basegrain software (Table 1). Only significant statistical linear relationships were found from D_{75} between the predicted and manually measured percentiles by the procedure using ImageJ software (Table 1). For SediNet, significant statistical relationships were found for D_{10}, D_{16}, D_{25}, and D_{84}, respectively. Whereas for PebbleCounts, significant associations were found from the D_{75} (Table 1). For the D_{10}, the R-square value was close to 0 for PebbleCounts.

Through the application of linear regressions, a reduction in NRMSE and NMAE occurred for all percentiles, and all procedures between the corrected-predicted percentiles and manually measured percentile due to a high reduction of the previous underestimation (Figures 7 and 8). For DGS software, the maximal NRMSE and NMAE values of percentile errors were equal to 20 and 17%, respectively. For Basegrain software, the maximal RMSE and NMAE values of the percentile errors were equal to 20 and 16%, respectively. For the ImageJ procedure, the maximal RMSE and NMAE values were equal to 40 and 33%, respectively (Figure 7). For SediNet, the maximal RMSE and NMAE values were equal to 33 and 23%, respectively. Finally, for PebbleCounts, the maximal RMSE and NMAE values were equal to 38 and 33% excluding the D_{10}.

4 | DISCUSSION

4.1 | Comparison of software accuracy

Our results showed that all methods underestimated the GSD with greater error is compared to the reference GSD obtained through the manual approach. This underestimation is explained by an over-segmentation of particles due to petrographic variation (Sime & Ferguson, 2003; Strom et al., 2010; Warrick et al., 2009). To reduce the error estimations, a calibration correction must be applied to improve the GSD estimation, such as that proposed by Chardon et al. (2020) (Figures 7 and 8). Our results show that both DGS and Basegrain are reliable software programmes to estimate the GSD based on digital images after linear regression correction (Figure 8). The maximal value of error estimation was less than 18% (NMAE) after the linear correction (Figure 7). The other three software packages are also reliable for percentiles estimation coarser than the D_{50} (Figure 7). The maximumrror estimation was equal to 22% (NMAE for SediNet) after linear correction (Figure 7).

4.2 | Software advantages and limitations

Each software package has advantages and limitations. For DGS software, the GSD was obtained quickly, and no extra preprocessing steps other than a median filter application was necessary.

FIGURE 6 Predicted percentiles of the grain size distribution (GSD) for the three methods according to manually measured percentiles before calibration. The black line and dotted black line correspond to the y = x and y = 1.5x line equations, respectively. Continuous black line, dashed black line, and dotted black line correspond to y = x equation, y = 0.5x equation, and y = 0.25x equation, respectively [Color figure can be viewed at wileyonlinelibrary.com]

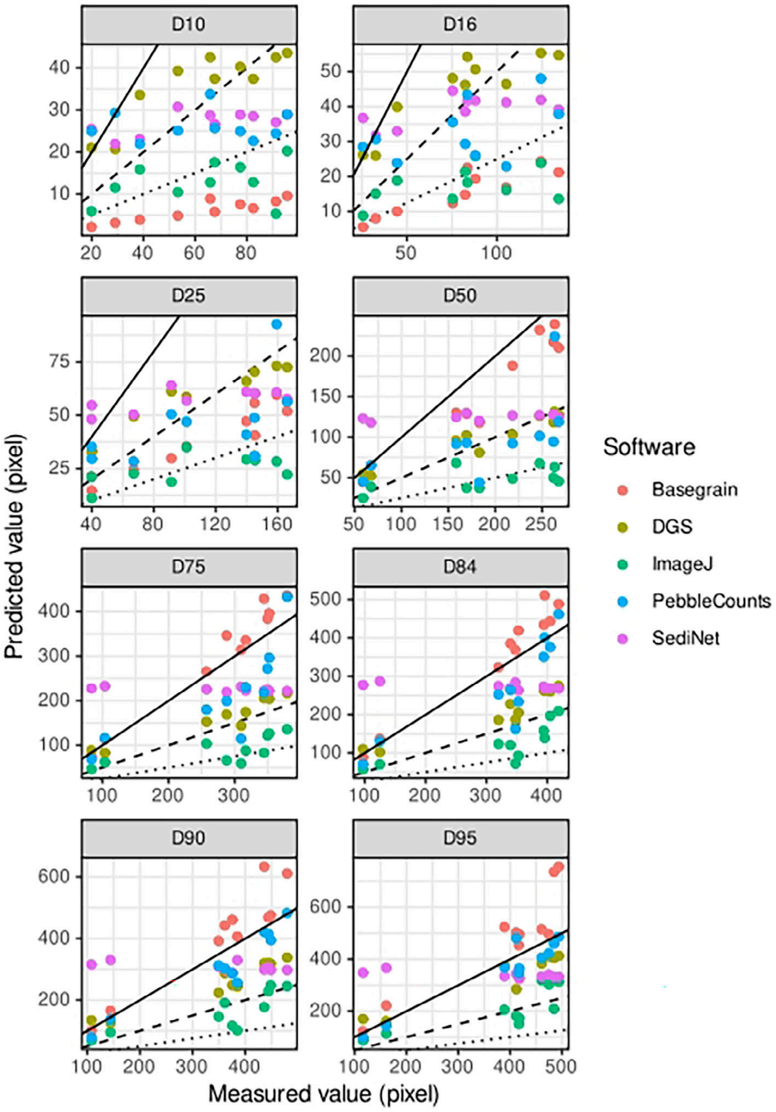

Nevertheless, this software is similar to a "black box" with no means to directly observed the detected particles and perform error localization on digital images, which does not allow the evaluation of which parameters primarily influence the particle detection. This means that there is no possible way to change the software parameters. The same limitation occurs for SediNet due to the deep learning method used. For PebbleCounts software, the advantage is that only one parameter is required from the user before computation, and the results of the grain identification are visible in a new window. On the other hand, Basegrain software allows you to view the detected particles and spatial errors but also allows operator intervention to modify or delete the detected particle outlines. However, in some cases, numerous visual checks may be necessary during the preprocessing steps (n = 5) to obtain satisfactory results. In our cases, to be consistent with the goal of quick and easy data processing, no calibration steps were implemented. For the ImageJ procedure, the main limitation is the application of step 3, which consists of applying an automatic threshold for black and white transformation that is necessary for the application of the watershed algorithm. Because pixel color values differ between each digital image, it is very difficult to find a single threshold for a set of digital images. In addition, several manual preprocessing steps required for this procedure increase the processing time (Figure 4), which may be problematic for large datasets.

TABLE 1 R-square values of linear regressions and *p*-value between grain size percentiles estimated for each software packages according to grain size percentiles estimated manually

	DGS		Basegrain		ImageJ		PebbleCounts		SediNet	
Percentile	R^2	*p*-value	R^2	*p*-value	R^2	*p*-value	R^2	*p*-value	R^2	*p*-value
D_{10}	0.76	0.00096	0.84	0.00018	0.12	0.33	0.04	0.31	0.41	0.047
D_{16}	0.79	0.00065	0.80	0.00052	0.15	0.26	0.22	0.17	0.42	0.043
D_{25}	0.89	4e-05	0.91	2.2e-05	0.37	0.061	0.35	0.075	0.48	0.026
D_{50}	0.92	1e-05	0.94	3.7e-06	0.35	0.07	0.40	0.053	0.40	0.051
D_{75}	0.92	1.4e-05	0.97	2.8e-07	0.51	0.02	0.59	0.0087	0.38	0.057
D_{84}	0.90	2.4e-05	0.96	5.3e-07	0.57	0.011	0.72	0.0017	0.42	0.042
D_{90}	0.92	9.4e-06	0.90	2.6e-05	0.64	0.0054	0.90	2.4e-07	0.36	0.063
D_{95}	0.90	2.9e-05	0.84	0.00021	0.63	0.0065	0.92	1.4e-05	0.40	0.052

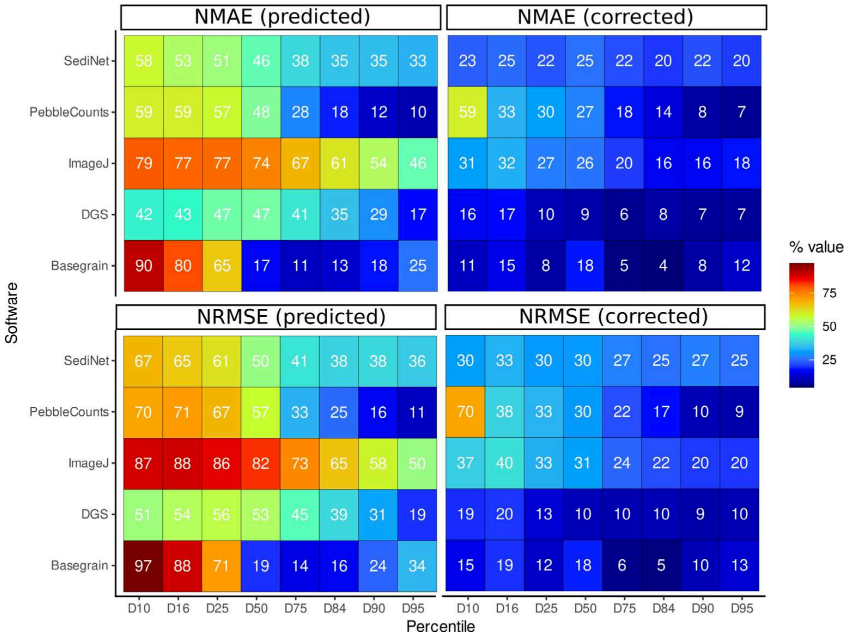

NMAE (predicted)

Software	D10	D16	D25	D50	D75	D84	D90	D95
SediNet	58	53	51	46	38	35	35	33
PebbleCounts	59	59	57	48	28	18	12	10
ImageJ	79	77	77	74	67	61	54	46
DGS	42	43	47	47	41	35	29	17
Basegrain	90	80	65	17	11	13	18	25

NMAE (corrected)

Software	D10	D16	D25	D50	D75	D84	D90	D95
SediNet	23	25	22	25	22	20	22	20
PebbleCounts	59	33	30	27	18	14	8	7
ImageJ	31	32	27	26	20	16	16	18
DGS	16	17	10	9	6	8	7	7
Basegrain	11	15	8	18	5	4	8	12

NRMSE (predicted)

Software	D10	D16	D25	D50	D75	D84	D90	D95
SediNet	67	65	61	50	41	38	38	36
PebbleCounts	70	71	67	57	33	25	16	11
ImageJ	87	88	86	82	73	65	58	50
DGS	51	54	56	53	45	39	31	19
Basegrain	97	88	71	19	14	16	24	34

NRMSE (corrected)

Software	D10	D16	D25	D50	D75	D84	D90	D95
SediNet	30	33	30	30	27	25	27	25
PebbleCounts	70	38	33	30	22	17	10	9
ImageJ	37	40	33	31	24	22	20	20
DGS	19	20	13	10	10	10	9	10
Basegrain	15	19	12	18	6	5	10	13

FIGURE 7 Values of normalized root mean square error (NRMSE) (predicted and corrected) and normalized mean absolute error (NMAE) (predicted and corrected) for each software packages. Predicted and corrected correspond respectively to no calibrated and calibrated results after linear regression application [Color figure can be viewed at wileyonlinelibrary.com]

4.3 | Future research

The main advantage of using terrestrial digital images rather than aerial images or three-dimensional techniques (photogrammetric or LiDAR data) is the low material cost. It is also a less time-consuming postprocessing approach as most of the measurement errors could be avoided during the field data collection (vegetation, biofilm, sun, etc.), and less specific technical knowledge is required compared to three-dimensional approaches. Thus, this method could be easily used by river managers to quickly estimate the bed GSD on both clean above and underwater bars for the planning step of river restoration projects, evaluating natural changes or integrate bed GSD spatial distribution in numerical hydrosedimentary models. However, questions still remain: What is the best sampling procedure to integrate the spatio-temporal variability of the GSD? Because digital images allow the estimation of the local bed grain size quickly, how should the GSD be estimated from this sampling procedure at a larger spatial scale, similar to aerial or three-dimensional approaches? Should the approach be a compromise between the quantity and/or quality of the data available? More studies have to be conducted to determine a robust sampling protocol using digital images. Each of these sampling protocols should be guided by (i) the main objective of the study, (ii) the sampling effort, and (iii) the precision, which must be consistent with the final use of the data.

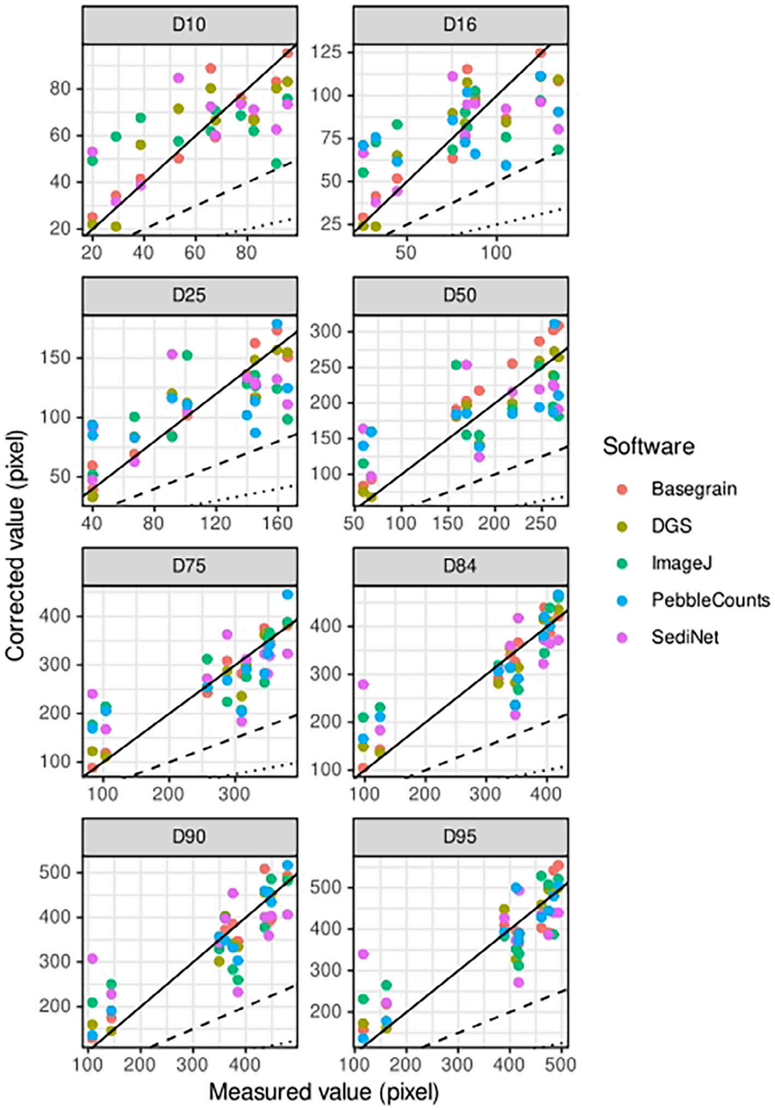

FIGURE 8 Predicted percentiles of grain size distribution (GSD) for the three methods according to manually measured percentiles after calibration. Continuous black line, dashed black line, and dotted black line corresponds to y = x equation, y = 0.5x equation, and y = 0.25x equation, respectively [Color figure can be viewed at wileyonlinelibrary.com]

5 | CONCLUSION

The purpose of this study was to evaluate and compare the accuracy of GSD estimations from ten digital images recorded on the Rhine River using five software programmes. Results showed that all software programs underestimated manually measured GSDs. However, after linear regression correction, the NMAE decreased and did not exceed 18% for the DGS and Basegrain software packages for all percentiles. For the three other software packages, the estimation was reliable for percentiles higher than the D_{50} with an NMAE below 22%. This study shows that it is possible to estimate the bed GSD of clean substrates in a precise manner using DGS and Basegrain software packages for the entire distribution and the three other software packages for percentiles equal and higher than the D_{50}. However, a calibration step must be applied in all cases.

DATA AVAILABILITY STATEMENT

Data available on request from the authors.

ORCID

Valentin Chardon https://orcid.org/0000-0001-7169-2057

REFERENCES

Arnaud, F., Piégay, H., Schmitt, L., Rollet, A. J., Ferrier, V., & Béal, D. (2015). Historical geomorphic analysis (1932–2011) of a by-passed river reach in process-based restoration perspectives: The old Rhine downstream of the Kembs diversion dam (France, Germany). *Geomorphology*, *236*, 163–177. https://doi.org/10.1016/j.geomorph.2015.02.009

Baptista, P., Cunha, T. R., Gama, C., & Bernardes, C. (2012). A new and practical method to obtain grain size measurements in sandy shores based on digital image acquisition and processing. *Sedimentary Geology*, *282*, 294–306. https://doi.org/10.1016/j.sedgeo.2012.10.005

Barnard, P. L., Rubin, D. M., Harney, J., & Mustain, N. (2007). Field test comparison of an autocorrelation technique for determining grain size using a digital 'beachball' camera versus traditional methods. *Sedimentary Geology*, *201*(1–2), 180–195. https://doi.org/10.1016/j.sedgeo.2007.05.016

Brasington, J., Vericat, D., & Rychkov, I. (2012). Modeling river bed morphology, roughness, and surface sedimentology using high resolution terrestrial laser scanning. *Water Resources Research*, *48*(11), W11519. https://doi.org/10.1029/2012WR012223

Bunte, K. & Abt, S. R. (2001). Sampling surface and subsurface particle-size distributions in wadable gravel-and cobble-bed streams for analyses in sediment transport, hydraulics, and streambed monitoring (RMRS-GTR-74; p. RMRS-GTR-74). Technical report. U.S. Department of Agriculture, Forest Service, Rocky Mountain Research Station. https://doi.org/10.2737/RMRS-GTR-74

Buscombe, D. (2019). SediNet: A configurable deep learning model for mixed qualitative and quantitative optical granulometry. *Earth Surface Processes and Landforms*, *45*(3), 638–651. https://onlinelibrary.wiley.com/doi/abs/10.1002/esp.4760

Buscombe, D. (2013). Transferable wavelet method for grain-size distribution from images of sediment surfaces and thin sections, and other natural granular patterns. *Sedimentology*, *60*(7), 1709–1732. https://doi.org/10.1111/sed.12049

Carbonneau, P. E., Lane, S. N., & Bergeron, N. E. (2004). Catchment-scale mapping of surface grain size in gravel bed rivers using airborne digital imagery. *Water Resources Research*, *40*(7), W07202. https://doi.org/10.1029/2003WR002759

Chang, F.-J., & Chung, C.-H. (2012). Estimation of riverbed grain-size distribution using image-processing techniques. *Journal of Hydrology*, *440–441*, 102–112. https://doi.org/10.1016/j.jhydrol.2012.03.032

Chardon, V., Schmitt, L., Arnaud, F., Piégay, H., & Clutier, A. (2021). Efficiency and sustainability of gravel augmentation to restore large regulated rivers: Insights from three experiments on the Rhine River (France/Germany). *Geomorphology*, *380*, 107639. https://doi.org/10.1016/j.geomorph.2021.107639

Chardon, V., Schmitt, L., Piégay, H., & Lague, D. (2020). Use of terrestrial photosieving and airborne topographic LiDAR to assess bed grain size in large rivers: A study on the Rhine River. *Earth Surface Processes and Landforms*, *45*(10), 2314–2330. https://doi.org/10.1002/esp.4882

Detert, M., & Weitbrecht, V. (2012). Automatic object detection to analyze the geometry of gravel grains – A free stand-alone tool. In R. M. Muños (Ed.), *River flow 2012* (pp. 595–600). London: *Taylor & Francis Group*.

Graham, D. J., Reid, I., & Rice, S. P. (2005). Automated sizing of coarse-grained sediments: Image-processing procedures. *Mathematical Geology*, *37*(1), 1–28. https://doi.org/10.1007/s11004-005-8745-x

Graham, D. J., Rollet, A. J., Piégay, H., & Rice, S. P. (2010). Maximizing the accuracy of image-based surface sediment sampling techniques. *Water Resources Research*, *46*(2), 1–15. https://doi.org/10.1029/2008WR006940

Heritage, G. L., & Milan, D. J. (2009). Terrestrial laser scanning of grain roughness in a gravel-bed river. *Geomorphology*, *113*(1–2), 4–11. https://doi.org/10.1016/j.geomorph.2009.03.021

Hodge, R., Brasington, J., & Richards, K. (2009). Analysing laser-scanned digital terrain models of gravel bed surfaces: Linking morphology to sediment transport processes and hydraulics. *Sedimentology*, *56*(7), 2024–2043. https://doi.org/10.1111/j.1365-3091.2009.01068.x

Lang, N., Irniger, A., Rozniak, A., Hunziker, R., Wegner, J. D., & Schindler, K. (2021). GRAINet: Mapping grain size distributions in river beds from UAV images with convolutional neural networks. *Hydrology and Earth System Sciences*, *25*, 2567–2597. https://doi.org/10.5194/hess-25-2567-2021

Lejot, J., Piégay, H., Hunter, P. D., Moulin, B., & Gagnage, M. (2011). Utilisation de la télédétection pour la caractérisation des corridors fluviaux: Exemples d'applications et enjeux actuels. *Géomorphologie: Relief, Processus, Environment*, *17*(2), 157–172. https://doi.org/10.4000/geomorphologie.9362

Purinton, B., & Bookhagen, B. (2019). Introducing PebbleCounts: A grain-sizing tool for photo surveys of dynamic gravel-bed rivers. *Earth Surface Dynamics*, *7*(3), 859–877. https://doi.org/10.5194/esurf-7-859-2019

Purinton, B., & Bookhagen, B. (2021). Tracking downstream variability in large grain-size distributions in the south-Central Andes. *Journal of Geophysical Research - Earth Surface*, *126*, e2021JF006260. https://doi.org/10.1029/2021JF006260

Rubin, D. M. (2004). A simple autocorrelation algorithm for determining grain size from digital images of sediment. *Journal of Sedimentary Research*, *74*(1), 160–165. https://doi.org/10.1306/052203740160

Sime, L. C., & Ferguson, R. I. (2003). Information on grain sizes in gravel-bed Rivers by automated image analysis. *Journal of Sedimentary Research*, *73*(4), 630–636. https://doi.org/10.1306/112102730630

Strom, K. B., Kuhns, R. D., & Lucas, H. J. (2010). Comparison of automated image-based grain sizing to standard pebble-count methods. *Journal of Hydraulic Engineering*, *136*(8), 461–473. https://doi.org/10.1061/(ASCE)HY.1943-7900.0000198

Sulaiman, M. S., Sinnakaudan, S. K., Ng, S. F., & Strom, K. (2014). Application of automated grain sizing technique (AGS) for bed load samples at Rasil River: A case study for supply limited channel. *Catena*, *121*, 330–343. https://doi.org/10.1016/j.catena.2014.05.013

Turley, M. D., Bilotta, G. S., Arbociute, G., Chadd, R. P., Extence, C. A., & Brazier, R. E. (2017). Quantifying submerged deposited fine sediments in Rivers and streams using digital image analysis: Quantifying fine sediment in rivers and streams using DIA. *River Research and Applications*, *33*(10), 1585–1595. https://doi.org/10.1002/rra.3073

Vázquez-Tarrío, D., Borgniet, L., Liébault, F., & Recking, A. (2017). Using UAS optical imagery and SfM photogrammetry to characterize the surface grain size of gravel bars in a braided river (Vénéon River, French Alps). *Geomorphology*, *285*, 94–105. https://doi.org/10.1016/j.geomorph.2017.01.039

Warrick, J. A., Rubin, D. M., Ruggiero, P., Harney, J. N., Draut, A. E., & Buscombe, D. (2009). Cobble cam: Grain-size measurements of sand to boulder from digital photographs and autocorrelation analyses. *Earth Surface Processes and Landforms*, *34*(13), 1811–1821. https://doi.org/10.1002/esp.1877

Woodget, A. S., Fyffe, C., & Carbonneau, P. E. (2018). From manned to unmanned aircraft: Adapting airborne particle size mapping methodologies to the characteristics of sUAS and SfM. *Earth Surface Processes and Landforms*, *43*(4), 857–870. https://doi.org/10.1002/esp.4285

How to cite this article: Chardon, V., Piasny, G., & Schmitt, L. (2021). Comparison of software accuracy to estimate the bed grain size distribution from digital images: A test performed along the Rhine River. *River Research and Applications*, 1–10. https://doi.org/10.1002/rra.3910

Annexe 2 : Conference paper 3DGeoInfo, 2020, Londre

4D GIS FOR MONITORING RIVER BANK EROSION AT MEANDER BEND SCALE: CASE OF MOSELLE RIVER

M. Koehl [1,*], G. Piasny [2], V. Thomine [1], P-A. Garambois [3], P. Finaud-Guyot [4], S. Guillemin [1], L. Schmitt [2]

[1] ICube Laboratory UMR 7357, INSA Strasbourg, France
{mathieu.koehl, valentin.thomine, samuel.guillemin}@insa-strasbourg.fr
[2] University of Strasbourg – LIVE (Laboratoire Image, Ville, Environnement) UMR 7362 – CNRS – Unistra - ENGEES, France
{guillaume.piasny, laurent.schmitt}@unistra.fr
[3] IRSTEA, Aix-en-Provence, France. pierre-andre.garambois@irstea.fr
[4] HydroSciences Montpellier, Polytech Montpellier, Montpellier, France. pascal.finaud-guyot@umontpellier.fr

KEY WORDS: Morphodynamic monitoring, diachronic analysis, geodetic surveying, photogrammetry, UAV, 4D GIS.

ABSTRACT:

The "Wild Moselle" regional nature reserve extends over 13 km at the western foothills of the Vosges Mountains. The hydrological regime of the river is characterized by high flow in winter and spring and low flow in summer. Its average slope is 0.12 % and its average bankfull width is 60 m. The coarse sediment load comes mainly from bank erosion. Although this sector is relatively less affected by past or present human activities, the propagation of morphodynamic adjustments initiated by actions carried out both upstream and downstream of this sector impacts the current functioning of the river. These erosion waves converge today towards the central part of the reserve, which led to the collapse of the central pier of the Bainville-aux-Miroirs bridge during a 2-year flood in 2011, and could induce potential risks of defluviation which may destabilize infrastructures. In this context, the study carried out aims to characterize and anticipate the morphodynamic evolutions of the Moselle to be able to propose scenarios of management and restoration of the lateral mobility of the river. For this purpose, a 2D hydro-sedimentary model is being built over the entire reserve, combined with a detailed morpho-sedimentary monitoring. In order to improve the understanding of the lateral migration of the Moselle River, a photogrammetric monitoring was carried out along the concave bank of the most active meander of the studied sector. To follow this morphological evolution more closely, it was decided to establish a 4D GIS. The objective of this monitoring is to compare the rate of bank retreat with hydrodynamic parameters in order to estimate the geotechnical properties of the bank. Comparison of the observed and modelled bank retreat must thus allow these different parameters to be calibrated in the hydro-sedimentary model. As part of this work, this paper aims to highlight the use of 4D GIS to monitor bank retreat at the scale of a meander bend and is divided into three different parts: (i) a state of art to situate the study into the current knowledge and technologies, (ii) a presentation of the study area and the measurements carried out and (iii) a description of the different 3D or 4D data produced and the consequent spatial analyses.

1. INTRODUCTION

Data management and representation has made great progress last decades notably in moving from 2D to 3D and integrating time. This type of representation has developed considerably in the world of geo-information, mainly because of the evolution of processing and visualization algorithms but also thanks to the multiplication of survey techniques. As a result, it becomes easier and easier to model a portion or even a territory in 3D. Two technologies play a major role in these developments: laser-scanning and photogrammetry.

Pfeifer (2007) defines terrestrial laser scanning as a data acquisition technique using laser light to directly measure, in a regular frame, the coordinates of 3D points on surfaces at an Earth position. A 3D laser scanner is a terrestrial device (TLS) that uses this process to determine X, Y and Z points coordinates in order to acquire a point cloud of the area. Laser-scanning of an area using a laser scanner, whether terrestrial or aerial, provides 3D point clouds of the entire area with a configurable point density depending on the equipment and the recording conditions.

The other technique implemented to obtain 3D models, is based on photogrammetry from images that can also be aerial, from UAV, or terrestrial. Aerial photography has long been used for map applications. Many applications result from it. One of its main advantages is the minimization of field work. Photogrammetry has now become a widely used tool even for local scale mapping applications. This technique allows the user to obtain 3D data from an area of interest. It is also used to produce orthophotos. Photogrammetry has also experienced a new boom with the development of the use of UAVs (unmanned aerial vehicles) for mapping, particularly on a larger scale. Photogrammetry by UAV is particularly interesting in sites requiring rapid intervention, including the case of inspection and monitoring (Murtiyoso *et al.*, 2017) (Jaud *et al.*, 2014). It is therefore possible, from images with well-defined overlapping areas, to determine the relief and contours of an object or territory in the form of point clouds obtained from dense matching techniques.

Digital Terrain Models (DTM) and Digital Surface Models (DSM) are used as digital representations of the natural terrain. Such acquisitions can be made several times under the same conditions and with sufficient precision to be compared. The multi-temporal data also allow to display local changes in topography. Indeed, by comparison with a reference model, topographic and/or height changes can be quantified and represented. This was used to evaluate the accuracy of digital surface model (DSM) of river-channel morphology derived from

---

[*] Corresponding author

the imagery acquired with a low-cost digital camera on board an unmanned multi-copter (Watanabe and Kawahara, 2016). Cross-sections make it possible to highlight in a very explicit way these topographical evolutions. The DTM/DSM generated directly from the point cloud is an ideal support to analyze morphological evolutions in some cases and estimate sediment budgets (Eschbach *et al.*, under review; Rivas Casado *et al.*, 2017). By combining the DTM and aerial photographs, it is also possible to produce georeferenced orthophotos that can be integrated into the 4D GIS and serve as additional support for analysis, especially on smaller scales (Dawod *et al.*, 2014). The advantages that UAVs can provide for the survey of small areas, as meander bends, are however very interesting. UAVs are alternatives to quickly recording data (images) to compute a 3D model of a small area. In fact, UAVs show the advantage of being inexpensive, whether in financial or human terms, and their size and weight make them easy to deploy and implement.

Considering these advantages, a photogrammetric monitoring using UAV was carried out along the concave bank of the most active meander of the Moselle River in order to better understand and model the lateral migration of the river. In order to survey this fluvial morphodynamic process more closely, a 4D GIS has been established along the meander bend. The objective of this monitoring is to assess the bank erosion rates according to hydrodynamic parameters (discharges, water levels, flow velocities, shear stresses, etc.) and geotechnical properties of the eroded bank (rest angle, bank sediment stratigraphy, vegetation, etc.). Subsequently, comparison of observed vs modelled bank retreat should allow calibrating the geotechnical parameters into a 2D hydro-sedimentary model. This paper is divided into three parts which: (i) describe steps from photogrammetric monitoring to point of clouds construction, (ii) present a method to extract bank profiles and (iii) show how to integrate photogrammetric data into a GIS also including other topo-bathymetric data.

1.1 Study site

The Moselle River drains a catchment area of 1976 km² from its source at Bussang in the Vosges Mountains to Tonnoy at the Lorraine plateau. The "Wild Moselle" regional nature reserve extends over 13 km at the western foothills of this massif. The river's hydrological regime is characterized by high flow in winter and spring and rather low flow in summer. Its average slope is 0.12 % and its average bankfull width is 60 m. The load originates quasi-exclusively from bank erosion. Although this sector is relatively less affected by local past or present human activities (bank stabilization, river bed gravel extraction, floodplain gravel mining, etc.), the propagation of morphodynamic adjustments initiated by actions carried out both upstream and downstream this sector impact the current functioning of the river: regressive and progressive erosions that can foster strong lateral erosion, meander cutoff, channel contraction, etc. So the waves of both regressive and progressive erosion converge today towards the central part of the reserve, which led to the collapse of the central pier of the Bainville-aux-Miroirs' bridge during a 2-year flood in 2011. These dynamics could also induce a potential risk of avulsion which may destabilize other infrastructures along the studied river reach. In this context, the underway study aims to characterize and anticipate morphological evolutions of the Moselle River to be able to propose scenarios of management and restoration of the lateral mobility of the river. To reach this purpose, a 2D hydro-sedimentary model is being built over the entire natural reserve, which is combined with a detailed morpho-sedimentary monitoring. This consists in topo-bathymetric LiDAR data, hydrological surveys (limnimeters, ADCP - Acoustic Doppler Current Profilers), and morpho-sedimentary surveys (sediment tracking - 2500 pit-tags, grain size measurements on both surface and subsurface).

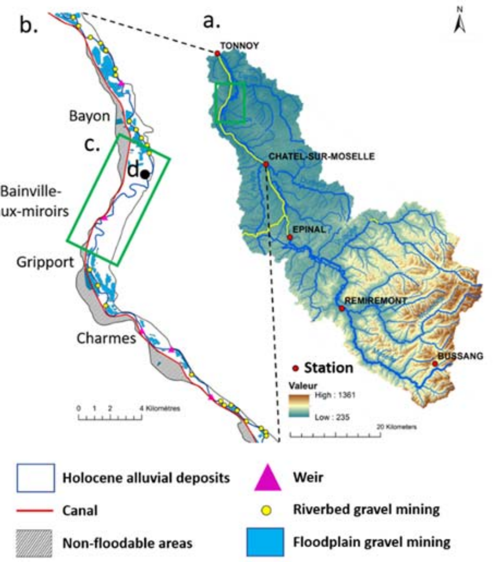

a. Catchment of the Moselle River upstream Tonnoy
b. Valley bottom of the Moselle River from Châtel-sur-Moselle to Tonnoy
c. "Wild Moselle" Regional naturel reserve and
d. Studied meander bend

Figure 1: Study site location.

2. BANK SURVEY

2.1 From UAV photogrammetric data acquisition to point clouds

To highlight the evolutions of the banks of the Moselle, it is necessary to be able to compare topographical data at different dates. In order to obtain results showing significant changes, it was decided to acquire data after each morphogenic flood, when the water level was low enough to characterize the complete bank profile, from the bank top to the bank toe. As shown in Figure 4, several floods occurred during 2018-19. For accessibility, timing and organization reasons, four dates were chosen for the recording of in situ data. As previously defined, it was decided to test the acquisition of photogrammetric data using a DJI Phantom 3 UAV. The covered area consisted in the concave bank for a length of about 700 m.

Following the classic considerations (Remondino *et al.*, 2011), a typical image-based surveying with UAV systems requires a mission planning, GCPs measurement for geo-referencing, image recording, camera calibration, and image orientation, image processing for 3D modeling and information extraction.

The first date was an experimental operation to define the first state of the meander and to calibrate the field operations.

More than 1,000 images (Table 1) were recorded during each mission, whether in nadiral or oblique shots (Figure 2). On some of them, coded circular targets are visible. These were used to materialize GCP (Figure 3): the GCP coordinates were then measured with a geodetic GNSS receiver. The measured and automatically extracted points using *Agisoft Metashape* software are in the centre of the targets and their coordinates have been determined in the French RGF93-CC49 system.

The flight plan was executed manually. As authorized in France for visual drone flights, it consisted of several 300 m long areas. Each areas was recorded in multiple passages with nadiral shots and several passages with oblique views at 30° and 60°, perpendicular to the bank or inclined by 30°. The overlapping of the successive photos is about 60%. The flight time of about twenty minutes made it possible to make these shots without problems. The shooting trigger was set to automatic shooting at 2 s. The height of the flight was between 20 and 40 meters which allowed to obtain a pixel size of 1 cm.

Limnimeters have also been located upstream and downstream of the meander in order to records water heights during the studied periods.

Figure 2: Nadiral (top) and oblique (down) images of the studied bank.

Generation of point clouds.

Large quantities of images were therefore acquired by drone for each measurement campaign. Among this mass of data for each campaign, a sorting was carried out, to preserve only images with a good quality.

Two selection methods were applied: (i) a qualitative selection apparent to a visual analysis of the images to eliminate the unusable images (duplicates, under or overexposed images). In this first method, the operator's analysis is heavily used to make a manual selection; (ii) a quantitative selection using the *Metashape* software to estimate the quality of an image, by means of a coefficient. A blurry image, therefore unusable, will have a coefficient of 0.50. To maintain only good quality images, the acceptability threshold for this coefficient has been set at 0.75. Figure 2 shows the number of images acquired and the number finally used in processing, corresponding to a ratio from about 50 to 80%. In the end, the selection was a little harsher for the first and third acquisition campaign because of the weather conditions (very hot sunshine). Nevertheless, the number of photos used was sufficient to meet the overlay criteria.

Date	# images	# used images	ratio	# Chunks
05/03/2018	1443	835	0.58	5
26/03/2018	1302	1015	0.78	2
12/02/2019	1145	620	0.54	6
03/04/2019	1179	865	0.73	7

Table 1: Images used

The UAV used to take pictures of the meander was a DJI Phantom 3 pro drone. This device has the advantage of being light and easy to handle. It has its own positioning system (GNSS) which gives the position of the drone at each shot with a quasi-metric accuracy. However, this relative inaccuracy has been a disadvantage in the calculation of precise camera locations since the software relies on these initial values. Consequently, the coordinates available in the metadata (Exif) of the images were not used.

Figure 3: Bank morphology and coded targets as GCPs

Identification and visualization of GCPs in a GIS.

As the length of the studied meander is quite substantial, the number of available coded targets for georeferencing was too low. These were therefore reused several times using the same cut-out as allowed by the maximum flight distances. The targets were renamed and matched thanks to their location in a GIS layer (Figure 4).

Figure 4: GCPs in GIS layer

Creation of the point clouds: For organizational reasons, each model was divided into Chunks, treated separately, and then merged into a single point cloud per campaign. The different processing steps followed a classic photogrammetric process: (i) relative orientation of the images – Align Photos – to move from image coordinates to model coordinates from which a sparse point cloud can be generated. This was done through the automatic extraction of key points in each image which are then paired with the key points of neighboring images to generate tie points. Sfm (Structure from motion) algorithms then allowed the calculation of the relative orientation of the images from which was deduced a 3D point cloud; (ii) georeferencing of the point cloud thanks to the GCPs imported and detected automatically (markers) thanks to the coded targets - Optimize Camera -. The accuracy of the different obtained 3D models was about 2-3 cm; (iii) another adjustment was undertaken, but this time to check the criterion of accuracy. Some GCPs were transformed into Check Points. Errors on Check Points were always greater than errors on GCPs which denotes an existence of a systematism that could be explained by a pixel size larger than the precision of the coordinates. However, we get an accurate model. The next step is the generation of the dense point cloud - Build Dense Cloud -. At this level, the software increases the amount of points by densifying the cloud from the images. Densification quality parameters can be set at this stage. The number of points in high quality is, for example, four times higher than that obtained by placing the parameter at Medium. For example, for a band 700 m long over a depth of 30 m, 4.4 million and 1.1 million of points, respectively. Last step was to clean out the unnecessary noises and points and reduce the model to a 10 m strip around the bank. After this stage, 4 georeferenced 3D point clouds, denoised and cleaned were available for analysis and interpretation (Figure 5).

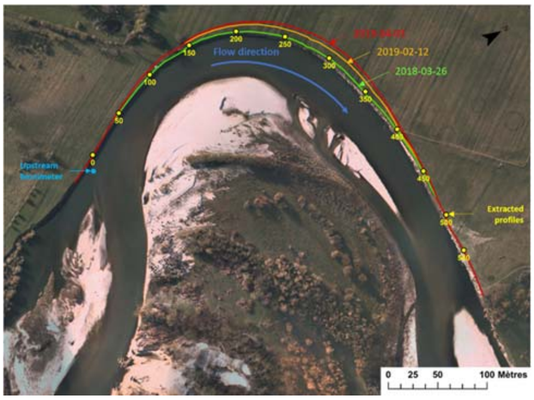

Figure 5: Planimetric evolution of the meander bend during the studied period

2.2 Profile extraction

From these point clouds, it was possible to analyze the erosion of the banks over time, and in particular the impact of each flood. The best way to show the planimetric evolution was to directly compare the four point clouds. For this we used the *CloudCompare* software package, which is a tool allowing to compare of point clouds. This analysis is intended to identify areas of high and low bank retreat. The interoperability between *Metashape* and *CloudCompare* was achieved through the LAS or OBJ formats. LAS is a file format designed for the interchange and archiving of LiDAR point cloud data. It is an open, binary format specified by the American Society for Photogrammetry and Remote Sensing (ASPRS). The format is widely used and regarded as an industry standard for LiDAR data. From our field observations, we expected significant deviations (in the order of several meters). Despite *CloudCompare* is an adequate tool to distinguish changes between two nearby point clouds (for example, for auscultation), but was not efficient in our case. We therefore used the overlay of georeferenced point clouds to quantify the bank erosion.

It was then necessary to analyze the bank evolutions with another medium to have more information about it. The realization of cross-sections is an interesting option, but only with a 2D view (in this case x and z). *Metashape* does not offer tools to directly calculate profiles. For this reason the data were exported and superimposed in *3DReshaper* software package. The realization of cross-sections required the definition of an axis according to which these were to be calculated. For such needs, all point clouds have to rasterized in *CloudCompare* with a grid size of 1 m, when local slopes were calculated using *ArcGIS* package. Based on slope discontinuity, a line was draw along the river banktop for each campaign, from the limnimeter to the downstream opposite side. Considering that profiles were built perpendicularly to the banktop line, this line was smoothed using Bezier curves tools, in order to estimate as far as possible vertical profiles. The reference line chosen to build profiles was the banktop line of the first acquisition. Vertical profiles were automatically extracted each 10 m using *3DReshaper* software with a section thickness of 0.01 m and a maximal edge distance of 0.5 m. Profiles were extracted from 0 to 540 m which corresponds to the overlapping area between all surveys. The profiles length of 15 m is constant and corresponds to the observed maximal bank retreat.

Extracted profiles were manually cleaned in Autodesk in order to remove points corresponding to vegetation and smooth the bank profiles. Each cleaned 2D lines was saved as DXF *AutoCAD* file and a *Matlab* program was developed in order to automatically open these files and superimpose them (figure 6).

The stratigraphical limit between the fine and coarse sediment layers was visually defined using point cloud textured 3D model of the first survey, because the image brightness allowed to identify both layers.

The elevation of this limit was supposed to be constant during the surveying period.

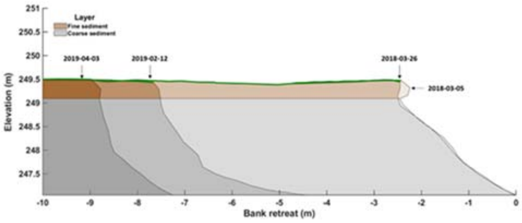

Figure 6: Bank retreat observed at 220 m from 2020-03-26 to 2019-04-03

Submerged data was however not exploitable in the sense that it was highly noisy, due to the reflection of water and the change of medium. Therefore, to be consistent, each profile was cut off at the elevation corresponding to the highest water level being observed during all of the surveys. In fact, water levels of the first and last surveys were relatively low and similar, but the water level of the third survey was 60 to 70 cm higher. Thus, the water level measured during this campaign was used as lowest reference. This shows the importance to collect data during low flow in order to dispose of the most complete bank profile. But, as indicated in figure 7, available survey windows were restricted over the year and especially during the spring and the winter.

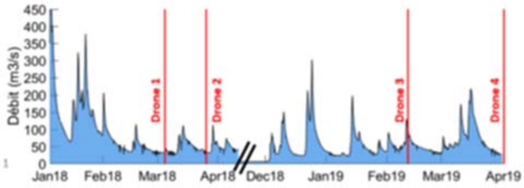

Figure 7: Hygrogram recorded during the studied year

3. DIACHRONIC PROFILE ANALYZES

Areas under each bank profile (figure 6) were calculated in *Matlab* and the eroded surfaces were deduced by subtracting values obtained between each survey. As the bank height varied along the meander bend, each bank profile was normalized, in order to be able to compare the surface eroded between profiles extracted at different locations. Therefore, for each profile, the banktop elevation was considered as 1 m, while the bank toe elevation was considered as 0 m. Thus, if between two surveys, the bank retreated of 1 m and the shape of the both bank profiles was constant, the calculated eroded surface equals 1 m². For each profile, eroded areas were cumulated and represented in figure 8. There are no values at 400 m because of the presence of a tree, which felled into the channel during the study. Finally, in order to compare the observed eroded areas to the observed retreats of the banktop, a *Matlab* program was developed to automatically identify banktop positions along the profiles. Banktop retreats of the first studied flood were not represented because the banktop positions were nearly identical.

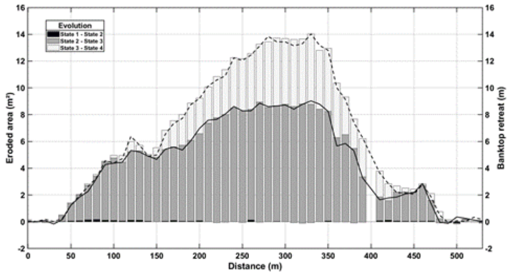

Figure 8: Cumulative normalized eroded areas (diagrams) and corresponding banktop retreats (curves)

Results show that concave bank of the meander bend was barely eroded between the first and the second surveys corresponding to an unique flood that occurred in March 2018. This means that bank erosion threshold lies close or above to a discharge of approximately 120 m^3/s. Comparison between second and third surveys shows that bank erosion of the meander bend started at 30 m and ended at 500 m (fig. 9). Maximal bank retreats were observed between 240 m and 350 m with an average value of -8 m. On the whole, the plan view of the observed bank retreat is oval shaped, with discontinuities located around 150 m and 400 m. Between 120 m and 150 m, the thickness of the fine sediment layer reached 1 m to 1.5 m, while this value was about 0.4 m to 0.5 m along the whole meander. This stratigraphic variation of the bank profile is due to the presence of a paleochannel that was filled by fine sediments over the time. Another paleochannel was also visible at 270 m, 350 m and 410 m, but with a reduced width (5-10 m) and depth (0.6-0.8 m). However, the erodibility of the fine sediment layer is lower than this of the gravel layer, due to cohesion forces. Thus, the presence of former channels into the concave bank controls the bank retreat rate, and more generally the current morphodynamics of the meander (Eschbach *et al.*, under review).

Furthermore, bank retreat discontinuities observed at 150 m and 400 m are also due to the presence of a road that was eroded during 2011 and which currently continues to be eroded (figure 5). Along this road some trees are now located close to the banktop and their roots now enhance the bank stability. However, at 400 m, it is no longer the case as shown by the comparison between the third and the fourth surveys. During the two last survey periods, observed bank erosions were concentrated in the center part of the meander bend, but were slightly higher in the downstream part of the meander bend. Maximal bank retreat was in average 14 m which results in a total bank erosion of 14 m during the last survey period. Globally, banks were stable at the beginning and the end of the meander bend due to low hydraulic conditions and also because they are stabilized by vegetation, blocks and/or fine sediments.

4. INTEGRATION OF PHOTOGRAMETRIC DATA INTO GIS AND COUPLING WITH BATHYMETRIC DATA

The point cloud extracted from the last photogrammetric campaign was combined with a bathymetric survey in order to study the development of the meander bend. Bathymetric data were collected using an acoustic Doppler current profiler (ADCP) coupled with an accurate differential GPS (DGPS). Recorded water depths were associated to DGPS coordinates during the post-processing via timecode according to a time step of 1 second. Field measurements were carried out after the photogrammetric campaign at higher water levels to have an overlay between both datasets and facilitate point clouds merging. The boat trajectory followed a zigzag path from one side to the other side of the river to optimized the river bed mapping and simplify interpolation between each transects. Some longitudinal profiles were also carried over the thalweg and along both river banks to complete this dataset and characterize the maximum lateral extension of the river bend. However, longitudinal extension of the bathymetric survey was reduced to the central part of the meander compared to photogrammetric surveys due to riffles located at each bend inflection which prevents taking measurements from a boat. Moreover, as the water levels were low during the survey, acoustic beams were concentrated in a small area and lateral beams did not improve the river bed mapping. Therefore, only the vertical beam was used to map the meander bend bottom. These bathymetry points were interpolated using a Triangular irregular networks (TIN) available in *ArcGIS* software. Edges of the TIN were manually adjusted in order to connect nodes between transects according to flow paths. Some bathymetry outlier points were delete as well during the TIN construction. Meanwhile, image-based point clouds was rasterized in *CloudCompare*, with a grid size of 1 m, to be consistent with the LiDAR resolution. This raster was converted to points and points were added to the previous TIN. During these steps, data resolution was altered by averaging elevation of points contained in cells, but this process is considered as negligible at the scale of our study. Results may however be affected by this approach in case of over-hanging riverbanks, in this instance cantilevered bank profile are replaced by a vertical wall throughout rasterization. As shown in this study, the cantilever is not the main bank failure mechanisms along the meander bend, which justifies the method we used. Likewise, this data are integrated in a 2D mesh and modelling results will be compared to a topo-bathymetric LiDAR. So, the bank retreat of the basal layer will not be investigated here.

Furthermore, before merging photogrammetric and bathymetric point clouds, underwater points were deleted from the image-based dataset. Indeed, elevation accuracy of underwater points was difficult to estimate without underwater ground control points at the time of the survey. However, the influence of refraction on underwater three-dimensional reconstruction may be estimated, but this may also be affected by the water turbidity. Considering that turbidity varied from one campaign to the other, integration of underwater points did not seem relevant as a quick and easy way to study bank retreat. In fact, most surveys were carried out with a water level below the bank toe. So, all the bank profiles were characterized satisfactorily. At the end of the data processing, the TIN model including concave bank and river bed was converted to a raster with a grid size of 1 m.

Comparison between bathymetric surveys and LiDAR topo-bathymetric acquisition shows an average offset of 9 cm of the river bed elevation all over the reserve. Although absolute elevation of photogrammetric and bathymetric data is supposed to be more reliable than LiDAR data, it was more convenient to shift the elevation of the raster over the meander bend than over the whole river reach. Indeed, as part of this study, monitoring of morphological evolution of the river bend allows to use relative elevations.

Finally, both meander and LiDAR rasters were superimposed and mosaiced together in order to constitute the pre-flood topography. This approach was possible because the LiDAR acquisition followed the studied flood, without that other morphogenic events occurred. In fact, we could also use the LiDAR from the past year to build the pre-flood state, but occurrence of several floods before studied period made us consider that post-flood LiDAR was more representative of the initial topography of the river. However, post-flood LiDAR acquisition took place at the end of the summer, mass failures could also have occurred due to river dewatering, which may have modified bank profiles without floods. Thus, eroded areas could be overestimated by this comparison, but at the scale of the observed bank retreat this potential amount of sediment is considered to be negligible. Comparison of pre and post-flood states is presented in figure 9, the TIN model based on bathymetric and photogrammetry cloud of points overlay LiDAR Digital Elevation Model (DEM). Four cross-sections were extracted from both DEM and superposed in order to show the morphological evolution of the river bend:

- first cross-section shows that pre-flood profile is well fitted to post-flood profile at the upstream part of the meander. This shows that no lateral erosion occurred during the studied period on this area;
- this was also the case at the end of the river bend, downstream the last cross-section. This confirms that TIN elevation is well adjusted to the LiDAR DEM and validates the accuracy of data acquisition and of the TIN construction process;
- intermediate cross-sections also show a good fit between field measurements and LiDAR acquisition when comparing floodplain elevations. The fact that not morphological evolutions are observed between pre and post-flood states at the TIN extremities ensures that field surveys extends enough upstream and downstream of the studied area.

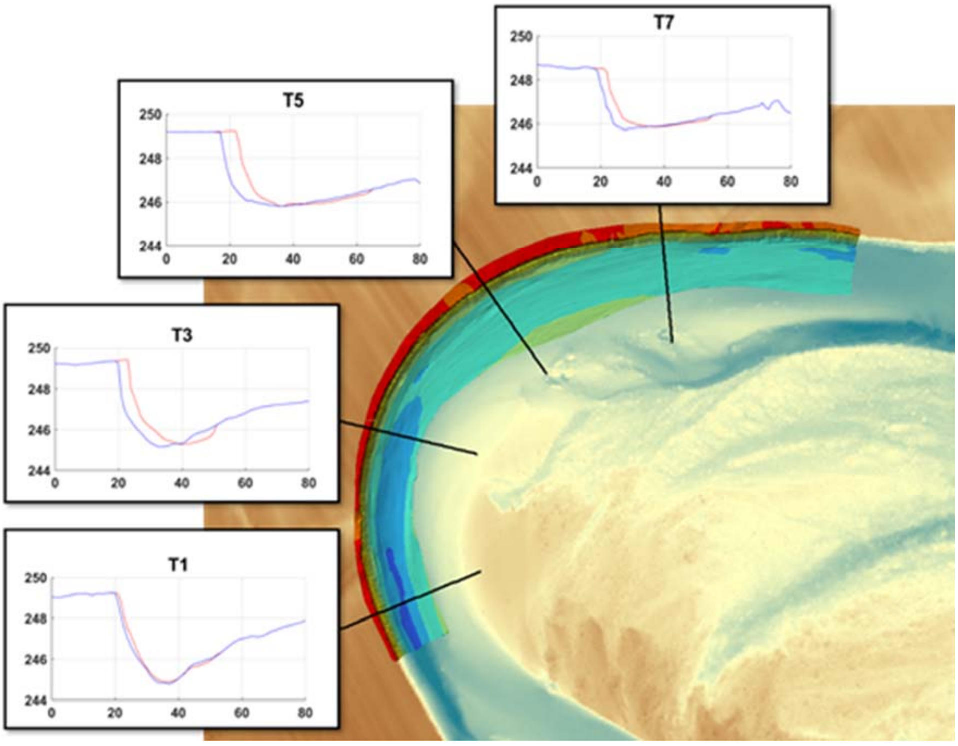

Figure 9: Extracted cross-sections of pre-flood TIN model and post-flood LiDAR DEM of the meander bend.

As presented in figure 9, maximal bank retreat was observed in the bend apex where approximately 4 m of bank material was eroded. Bathymetric survey contributes to study the morphological evolution of the river bed throughout meander lateral migration. Regardless to the cross-section position, results show that river depths remain relatively unchanged with the development of the meander bend. The deepest and shallowest sectors were respectively located at the upstream and downstream extremities of the studied sector, which is in accordance with a pool-riffle fluvial forms. In fact, riffle areas are generally located at bend inflections and spatial distribution of this geomorphological units remains relatively constant over time. Although, meander shifting dynamics does not appear to modify cross-sections shape, sediment deposition rates at the convex bank seems to be longitudinally distributed. Indeed, the amount of sediment deposited at the middle and the tail of this bank (cross-sections T5 and T7) is significantly lower than at his head (cross-section T3). These dynamics are associated with the progradation of the point bar head to the downstream direction as the meander bend develops. As highlighted by a step of a few centimeters at the junction between pre and post-flood states (cross-section T3), the progradation of bar head leads to overestimate the bar head elevation at the pre-flood state. Indeed, without photogrammetric or bathymetric data, the initial topography of the emerged convex bank was characterized by data acquired during LiDAR surveys. This local topographic extrapolation could change flow patterns modelling which could influence sediment transport results. Therefore, we suggest to conduct at the same time photogrammetric monitoring over the concave and the convex banks in order to survey the morphological evolution of the entire meander bend. They are other elements that could impact results of hydro-morphological modelling such as log-jams or riparian vegetation (Eschbach, under review). Fortunately, prior to the beginning of this study, a ten-year flood removed all log-jams of the meander bend, so that hydraulic effects of log-jams became negligible.

5. CONCLUSION

This project located on a particularly active meander of the Moselle River is part of a larger project that extends over the "Wild Moselle" nature reserve. The accurate 3D information acquired over several periods allows to follow the evolution of the banks in a particularly accurate way. The implementation of the drone, coded targets and GPS allows the acquisition of data for the monitoring of the banks in only a few hours.

Data processing needs the same time laps, and the process put in place as well as *Matlab* workflow now makes possible to generate profiles and calculate volumes of bank erosion automatically. It is thus that such a project makes it possible to meet specialists from different fields, including topography and cartography with those of fluvial geomorphology.

6. PERSPECTIVES

A great amount of data has been acquired in recent years to study the Moselle River.

3D treatments play a fundamental role in modelling the knowledge of hydro-morphological phenomena.

The temporal dimension is also of crucial importance, especially in a context of high river morphodynamics. All data will be useful to build, calibrate and validate a 2D hydraulic and morpho-sedimentary model, to propose scenarios of management and restoration of the lateral mobility of the Moselle River.

Figure 10: Stitched panoramic image of the studied meander (2019-03)

REFERENCES

Berni, J. A. J., Zarco-Tejada, P. J., Su_arez, L., and Fereres, E., 2009. Thermal and narrowband multispectral remote sensing for vegetation monitoring from an Unmanned Aerial Vehicle. *In: IEEE Transactions on Geoscience and Remote Sensing, 47(3)*, pp. 722-738.

Casella, E., Rovere, A., Pedroncini, A., Strark, C. P., Casella, M., Ferrari, M., and Firpo, M., 2016. Drones as tools for monitoring beach topography changes in the Ligurian Sea (NW Mediterranean). *In: Geo-Marine Letters, 36*: pp. 151-163.

Dawod, G., Mirza, M., Al-Ghamdi, K., Elzahrany, R., 2014. Projected impacts of land use and road network changes on increasing flood hazards using a 4D GIS: A case study in Makkah metropolitan area, Saudi Arabia. *In: Arab J Geosci* (2014) 7:1139–1156. DOI: 10.1007/s12517-013-0876-7

Eschbach, D., Grussenmeyer, P., Koehl, M., Guillemin, S., Schmitt, L., *under review*. Combining geodetic and geomorphic methods to monitor restored side channels: feedback from the Upper Rhine.

Hamshaw, S., D., Engel, T., Rizzo, D., M., O'Neil-Dunne, J. and Dewoolkar, M., 2019. Application of unmanned aircraft system (UAS) for monitoring bank erosion along river corridors, *In: Geomatics, Natural Hazards and Risk*, 10:1, 1285-1305, DOI:10.1080/19475705.2019.1571533

James, M. R., and Robson, S., 2012. Straightforward reconstruction of 3D surfaces and topography with a camera: Accuracy and geoscience application, *In: J. Geophys. Res.,117*, F03017, doi:10.1029/2011JF002289.

Jaud, M., Delacourt, C., Allemand, P., Grandjean, P., Ammann, J., Cancouët, R., Deschamps, A., Varrel, r., Cuq, V., and Suanez, S., 2014. DRELIO : Un drone hélicoptère pour le suivi des zones littorales. *In: Revue Paralia, 7*: s02.1-s02.12.

Lague, D., Launeau, P., Michon, C., Gouraud, E., Juge, C., Gentile, W., Crave, A., and Hubert-Moy, L., 2016. Le LiDAR aéroporté topo-bathymétrique pour la caractérisation et le suivi des corridors fluviaux : premiers résultats et perspectives. Journée Tehnique Avancées, apports et perspectives de la télédétection pour la caractérisation physique des corridors fluviaux.

Mallet, C., Bulteau, T., Maugard, F., Rosebery, D., Garnier, C., Mugica, J., Ayache, B., Hoareau, A., Bernon, N., Paris, F., and Nicolae Lerma, A. (2018). L'observatoire de la côte aquitaine : bases de données pour la compréhension des évolutions géomorphologiques. Journées Nationales Génie Côtier - Génie Civil 2018.

Murtiyoso, A., Koehl, M., Grussenmeyer, P., Freville, T., 2017. Acquisition and processing protocols for UAV images: 3D modeling of historical buildings using photogrammetry. *In: ISPRS Annals of the Photogrammetry, Remote Sensing and Spatial Information Sciences*, Volume IV-2/W2, 2017, pp. 163-170. doi:10.5194/isprs-annals-IV-2-W2-163-201

Nagle, D. B. and Wright, C. W. (2016). Algorithms used in the airborne LiDAR processing system (alps). *In: U.S. Geological Survey Open-File Report 2016-1046.*

Nex, F., Remondino, F., 2014. UAV: platforms, regulations, data acquisition and processing, in: Remondino, F., Campana, S. (Eds.), 3D Recording and Modelling in Archaeology and Cultural Heritage: Theory and Best Practices. Archaeopress,Oxford, England, pp. 73–86.

Pfeifer, N., 2007. Overview of TLS systems, overall processing and applications. ISPRS summer school 2007, 47(3): pp. 722-738.

Remondino, F., Barazzetti, L., Nex, F., Scaioni, M., Sarazzi, D., 2011. UAV photogrammetry for mapping and 3D modeling – Current status and future perspectives. *In: Int. Arch. of the Photogrammetry, Remote Sensing and Spatial Information Sciences*, Volume XXXVIII-1/C22, 2011, pp. 25-31.

Rivas Casado, M., Ballesteros González, R., Ortega, J. F., Leinster, P. and Wright, R., 2017. Towards a Transferable UAV-Based Framework for River Hydromorphological Characterization. *In: Sensors 2017, 17, 2210*, 22 pages. doi:10.3390/s17102210

Watts, A. C., Ambrosia, V. G., and Hinkley, E. A. (2012). Unmanned Aircraft Systems in remote sensing and scientfic research: classification and considerations of use. In: *Remote Sensing, 4*: pp. 1671-1692.

Watanabe Y., Kawahara Y., 2016. UAV photogrammetry for monitoring changes in river topography and vegetation. *In: Procedia Engineering 154 (2016)*, pp. 317 – 325. doi: 10.1016/j.proeng.2016.07.482

Annexe 3 : Abstract WLRI 4th Conference, 2021, Moscou

COUPLING TOPOGRAPHIC AIRBORNE LIDAR AND PHOTO-SIEVING METHODS FOR GRAIN-SIZE MAPPING

Piasny, G.[1], Chardon, V.[1], Garambois, P-A.[2], Finaud-Guyot, P.[3], Lague, D.[4], Schmitt, L[1]

[1] *CNRS UMR 7362 LIVE, University of Strasbourg, Strasbourg, France*
[2] *IRSTEA, Aix-en-Provence, France*
[3] *HydroSciences Montpellier, Polytech Montpellier, Montpellier, France*
[4] *CNRS UMR 6118 GEOSCIENCES Rennes, University of Rennes 1, Rennes, France*

Quantification and spatialization of grain size distribution (GSD) of riverbed surfaces is crucial for morpho-sedimentary survey and modeling, as well as ecological studies. Recently, new remote sensing methods were tested as UAV-Sfm and terrestrial LiDAR by using roughness metrics. However, these methods are not usable for river reaches of several tens of kilometers.

In this paper, we tested the capacity of an airborne topographic LiDAR to estimate the bed GSD using both roughness metric (rh) and return pulse intensity on two large gravel bed rivers with different grain size properties: the Old Rhine River (D_{50} = 27 to 130 mm and D_{84} = 33 to 180 mm) and the Moselle river (range D_{50} = 38 to 56 mm and range D_{84} = 44 to 64 mm). Field manual measurements (Wolman, 1954) were simultaneously performed to build statistical models between the two proxies and the field GSD. Photo-sieving was also used to calibrate Lidar data and to compare results of continuous and discontinuous GSD mapping.

Our results showed that both metrics can be used as proxies to accurately estimate the GSD on the two rivers. Photo-sieving can also be used to calibrate the airborne LiDAR surveys. Nevertheless, when automatic image treatment is aimed, particular attention should be paid to environmental conditions during field sampling, especially solar conditions (intensity and angle) and shooting distance.

The use of topographic LiDAR method offers the opportunity to map the GSD of emerged channel bars in addition to classical use of LIDAR i.e. accurate channel morphological characterization and sediment balance. These maps can be used for morphodynamic survey, hydraulic and sediment transport modelling, as well as riverine habitat characterization in order to integrate the variability of GSD in both longitudinal and lateral dimension.

Annexe 3 : Résumé colloque TSMR - CFBR, 2022, Paris

Combinaison de mesures acoustiques et de prélèvements sédimentaires pour le suivi de la charge de fond de rivières : application à la Moselle

Combining acoustic survey and sediment sampling to survey river bedload dynamics: application on the Moselle River

Auteur correspondant : **Guillaume PIASNY**, UMR 7362, CNRS-Université de Strasbourg-ENGEES, 3 rue de l'Argonne, 67000 Strasbourg, guillaume.piasny@live-cnrs.unistra.fr

Auteurs de la communication : **Thomas GEAY**, BURGEAP R&D, Grenoble, France
Sébastien ZANKER, EDF-DTG, Grenoble, France
Pierre-André GARAMBOIS, IRSTEA, Aix-en-Provence, France
Pascal FINAUD-GUYOT, HydroSciences Montpellier, Polytech Montpellier, France
Laurent SCHMITT, CNRS LIVE UMR 7362, Strasbourg, France

1. Introduction

La réserve naturelle régionale de la « Moselle Sauvage » s'étend sur 13 km au piémont occidental du massif vosgien. Le régime hydrologique de la rivière, de type pluvial océanique, se caractérise par de hautes eaux hivernales et printanières et des basses eaux estivales. Le lit mineur du tronçon étudié est méandriforme avec une sinuosité de 1,35. Sa pente moyenne est de 1,2 ‰ et sa largeur moyenne à plein bords de 60 m. La charge sédimentaire grossière est essentiellement issue de l'érosion des berges, dont les particules grossières présentent un D_{50} de 14mm. Bien que ce secteur soit relativement épargné d'actions anthropiques passées directes (endiguements, extractions de sédiments en lit mineur…), la propagation de réajustements morphodynamiques initiés par des actions effectuées en amont et en aval de ce secteur impacte le fonctionnement actuel de la réserve : érosions régressive et progressive, contraction du lit... Ces fronts d'érosion convergent aujourd'hui vers le secteur central de la réserve, ce qui a conduit à l'affaissement de la pile centrale du pont de Bainville-aux-Miroirs lors d'une crue biennale en 2011, et pourrait entraîner dans le futur une défluviation du lit mineur avec des risques significatifs pour des infrastructures. Dans ce contexte, l'étude dans laquelle s'inscrit cette communication vise à caractériser et anticiper les évolutions morphodynamiques de la Moselle pour proposer des scénarios de gestion et de restauration de la mobilité du cours d'eau. Pour cela, un modèle hydro-sédimentaire 2D est en cours de construction sur toute la zone, combiné à un suivi morpho-sédimentaire détaillé. Ce dernier consiste en des levés topo-bathymétriques (LiDAR), des mesures hydrologiques (limnimètres, ADCP), des mesures granulométriques (de surface et de subsurface) et un traçage sédimentaire (2500 pit-tags). Plusieurs méthodes innovantes *in situ* ont également été mises en œuvre pour suivre en continu la charge de fond, ce qui est un élément pertinent pour la calibration du modèle hydro-sédimentaire [2], bien que cela soit rarement réalisé. L'objectif de cette communication est (i) de présenter le protocole expérimental multi-méthodes ayant permis le suivi en continu de la charge de fond de la Moselle et (ii) de montrer les apports de cette approche pour la compréhension de la dynamique sédimentaire du linéaire fluvial étudié et pour sa modélisation.

2. Matériel et méthodes

Un hydrophone installé en mars 2018 sur la rive gauche de la Moselle, au droit du pont de Bainville-aux-Miroirs, enregistre en continu les bruits générés par l'écoulement et les sédiments charriés. Pour calibrer cette mesure continue mais localisée en pied de berge, des mesures acoustiques discontinues ont été effectuées à l'échelle de la section en travers selon la méthode de « jaugeage » proposée par Geay et al. [1]. Cette méthode permet de vérifier si la mesure du capteur situé en berge est représentative de la section complète. Dix campagnes de mesures acoustiques ont été conduites lors d'évènements hydrologiques ayant des périodes de retour comprises entre un et quatre ans (de 160 à 450 m^3/s). Enfin, dans le but de relier la puissance acoustique à un débit solide, trois campagnes de prélèvements directs ont été réalisées à l'aide d'un préleveur de type Helley-Smith pour des débits variant entre 220 et 290 m^3/s.

3. Résultats et perspectives

Une bonne corrélation est observée entre les prélèvements de la charge de fond et les mesures acoustiques le long de la section en travers (figure 1a). La relation obtenue entre la puissance acoustique et le débit solide, moyennés sur la section, est cohérente avec le modèle général proposé par Geay et al. [1]. Il est donc possible d'estimer le débit solide de la Moselle à l'aide des cartographies acoustiques et de comparer ces résultats à ceux de la modélisation. Par ailleurs, on constate que la mesure acoustique en berge est corrélée avec la moyenne des mesures acoustiques réalisées sur la section en travers, ce qui signifie que la mesure en berge est bien représentative de la section complète de la Moselle. Ainsi, l'ensemble des données acquises permet d'estimer en continu la charge de fond de la Moselle à Bainville-aux-Miroirs, ce qui offre la possibilité d'une étude fine de la dynamique temporelle de ce paramètre.

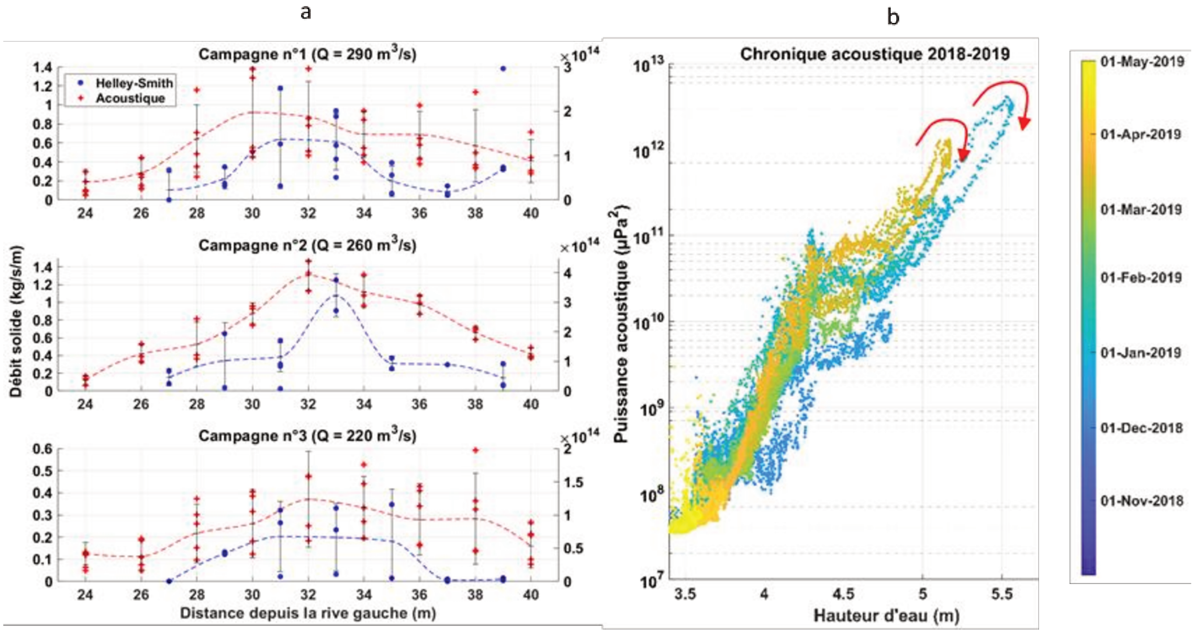

Figure 1 : Comparaison des mesures par prélèvements Helley-Smith et jaugeages acoustiques le long de la section en travers (a) et chronique de la variation de la puissance acoustique en fonction de la hauteur d'eau (b).

La figure 1b montre ainsi que la puissance acoustique (i.e. la charge de fond) est plus faible durant la phase de décrue que durant la phase de crue (facteur 5), pour un même niveau d'eau, ce qui traduit un effet d'hystérésis horaire (flèche rouge). Cet effet est particulièrement marqué lors de la première crue morphogène de la période des hautes eaux de l'hiver 2018-2019, après 6 mois d'étiage, mais il se répète également, avec une plus faible amplitude, lors les crues ultérieures. Par ailleurs, les résultats montrent que le charriage augmente progressivement, pour un niveau d'eau donné, d'une crue à l'autre, montrant que la succession des crues tend à faciliter la mobilisation des sédiments et à augmenter le flux sédimentaire. Ces résultats confirment que le seuil critique de mise en mouvement des sédiments varie, de crue morphogène en crue morphogène, au cours d'une même période de hautes eaux. La chronologie des crues est donc un paramètre important à prendre en compte dans l'étude de la dynamique morpho-sédimentaire du cours d'eau. L'intégration de ce phénomène dans la modélisation morpho-sédimentaire en cours d'élaboration, par la modulation du seuil critique de mise en mouvement, devrait donc permettre d'améliorer la modélisation de l'évolution morphodynamique de la Moselle.

REFERENCES

[1] Geay, T., Zanker, S., Misset, C., & Recking, A. (in review). Passive acoustic measurement of bedload transport: towards a global calibration curve? Journal of Geophysical Research: Earth Surface.

[2] Jodeau, M. (2007). Morphodynamique d'un banc de galets en rivière aménagée lors de crues (Thèse de doctorat). Université Claude Bernard – Lyon I.

Annexe 4 : Abstract AFEQ 13th Conference, 2022, Strasbourg

Hydro-Morphological Study and Modelling of the “Wild Moselle”

Guillaume PIASNY[1], Laurent SCHMITT[1], Pierre-André GARAMBOIS[2], Pascal FINAUD-GUYOT[3]

[1]LIVE Laboratory, CNRS-University of Strasbourg (UMR 7362), Strasbourg, France
[2]INRAE, Aix-en-Provence, France
[3]HydroSciences Montpellier, Polytech Montpellier, Montpellier, France

Abstract

The “Wild Moselle” is a regional nature reserve which extends over a length of 12.5 Km and includes one of the most dynamic sections of large river of North-East France. Although this meandering sector was relatively preserved from human activities, the propagation of upstream and downstream morphological adjustments initiated by past gravel mining carried out at the edge of the reserve affect the current functioning of the river. Regressive and progressive erosion fronts that converge to the central part of the reserve triggered channel contraction and incision as well as strong lateral erosion and meander cutoffs. This morphodynamic exhibits risks of capture of the main channel by floodplain gravel pits and river avulsion which may bypass a diversion dam and affect power generation. In order to anticipate and assess these impacts, a detailed morphodynamic diagnosis of the river is carried out, according to different spatial and temporal scales. A field monitoring has started in summer 2017, with topo-bathymetric surveys (topo-bathymetric LIDAR and drone photogrammetry), water level monitoring (13 limnimeters), gauging measurements (ADCP) and a survey of sedimentary dynamics (2500 RFID gravel tracers, bedload measurement using a Helley-Smith sampler, grain size measurements of both the surface and the subsurface layers, 2 hydrophones and 7 painted bed patches). At the same time, a 1D (HEC-Ras) and a 2D (Telemac/Sisyphe) hydro-sedimentary models where calibrated in order to reproduce observed dynamics and anticipate future evolutions of the study reach. On the basis of the combined two approaches (morphodynamic diagnosis and hydro-sedimentary models), various prospective scenarios of morphosedimentary evolution, for different hydrological forcing and management choices (e.g. removal of some bank protection, dam removal) are explored to assist managers to choose the most efficient and sustainable management options.

Keywords: Wild Moselle; Morphodynamic; Sediment transport; Hydro-sedimentary model

Guillaume PIASNY

Approche expérimentale et numérique en morphodynamique des cours d'eau : application à la gestion de la mobilité latérale de la Moselle sauvage

Résumé

Cette thèse porte sur le suivi et la modélisation de la morphodynamique du dernier tronçon de grand cours d'eau à lit mobile du nord-est de la France, situé au sein de la réserve naturelle régionale de la Moselle Sauvage. Bien que ce tronçon ait été relativement épargné d'actions anthropiques directes, la propagation de réajustements morphologiques initiés par des interventions effectuées en amont et en aval de ce secteur impacte le fonctionnement actuel de l'hydrosystème. Afin d'évaluer et d'anticiper ces impacts, un diagnostic hydromorphologique fin, reposant sur (i) une analyse historique, (ii) des mesures *in situ* multi-sources et (iii) des modélisations numériques, a été réalisé. La mise en cohérence modèle-données, réalisée selon une méthodologie inédite basée sur des échelles spatio-temporelles emboitées, a permis d'améliorer à la fois la connaissance des processus physiques et l'estimation des paramètres-clés du transport sédimentaire, tels que la contrainte critique de mise en mouvement et le taux de transport sédimentaire pour différentes tailles de particules. Ces travaux doivent permettre d'étudier différents scénarios de gestion, voire de restauration de la morphodynamique du cours d'eau.

Mots clés : morphodynamique, transport sédimentaire, modélisation hydro-sédimentaire.

Résumé en anglais

This thesis focuses on the monitoring and modeling of the morphodynamics of the last reach of a large mobile-bed river in northeastern France, located within the regional nature reserve of the "Wild Moselle." Although, this reach has been relatively spared from direct human activities, the propagation of morphological readjustments initiated by interventions carried out upstream and downstream of this sector impacts the current functioning of the hydrosystem. In order to assess and anticipate these impacts, a detailed hydromorphological diagnosis, based on (i) historical analysis, (ii) multi-source *in situ* measurements, and (iii) numerical modeling, was conducted. Achieving model-data consistency, using an innovative methodology based on nested spatio-temporal scales, has improved both the understanding of physical processes and the estimation of key parameters of sediment transport, such as the critical shear stress and the sediment transport rate for different particle sizes. This work aims to explore various management or restoration scenarios of the river morphodynamic.

Keywords: morphodynamic, sediment transport, hydro-sedimentary modeling.